Politecnico di Torino

ScuDo
Scuola di Dottorato ~ Doctoral School
WHAT YOU ARE, TAKES YOU FAR

Doctoral Dissertation
Doctoral Program in Civil and Environmental Engineering (38^{th}cycle)

Multi-scale Hyperspectral Characterisation of Mineral Systems Relevant to CRMs

Integration of Satellite Observations and Laboratory Analysis

By

Giorgia Carano

******

Supervisor(s):
Prof. Blengini Giovanni Andrea, Supervisor
Prof. Boccardo Piero, Co-Supervisor
Dott.ssa Claudia Baranzelli, Co-Supervisor

Doctoral Examination Committee:
Prof. van der Meijde Mark, Referee, University of Twente
Prof. Perotti Luigi, Referee, University of Turin

Politecnico di Torino
2026

Declaration

I hereby declare that, the contents and organization of this dissertation constitute my own original work and does not compromise in any way the rights of third parties, including those relating to the security of personal data.

Giorgia Carano
2026

* This dissertation is presented in partial fulfillment of the requirements for **Ph.D. degree** in the Graduate School of Politecnico di Torino (ScuDo).

A quo

Acknowledgements

I would like to begin by expressing my sincere gratitude to my supervisor, Giovanni Andrea Blengini, and to my co-supervisors Piero Boccardo and Claudia Baranzelli, for giving me the opportunity to undertake this PhD journey and for contributing, each in their respective roles, to my personal and professional growth over the past three years.

This research was carried out within a PhD scholarship funded by the Italian National Recovery and Resilience Plan (PNRR). In particular, this research was funded by the European Union – NextGenerationEU – Mission 4 "Education and Research" – Component 2 "From Research to Business" – Investment 3.1 "Fund for the realisation of an integrated system of research and innovation infrastructures" – Project IR0000037 – GeoSciences IR – CUP I53C22000800006.

In an initial moment of uncertainty — the first of many that one may encounter along a path of growth such as this — I would like to thank Susanna, who suggested that I attend the course "Geological Remote Sensing for Exploration and Mining Geologists", held in Istanbul in November 2023. Before that experience, Remote Sensing was something rather vague to me; it still is, perhaps, but a little less so, and with the reassuring awareness that there is always more to learn.

I am grateful to Bruno Portela who, by recognising this initial uncertainty, encouraged me to carry out my research period abroad at the institute where he works. This advice led me to Enschede, to the ITC at the University of Twente — a place that truly changed me. What was initially planned as a six-month experience turned into something much greater: a discovery, a surprise, and an inspiring environment that exceeded all expectations, to the point that I decided to extend my stay for an additional four months. In total, one year of my three-year PhD was spent in Enschede, a period that proved to be fundamental for my development.

I would therefore like to thank all the people at ITC who, each in their own way, supported and enriched me during this time. In particular, I would like to thank Bruno Portela and Harald van der Werff: I am deeply grateful for everything you taught me, for all that I had the opportunity to learn from you, and for your great patience. A special thanks goes to Arjan, without whom the entire laboratory component of this work would not have been possible.

I would also like to thank, in no particular order: Mark, Bart, Andries, Chris, Wim, Dinand, Ashok, Janneke, Hakan, Luigi, Frank, Camilla, Jonathan, Lise-Lotte, Karin and Kathrin. I would also like to express my sincere gratitude to Tshiningayamwe Mbili (University of Namibia), without whom it would not have been possible to obtain the twenty samples that were collected and shipped to the Netherlands for this research.

A heartfelt thank you goes to those who became friends and family during my time in Enschede: Tarlan, Mateo, Rodolfo and Janneka. To the four of you, my deepest thanks. We supported each other through everything, and we will continue to do so, even if our paths have temporarily diverged.

Thanks also to the rest of the "gang": Elinor, Sandy, Prajwal, Ali, Amin, Nestor, Yaser, Isaac, Tatenda, Anna, Nunzia, Shawn, Ghaliel, and all of his brothers, who were always ready to come to fix my bicycle and not only. All these people, together with many others I am surely forgetting, welcomed me and never made me feel alone: thank you from the bottom of my heart.

Back in Turin, I would like to thank my fellow PhD companions: Gyslain, Ghadi, David and Oveis. We worked along parallel paths, but sharing (at least part of) the office time with you was, honestly, a lot of fun.

A special thank you goes to my flatmate Andrea, for always supporting me and putting up with me, with a patience that should not be taken for granted.

I would also like to thank my close friends. First and foremost, Fabiana: more than a friend, you are a sister to me, without any exaggeration. I cannot imagine my life without you. Thank you as well to Flo and Annalisa, for always being there, each in your own way. I would also like to thank my cousin Filippo, with whom, despite living in the same city, I still manage to see far too little.

I am deeply grateful to Michele — together with Silvia and the little (now not-so-little) "fagiolino", who is almost three years old, because without you I would never

have managed to navigate the bureaucratic labyrinth and administrative procedures of the Politecnico.

A sincere thank you goes to the Wesson family — Brian and Amelia — for supporting my PhD experience and for giving me, over the years, the opportunity to learn so much across different geological contexts.

I would also like to thank my colleagues Riccardo, Tom and Jörg: you are not only a team, but also a family, and I truly love the moments we share together in the field.

My heartfelt thanks go to my family, who have always been a great source of support. We have argued, we still argue, and we probably always will, but you have never stood in the way of any of my choices. A special thank you goes to my brother Stefano, of whom I am immensely proud.

I would also like to thank Carol, a gentle soul, and Carmen, who is not only the best neighbour one could ever wish for, but has truly become a second mother to me.

Finally, I would like to acknowledge the person I met only recently, who has shared this final stretch of the journey with me and, perhaps, may also be part of what comes next — who knows.

Lastly, I would like to acknowledge myself, for not giving up when it would have been easier to do so, and for learning, slowly and sometimes painfully, when to persist and when to let go. This balance, more than any result, is perhaps the most valuable outcome of this journey.

I will stop here, fully aware that I have certainly forgotten someone, and also to avoid letting these acknowledgements become longer than the thesis itself. To all of you, my sincere and deepest thanks.

Abstract

The accelerating transition towards low-carbon energy systems and digital technologies is driving an unprecedented increase in demand for Critical Raw Materials (CRMs), intensifying pressure on global mineral supply chains and amplifying concerns related to supply security, geopolitical dependence, and environmental sustainability. In response, the European Union has placed CRMs at the core of its industrial and strategic agenda, emphasising the need for diversified sourcing, improved geological knowledge, and innovative exploration approaches capable of supporting early-stage decision-making while minimising environmental impact.

Within this framework, this thesis investigates the potential of satellite-based hyperspectral remote sensing to contribute to CRMs exploration, with a particular focus on the Earth Surface Mineral Dust Source Investigation (EMIT) mission. EMIT provides contiguous hyperspectral coverage across the visible to short-wave infrared (VNIR–SWIR) range at 60 m spatial resolution, enabling the detection of subtle mineralogical variations that are difficult to resolve using conventional multispectral data.

The research adopts a multi-scale and multi-method approach integrating satellite hyperspectral observations, laboratory hyperspectral imaging, point-based reflectance spectroscopy, X-ray diffraction, and geochemical screening by portable X-ray fluorescence. Two complementary case studies located in southern Namibia are used to assess the applicability of hyperspectral techniques across spatial scales and geological settings. The first case study focuses on the Haib porphyry copper system, where EMIT data are employed to investigate hydrothermal alteration patterns through the analysis of spectral shifts in the Al–OH absorption feature of white micas at around 2200 nm. Variations in the wavelength position of this feature provide insights into compositional changes in muscovite related to alteration intensity and fluid evolution, allowing mineralogical zonation associated with porphyry-style mineralisation to be

assessed using transparent and unsupervised approaches such as wavelength mapping and band ratios.

The second case study targets carbonatite-hosted mineralisation along the Kudu Lineament. EMIT observations are complemented by detailed laboratory-scale analyses conducted on twenty carbonatite hand specimens from the Dicker Willem complex. These analyses include SWIR-based carbonate mineral classification using wavelength mapping and decision tree approaches, as well as VNIR investigations aimed at identifying neodymium-related absorption features. Laboratory hyperspectral imaging, point spectroscopy using a Halo spectrometer, and mineralogical and geochemical characterisation provide essential validation for the interpretation of spectral signatures observed.

Results demonstrate that EMIT hyperspectral imagery is effective in mapping mineralogical variability and alteration assemblages at regional scale in arid and semi-arid environments. In the carbonatite case study, however, neodymium-related spectral features are not directly detectable in EMIT data, likely due to the combined effects of spatial resolution, spectral mixing, and the dominance of other mineral phases at the pixel scale. At laboratory scale, neodymium can exhibit diagnostically useful VNIR absorption features under favourable conditions; nevertheless, high elemental concentrations measured by geochemical screening do not necessarily translate into clear spectroscopic signatures. Grain size, mineralogical context, phase mixing, and signal-to-noise limitations have a strong control on the detectability of rare earth element features in hyperspectral data.

Overall, this work highlights both the opportunities and current limitations of spaceborne hyperspectral remote sensing for CRMs exploration. By systematically integrating satellite-scale observations with laboratory-based validation, the thesis provides a robust framework for linking European raw materials policy objectives with practical, scalable, and environmentally responsible exploration methodologies.

Contents

List of Figures

List of Tables

Nomenclature

Roman Symbols

BOA Bottom of Atmosphere

CRMs Critical Raw Materials

DN Digital Number

EI Economic Importance

EMIT Earth Surface Mineral Dust Source Investigation

EU European Union

HREE Heavy Rare Earth Elements

ICP-MS Inductively Coupled Plasma Mass Spectrometry

IR Infrared

LREE Light Rare Earth Elements

LWIR Long-Wave Infrared

MWIR Mid-Wave Infrared

MWM Minimum Wavelength Mapper

REE Rare Earth Elements

REO Rare Earth Oxides

RMI Raw Materials Initiative

ROI Region of interest

RS Remote Sensing

SR Supply Risk

SRMs Strategic Raw Materials

SWIR Short-Wave Infrared

TIR Thermal Infrared

TOA Top of Atmosphere

VNIR Visible and Near-Infrared

XRD X-Ray Diffraction

XRF X-Ray Fluorescence

Greek Symbols

λ Wavelength

c Speed of light

Chapter 1

Critical Raw Materials and Sustainable Mineral Exploration

1.1 Critical Raw Materials in the European Green and Digital Transition

The global transition towards low-carbon energy systems and digital technologies is fundamentally reshaping patterns of resource consumption and placing unprecedented pressure on mineral supply chains. Unlike conventional fossil fuel–based energy systems, renewable energy technologies, electric mobility, and digital infrastructures are inherently material-intensive, requiring large quantities of mineral raw materials. As a consequence, access to reliable and secure supplies of these materials has emerged as a central challenge for modern economies [1].

Future demand trends indicate a significant intensification of this pressure. According to OECD projections, global material demand is expected to more than double, increasing from approximately 79 billion tonnes today to 167 billion tonnes by 2060. This rapid growth is anticipated to exacerbate global competition for mineral resources, increasing the likelihood of supply constraints and geopolitical tensions. Raw materials form the starting point of all industrial value chains; disruptions at this initial stage can therefore propagate throughout entire economic sectors [2].

In response to these emerging challenges, the European Commission has developed a structured framework to assess the criticality of raw materials based on two key criteria: *Economic Importance* (EI) and *Supply Risk* (SR), as schematically illustrated in Fig. 1.1. Economic Importance reflects the role of a material across industrial value chains and its contribution to economic activity, whereas Supply Risk captures the likelihood of supply disruption. The latter accounts for factors such as production concentration, governance conditions in supplier countries, trade restrictions, import reliance, and recycling rates [2].

The criticality assessment methodology was developed by the European Commission in cooperation with the *Ad hoc Working Group on Defining Critical Raw Materials* (AHWG) and formally adopted in 2017. Within this framework, materials are evaluated quantitatively using the EI and SR indicators and are classified as critical when both exceed predefined threshold values, namely SR $\geq$ 1.0 and EI $\geq$ 2.8 (rounded to one decimal). This approach ensures a transparent and reproducible assessment of criticality and allows for periodic updates to reflect changes in market conditions, technological developments, and global supply dynamics.

Many raw materials exhibit highly concentrated production and processing stages, often dominated by a limited number of countries. Such structural concentration increases exposure to geopolitical instability, trade disruptions, and market volatility, rendering supply chains particularly vulnerable to external shocks. Recent global events have further highlighted these vulnerabilities, underlining the importance of robust and well-informed methodologies for assessing supply risk and economic relevance [2].

Beyond supply security, the increasing demand for mineral raw materials raises important sustainability concerns. Expanding production to meet future demand must be balanced against the need to minimise environmental impacts, reduce land disturbance, and ensure responsible sourcing practices. These considerations emphasise the importance of improving geological knowledge and exploration efficiency, particularly at early stages of the resource development cycle, when strategic decisions regarding land use and investment are made.

In this context, enhancing the understanding of mineral systems and their spatial distribution represents a prerequisite for informed decision-making and long-term resource management. Advanced exploration approaches capable of operating at regional to local scales, while limiting environmental impact, are therefore increasingly

relevant. Among these, remote sensing and hyperspectral techniques offer significant potential to support the identification and characterisation of mineral resources, providing a foundation for more targeted, efficient, and responsible exploration strategies.

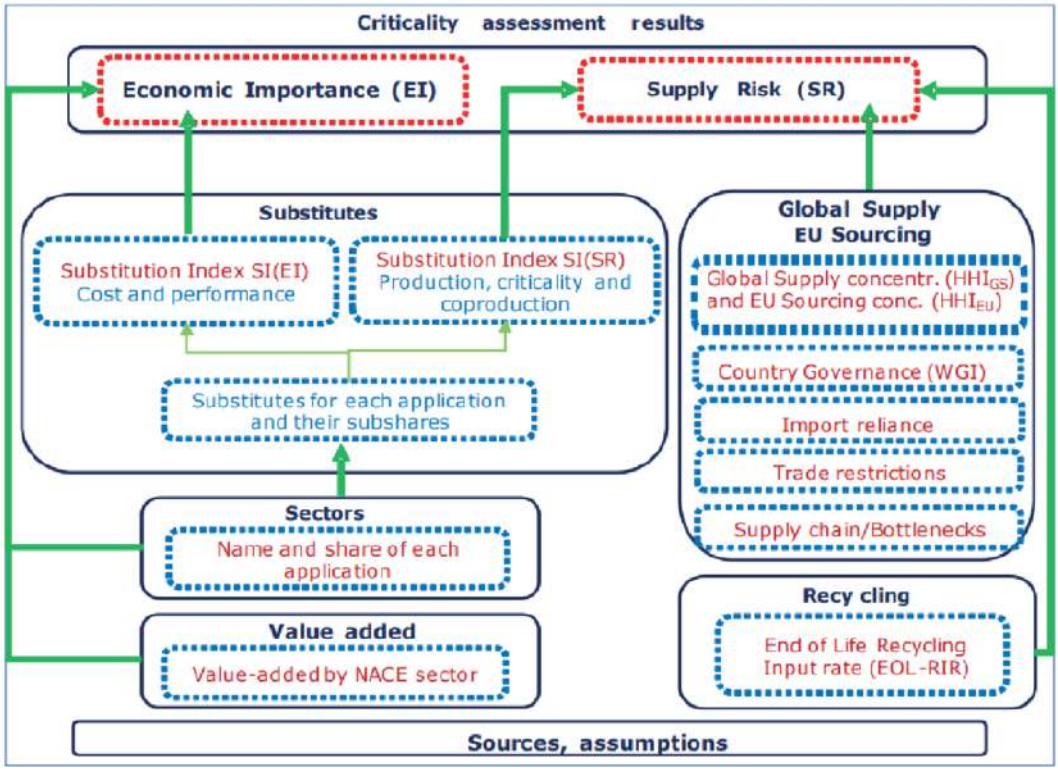

Fig. 1.1 Schematic representation of the criticality assessment framework, illustrating the components contributing to Economic Importance (EI) and Supply Risk (SR), including substitution, global supply and EU sourcing, sectoral value added, and end-of-life recycling (from [2]).

1.2 The EU Critical Raw Materials Act: from Dependency to Strategic Autonomy

In response to growing supply risks and intensifying global competition for mineral resources, the European Union has progressively strengthened its policy framework on CRMs. This process culminated in the proposal of the Critical Raw Materials Act (CRM Act) in March 2023 and its subsequent entry into force on 23 May 2024,

representing a cornerstone of the EU's strategy to enhance economic resilience, industrial competitiveness, and strategic autonomy [2, 3].

The CRM Act builds upon more than a decade of policy development initiated under the EU Raw Materials Initiative (RMI) launched in 2008. One of the primary objectives of the RMI was to establish a systematic and transparent assessment of raw material criticality at the EU level, supporting a diversification strategy for securing non-energy raw materials essential to European industrial value chains and societal well-being. As part of this effort, the European Commission introduced a periodically updated list of CRMs, first published in 2011 and revised every three years to reflect evolving market conditions, technological developments, and geopolitical dynamics.

The successive criticality assessments illustrate a clear upward trend in both the number of materials evaluated and those identified as critical. The 2011 assessment identified 14 CRMs out of 41 candidate materials; this number increased to 20 out of 54 in 2014, 27 out of 78 in 2017, and 30 out of 83 in 2020. The most recent assessment, published in 2023, represents the fifth iteration and evaluated 70 candidates, comprising 67 individual materials and three material groups (ten heavy rare earth elements, five light rare earth elements, and five platinum-group metals). Of these, 34 materials were identified as CRMs [2] as shown in Fig. 1.2.

A key conceptual advancement introduced in the 2023 assessment is the distinction between Critical Raw Materials and Strategic Raw Materials (SRMs). SRMs represent a priority subset of CRMs that are considered vital for the deployment of green, digital, and defence technologies and for safeguarding the EU's long-term industrial and technological sovereignty. 17 of the 34 CRMs identified in 2023 were designated as strategic, reflecting their particularly high relevance for future-oriented value chains [2].

The CRM Act translates these assessments into a legally binding framework aimed at addressing the EU's structural dependence on external suppliers. For many CRMs, extraction, processing, and refining activities are highly concentrated in a small number of countries, exposing European industries to geopolitical risks, trade restrictions, and potential supply disruptions. Rather than pursuing full resource self-sufficiency, the Act promotes a model of "open strategic autonomy", seeking to reduce excessive dependencies while maintaining diversified and resilient global supply chains [3].

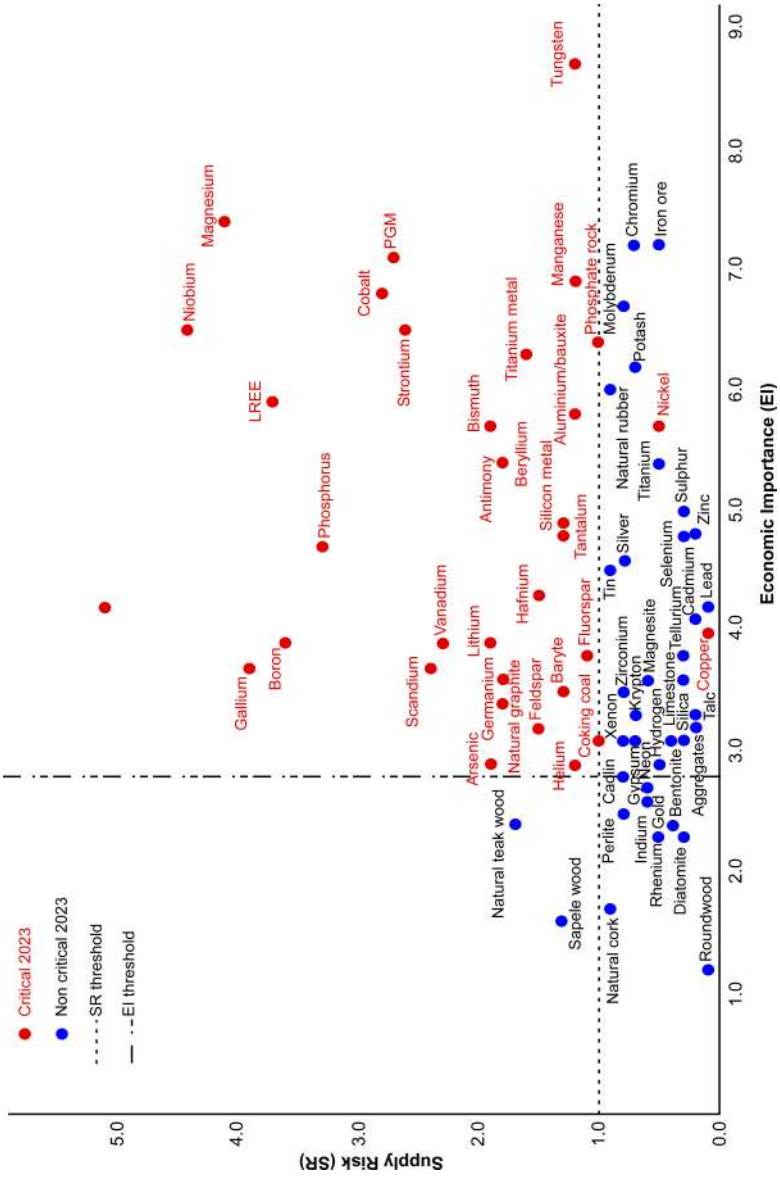

Fig. 1.2 Results of the European Union 2023 criticality assessment of raw materials, illustrating their classification based on economic importance and supply risk. Red symbols indicate materials classified as critical, while blue symbols represent non-critical materials. Dashed lines denote the threshold values used by the European Commission to define criticality. Materials plotted in the upper-right quadrant exceed both thresholds and are therefore identified as Critical Raw Materials (CRMs). Notably, copper and nickel do not exceed the criticality thresholds and are thus not classified as CRMs; however, they are included in the EU list of Strategic Raw Materials due to their essential role in the energy transition and industrial applications. (modified from [2]).

To operationalise these objectives, the CRM Act establishes clear quantitative benchmarks to be achieved by 2030. These include the targets that at least 10% of the EU's annual consumption of CRMs should originate from domestic extraction, 40% from processing within the EU, and 25% from recycling. In addition, the Act sets a diversification threshold whereby no more than 65% of the EU's annual consumption of any single CRM may be supplied by one third country [2, 3]. Together, these targets reflect a comprehensive value-chain approach, integrating primary production, processing capacity, and circular economy principles.

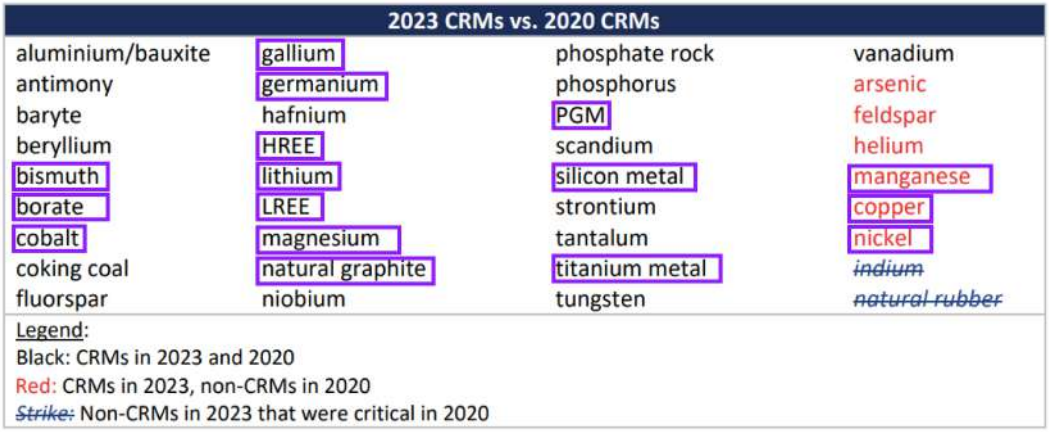

Fig. 1.3 Comparison between the CRMs lists adopted by the European Union in 2020 and 2023. Materials shown in black were classified as critical in both assessments, while materials highlighted in red represent newly identified CRMs in the 2023 update. Materials shown with strikethrough indicate those that were classified as critical in 2020 but are no longer considered CRMs in 2023. Purple boxes highlight materials that were additionally designated as Strategic Raw Materials in the 2023 assessment, reflecting their key role for the green and digital transition and for the EU's strategic autonomy (modified from [2]).

A further central pillar of the CRM Act is the identification and support of Strategic Projects, defined as initiatives that make a significant contribution to the security of supply of Critical and SRMs. Such projects may involve mining, processing, recycling, or substitution activities and can be located both within the EU and in partner countries. To accelerate their implementation, the Act introduces measures to streamline permitting procedures, improve access to financing, and enhance coordination among Member States. At the same time, Strategic Projects are required to comply with stringent environmental, social, and governance (ESG) standards, ensuring that supply security objectives are aligned with sustainability and responsible sourcing principles [3].

Overall, the CRM Act marks a shift from reactive criticality assessment towards a proactive and integrated policy framework. By combining quantitative targets, strategic project support, and high sustainability standards, the Act seeks to strengthen the EU's capacity to secure reliable and sustainable access to mineral resources that are essential for the green and digital transition.

1.3 Strategic Supply Chains, Corridors, and International Partnerships

The increasing strategic importance of Critical and Energy Materials has brought renewed attention to the spatial configuration of global supply chains and to the infrastructures that support them. The extraction, processing, and transport of mineral resources are embedded within complex transnational networks whose efficiency and resilience depend not only on geological endowment, but also on logistics, political stability, regulatory frameworks, and institutional cooperation. In this context, the EU has progressively adopted a territorial perspective on raw material security, recognising that supply resilience is strongly conditioned by the spatial organisation of infrastructure, production areas, and trade routes.

Recent studies have emphasised the role of transport and economic corridors as key enablers of secure and diversified supply chains. These corridors integrate mining districts with ports, processing facilities, and industrial hubs, thereby linking resource-rich regions to global markets. Within European policy discussions, strategic corridors have emerged as critical components of the EU's external dimension of raw materials security, particularly in relation to partnerships with resource-rich third countries [4].

The concept of a resource corridor extends beyond the notion of physical infrastructure. According to the World Bank, a resource corridor can be defined as "a sequence of investments and actions to leverage a large extractive industry investment in infrastructure, goods and services into viable economic development and diversification along a specific geographic area" [5]. This definition highlights the multifunctional nature of corridors, which combine transport infrastructure with institutional arrangements, investment flows, and governance mechanisms aimed at supporting broader territorial development.

Building on this framework, Baranzelli et al. [6] introduced the concept of EU–Africa Strategic Corridors, which further expands the corridor notion to include not only linear infrastructure elements, but also the surrounding territories influenced by them. From this perspective, strategic corridors encompass adjacent rural and urban areas, forming integrated spatial systems that support the development of value chains, enhance territorial organisation, and foster economic diversification. These corridors are intended to facilitate mobility and trade both within Africa and between Africa and Europe, while creating employment opportunities and strengthening industrial linkages across regions.

Large-scale investments in cross-border corridors have become a priority for African governments, Regional Economic Communities, and the African Union, as well as for the European Union in the context of EU–Africa cooperation [4]. To support this process, the European Commission has developed an ad hoc methodology to identify and characterise Strategic Corridors using a wide range of indicators, more than 140, derived from large, multi-source datasets. This approach explicitly recognises the role of the mining sector and mineral resource aspect as key components in corridor identification and prioritisation.

Within this broader framework, Southern Africa represents a region of particular strategic relevance. The area hosts a wide range of mineral resources, including base metals, rare earth elements, and other materials considered critical or strategic for the European economy. Among Southern African countries, Namibia has emerged as a key partner for the EU due to its geological potential, relative political stability, and established mining sector. Recent bilateral agreements and strategic partnerships between the EU and Namibia explicitly emphasise cooperation on raw materials, renewable energy, and sustainable development as shared priorities [7].

Two of the potential EU–Africa Strategic Corridors identified by the European Commission intersect Namibia: the Lüderitz–Johannesburg–Durban corridor and, further north, the Walvis Bay–Kinshasa corridor [4]. Those corridors constitute a strategically significant axis linking inland mineral provinces of southern Namibia to the Atlantic coast. As discussed by Baranzelli et al. [4], this corridors play a central role in facilitating the transport of mineral resources towards export terminals, while also supporting broader regional development objectives. The spatial coincidence of mineral occurrences, infrastructure, and logistics along this corridor underscores its

relevance for both national development strategies and European efforts to diversify raw material supply chains.

The integration of strategic corridors into the EU's raw materials policy highlights the growing interdependence between geology, infrastructure, and geopolitics. Understanding the distribution, characteristics, and variability of mineral resources along these corridors is therefore a prerequisite for informed policy-making and investment decisions.

1.4 Mineral Exploration, Sustainability, and the Role of Remote Sensing

Securing a stable supply of CRMs requires not only diversification of supply chains and international partnerships, but also a transformation of mineral exploration strategies. Traditional exploration methods, while effective at local scales, are often time-consuming, costly, and associated with significant environmental disturbance. In the context of increasing sustainability requirements and stricter environmental regulations, there is a growing need for exploration approaches that can support early-stage resource assessment while minimising physical impact on the environment [8, 9].

The CRM Act explicitly recognises the importance of improving geological knowledge and exploration efficiency as a foundation for secure and sustainable supply chains. Early-stage exploration plays a crucial role in reducing uncertainty and guiding subsequent investment decisions, yet it is also the phase at which broad spatial coverage and rapid screening of prospective areas are most needed. In this respect, exploration technologies capable of operating at regional to continental scales are particularly valuable, especially in remote or underexplored regions where access is limited.

Remote sensing has long been recognised as a strategic tool for geological investigations and mineral exploration. By exploiting the interaction between electromagnetic radiation and surface materials, remote sensing enables the identification of lithological variations, structural features, and mineralogical assemblages associated with ore-forming processes. Optical and hyperspectral remote sensing, in particular, provide direct information on surface mineralogy through diagnostic spec-

tral absorption features, allowing the detection and mapping of alteration minerals [8, 10, 11].

Beyond its technical capabilities, remote sensing aligns closely with the sustainability objectives embedded in contemporary resource policies. As a non-invasive and repeatable technique, it allows large areas to be assessed without ground disturbance, thereby reducing the environmental footprint of exploration activities. Satellite-based observations also enable systematic and consistent monitoring over time, supporting responsible resource management and informed land-use planning. These characteristics make remote sensing particularly well suited to the early phases of exploration within strategically important regions, such as those associated with CRMs corridors and international supply networks.

Recent advances in sensor technology, data availability, and processing techniques have further expanded the role of remote sensing in mineral exploration. The emergence of spaceborne hyperspectral missions provides unprecedented opportunities to investigate mineralogical variability at regional scales, bridging the gap between traditional field-based studies and large-scale geological assessments. Within the framework of the EU's raw materials strategy, such technologies offer a powerful means to support exploration, enhance geological knowledge, and contribute to the development of secure and more sustainable CRMs supply chains.

1.5 Thesis Motivation and Objectives

The evolving geopolitical, economic, and environmental context surrounding CRMs highlights the need for innovative mineral exploration approaches that are both effective and sustainable. While policy frameworks such as the EU CRM Act emphasise secure supply chains, strategic partnerships, and improved geological knowledge, practical tools capable of supporting these objectives at appropriate spatial scales remain essential. In particular, there is a growing demand for exploration methodologies that can operate efficiently over large and often remote regions, while minimising environmental impact and supporting early-stage decision-making.

Within this framework, the motivation of this thesis is to evaluate the potential of satellite-based hyperspectral remote sensing as a tool for detecting and characterising subtle mineralogical variations relevant to CRMs exploration. Particular attention is

given to recent advances in spaceborne hyperspectral imaging, with a focus on data acquired by the *Earth Surface Mineral Dust Source Investigation* (EMIT) sensor. EMIT provides contiguous spectral information in the visible to shortwave infrared range at unprecedented spectral resolution for a spaceborne platform, offering new opportunities for mineralogical investigations at regional scale.

The research explores whether EMIT hyperspectral data can deliver meaningful geological insights that were previously achievable mainly through airborne surveys or detailed field-based investigations. To address the inherent limitations of satellite data, this study adopts a multi-scale approach that integrates spaceborne observations with laboratory-based analyses of hand specimens.

The primary objectives of this thesis are therefore to:

(i) investigate the capability of EMIT satellite-based hyperspectral remote sensing data to identify and map diagnostic mineralogical features potentially associated with CRMs, and to evaluate their applicability through selected case studies located in strategically relevant regions;

(ii) evaluate the effectiveness of relatively simple and transparent analytical approaches, such as wavelength mapping, spectral indices, and band ratios, in capturing compositional variations within key mineral groups;

(iii) assess the added value of integrating spaceborne hyperspectral observations with laboratory-scale analyses, including X-ray diffraction (XRD), portable X-ray fluorescence (pXRF), and hyperspectral imaging of hand specimens.

By addressing these objectives, this work aims to contribute to the broader effort of integrating advanced remote sensing technologies into sustainable mineral exploration workflows. In doing so, the thesis seeks to bridge the gap between European raw materials policy objectives and practical, scalable exploration tools, while highlighting the importance of linking regional-scale satellite observations with detailed laboratory-scale mineralogical characterisation.

Chapter 2

Remote Sensing as a Strategic Technology for Mineral Exploration

2.1 Introduction

Remote sensing (RS) has been defined in several ways within the scientific literature. A widely accepted definition describes it as the acquisition of information about the Earth's surface without direct physical contact, achieved through the detection, recording, and analysis of reflected or emitted electromagnetic energy [12]. A complementary perspective frames RS as the science of acquiring, processing, and interpreting images and related data collected by aircraft and satellites, documenting the interaction between electromagnetic radiation and matter [8, 11]. Together, these definitions emphasise both the physical foundations of remote sensing and its analytical and interpretative dimensions, which underpin its application to geological and mineral exploration.

Remote sensing operates through a sequence of processes that describe how electromagnetic energy is generated, modified, and ultimately recorded as usable information. The process begins with an external energy source, typically the Sun, whose radiation propagates through the atmosphere and undergoes wavelength-dependent scattering and absorption by gases, aerosols, and suspended particles (Fig. 2.1). These atmospheric interactions selectively attenuate portions of the electromagnetic spectrum, allowing only specific wavelength intervals to reach the Earth's surface.

Once incident radiation interacts with surface materials, it is partitioned into reflected, absorbed, and transmitted components according to their physical and chemical properties.

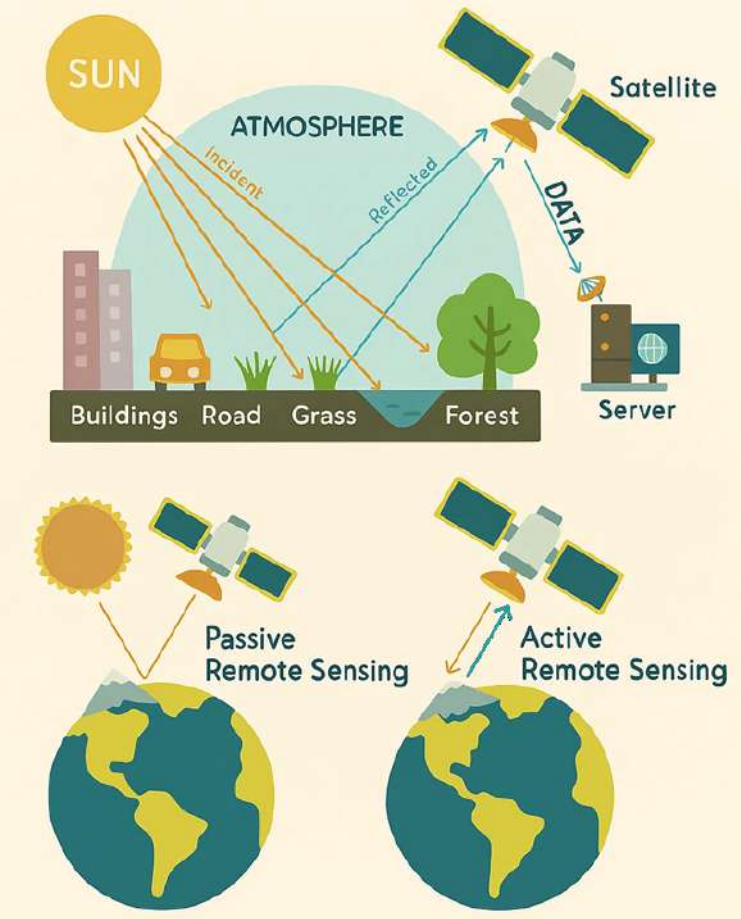

Fig. 2.1 Schematic representation of the remote sensing process, illustrating the interaction of solar radiation with the Earth's surface and atmosphere, the recording of reflected or emitted energy by satellite sensors, and the distinction between passive and active remote sensing systems.

From a physical perspective, these interactions obey the principle of energy conservation, whereby the incident electromagnetic energy at a given wavelength is distributed as:

$$E_{\text{Incident}}(\lambda) = E_{\text{Reflected}}(\lambda) + E_{\text{Absorbed}}(\lambda) + E_{\text{Transmitted}}(\lambda) \tag{2.1}$$

These interactions can be summarised into three fundamental behaviours:

1. **Transmission**, whereby a fraction of the incident energy passes through the atmosphere and, depending on material properties, may also penetrate the surface;

2. **Absorption**, during which energy is taken up by atmospheric constituents or surface materials through electronic or molecular excitation and may later be re-emitted as thermal radiation;

3. **Reflection and scattering**, where energy is redirected away from the surface, ranging from specular to diffuse behaviour depending on surface roughness, composition, and illumination geometry.

Remote sensing instruments record reflected or emitted electromagnetic radiation across a broad wavelength range, typically from the ultraviolet to the microwave domain. In the visible to near-infrared (VNIR) region, the recorded signal is dominated by reflected solar radiation and controlled primarily by electronic transitions, generally producing broad absorption features. In the short-wave infrared (SWIR), reflected radiation is influenced by molecular vibrational processes, resulting in narrower and more diagnostic absorption features. At longer wavelengths, the thermal infrared (TIR) region is characterised predominantly by emitted radiation related to vibrational processes, reflecting both solar heating and intrinsic thermal properties of surface materials [9].

The placement of RS instruments within specific portions of the electromagnetic spectrum is strongly constrained by atmospheric transmission windows, defined as wavelength intervals in which atmospheric absorption and scattering are minimised. These windows allow radiation to propagate efficiently between the Earth's surface and the sensor, and therefore largely determine which spectral regions can be exploited for optical and thermal remote sensing applications.

After surface interaction, the modified electromagnetic energy travels back through the atmosphere toward sensors onboard satellites or aircraft, where it is recorded digitally. The physical quantity measured by remote sensing instruments is radiance, defined as the amount of electromagnetic energy received per unit area, per unit solid angle, per unit time, and per unit wavelength interval. However, remotely sensed data are commonly distributed as digital numbers (DNs), which are dimensionless values proportional to radiance and dependent on sensor-specific characteristics.

To obtain geophysically meaningful variables suitable for quantitative analysis, several calibration and correction steps are required. These typically include:

1. **Radiometric calibration**, converting DN values into top-of-atmosphere (TOA) radiance using sensor-specific gain and offset parameters;
2. **Atmospheric correction**, compensating for scattering and absorption by atmospheric gases, aerosols, and water vapour to retrieve surface radiance or surface reflectance;
3. **Illumination correction**, accounting for variations in solar geometry and topography to improve spectral consistency across scenes.

Surface reflectance, defined as the ratio between reflected and incident radiation, represents a dimensionless quantity that allows direct comparison of spectral properties across space, time, and different sensors. Its retrieval is therefore a prerequisite for mineralogical and spectral analyses based on RS data.

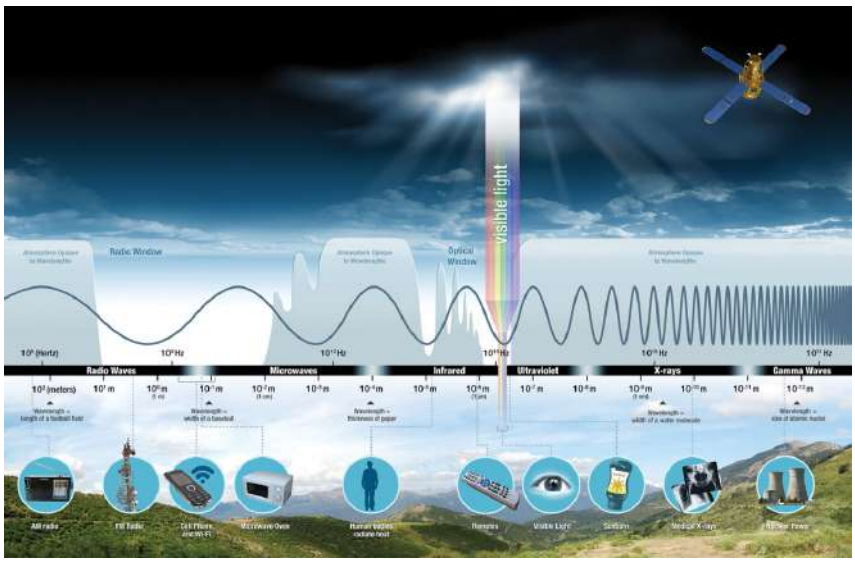

Fig. 2.2 View of the electromagnetic spectrum (https://science.nasa.gov/ems/01_intro/).

Electromagnetic radiation consists of two mutually perpendicular oscillating fields, an electric field and a magnetic field, both orthogonal to the direction of propagation (Fig. 2.3). These waves travel through space at the speed of light (c), and their behaviour is described by the fundamental relationship:

$$c = \lambda \nu \tag{2.2}$$

where λ denotes wavelength and ν frequency.

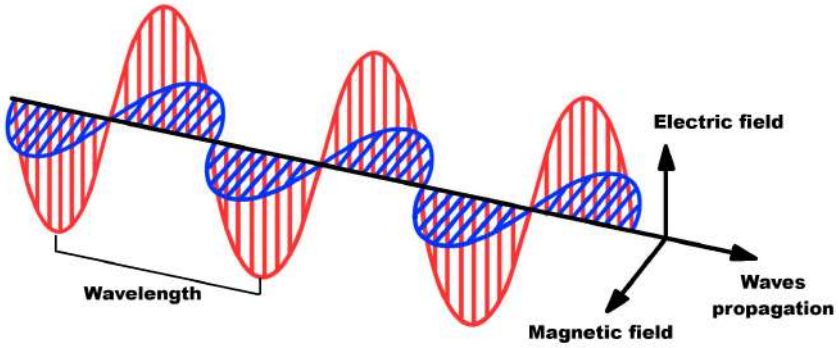

Fig. 2.3 Schematic representation of an electromagnetic wave, showing the oscillating electric and magnetic fields perpendicular to each other and to the direction of wave propagation.

The visible portion of the electromagnetic spectrum, spanning approximately 0.4–0.7 μm, represents only a small fraction of the total spectrum but forms the basis of human vision and conventional optical imaging. Beyond the visible region lies the infrared (IR) domain, which extends roughly from 0.7 to 100 μm and is commonly subdivided into reflected infrared (VNIR and SWIR) and thermal infrared (MWIR and LWIR). At even longer wavelengths, the microwave region underpins active remote sensing systems such as radar and synthetic aperture radar (SAR), enabling data acquisition independent of illumination and weather conditions.

RS systems can be broadly classified into passive and active sensors depending on the energy source employed. Passive sensors rely on natural radiation, primarily solar illumination or Earth-emitted thermal energy, whereas active sensors emit their own energy and measure the returned signal. This distinction has important implications for data availability, spatial resolution, and application domains.

Earth observation satellites operate in a range of orbital configurations selected according to mission objectives, including geostationary, low Earth, and Sun-synchronous orbits. In particular, low Earth and Sun-synchronous orbits are widely used for optical and hyperspectral missions due to their favourable balance between spatial resolution, global coverage, and revisit frequency.

The utility of remotely sensed data is governed by four fundamental resolution types: spatial, spectral, temporal, and radiometric resolution. Spatial resolution controls the smallest detectable surface feature, spectral resolution defines the number and width of spectral bands, temporal resolution determines revisit frequency, and radiometric resolution specifies the sensor's ability to discriminate subtle differences in energy intensity.

In digital imagery, the recorded signal is initially expressed as a **Digital Number (DN)**, whose range depends on the sensor's radiometric resolution:

$$0 \leq \mathrm{DN} \leq (2^n - 1) \tag{2.3}$$

To enable quantitative analysis, DN values must be converted into radiance using sensor calibration parameters:

$$L_\lambda = \frac{\mathrm{DN} - \mathrm{offset}}{\mathrm{gain}} \tag{2.4}$$

where L_λ is the spectral radiance at wavelength λ, and *gain* and *offset* are sensor-specific coefficients. This conversion represents a necessary intermediate step toward the retrieval of surface reflectance, which forms the basis for the spectral analysis methods employed in this research.

2.2 Remote Sensing for Geology and Mineral Exploration: State of the Art

RS has become a strategic tool in geological mapping and mineral exploration, enabling the detection of lithological variations, structural features, and alteration patterns over extensive areas. The principal motivation for its application to geology lies in the ability to map minerals and retrieve compositional information directly from the Earth's surface [10]. Much of the methodological development in the visible to VNIR, SWIR, MWIR, and TIR domains builds upon foundational laboratory spectroscopy studies by Hunt and Salisbury [13, 14], which established the diagnostic spectral basis for optical mineral identification.

The earliest geological applications of satellite RS date back to the launch of the Landsat Multispectral Scanner (MSS) in 1972. Early studies exploited simple VNIR band ratios to identify iron-oxide anomalies and broad lithological contrasts [15], following pioneering work that demonstrated the geological utility of ERTS (Earth Resources Technology Satellite) imagery [16]. These initial applications laid the foundation for the systematic use of satellite data in geological mapping.

A major advance occurred with the introduction of the Landsat Thematic Mapper (TM) in 1982, which significantly enhanced the capability to map lithology, structural features, and hydrothermal alteration. The addition of SWIR bands enabled more targeted discrimination of alteration minerals, and analytical techniques such as band ratios, decorrelation stretch, saturation enhancement, and principal component analysis proved highly effective in enhancing mineralogical and structural contrasts [10]. For example, the TM band 7/band 5 ratio remains widely used to highlight argillic alteration, while the band 3/band 1 ratio is commonly employed to emphasise iron-oxide–bearing surfaces [10].

A further milestone was the launch of the Advanced Spaceborne Thermal Emission and Reflectance Radiometer (ASTER) aboard NASA's Terra platform in 1999 [17–19]. ASTER's sensor configuration, comprising three VNIR bands at 15 m spatial resolution, six SWIR bands at 30 m, and five TIR bands at 90 m, markedly improved the mapping of alteration-related mineral groups. Its 60 km swath width, revisit interval of less than 16 days, and VNIR stereo capability made ASTER particularly well suited for regional geological investigations and topographic support [10]. Demonstrating its performance, Mars and Rowan [20] showed that ASTER effectively discriminates major hydrothermal alteration assemblages at sites such as Cuprite (Nevada) and Mountain Pass (California), including argillic (kaolinite, alunite, dickite), phyllic (sericite), and propylitic (calcite, epidote, chlorite) minerals. They also noted, however, that ASTER's spectral configuration limits fine-grained discrimination between compositionally similar minerals such as kaolinite and alunite [10].

Despite their accessibility and long-standing use, multispectral sensors such as Landsat, ASTER, and Sentinel-2 are constrained by their broad and discontinuous spectral bands. These limitations restrict the retrieval of detailed mineralogical information and hinder the detection of subtle compositional variations within alteration minerals [21, 10, 22]. The conceptual difference between multispectral and

hyperspectral imaging is illustrated in Fig. 2.4. Multispectral sensors acquire data in a limited number of relatively broad and discontinuous spectral bands, whereas hyperspectral sensors record hundreds of narrow and contiguous bands across the electromagnetic spectrum. This continuous spectral sampling enables hyperspectral systems to resolve subtle absorption features associated with mineralogical and compositional variability that are often not detectable using multispectral data.

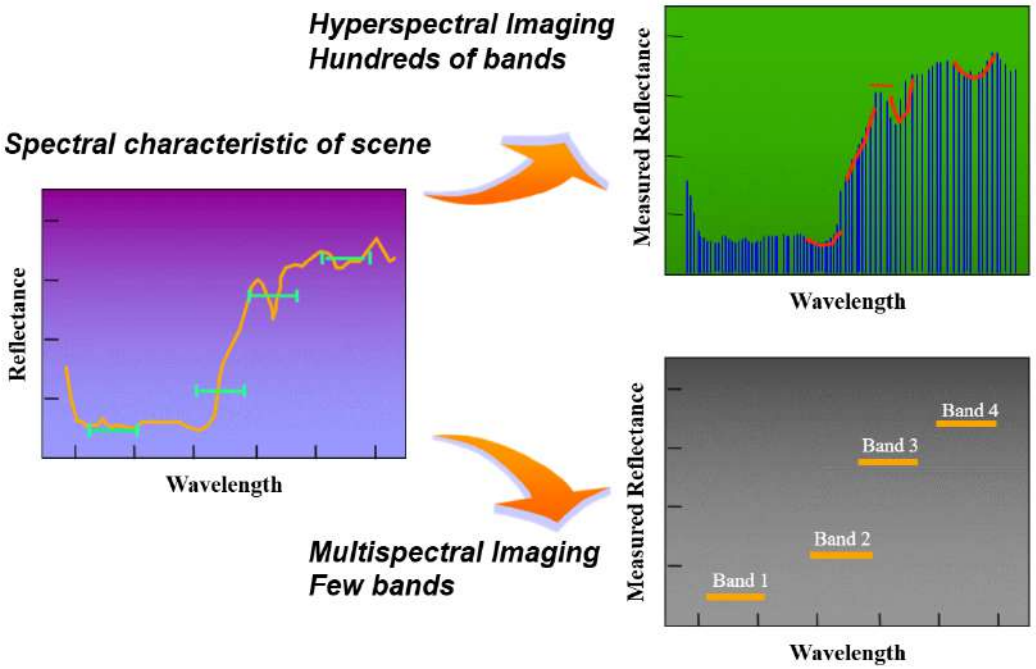

Fig. 2.4 Conceptual comparison between multispectral and hyperspectral imaging. Multispectral sensors sample the spectral response of a target using a limited number of broad and discrete spectral bands, whereas hyperspectral sensors acquire hundreds of narrow and contiguous bands, enabling a more detailed reconstruction of spectral absorption features and improved discrimination of surface materials and mineralogical variability; from [23].

The implications of this limitation are further illustrated in Fig. 2.5, which compares the spectral signatures of selected clay and sulfate minerals as recorded by multispectral and hyperspectral sensors, highlighting the loss of diagnostic detail in multispectral data.

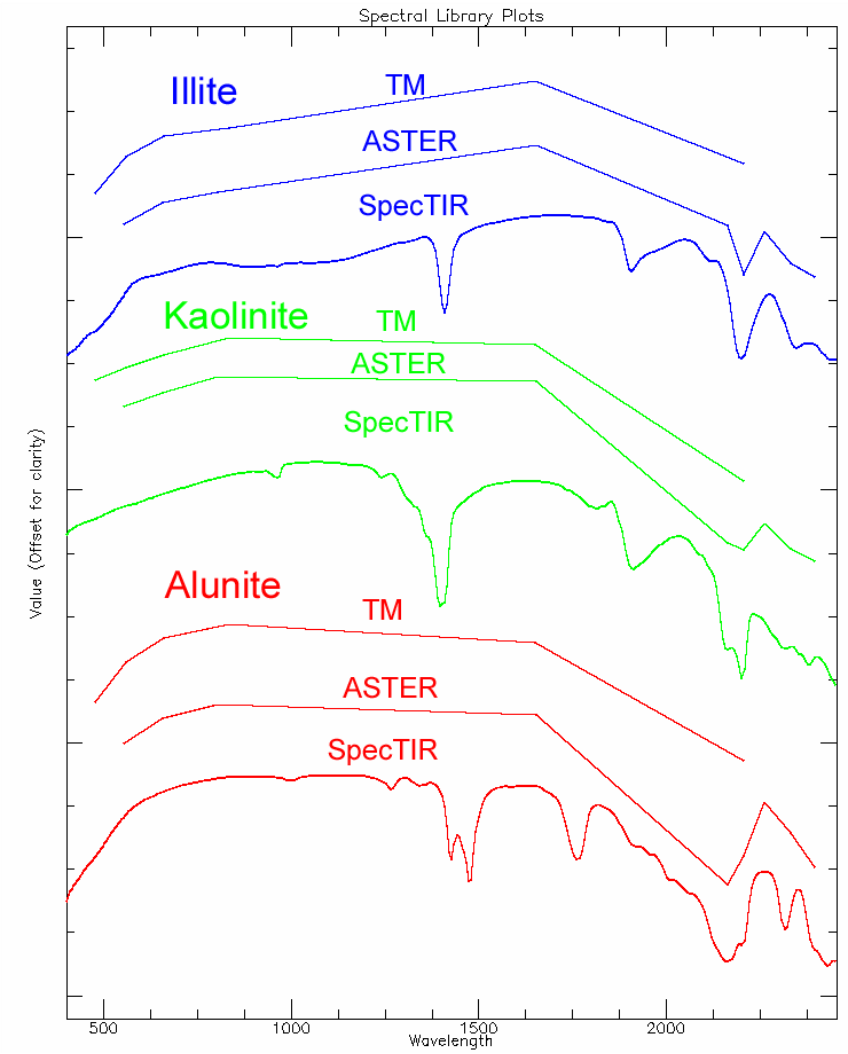

Fig. 2.5 Comparison of the spectral signatures of alunite, kaolinite, and illite as recorded by the multispectral sensors Landsat TM and ASTER, and the hyperspectral sensor SpecTIR, illustrating the enhanced diagnostic detail provided by hyperspectral measurements; modified from [9].

These constraints are largely overcome by hyperspectral sensors, which acquire hundreds of narrow and contiguous spectral bands, enabling precise detection of diagnostic absorption features. Since the late 1980s, airborne hyperspectral systems such as AVIRIS (Airborne Visible/Infrared Imaging Spectrometer), HyMap (Hyperspectral Mapper), and ProSpec TIR-VS have demonstrated exceptional capability in resolving subtle mineralogical and chemical variations associated with metasomatic zonation and ore-forming processes [24–28]. For instance, HyMap, developed by

Integrated Spectronics and known as Probe-1 in the United States, acquires 126 spectral channels spanning 0.4–2.5 μm.

NASA's Hyperion sensor, launched aboard EO-1 in 2000, represented the first spaceborne hyperspectral instrument, capturing 220 bands from 0.4 to 2.5 μm at 30 m spatial resolution [23]. Hyperspectral data have also played a crucial role in planetary science, with instruments such as CRISM and OMEGA enabling mineralogical mapping of planetary surfaces, notably Mars [10].

In recent years, the advent of new spaceborne hyperspectral missions, including PRISMA (Hyperspectral Precursor and Application Mission), EnMAP (Environmental Mapping and Analysis Program), and EMIT (Earth Surface Mineral Dust Source Investigation), has significantly expanded the potential of satellite-based mineral mapping. These sensors provide contiguous VNIR–SWIR spectral coverage and systematic regional-scale acquisitions at substantially lower operational cost than airborne surveys. Early applications of PRISMA and EnMAP demonstrate their ability to delineate hydrothermal systems and characterise mineralogical zonation, including compositional variations in white micas and chlorites indicative of fluid evolution pathways, as well as alteration zones associated with carbonate-hosted Zn–Pb deposits [29–31].

In parallel, technological advances such as high-resolution hyperspectral outcrop scanning [32, 33] and hyperspectral core logging [34–39] are transforming geological analysis at the outcrop and sample scale. Large-scale initiatives led by organisations such as the Australian Commonwealth Scientific and Industrial Research Organisation (CSIRO) and the United States Geological Survey (USGS) aim to produce regional to continental seamless geological maps through the integration of multispectral and hyperspectral datasets [40, 41].

The strength of RS for mineral exploration lies in its ability to detect diagnostic absorption features that produce unique spectral signatures, enabling reliable identification of minerals and alteration assemblages [9]. While hyperspectral sensors can often discriminate individual mineral species, multispectral systems typically allow only the identification of broader mineralogical classes. A fundamental limitation of optical RS is the extremely shallow penetration depth of the electromagnetic signal, typically only a few microns, making the technique most effective in arid and semi-arid environments where rock and soil surfaces are exposed [9]. Atmospheric effects, including scattering, absorption, and terrain-induced illumination variations,

must therefore be corrected using radiative transfer models [42–45], empirical scene-based methods [46], or field-calibrated approaches [10, 47]. Despite these challenges, remote sensing remains one of the most powerful approaches for mineral exploration over large areas, capable of mapping alteration minerals and detecting chemical variations that are often invisible even to experienced field geologists [9, 8].

2.3 Hyperspectral Remote Sensing: the EMIT Mission

Recent advances in satellite-based hyperspectral imaging have substantially expanded the scope of remote sensing applications in geology and mineral exploration, enabling the systematic acquisition of continuous spectral information at regional to global scales. Within this rapidly evolving landscape, the Earth Surface Mineral Dust Source Investigation (EMIT) mission represents a particularly promising, yet still underexplored, spaceborne hyperspectral sensor for geological applications.

EMIT was developed at NASA's Jet Propulsion Laboratory and launched on 14 July 2022 aboard the International Space Station (ISS). The instrument was originally designed to characterise the mineralogical composition of global dust-source regions in order to improve climate models and constrain the radiative forcing effects of airborne mineral dust [48]. EMIT acquires hyperspectral imagery across the 381–2493 nm spectral range using 285 contiguous bands, with an average spectral resolution of approximately 7.5 nm and a spatial resolution of 60 m [48, 49]. The sensor provides a swath width of approximately 74 km and exhibits high signal-to-noise ratios as well as excellent on-orbit spectral and radiometric stability, as demonstrated by recent validation studies [50].

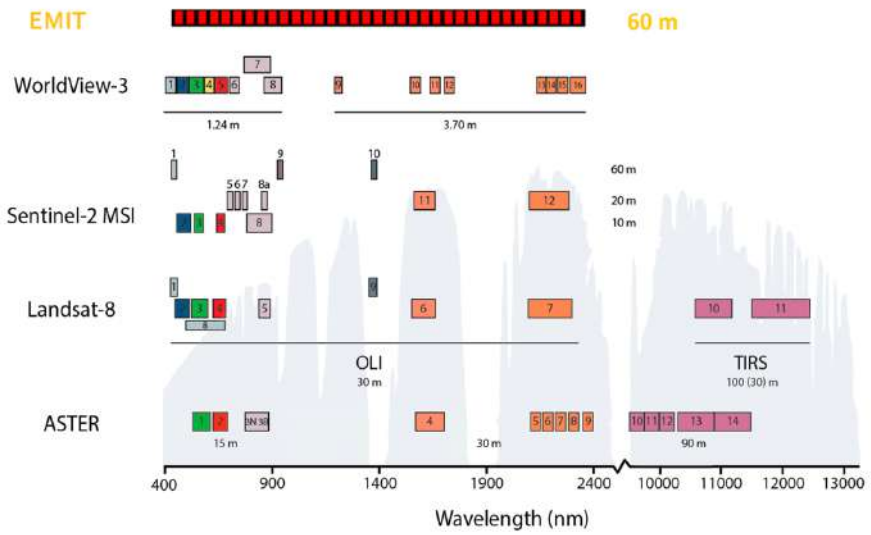

Fig. 2.6 Comparison of spectral coverage and band configuration of selected Earth observation sensors, including the hyperspectral EMIT instrument and commonly used multispectral sensors (WorldView-3, Sentinel-2 MSI, Landsat-8 OLI/TIRS, and ASTER). Multispectral sensors acquire data in a limited number of discrete and relatively broad spectral bands, whereas EMIT provides contiguous hyperspectral coverage across the VNIR–SWIR range at 60 m spatial resolution. The grey background represents atmospheric transmission and illustrates how sensor band placement is constrained by atmospheric transmission windows (modified from [51]).

Compared to commonly used multispectral sensors such as Landsat-8 OLI/TIRS, Sentinel-2 MSI, ASTER, and even high-resolution commercial platforms like World View-3, EMIT offers fully contiguous VNIR–SWIR spectral coverage, albeit at a coarser spatial resolution (Fig. 2.6). While multispectral systems sample only a limited number of discrete and relatively broad spectral bands, EMIT resolves the detailed shape and position of diagnostic absorption features, enabling more precise mineralogical discrimination. The practical implications of this difference are illustrated in Fig. 2.7, which compares the spectral response of carbonate-rich targets as represented by hyperspectral EMIT data and by spectrally resampled multispectral observations. The hyperspectral EMIT spectrum preserves subtle absorption feature positions and shapes, particularly in the SWIR carbonate absorption region around 2300–2350 nm, whereas multispectral sampling significantly reduces the spectral detail available for mineral discrimination.

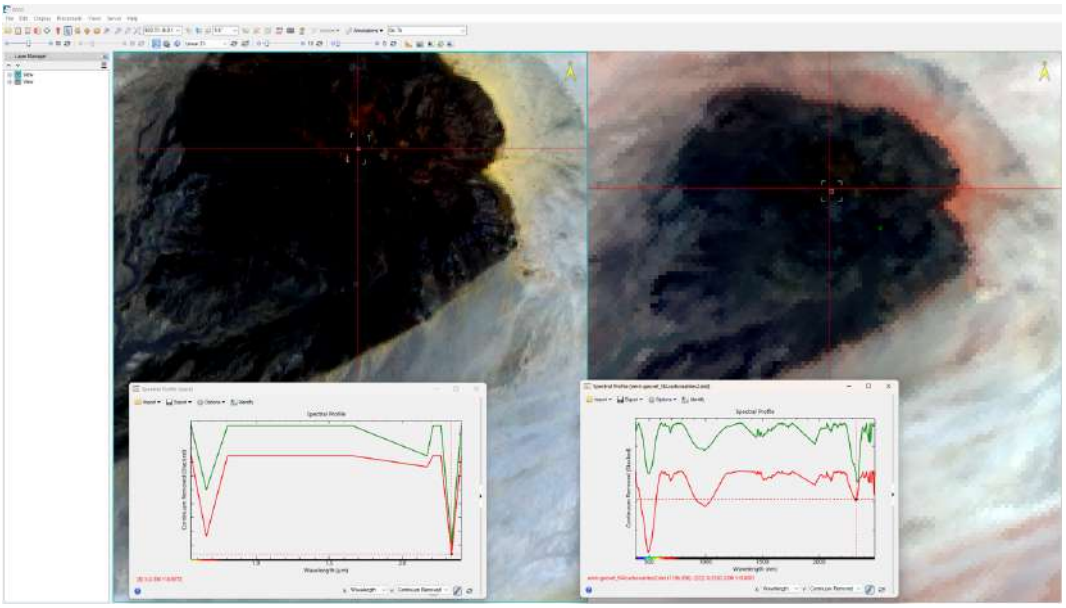

Fig. 2.7 Comparison between hyperspectral EMIT spectra and spectrally resampled multispectral representations over carbonate-rich targets from the Dicker Willem carbonatite complex, Namibia. The EMIT hyperspectral spectrum preserves the detailed shape and wavelength position of diagnostic carbonate absorption features in the SWIR region, allowing discrimination between calcite- and dolomite-dominated compositions. In contrast, multispectral sampling substantially reduces spectral detail and limits the detection of subtle compositional variations.

The placement of EMIT's spectral bands within atmospheric transmission windows further enhances its suitability for surface mineral mapping (Fig. 2.6).

The EMIT imaging concept is based on a push-broom hyperspectral acquisition strategy, in which reflected solar radiation from the Earth's surface is dispersed by a spectrometer and recorded by a detector array to produce calibrated image cubes (Fig. 2.8). Each pixel contains a full reflectance spectrum, allowing the generation of mineralogical maps through spectral analysis techniques such as wavelength mapping, band ratios, and spectral unmixing. Since its deployment on the ISS, EMIT has achieved near-global coverage, with extensive data availability over arid and semi-arid regions where exposed rock surfaces maximise spectral contrast (Fig. 2.9).

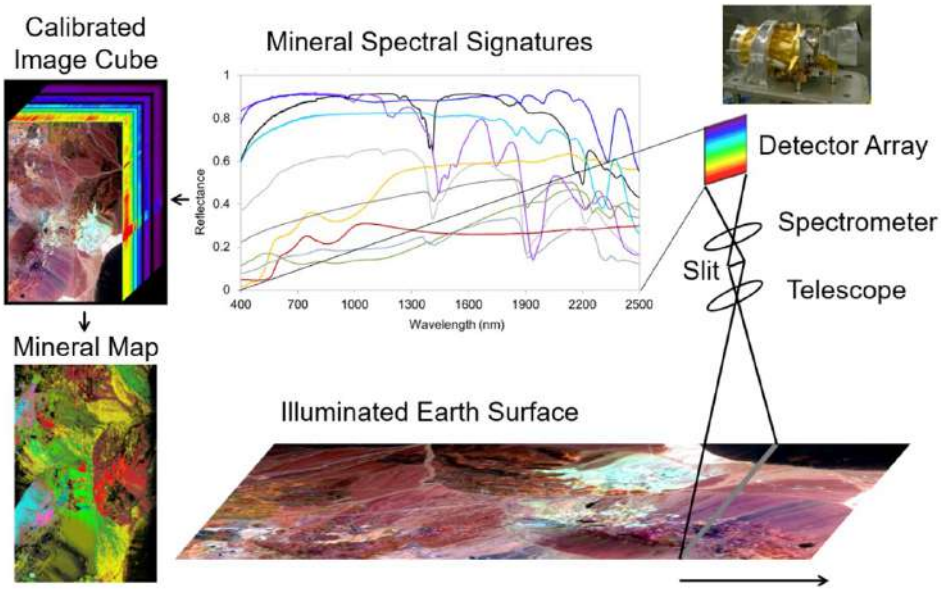

Fig. 2.8 Conceptual representation of the EMIT hyperspectral imaging principle and mineral mapping workflow. Reflected solar radiation from the Earth's surface is collected by the EMIT telescope mounted on the ISS and dispersed by the imaging spectrometer onto a detector array, producing a calibrated hyperspectral image cube. Each pixel contains a continuous VNIR–SWIR reflectance spectrum, from which diagnostic mineral spectral signatures are extracted to generate spatially explicit mineral maps (https://earth.jpl.nasa.gov/emit/instrument/overview/).

Although EMIT was not specifically conceived as a mineral exploration mission, recent studies have demonstrated that its capabilities extend well beyond its original dust-focused objectives. Clark et al. [52] showed that EMIT can resolve diagnostic absorption features associated with Fe-bearing minerals, carbonates, and white micas, including subtle shifts in Al–OH absorption wavelengths that reflect variations in mineral chemistry. Similarly, Portela et al. [27] demonstrated EMIT's ability to discriminate between alunite-rich and pyrophyllite-rich alteration assemblages, enabling interpretations of hydrothermal fluid evolution and alteration zoning at the regional scale. These results underline EMIT's potential as a versatile hyperspectral instrument for geological mapping and mineral system analysis.

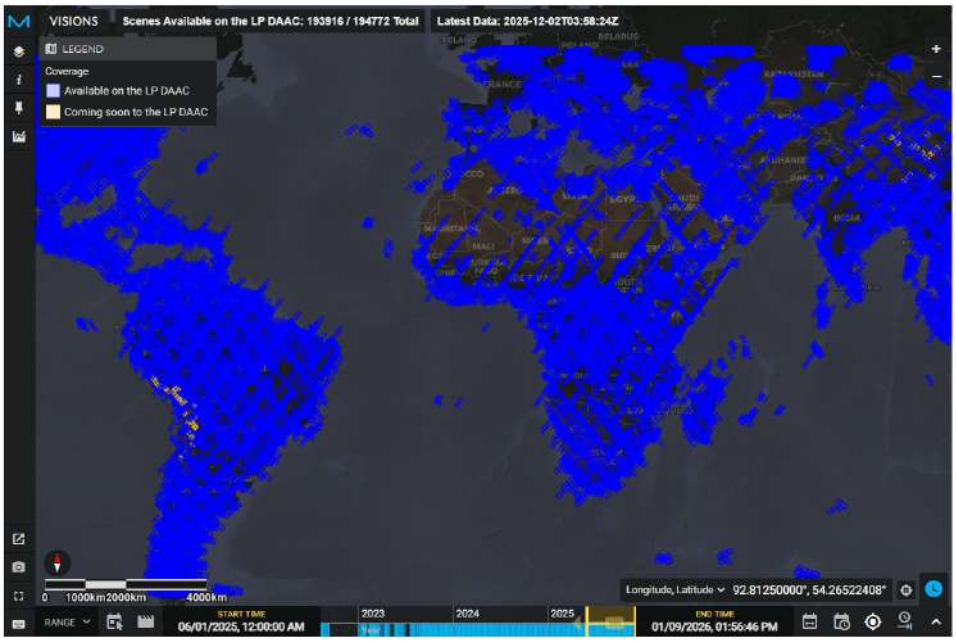

Fig. 2.9 Global spatial coverage of the EMIT hyperspectral sensor, showing the geographic distribution of acquired scenes. Blue swaths indicate areas where EMIT data are currently available, illustrating the near-global coverage achieved by the sensor (https://earth.jpl.nasa.gov/emit/data/data-portal/coverage-and-forecasts/).

Despite these encouraging applications, EMIT remains largely untested in magmatic environments, and, to date, no published studies have systematically assessed its performance in carbonatite-hosted mineral systems. This represents a significant knowledge gap, given that carbonatites commonly host economically important commodities, including rare earth elements, niobium, and phosphate, and exhibit distinctive spectral signatures in the VNIR–SWIR domain. Evaluating EMIT's ability to detect and characterise carbonatite mineralogy and associated alteration therefore constitutes a key opportunity to extend the geological applications of this mission and to assess its relevance for critical raw materials exploration.

2.4 Fundamental of mineral spectroscopy

Mineral spectroscopy investigates the interaction between electromagnetic radiation and minerals, focusing on the measurement and interpretation of wavelength-dependent spectral responses produced by reflection, emission, or scattering processes. In the context of optical remote sensing, mineral characterisation is primarily

based on reflectance spectroscopy, which analyses the fraction of incident solar radiation reflected by a surface as a function of wavelength.

In the VNIR–SWIR region, the spectral reflectance (ρ_λ) is defined as the ratio between the reflected radiant energy $E_R(\lambda)$ and the incident radiant energy $E_I(\lambda)$:

$$\rho_\lambda = \frac{E_R(\lambda)}{E_I(\lambda)} \tag{2.5}$$

This dimensionless quantity describes the intrinsic spectral behaviour of surface materials and forms the basis for mineral identification using hyperspectral data. In contrast, mineral spectroscopy in the TIR domain relies on emissivity, which quantifies the efficiency with which a surface emits thermal radiation as a function of wavelength. Although emissivity-based analysis is not the focus of this study, it provides complementary information on silicate and carbonate minerals at longer wavelengths.

Minerals selectively absorb electromagnetic radiation at characteristic wavelengths, producing diagnostic absorption features that reflect their chemical composition and crystal structure. In the solar-reflected portion of the spectrum (approximately 300–3000 nm), these features arise from several fundamental physical mechanisms, including electronic transitions, vibrational processes, charge-transfer reactions, and conduction-related effects [13, 53]. The distribution and nature of these mechanisms across the VNIR–SWIR domain were comprehensively described by Hunt [13], whose conceptual framework remains foundational for mineral spectral interpretation (Fig. 2.10).

In the VNIR region, spectral behaviour is dominated by electronic transitions, particularly crystal-field effects associated with transition metal ions such as Fe^{2+}, Fe^{3+}, Cr^{3+}, Co^{2+}, and Ni^{2+}. These processes generate broad and relatively shallow absorption features, typical of iron oxides and hydroxides (e.g. hematite, goethite, jarosite), as well as some rare earth element–related electronic absorptions. Because these features are often subtle, their detectability is strongly influenced by sensor signal-to-noise ratio and surface conditions.

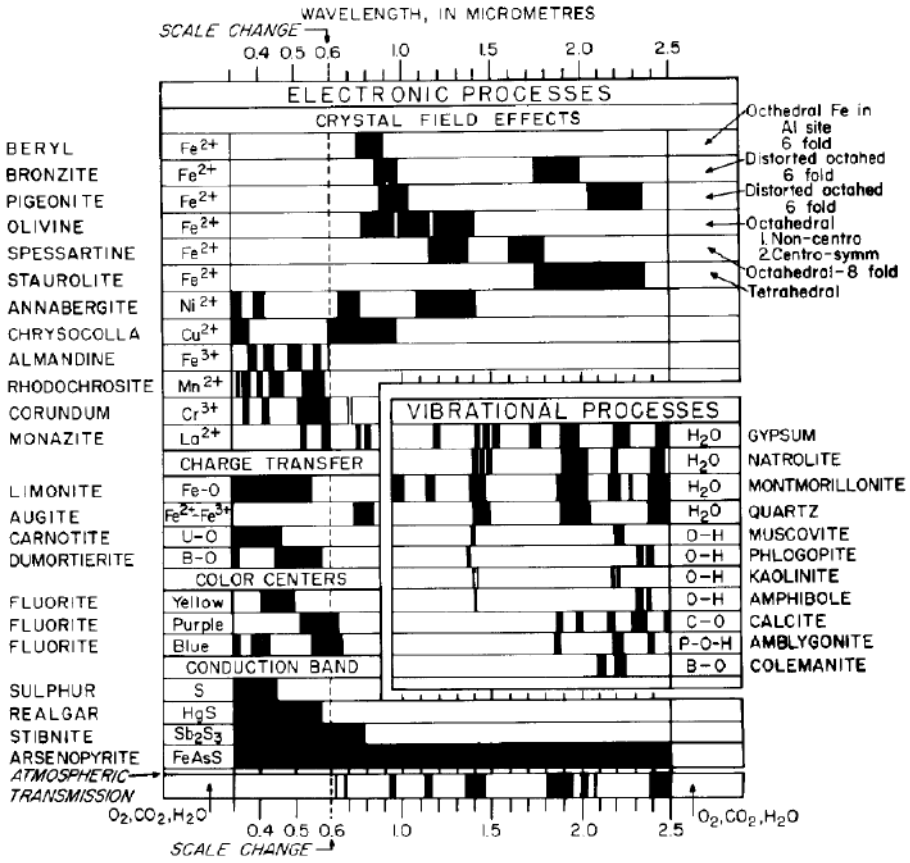

Fig. 2.10 Schematic summary of the main electronic and vibrational absorption processes responsible for diagnostic spectral features in minerals across the VNIR–SWIR wavelength range. The diagram illustrates the position and relative extent of absorption features associated with crystal-field electronic transitions, charge-transfer processes, colour centres, and molecular vibrations (e.g. OH, H_2O, CO_3^{2-}), highlighting their relationship to mineral chemistry and structure. Modified after [13].

In the SWIR region, mineral identification relies predominantly on vibrational absorption processes involving molecular bonds. The most spectrally significant groups include hydroxyl (OH^-), structurally bound water (H_2O), carbonates (CO_3^{2-}), sulfates (SO_4^{2-}), and ammonium (NH_4^+) [54]. These bonds produce narrow, well-defined absorption features that are highly diagnostic of mineral groups such as clays, phyllosilicates, amphiboles, sulfates, and carbonates. Key absorption wavelengths include approximately 1400 and 1900 nm for H_2O, around 2200 nm for Al–OH bonds (e.g. illite, kaolinite), near 2300 nm for Mg–OH bonds (e.g. chlorite), and between 2320 and 2350 nm for carbonate minerals such as calcite and dolomite [10].

Water plays a particularly important role in the SWIR domain, exhibiting strong absorption features near 1450, 1920, and 2700 nm, while being largely inactive in the VNIR region [55]. The presence of water can both enhance diagnostic information for hydrated minerals and complicate spectral interpretation due to overlapping absorptions. In addition, absorption feature characteristics are influenced by particle size and surface texture; finer-grained materials generally produce higher overall reflectance and deeper absorption features than coarse-grained or compact surfaces [55].

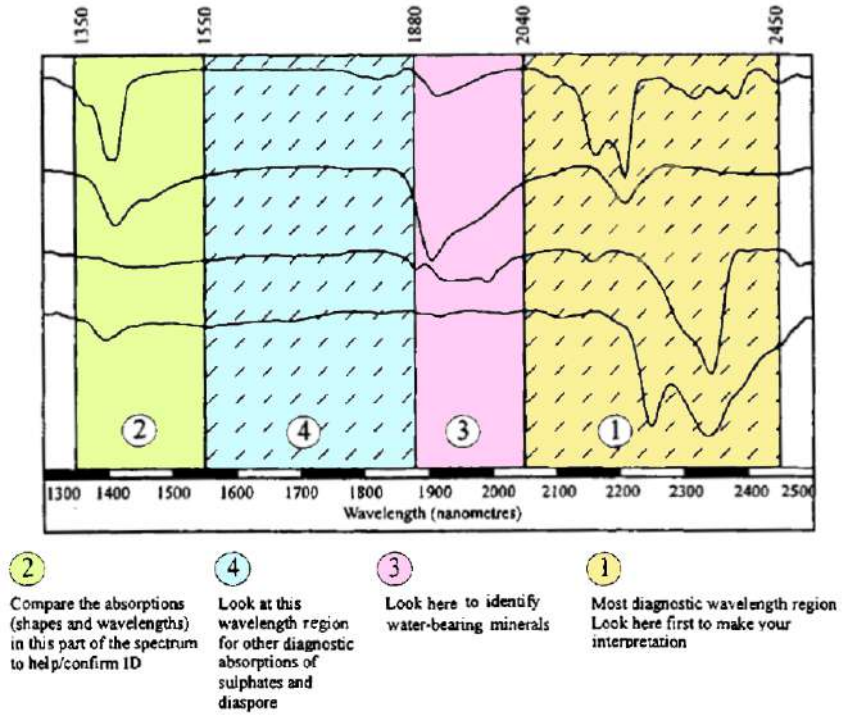

Fig. 2.11 Conceptual guide for the interpretation of mineral reflectance spectra in the SWIR region (approximately 1300–2500 nm). Coloured wavelength intervals highlight the most informative spectral regions for mineral identification, including diagnostic absorption features related to OH-bearing minerals, water, sulphates, and carbonates. The numbered sections indicate recommended steps for spectral interpretation, from initial inspection of the most diagnostic wavelength region to detailed comparison of absorption shapes and positions (modified from [54]).

To facilitate the comparison and interpretation of spectral features, preprocessing techniques such as continuum removal are commonly applied. Continuum removal normalises reflectance spectra by isolating absorption features from their background shape, allowing more consistent assessment of feature position, depth, and width across different samples or pixels [56]. These parameters are central to mineral iden-

tification: the wavelength position of absorption features reflects mineral chemistry, while feature depth is often related to mineral abundance, grain size, and mixture effects, and feature width and symmetry provide additional constraints on mineral structure and composition [54].

Environment of formation	Main spectrally active alteration minerals
High sulfidation epithermal	Alunite, pyrophyllite, dickite, kaolinite, diaspore, zunyite, smectite, illite
Low sulfidation epithermal	Sericite, illite, smectite, chlorite, carbonate
Porphyry: Cu, Cu-Au	Biotite, anhydrite, chlorite, sericite, pyrophyllite, zeolite, smectite, carbonate, tourmaline
Carlin-type	Illite, dickite, kaolinite
Volcanogenic massive sulfide	Sericite, chlorite, chloritoid, carbonates, anhydrite, gypsum, amphibole
Archean Lode Gold	Carbonate, talc, tremolite, muscovite, paragonite
Calcic skarn	Garnet, clinopyroxene, wollastonite, actinolite
Retrograde skarn	Calcite, chlorite, hematite, illite
Magnesium skarn	Fosterite, serpentine-talc, magnetite, calcite

Fig. 2.12 Summary of the main spectrally active minerals associated with different geological environments and mineralisation styles. The table highlights mineral groups that exhibit diagnostic spectral features in the VNIR–SWIR range and are therefore commonly targeted in RS–based mineral exploration. From [10].

Spectral interpretation in the SWIR region is guided by several well-established principles (Fig. 2.11). Most spectrally active minerals exhibit distinctive absorption features between 1300 and 2500 nm, with the most diagnostic region typically located between 2050 and 2450 nm. Within this interval, minerals can often be broadly classified according to the wavelength position of their deepest absorption feature, enabling discrimination between major mineral groups and alteration assemblages [54]. These relationships underpin the use of hyperspectral data for mapping alteration styles and mineral assemblages across different geological environments (Fig. 2.12).

In summary, mineral spectroscopy exploits the wavelength-dependent interaction between electromagnetic radiation and mineral matter to infer composition, structure, and alteration processes. The VNIR region is particularly sensitive to electronic absorptions associated with iron-bearing phases and selected REE-related features,

whereas the SWIR region provides robust diagnostic information for OH-bearing minerals, sulfates, and carbonates. The TIR region, although not addressed in this study, complements these observations by targeting fundamental lattice vibrations in silicates and carbonates. Together, these spectral domains form the physical foundation for hyperspectral mineral mapping in geological and mineral exploration applications.

2.5 Spectral analysis method used in this research

2.5.1 Minimum wavelength mapper

Considering that even minor shifts in the shape or wavelength position of spectral absorption features can reflect variations in mineralogy and chemical composition, these spectral parameters represent sensitive indicators of compositional changes within rocks and mineral assemblages. On this basis, Bakker et al. [57] and van Ruitenbeek et al. [58], from the Faculty of Geo-Information Science and Earth Observation (ITC), University of Twente (The Netherlands), developed a practical and robust approach to map the wavelength position of the deepest absorption feature in hyperspectral datasets.

This approach, known as the *Minimum Wavelength Mapper* (MWM), or simply *Wavelength Mapper*, combines information on both the wavelength position and the depth of the most prominent absorption feature on a per-pixel basis. The method is fully unsupervised, reproducible, and computationally efficient, making it particularly suitable for large hyperspectral datasets [56, 59]. The MWM was originally developed for the identification of minerals characterised by diagnostic vibrational absorption features in SWIR hyperspectral data, including planetary datasets acquired for Mars [58]. Subsequent studies have demonstrated its applicability also in the VNIR region, where electronic absorption features dominate [56, 59].

In this study, the Minimum Wavelength Mapper is implemented using the `HypPy` (Hyperspectral Python) software suite [60].

The MWM workflow begins with continuum removal, which normalises the reflectance spectrum and isolates diagnostic absorption features from the broader spectral background. The wavelength position and depth of the deepest absorption

feature are then estimated through parabolic interpolation (step 1; Fig. 2.13) applied to three adjacent spectral bands surrounding the reflectance minimum [58, 56]. This interpolation enables the detection of subtle wavelength shifts that are smaller than the nominal spectral sampling interval or full width at half maximum (FWHM) of the sensor bands, thereby enhancing sensitivity to compositional variations. In the step 2, the information extracted with the step 1 are merged together and the output consists of colour-coded maps in which each pixel represents the wavelength position of the deepest absorption feature, while colour intensity reflects the relative depth of that feature. These maps therefore provide a proxy for spatial variations in mineral composition, abundance, and distribution [26].

Further methodological details and performance assessments of the MWM are provided by van Ruitenbeek et al. [58] and Hecker et al. [56].

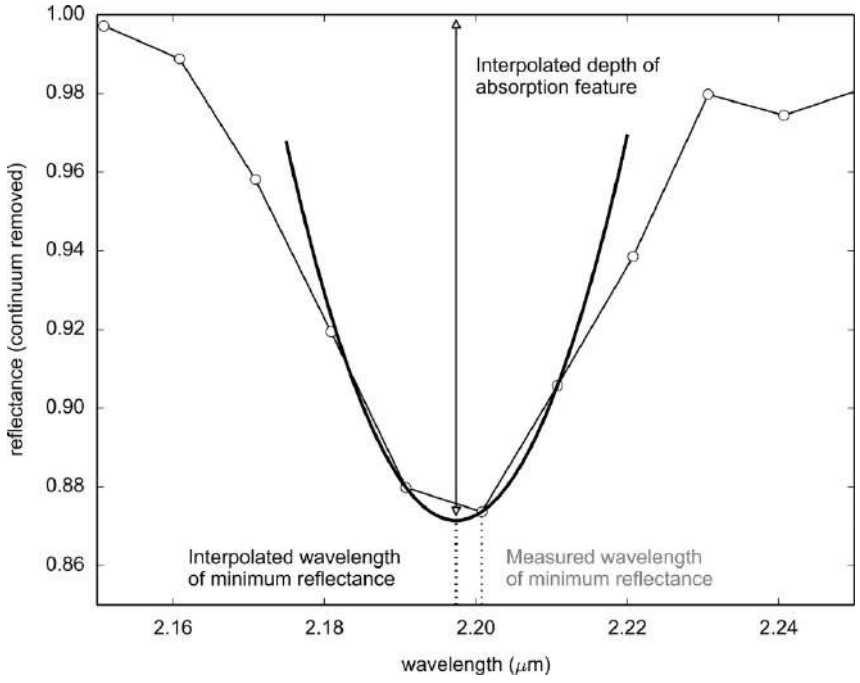

Fig. 2.13 Illustration of the parabolic interpolation approach used to estimate the wavelength position and depth of an absorption feature. Open circles denote the continuum-removed reflectance values at the original spectral band centres. Dashed lines indicate the location of the minimum reflectance at the discrete band level and the refined minimum derived from interpolation, respectively. This method enables the detection of wavelength shifts that are smaller than the nominal spectral sampling interval of the sensor (from [58]).

2.5.2 Band Ratios

Band ratios, often also referred to as spectral indexes, are spectral analysis techniques designed to enhance diagnostic information contained in remotely sensed data by exploiting wavelength-dependent variations in surface reflectance. In this context, the two terms are used interchangeably to indicate analytical formulations that combine reflectance values from selected spectral bands in order to emphasise specific spectral characteristics of surface materials.

A band ratio is computed by dividing the reflectance value of one spectral band by that of another on a pixel-by-pixel basis. This operation reduces the influence of illumination effects related to topography, surface albedo, and solar incidence angle, while simultaneously enhancing spectral contrasts linked to compositional differences. As a result, band ratios are particularly effective in highlighting mineralogical variations that may not be readily apparent in single-band imagery.

Although originally developed and widely applied using multispectral sensors such as Landsat [e.g. 8], ASTER [e.g. 61, 62] (an example of application is shown in Fig. 2.14), and Sentinel-2 [e.g. 63], band ratio approaches are equally applicable to hyperspectral datasets. In hyperspectral applications, the availability of narrow and contiguous spectral bands allows band ratios to be specifically tuned to diagnostic absorption features, thereby increasing sensitivity to subtle mineralogical and chemical variations.

When applied to hyperspectral data, band ratios are commonly constructed using bands located on the shoulders and at the minima of absorption features associated with electronic or vibrational processes. This makes them particularly suitable for enhancing for instance spectral responses related to Fe^{3+}-bearing oxides in the VNIR region, as well as carbonate and OH-bearing minerals in the SWIR region.

In this research, band ratios are employed as simple yet robust tools to complement wavelength-based mapping approaches. Their use enables the targeted enhancement of specific absorption features relevant to the mineral systems under investigation, while maintaining a high degree of interpretability and methodological reproducibility.

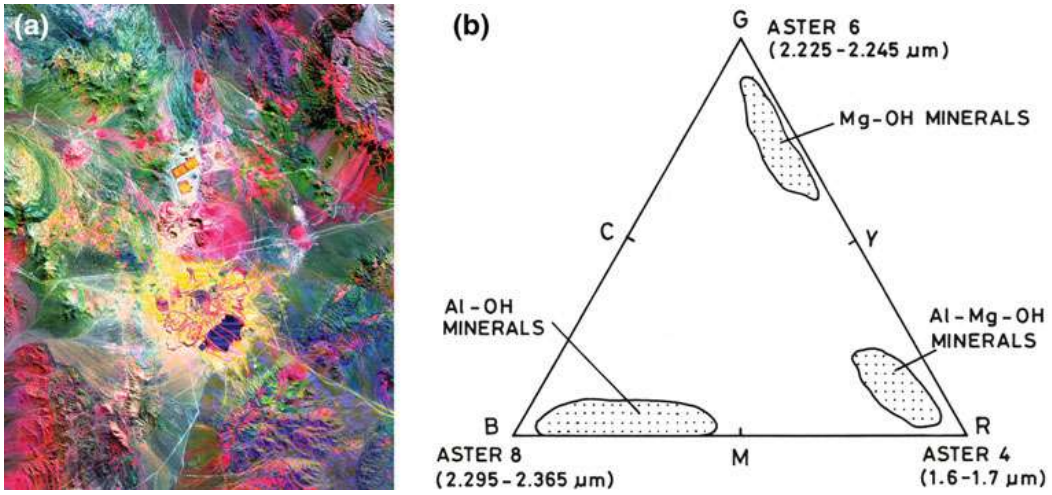

Fig. 2.14 Example of the application of band ratio and false-colour composite techniques to geological settings. (a) ASTER SWIR false-colour composite image of the Escondida open-pit mine (Chile), using bands 4, 6, and 8 displayed in RGB, respectively. Variations in colour highlight differences in alteration mineralogy, with Al–OH-bearing minerals appearing in blue–purple tones, Mg–OH-bearing minerals in green–yellow tones, and Al–Mg–OH-bearing minerals in red shades. (b) Corresponding ternary colour diagram used for the interpretation of the spectral responses displayed in the false-colour composite. From [11].

Chapter 3

Case studies

3.1 Introduction and regional geological framework

To assess the capability of EMIT data in detecting subtle mineralogical variations, this chapter presents the application of a set of basic yet robust spectral analysis techniques to two selected case studies. The adopted approaches were intentionally chosen to minimise processing complexity while maximising the interpretability of spectral information related to key mineralogical processes observable in hyperspectral data. In particular, two complementary methods were employed: wavelength mapping and spectral band ratio analysis.

The selected case studies, located in Namibia, represent contrasting geological settings characterised by distinct alteration mineralogies. The first focuses on muscovite-bearing hydrothermal alteration associated with the Haib porphyry copper system, while the second examines carbonate-dominated lithologies along the Kudu Lineament. The latter case study forms the basis of Carano et al. (2026) [64], which investigated compositional zonation in carbonatite complexes along the Kudu Lineament using EMIT hyperspectral imagery. Following the methodological overview, a brief geological context is provided to frame the selection of the two case studies.

The tectonic framework of southern Africa is characterised by several large Archean cratons and smaller cratonic fragments, interconnected by younger mobile belts formed during successive orogenic events. The present-day configuration largely developed during the Pan-African orogeny, which spanned from the late Neoproterozoic to the Cambrian [65]. Namibia exhibits a particularly complex

geological architecture, comprising Precambrian basement complexes intruded by younger magmatic systems, resulting in a wide diversity of lithologies and mineralisation styles. The southwestern part of the country is predominantly underlain by the Namaqua Natal Province, a Proterozoic domain that experienced multiple tectono-metamorphic events. In addition to these basement units, Namibia hosts several important magmatic provinces, including carbonatite complexes and alkaline intrusions, which are of significant geological and economic importance due to their association with rare earth elements, copper, and other strategic minerals.

Within this regional framework, the two study areas are located in contrasting geological settings in southern and south-western Namibia, respectively (Figs. 3.1a,b), providing an ideal basis for evaluating the performance of EMIT across different mineral systems.

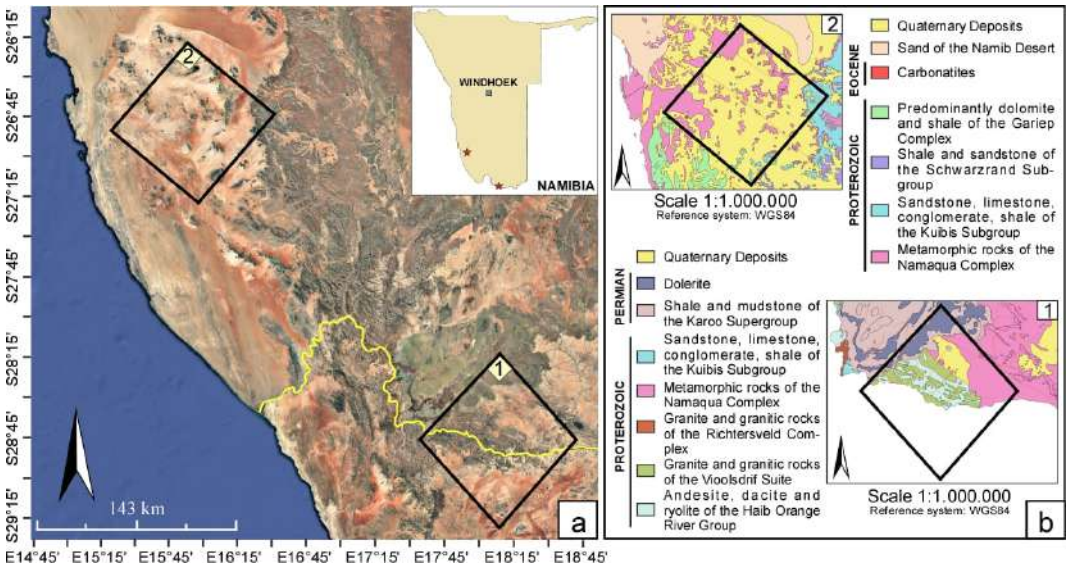

Fig. 3.1 (a) Location of the two study areas in Namibia (black polygons and red stars) (https://earth.google.com/web); (b) Geological map extracts of the two study areas at a scale of 1:1.000.000 (Geological Survey of Namibia, https://www.mme.gov.na/gsn/data/).

3.2 Case Study 1: Haib Porphyry Copper System

3.2.1 Geological setting

The Haib region is located in the extreme southern part of Namibia, within the Namaqua Natal Province, in the Karas Region, north of the Orange River along the border with South Africa (Fig. 3.2). As part of the broader tectonostratigraphic framework of the Namaqua Natal Province, the study area lies within a Proterozoic metamorphic domain shaped by multiple orogenic events and complex crustal evolution.

Geologically, the Haib area is situated within the western sector of the Namaqua Natal Province, a NW–SE–trending Proterozoic metamorphic belt that records the effects of both the Orange River Orogeny ($\sim$2.0–1.7 Ga) and the later Namaqua Orogeny ($\sim$1.4–1.1 Ga) [66]. Rocks associated with the Orange River Orogeny dominate the study area and have undergone regional metamorphism under greenschist-facies conditions [67]. These units form part of the broader tectonostratigraphic architecture of the Richtersveld Subprovince within the western Namaqua Natal Province.

Within the study area, the lithological succession can be broadly subdivided, from oldest to youngest, into several key units. The oldest rocks comprise a volcano-sedimentary sequence locally referred to as the Orange River Group, which is dominated by calc-alkaline volcanic rocks ranging in composition from basalt to rhyolite. This group includes the Feldspar Porphyry unit, which hosts copper mineralisation [68]. The Orange River Group is intruded by the Vioolsdrift Intrusive Suite, which consists of mineralised quartz–feldspar porphyry as well as a range of mafic to felsic intrusive rocks, including basic–ultrabasic complexes, diorite, tonalite, granodiorite, adamellite, and leucogranite. Both the Orange River Group and the Vioolsdrift Intrusive Suite are, in turn, intruded by the Richtersveld Intrusive Suite, characterised by amphibolite, syenite, and granite lithologies [69].

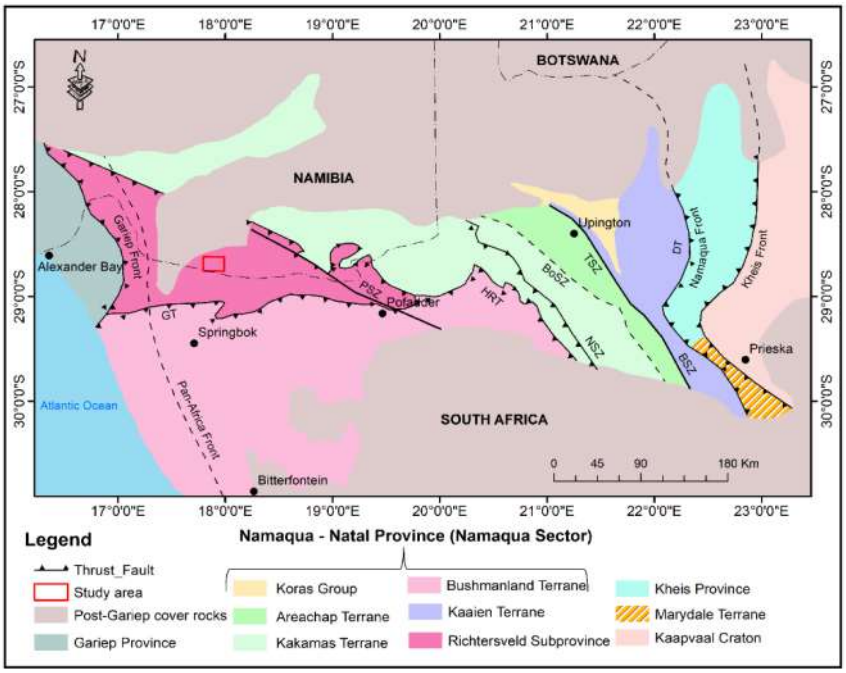

Fig. 3.2 Map illustrating the main tectonostratigraphic subdivisions of the Namaqua Natal Province. The location of the Haib study area is highlighted by the red rectangle [69].

In addition to these units, the area also presents metamorphic rocks associated with the Namaqua Orogeny [66], sedimentary rocks of the Karoo Supergroup, Permian dolerite intrusions, and unconsolidated Quaternary deposits, reflecting the prolonged and multi-stage geological evolution of the region.

3.2.2 Data set

The dataset used in this study consists of a cloud-free Level-2A EMIT reflectance scene EMIT_L2A_RFL_001_20220903T101546_2224607_019, freely available through NASA's Earthdata Search portal (https://search.earthdata.nasa.gov/search). EMIT Level-2A products provide Bottom-Of-Atmosphere (BOA) surface reflectance data derived from calibrated at-sensor radiance measurements. The original sensor measurements are first converted from digital numbers (DN) into calibrated spectral radiance (Level-1B), representing Top-Of-Atmosphere (TOA) radiance. Subsequently, atmospheric correction procedures are applied to compensate for atmospheric absorption and scattering effects, yielding BOA surface reflectance suit-

able for quantitative spectral and mineralogical analysis. The atmospheric correction applied to the EMIT Level-2A product is performed through the EMIT Science Data System using the ISOFIT (Imaging Spectrometer Optimal FITting) radiative transfer modelling framework [49, 70].

The product was georeferenced using geographic lookup tables (GLTs) and subsequently cropped to the spatial extent of the study area. As atmospheric correction had already been applied by the data provider, reflectance information was unavailable within the 1327–1431 nm and 1771–1959 nm wavelength intervals due to strong atmospheric water vapour absorption. In addition, wavelengths affected by instrumental artefacts in the 984–1014 nm region were excluded from further analysis.

For the purposes of this study, the dataset was then spectrally subset to retain only the 1100–2400 nm wavelength range, focusing the analysis on spectral regions most relevant for mineralogical discrimination. The use of BOA reflectance ensures that the observed spectral variations are primarily related to surface mineralogical properties rather than atmospheric effects.

3.2.3 Analysis

Target mineralogy: white mica

In order to investigate mineralogical variability and spatial distribution patterns within the Haib area, the analysis focused on OH-bearing alteration minerals, with particular emphasis on white mica. White micas, such as muscovite, exhibit well-defined diagnostic absorption features in the SWIR region, most notably the Al–OH absorption feature centred around 2200 nm (Fig. 3.3). Variations in the position and shape of this feature have been widely used to infer changes in mineral chemistry, alteration intensity, and fluid–rock interaction processes.

Previous studies have demonstrated the effectiveness of hyperspectral remote sensing for the characterisation of white mica compositions and their spatial variability in altered systems (e.g., [54, 71–73, 26]). On this basis, the analytical workflow adopted in this study employs multiple spectral techniques designed to capture both the distribution and compositional variability of white mica across the study area.

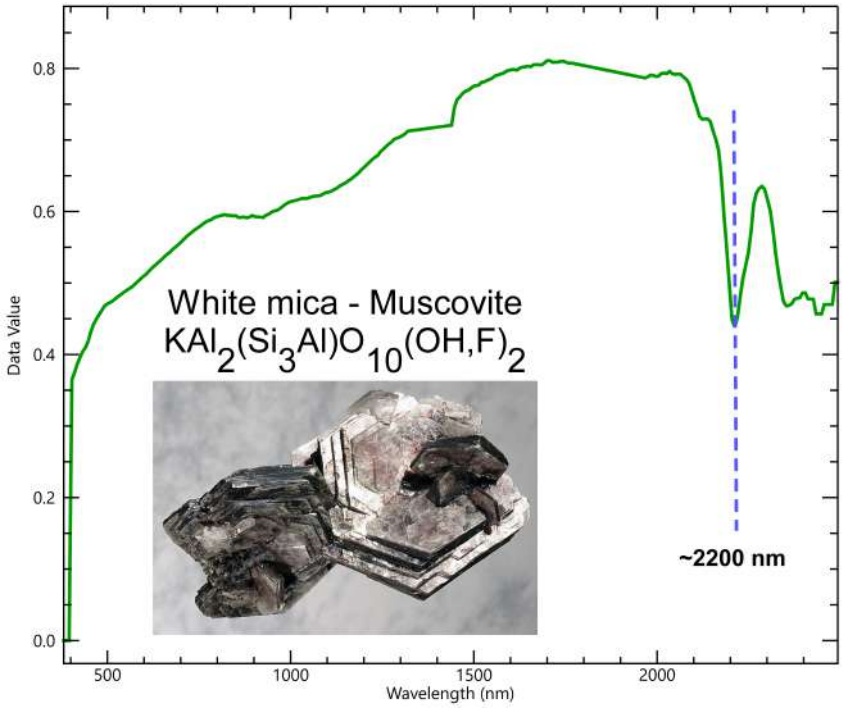

Fig. 3.3 Reflectance spectrum of muscovite (white mica) extracted from the USGS spectral library. The spectrum exhibits a diagnostic Al–OH absorption feature centred at approximately 2200 nm, highlighted in the figure, which is characteristic of white micas. The inset photograph shows a hand specimen of muscovite, reproduced from Mindat (https://www.mindat.org/min-2815.html).

3.2.4 Methodology

Wavelength mapping

Wavelength mapping was applied to investigate the spatial distribution of diagnostic SWIR absorption features across the study area, with particular emphasis on wavelengths associated with OH-bearing alteration minerals. This approach enables variations in the position of absorption minima to be visualised spatially and provides an effective means of assessing mineralogical variability. The parameters adopted for the generation of the wavelength maps are summarised in Table 3.1.

Table 3.1 Parameters used for wavelength mapping and target mineralogy over the Haib area.

Product	**Step 1 (nm)**	**Step 2 (nm)**	**Target mineralogy**
WM 1	2100–2400	2100–2400	OH-bearing minerals for surface mineralogy
WM 2	2150–2250	2150–2250	White mica and its variation

Band Ratio

In addition to wavelength mapping, spectral band ratio analysis was employed as a complementary spectral technique to further investigate mineralogical variations within the Haib area. This method exploits differences in reflectance between selected wavelength regions to enhance specific absorption features and improve the discrimination of spectrally similar mineral groups.

Representative spectra were extracted using ENVI from the SWIR wavelength maps (2100–2400 nm). Spectral sampling was performed on pixels corresponding to distinct absorption domains identified in the wavelength mapping products.

Reference wavelength intervals for diagnostic absorption features were adopted following Pontual et al. [54], namely 2160–2220 nm for Al–OH, 2230–2296 nm for Fe–OH, and 2306–2365 nm for Mg–OH/CO_3. Within each reference interval, the dominant absorption features were identified and appropriate shoulder wavelengths were selected to define mineral-specific band ratios.

Based on this procedure, the ratios 2145/2204 nm for Al–OH, 2234/2248 nm for Fe–OH, and 2382/2345 nm for Mg–OH/CO3 were selected and applied. The ratio products were subsequently combined into a false-colour composite image to provide an integrated representation of mineralogical variability across the study area.

3.2.5 Results

A wavelength map covering the 2100—2400 nm interval (WM1; Table 3.1) was generated by applying this interval consistently in both step 1 and step 2 of the processing workflow to provide a regional overview of SWIR-active minerals across the Haib study area (Fig. 3.4a). The resulting map reveals pronounced spatial

variability in spectral behaviour expressed by two dominant colour domains. Areas characterised by green hues correspond to pixels where absorption minima occur at shorter wavelengths, close to 2200 nm, whereas red to magenta colours indicate absorption minima shifted towards longer wavelengths, around 2350 nm (Fig. 3.4b). Regions displayed in black represent surfaces where SWIR-active minerals are absent or where absorption features are too weak to be reliably detected.

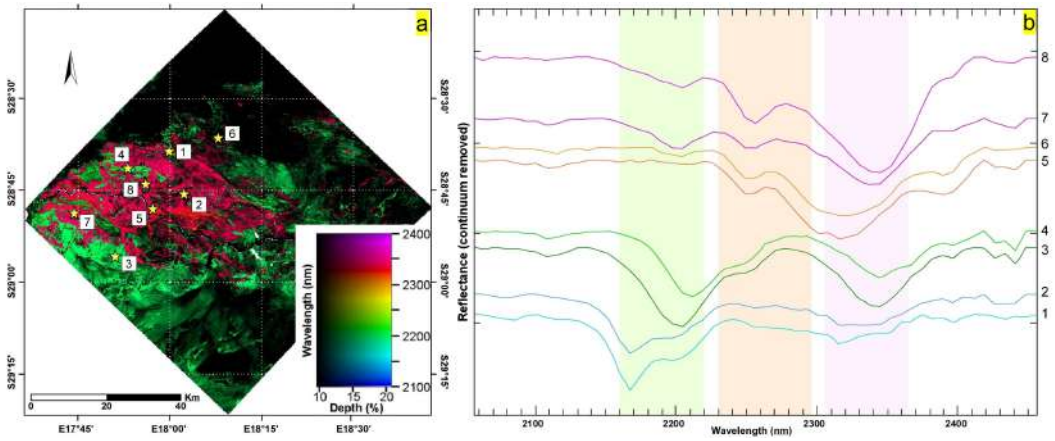

Fig. 3.4 (a) Product WM 1: SWIR overview wavelength map over the Haib area in the range 2100-2400 nm. The colours correspond to groups of absorption features having similar wavelengths; (b) Example of spectra. The colour of each spectrum corresponds to the colour of its respective pixel in the map (a), with the location of each spectrum marked by a number from 1 to 8, accompanied by a star on the map. The light bands in the background represent respectively, from left to right, Al-, Fe-, Mg-OH/CO_3 intervals of diagnostic absorption features as per [54].

The refined SWIR 2200 nm wavelength map (WM2; Table 3.1), generated in step 2 by restricting the analysis to the narrower 2150–2250 nm wavelength interval, further highlights variability within Al–OH-bearing mineral assemblages (Fig. 3.5a). Progressive colour variations correspond to systematic shifts in absorption minima from approximately 2197 nm to 2211 nm. Representative spectra extracted from selected pixels indicate gradual variations in the position of the Al–OH absorption feature (Fig. 3.5b).

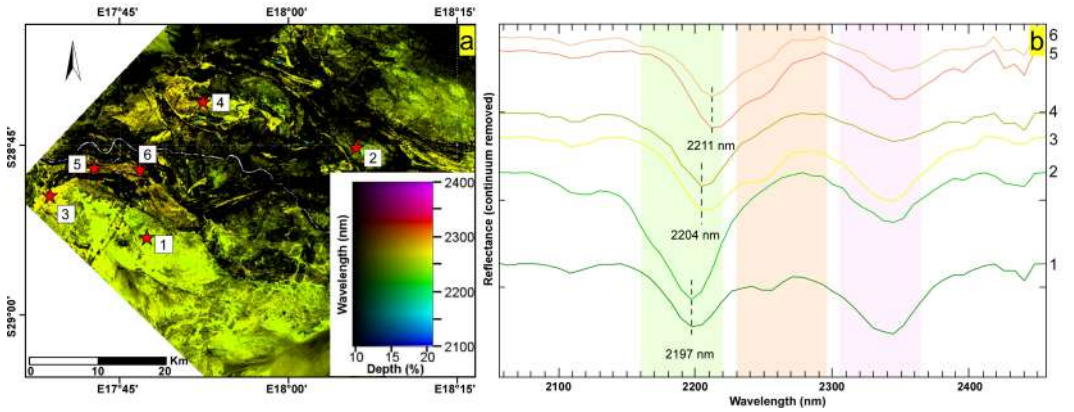

Fig. 3.5 (a) Product WM 2: SWIR wavelength map in the 2150-2250 nm wavelength range. The colour of pixels, ranging from green to orange, correspond to the main muscovite absorption peak shifting toward longer wavelengths; (b) Muscovite spectra. The colour of each spectrum corresponds to the colour of its respective pixel in the map (a), with the location of each spectrum marked by a number from 1 to 6, accompanied by a star on the map. The light bands in the background represent respectively, from left to right, Al-, Fe-, Mg-OH/CO_3 intervals of diagnostic absorption features as per [54].

The spectral band ratio products further enhance the spatial distribution of specific alteration-related mineral groups. The Al–OH-sensitive ratio highlights areas enriched in white mica and related minerals (Fig. 3.6), while the Fe–OH-sensitive ratio enhances Fe-bearing alteration minerals (Fig. 3.7). Similarly, the Mg-OH/CO_3-sensitive ratio delineates regions associated with Mg-rich mineral phases (Fig. 3.8).

The three ratio products were subsequently combined into a false-colour composite image (Fig. 3.9), providing a synoptic representation of mineralogical variability across the study area. Comparison with the geological map reveals a close correspondence between spectral domains, lithological contacts, and major structural features.

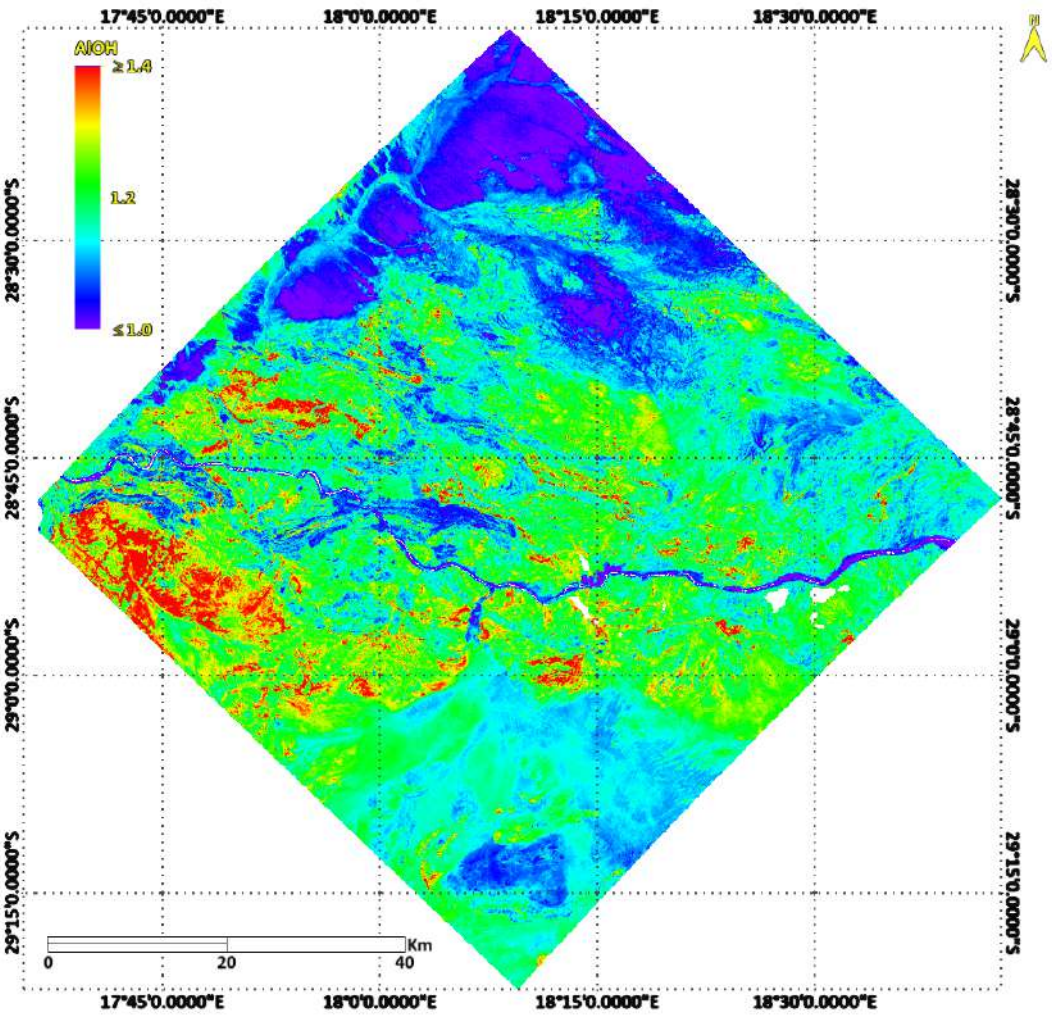

Fig. 3.6 Spectral band ratio map of the Haib study area highlighting the spatial distribution of Al–OH–bearing minerals such as white mica. Al–OH–sensitive ratio applied: 2145/2204 nm. Higher ratio values indicate stronger expression of the targeted absorption features.

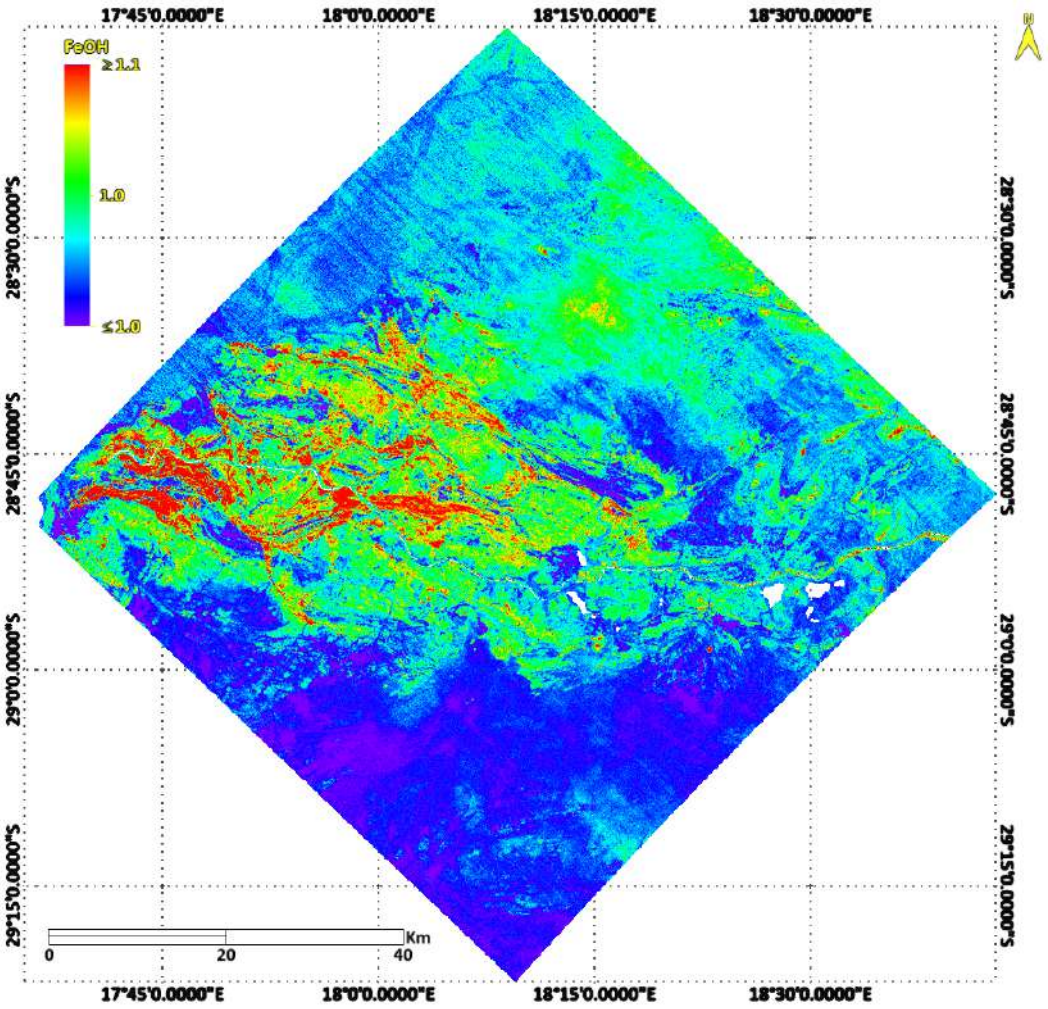

Fig. 3.7 Spectral band ratio map of the Haib study area enhancing the spatial distribution of Fe-bearing alteration minerals. Fe–OH–sensitive ratio applied: 2234/2248 nm. Higher ratio values indicate stronger expression of the targeted absorption features.

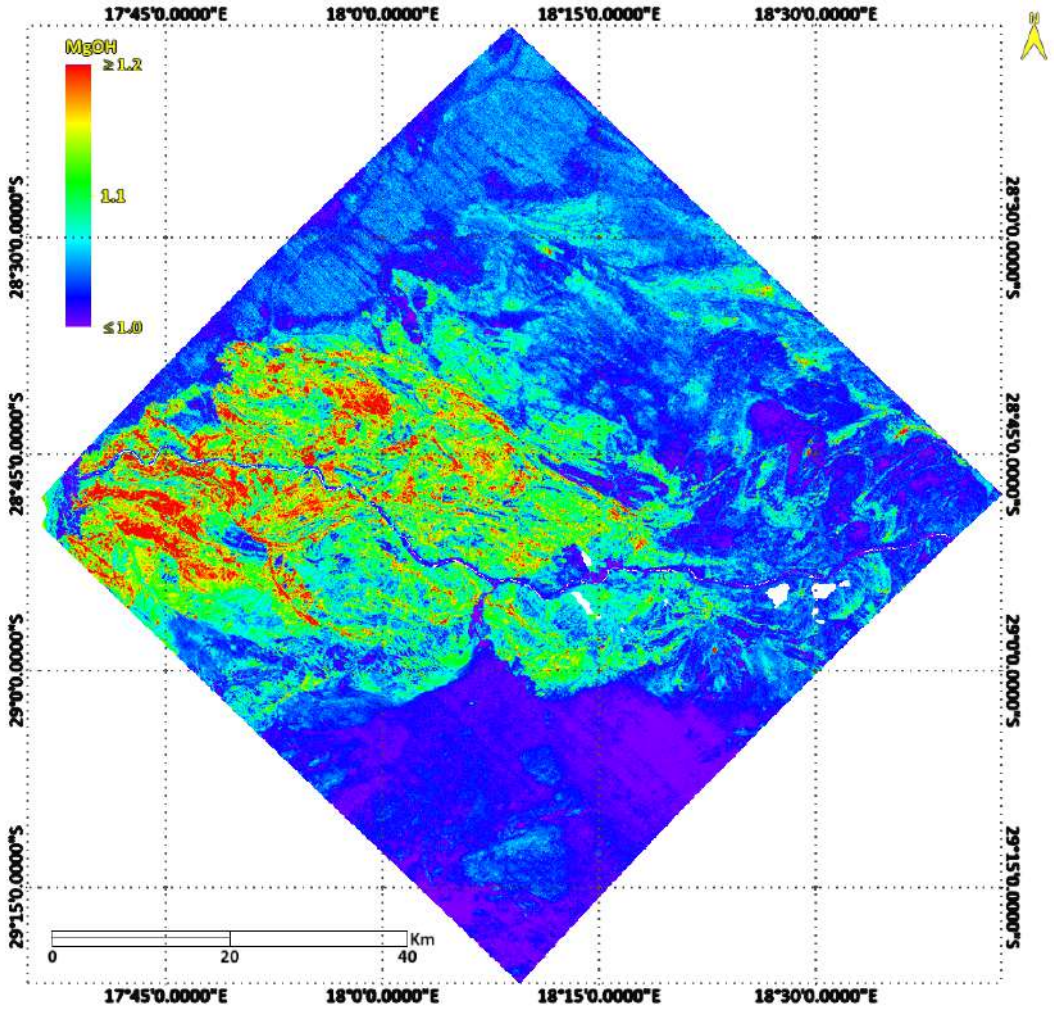

Fig. 3.8 Spectral band ratio map of the Haib study area highlighting the spatial distribution of Mg-rich minerals. Mg–OH/CO_3^{2-}–sensitive ratio applied: 2382/2345 nm. Higher ratio values indicate stronger expression of the targeted absorption features.

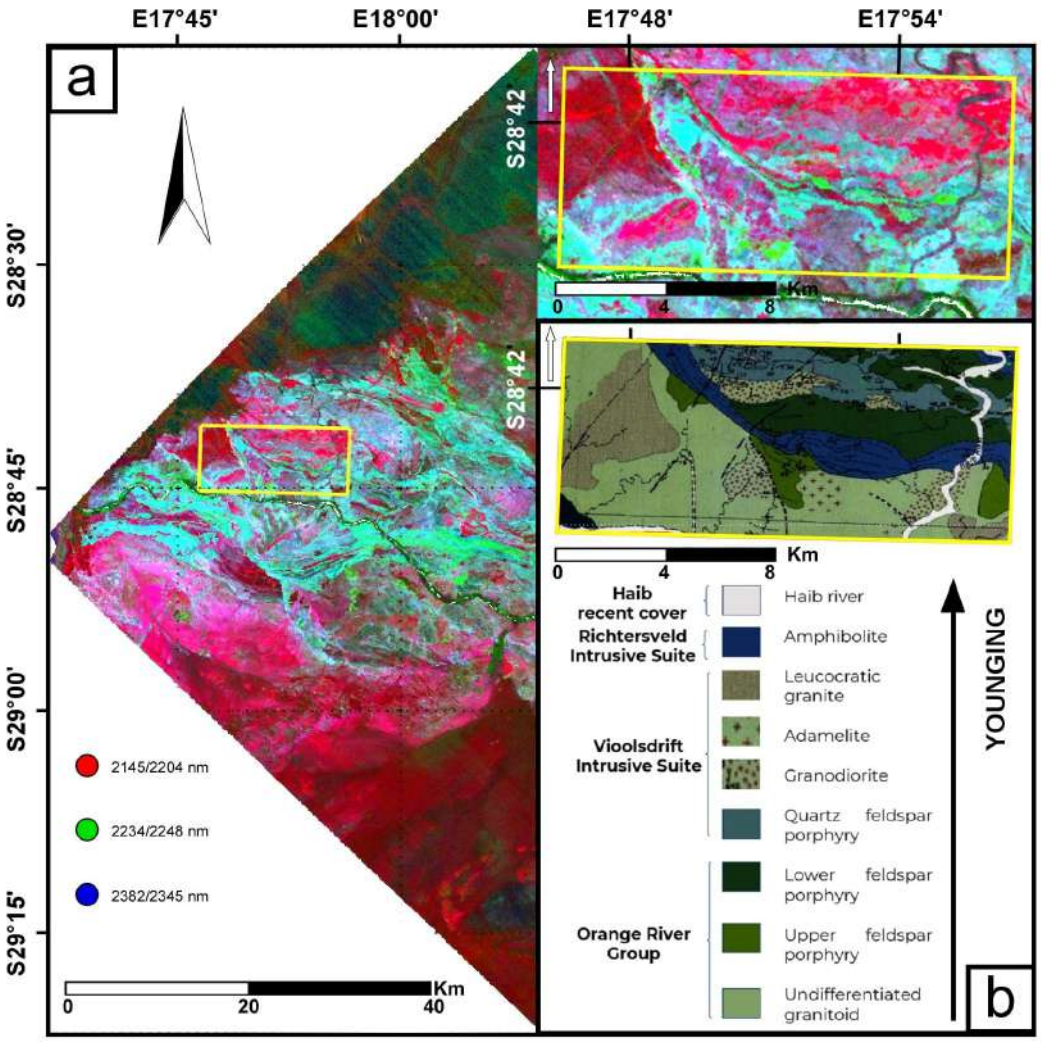

Fig. 3.9 (a) False colour composite map of the Haib area obtained using the following ratios: 2145/2204 nm for red, 2234/2248 nm for green, and 2382/2345 nm for blue. The zoomed-in section (yellow rectangle) is shown for comparison with the published geological map section; (b) Geological map of the area modified from [67].

3.2.6 Discussion

The application of EMIT hyperspectral data over the Haib area demonstrates the effectiveness of spaceborne imaging spectroscopy in resolving mineralogical variability associated with hydrothermal alteration systems. The combined use of wavelength mapping and spectral band ratio techniques provides complementary insights into

both the distribution and compositional variability of alteration minerals, particularly muscovite, at the district scale.

Wavelength mapping within the 2100—2400 nm interval successfully discriminates OH-bearing mineral assemblages, separating areas characterised by absorption features near 2200 nm from zones exhibiting longer-wavelength responses (Fig. 3.4). The refined analysis focused on the Al–OH absorption region reveals systematic shifts in muscovite absorption minima from approximately 2197 nm to 2211 nm (Fig. 3.5). These values are consistent with previously reported ranges for muscovite compositional variations driven by octahedral cation substitution, particularly Al–Mg exchange [74, 26, 73, 75, 71]. Such spectral shifts are commonly interpreted as indicators of evolving hydrothermal fluid conditions, including changes in temperature, fluid composition, or water–rock interaction intensity.

The spatial coherence of these wavelength variations suggests that the observed patterns reflect systematic alteration zoning rather than random spectral noise or surface effects. This interpretation is further supported by the spectral band ratio composites, which highlight the distribution of Al–OH-, Fe–OH-, and Mg–OH-bearing minerals and show a close spatial correspondence with known lithological boundaries and structural elements. In particular, the false-colour composite map, and its zoomed comparison with the geological map of Blignault [67], reveals that several lithological contrasts and major structural lineaments are clearly recognisable in the spectral data. The alignment between spectral patterns and mapped geological features indicates that the mineralogical contrasts detected by EMIT are geologically meaningful and reproducible.

From a CRMs perspective, the identified mineralogical patterns may also have implications for exploration targeting within porphyry systems. Although copper mineralisation itself is not directly detectable through SWIR hyperspectral techniques, alteration minerals such as white mica may act as indirect vectors towards potentially mineralised zones. Variations in muscovite chemistry and associated hydrothermal zonation have been widely linked to evolving fluid conditions in porphyry environments and may therefore provide valuable information for identifying areas of increased exploration interest. In this context, the spatial patterns resolved by EMIT suggest that spaceborne hyperspectral data may contribute to regional-scale screening and prioritisation of prospective areas associated with Cu-bearing mineral systems.

3.3 Case Study 2: Carbonatite Complexes along the Kudu lineament

3.3.1 Geological setting

The second study area encompasses the Twyfelskupje and the Dicker Willem carbonatites, located within the Tsau-ǁKhaeb (Sperrgebiet) National Park in southwestern Namibia (Figs. 3.1a,b and 3.10a). This region, historically restricted due to diamond mining activities, has only recently become more accessible to detailed geological studies. These carbonatites are aligned along the NNE-SSW striking Kudu lineament and conjugate structures [76].

In the area, the basement rocks of the Namaqua Natal Province predominantly consist of strongly foliated biotite-quartz feldspar gneiss, with lesser amounts of pegmatite, quartz schist, quartzite, and amphibolite [77]. Three major alkaline magmatic events are recognized in the region between Lüderitz and Aus: 1) the first event, associated with the Namaqua Orogeny around 1.1 Ga, is characterized by significant intrusive alkaline magmatism; 2) the second event occurred around 130 Ma, forming the Lüderitz Alkaline Province; 3) the third and youngest event involved both alkaline and carbonatitic magmatism [76]. Though age constraints are limited, with Dicker Willem dated to approximately 49±1 Ma (K-Ar on muscovite and Rb-Sr on mica-calcite); [78], it is likely that, for the spatial relationship, the Twyfelskupje carbonatite also belongs to this event [79].

The Dicker Willem, is one of the most well-studied carbonatites in the region (Figs. 3.10b,d). Spanning approximately 3 km in diameter and rising 600 m above the Namib Desert, is composed almost entirely of carbonatite. Primary textures are largely well-preserved [80, 81]. It contains early coarse-grained pyroxene-biotite-magnetite calcite carbonatite (sövite; [82]), which appears as xenoliths and screens situated within and among sheets of a later-formed, fine-grained calcite carbonatite (alvikite; [83]) (Fig. 3.10d).

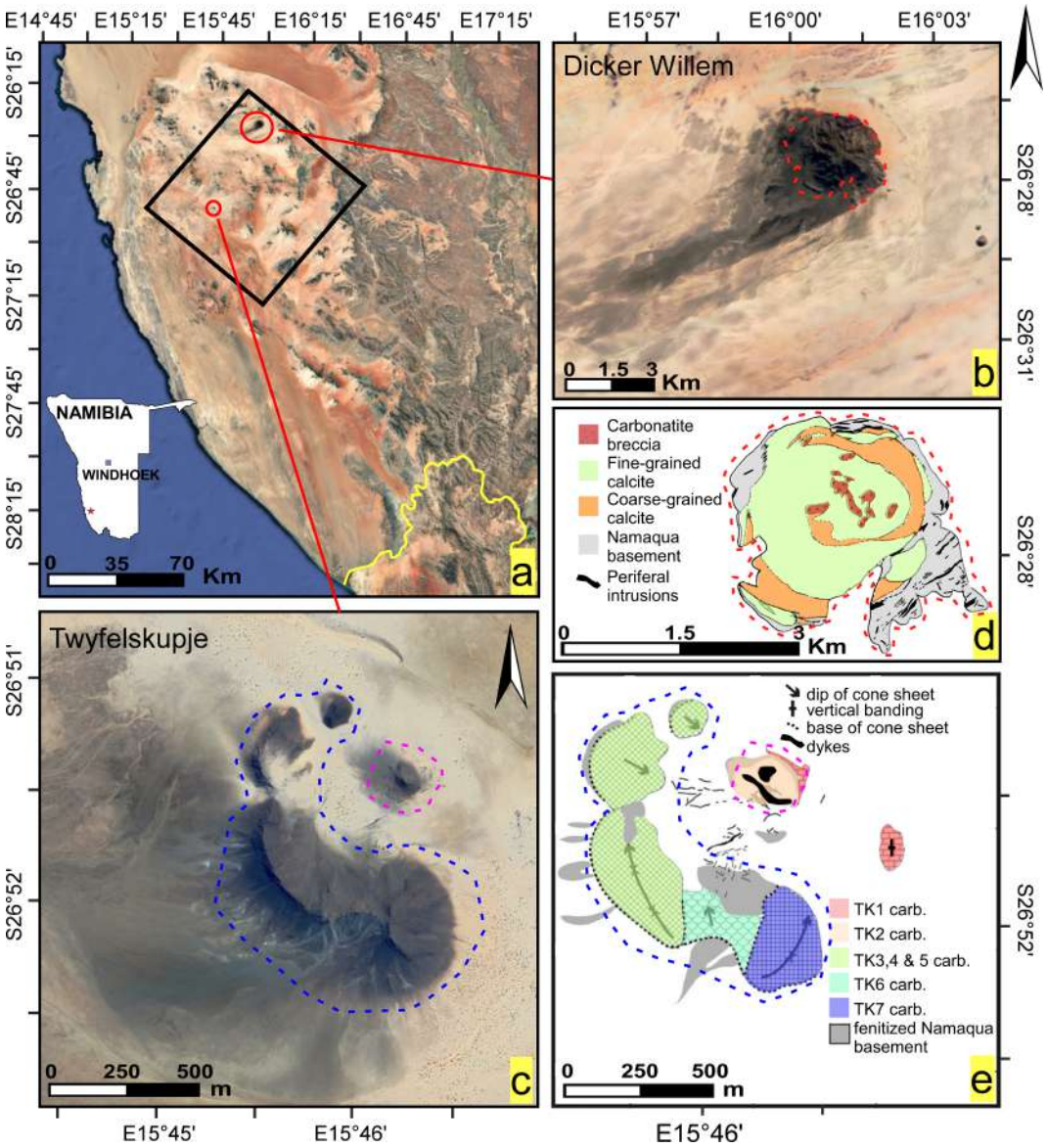

Fig. 3.10 (a) Location of the Dicker Willem and Twyfelskupje carbonatite complexes (red circles) within the Tsau-ǁKhaeb (Sperrgebiet) National Park, southwestern Namibia (https://earth.google.com/web). (b) The Dicker Willem carbonatite complex; the dashed outline indicating the area corresponding to the geological map shown in panel (d). (c) The Twyfelskupje carbonatite complex, where the central core is highlighted by a pink hatch and the peripheral zones are shown in blue, indicating the geological units represented in panel (e). (d) Geological map of the Dicker Willem carbonatite complex (modified after [83]). (e) Simplified geological map of the Twyfelskupje carbonatite complex (modified after [77]). Panels (a–e) are modified from [64].

The Twyfelskupje carbonatite represents another important intrusion within the region (Figs. 3.10c,e). This circular group of hills, approximately 1 km in diameter, remains tectonically undeformed. Marlow et al. [77] identify and describe eight distinct areas within the complex. Specifically, the central part includes TK1A, TK1B, and TK2, while the peripheral zone is designated from TK3 to TK7 (Fig. 3.10e). The central carbonatites in the Twyfelskupje complex consist of plug-like bodies (TK1) and a network of dykes (TK2), with distinct banding attributed to variations in yellow REE-bearing fluorcarbonate minerals and transitions between calcic and slightly dolomitic carbonatites. In the peripheral zone, cone sheets of calcic, dolomitic, and ferric carbonatites dominate. A general trend is observed where CaO decreases relative to MgO from the center to the periphery, accompanied by a reduction in the weight percent of rare earth oxides (REO) moving outward [77].

3.3.2 Data set

The analysis for this study area was based on a cloud-free Level-2A EMIT reflectance scene EMIT_L2A_RFL_001_20230125T100653_2302506_009, available through NASA's Earthdata Search portal (https://search.earthdata.nasa.gov/search). EMIT Level-2A products consist of atmospherically corrected Bottom-Of-Atmosphere (BOA) surface reflectance data derived from calibrated Level-1B Top-Of-Atmosphere (TOA) radiance measurements. The atmospheric correction workflow implemented within the EMIT Science Data System is based on the ISOFIT (Imaging Spectrometer Optimal FITting) radiative transfer modelling framework [49, 70], allowing the retrieval of surface reflectance suitable for quantitative spectral analysis.

Prior to analysis, the dataset was georeferenced through the use of geographic lookup tables (GLTs) and restricted to the boundaries of the study area. Because the product had already undergone atmospheric correction by the data provider, reflectance values were not available in the 1327–1431 nm and 1771–1959 nm wavelength intervals due to strong atmospheric water vapour absorption. Additional spectral filtering was subsequently applied to the remaining data to exclude bands affected by artefacts in the 984–1014 nm range [64].

3.3.3 Analysis

Target mineralogy: carbonate minerals

In order to investigate mineralogical variability and compositional zonation within the carbonatite-related systems along the Kudu Lineament, the analysis focused on carbonate minerals, with particular emphasis on the discrimination between calcite and dolomite. Carbonates exhibit diagnostic absorption features in the SWIR region associated with vibrational overtones of the CO_3^{2-} group, most notably in the 2300–2350 nm wavelength range (Fig. 3.11). The precise position and shape of these absorption features are sensitive to cation substitution within the carbonate lattice, allowing calcite- and dolomite-dominated assemblages to be distinguished based on systematic wavelength shifts.

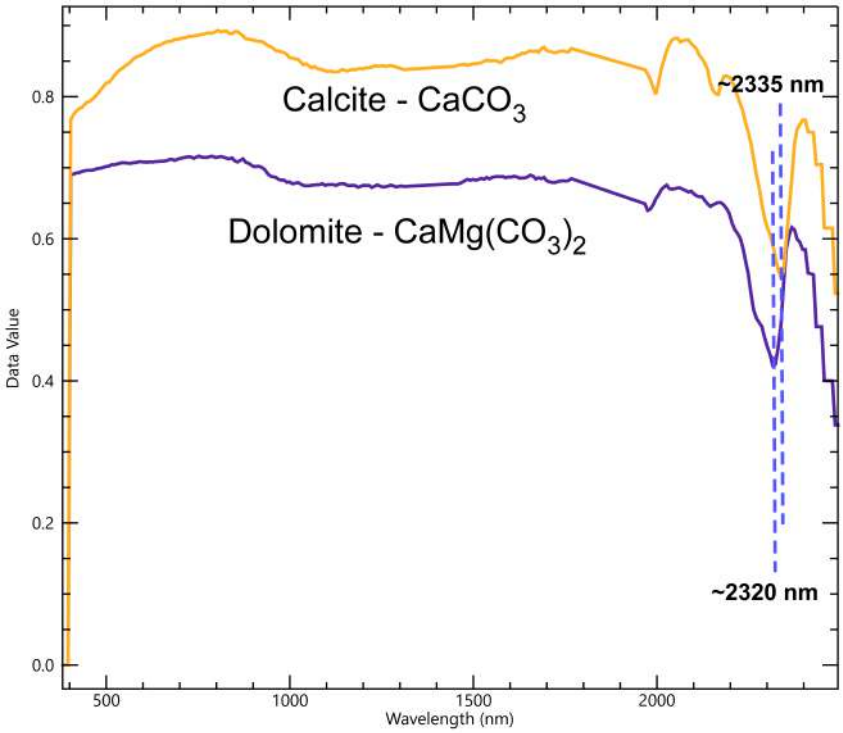

Fig. 3.11 USGS library reflectance spectra of calcite and dolomite showing a diagnostic Mg–OH/CO_3 absorption feature, with the absorption minimum of calcite occurring at longer wavelengths than that of dolomite.

In particular, dolomite typically shows absorption minima at shorter wavelengths compared to calcite, reflecting differences in crystal chemistry related to Ca–Mg

substitution. Therefore, mapping spatial variations in the wavelength position of the main carbonate absorption feature enables the identification of carbonate zonation patterns at the satellite scale.

3.3.4 Methodology

Wavelength mapping

To investigate spatial patterns in surface mineralogy within the second study area, wavelength mapping was applied using three different spectral configurations, each designed to emphasise specific mineralogical groups (Table 3.2).

The first wavelength mapping product (WM1) employed a broad SWIR interval between 2100 and 2400 nm in both processing steps in order to capture minerals exhibiting diagnostic absorption features across the SWIR region, including OH-bearing phases and carbonate minerals.

The second wavelength mapping product (WM2) was specifically designed to enhance carbonate-rich lithologies. The first processing step retained the broad 2100–2400 nm interval, whereas the second processing step was restricted to the narrower 2320–2350 nm range to isolate absorption features associated with Mg–Ca–Fe carbonates. Although phyllosilicates may exhibit secondary absorptions within this interval, the wavelength mapping algorithm identifies only the dominant absorption feature, preferentially highlighting carbonate-rich pixels.

The third wavelength mapping product (WM3) focused on Fe-bearing minerals, particularly Fe^{3+} oxides. For this purpose, the VNIR interval from 700–1200 nm was applied in the first processing step and subsequently restricted to 850–1000 nm in the second step.

The resulting wavelength maps were generated using an automatic depth stretch (30–95 percentile stretch). To facilitate the identification of subtle spectral variations potentially associated with minor mineral occurrences, the stretch was subsequently refined to include absorption depths between 0–20% for SWIR products and 0–8% for VNIR products.

Table 3.2 Wavelength mapping parameters applied to the Kudu carbonatite complexes for detecting compositional variations in carbonate minerals and Fe^{3+} oxides using EMIT hyperspectral data.

Product	Step 1 (nm)	Step 2 (nm)	Target mineralogy
WM 1	2100–2400	2100–2400	OH-bearing minerals for surface mineralogy
WM 2	2100–2400	2320–2350	Carbonate minerals and their compositional variations (Mg–Ca–Fe)
WM 3	700–1200	850–1000	Fe^{3+} oxides (hematite, goethite)

Band Ratio

Building on the diagnostic wavelength intervals reported by Pontual et al. [54], spectral band ratios were defined to enhance minerals associated with Al–OH, Fe–OH, and Mg–OH/CO_3 absorptions. Specifically, the wavelength intervals 2185–2225 nm, 2230–2296 nm, and 2306–2365 nm were selected to target Al–OH-bearing phases, Fe-bearing minerals, and carbonate-related assemblages, respectively.

To account for the spectral characteristics of EMIT and improve ratio robustness, each absorption feature was normalised using a reference shoulder located near 1600 nm. This wavelength region exhibits relatively stable reflectance and limited atmospheric or mineralogical interference, making it suitable as a common denominator.

The calculated band ratios were subsequently combined into a false-colour composite image to provide an integrated representation of spatial mineralogical variability.

3.3.5 Results

The wavelength map spanning the 2100–2400 nm interval (WM 1; Table 3.2) provides an overview of the spatial distribution of minerals exhibiting diagnostic OH-related and carbonate absorption features (Figs. 3.12a, d, 3.13a, and 3.14a). At the Dicker Willem complex, pixels characterised by green colours are associated with absorption minima at shorter wavelengths, around 2200 nm, whereas magenta hues indicate longer-wavelength absorptions near 2340 nm. In contrast, the Twyfelskupje outcrop is largely dominated by dark magenta tones (Fig.3.14a).

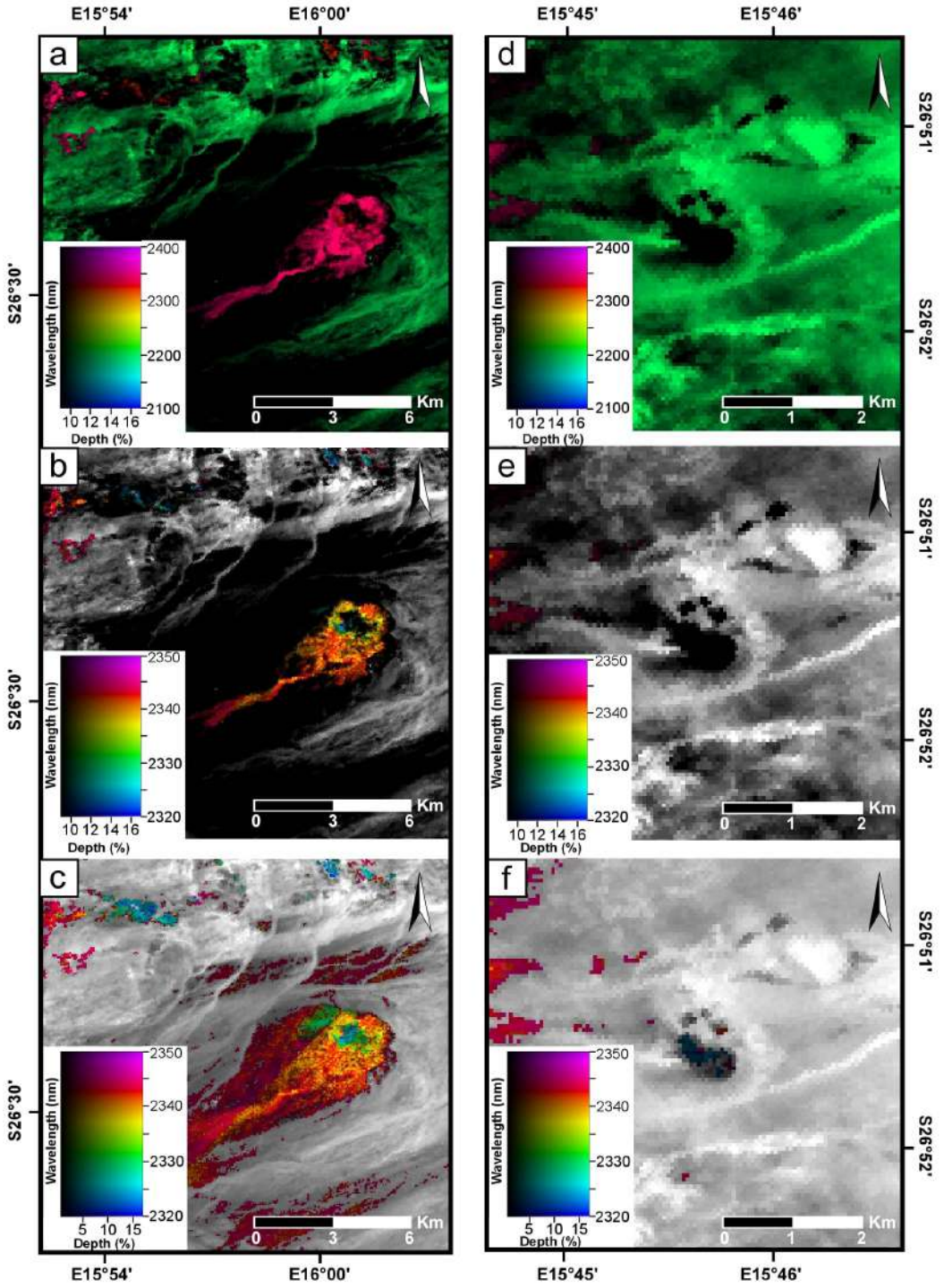

Fig. 3.12 (a) Product WM 1: Wavelength map 2100—2400 nm over Dicker Willem; (b) Product WM 2: Wavelength map 2320—2350 nm (step 2) over Dicker Willem; (c) Wavelength map 2320—2350 nm (step 2) with different stretches for depth over Dicker Willem; (d) Product WM 1: Wavelength map 2100–2400 nm over Twyfelskupje; (e) Product WM 2: Wavelength map 2320—2350 nm (step 2) over Twyfelskupje; (f) Wavelength map 2320—2350 nm (step 2) with different stretch for depth over Twyfelskupje.

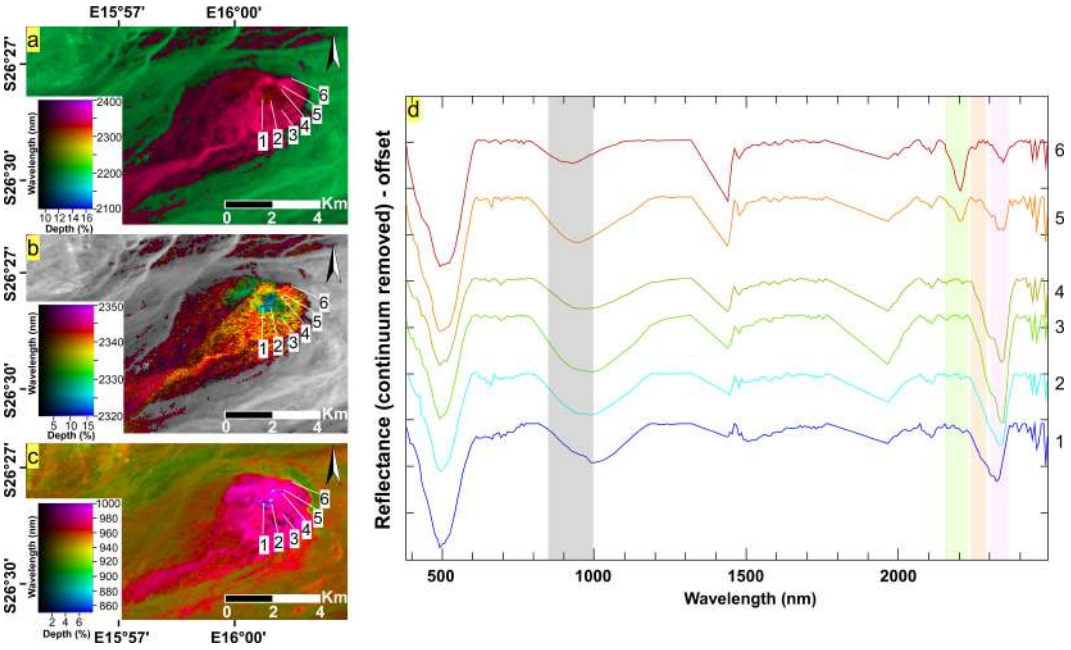

Fig. 3.13 (a) Wavelength map of the Dicker Willem carbonatite complex generated over the 2100—2400 nm interval (WM 1); (b) Wavelength map focusing on the narrower 2320—2350 nm range (WM 2); (c) Wavelength map covering the 850—1000 nm interval (WM 3); (d) Representative reflectance spectra extracted from the Dicker Willem carbonatite complex (spectra 1–6). For visual comparison, the colour of each spectrum corresponds to the colour of the associated pixels shown in panel (b), and spectra have been vertically offset for clarity. Shaded bands in the background indicate the diagnostic wavelength intervals for Al–OH, Fe–OH, and Mg–OH/CO_3^{2-} absorption features, following [54]. Modified from [64].

To refine the characterisation of spatial mineralogical variability, two additional wavelength maps were generated: a focused SWIR map covering 2320—2350 nm (WM 2; Table 3.2 and Figs. 3.12b, e, 3.13b, and 3.14b) and a VNIR map in the 850—1000 nm range (WM 3; Figs. 3.13c, and 3.14c). The 2320—2350 nm map emphasises carbonate-related absorption features and reveals contrasting spatial trends between the two complexes. At Dicker Willem, absorption minima display a progressive outward shift from shorter wavelengths near the centre to longer wavelengths toward the margins. Conversely, at Twyfelskupje, the spatial pattern shows an outward transition from longer to shorter wavelength absorptions, despite the generally shallow spectral features observed in this range (Fig.3.14b).

The VNIR wavelength map (WM 3; Table 3.2 and Figs. 3.13c, and 3.14c), targeting Fe^{3+}-bearing oxide minerals, highlights additional spatial organisation.

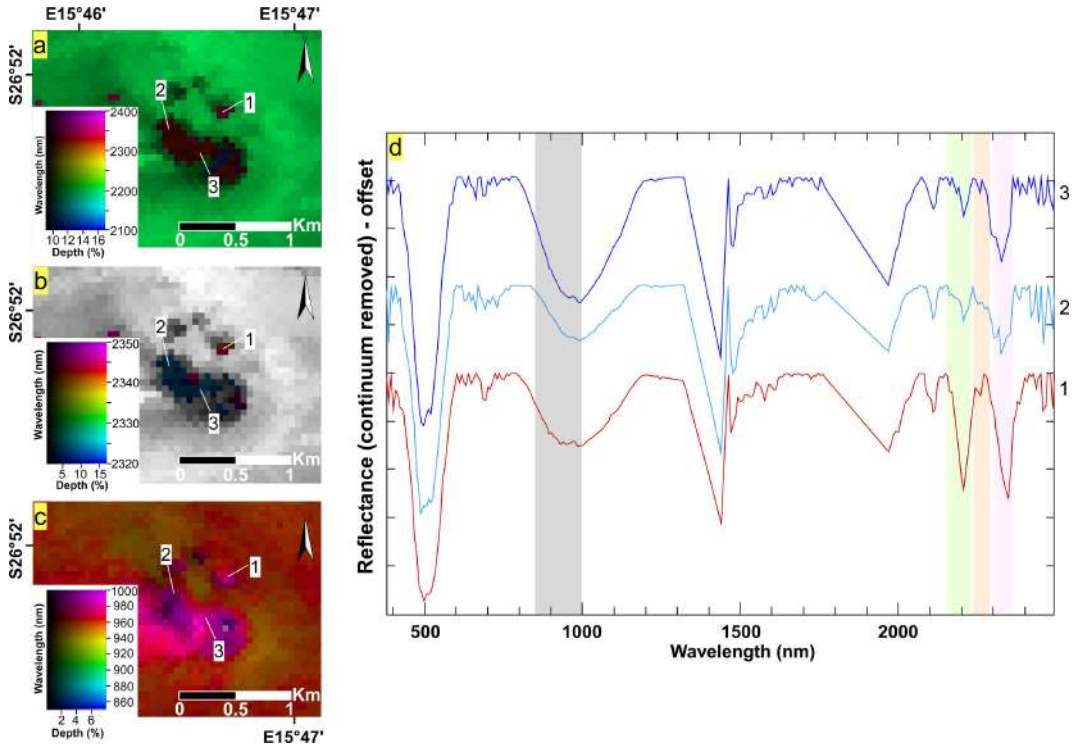

Fig. 3.14 (a) Wavelength map of the Twyfelskupje carbonatite complex generated over the 2100—2400 nm interval (WM 1); (b) Wavelength map restricted to the 2320—2350 nm range (WM 2); (c) Wavelength map covering the 850—1000 nm interval (WM 3); (d) Representative reflectance spectra extracted from the Twyfelskupje carbonatite complex (spectra 1–3). For comparison, the colour assigned to each spectrum corresponds to the colour of the associated pixels shown in panel (b), and spectra are vertically offset for clarity. Shaded background bands indicate the diagnostic wavelength intervals for Al–OH, Fe–OH, and Mg–OH/CO_3^{2-} absorption features, following [54]. Modified from [64].

At Dicker Willem, longer-wavelength absorption features are concentrated in the central portion of the intrusion, while shorter-wavelength features predominantly form a surrounding peripheral zone. A comparable, though less distinct, zoning pattern is also observed at Twyfelskupje.

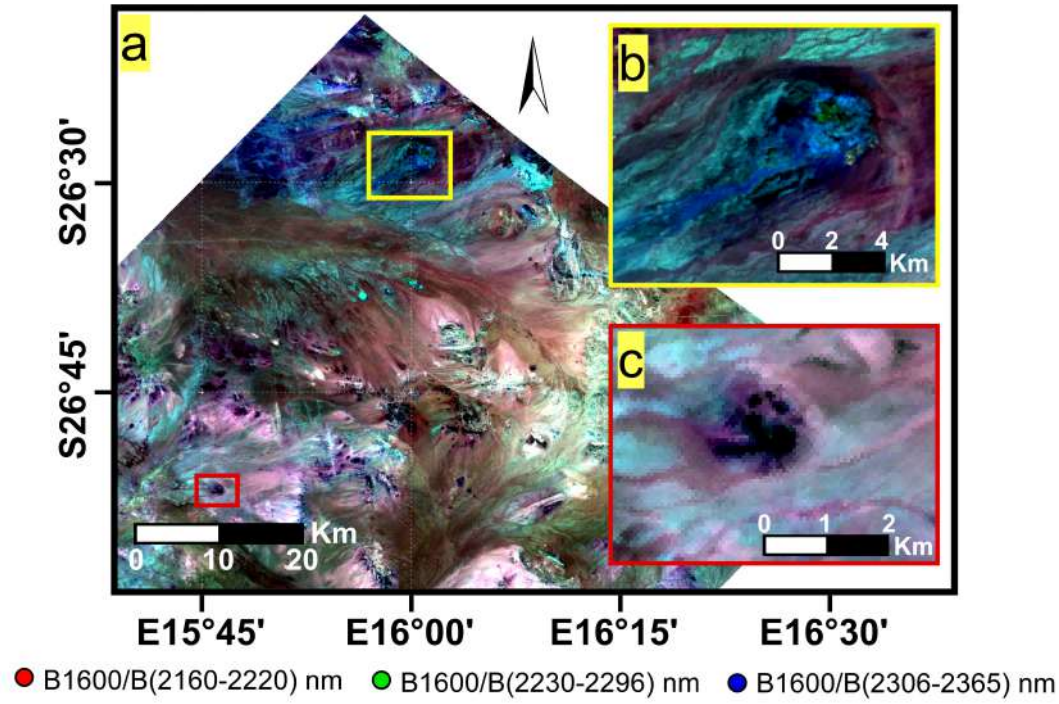

Fig. 3.15 (a) False-colour composite of the study area generated by combining spectral band ratios sensitive to key mineral groups: B1600/B2160–2220 nm assigned to the red channel (Al–OH), B1600/B2230–2296 nm to the green channel (Fe–OH), and B1600/B2306–2365 nm to the blue channel (Mg–OH/CO_3^{2-}); (b) Enlarged view of the Dicker Willem carbonatite complex; (c) Enlarged view of the Twyfelskupje carbonatite complex. Adapted from [64].

Further insight into mineralogical variability is provided by the false-colour composite image derived from the Al–OH, Fe–OH, and Mg–OH/CO_3 band ratio products (Fig.3.15a). At Dicker Willem, dark magenta colours indicate areas where Al–OH and Mg–OH/CO_3 absorptions spatially coincide, whereas blue and cyan tones correspond to regions dominated by Mg–OH/CO_3 and Fe–OH spectral responses. Green pixels delineate zones characterised by Fe–OH signatures concentrated towards the central part of the complex (Fig.3.15b).

In contrast, the false-colour composite generated for Twyfelskupje does not reveal a clearly organised spatial pattern (Fig.3.15c), consistent with the more subdued trends observed in the wavelength mapping products.

3.3.6 Discussion

The spectral patterns identified using EMIT data align well with existing conceptual models of carbonatite systems, particularly those involving magmatic differentiation, fluid–rock interaction, and subsequent hydrothermal overprinting documented in previous field- and laboratory-based studies [83, 76]. The wavelength shifts observed across the Kudu carbonatite complexes provide insights into compositional variability that can be interpreted within this established geological framework.

Spatial variations in carbonate- and Fe^{3+}-related absorption features, highlighted by the 2320—2350 nm and 850–1000 nm wavelength maps, reveal distinct zonation patterns within the two complexes. At Dicker Willem, carbonate absorption minima progressively shift from shorter wavelengths near the centre (approximately 2322 nm) toward longer wavelengths at the margins (up to 2345 nm). This trend is consistent with a transition from Mg-rich carbonates toward more Ca- and Fe-enriched compositions (Fig. 3.16). Such a pattern corresponds well with petrological descriptions of a central sövite core surrounded by ferroan carbonatites (alvikite) forming concentric peripheral sheets [76], a configuration commonly attributed to magmatic differentiation and early-stage fluid–rock interaction during emplacement [83, 82]. However, the spectral evidence alone does not allow a definitive mineralogical attribution, and direct confirmation of this compositional gradient remains limited.

In contrast, Twyfelskupje exhibits an inverse spectral trend. Longer wavelength carbonate absorption features are concentrated toward the centre while progressively shorter wavelengths characterize the margins. Although whole-rock geochemical data indicate outward increases in MgO and decreases in CaO [77], detailed documentation of Fe enrichment toward the margins is scarce. The observed spectral pattern may therefore reflect either a comparable differentiation process expressed differently in space or the influence of metasomatic alteration. This interpretation is compatible with structural observations of cone-sheet intrusions and complex

emplacement geometries reported for Twyfelskupje [77], though further petrological investigations are required to constrain these relationships.

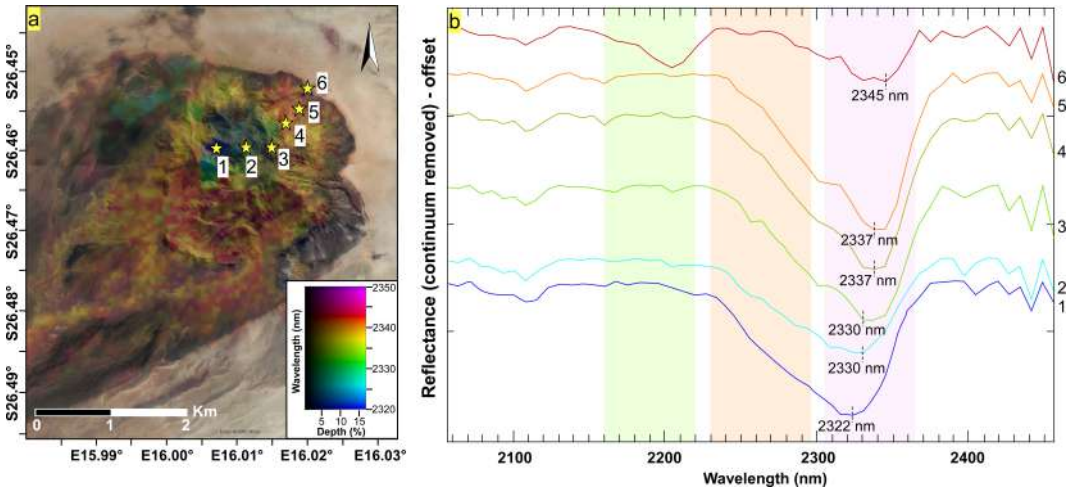

Fig. 3.16 (a) Wavelength map of the Dicker Willem carbonatite complex generated over the restricted 2320–2350 nm interval (WM 2); (b) Representative reflectance spectra extracted from the mapped areas (spectra 1–6), highlighting absorption features related to carbonate minerals. For visual comparison, the colour assigned to each spectrum corresponds to the colour of the associated pixels in the wavelength map, and spectra are vertically offset for clarity. Shaded background bands indicate the diagnostic absorption intervals for Al–OH, Fe–OH, and Mg–OH/CO_3^{2-} mineral groups. A systematic shift in absorption feature position from shorter to longer wavelengths is observed from the central portion of the complex toward its margins. Adapted from [64].

Additional constraints on mineralogical zonation are given by the 850–1000 nm wavelength map, which targets Fe^{3+}-bearing oxides. At Dicker Willem, a concentric arrangement is evident, with longer-wavelength absorption features, commonly associated with more crystalline goethite, concentrated near the core, and shorter-wavelength features distributed toward the margins (Fig. 3.17). This pattern is consistent with fluid-driven alteration processes and outwardly decreasing crystallinity, in agreement with studies linking goethite spectral behaviour to compositional and structural variability [84]. Such gradients may reflect progressive cooling or changes in fluid chemistry, including pH, during the late stages of carbonatite evolution [77]. In contrast, Twyfelskupje does not display a well-defined zonation in this wavelength range, likely due to the masking effects of surface coatings, weathering, or fine-grained textures that diminish VNIR spectral responses [77].

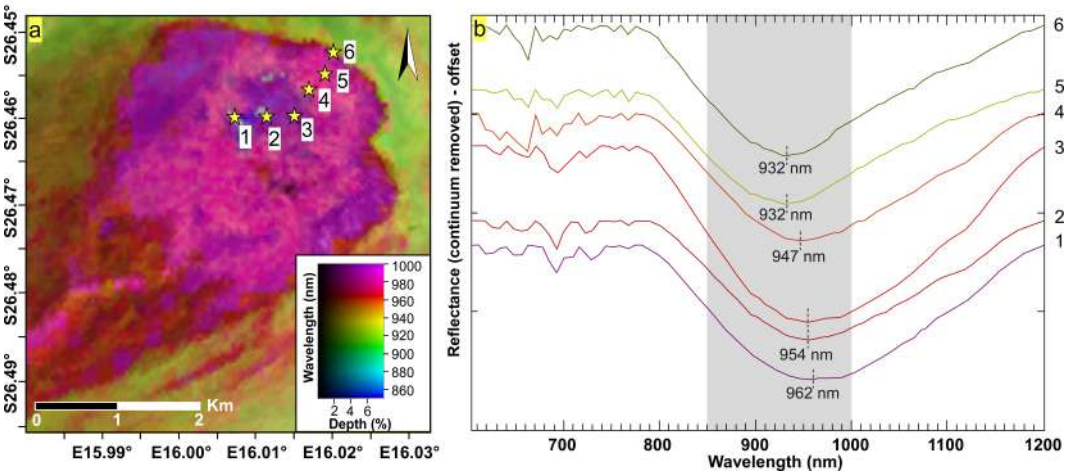

Fig. 3.17 (a) Wavelength map of the Dicker Willem carbonatite complex over the 850–1000 nm interval (WM 3); (b) Representative reflectance spectra (spectra 1–6) showing absorption features related to Fe^{3+}-bearing oxide minerals. The colour of each spectrum corresponds to the associated pixels in the wavelength map, and spectra are vertically offset for clarity. The shaded background indicates the diagnostic absorption region for Fe^{3+}-bearing oxides, with absorption features shifting from longer to shorter wavelengths from the core toward the margins. Adapted from [64].

The false-colour composite combining Al–OH, Fe–OH, and Mg–OH/CO_3^{2-} absorption features further supports the presence of mineralogical zoning, particularly at Dicker Willem (Fig. 3.15). Here, Fe–OH-related signatures dominate the central areas, while Mg–OH and mixed Al–Mg responses characterise the margins. When integrated with the wavelength mapping results, this spatial distribution suggests systematic mineral substitution trends and a magmatic-to-hydrothermal evolutionary pathway, consistent with earlier geological interpretations [83, 76]. Nonetheless, comprehensive mineralogical and geochemical validation is required to fully resolve the timing and extent of fluid evolution and alteration processes at both complexes.

Despite the clear zonation identified in major mineral groups, the detection of more subtle spectral features remains challenging. Diagnostic absorption bands associated with REEs minerals in the VNIR and SWIR ranges (e.g. [85, 86]) are not observed in this study. This limitation is likely related to the masking effects of Fe^{3+}-bearing oxides and the spatial resolution of EMIT (60 m), which may be insufficient to resolve discrete REE-bearing phases such as monazite or bastnäsite. Comparisons with previous studies using higher spatial resolution hyperspectral data,

such as EnMAP (30 m), highlight the inherent trade-off between spatial and spectral resolution in regional-scale remote sensing applications [29].

3.4 Conclusions

This study used hyperspectral data from the EMIT sensor to investigate mineralogical variations in two contrasting geological settings: hydrothermal muscovite alteration at Haib and carbonate and iron oxide zonation in the Kudu Carbonatite Complexes.

The generated wavelength maps and spectral band ratio composites provided critical insights into the mineralogical patterns at both sites. At Haib, wavelength mapping within the 2100—2400 nm range differentiated OH-bearing minerals (Fig. 3.4), highlighting muscovite-rich zones (green pixels) and Mg-rich zones (magenta pixels). A refined analysis around 2200 nm (Fig. 3.5) revealed a shift in muscovite absorption peaks from 2197 nm to 2211 nm, values consistent with those reported for compositional variations linked to octahedral cation substitution ([74, 26, 73, 75, 71]). This suggests a transition from Al-rich to Mg-rich muscovite, reflecting changes in fluid composition during hydrothermal alteration processes. The band ratio composites confirmed the distribution of Al-OH, Fe-OH, and Mg-OH-bearing minerals and corresponded well with known lithological and structural boundaries.

In the Kudu Carbonatite Complexes, spectral mapping in the 2320—2350 nm window highlighted compositional zoning within the carbonatite bodies. In Dicker Willem, a gradual shift in carbonate absorption peaks from 2322 nm at the core to 2345 nm outward was detected (Fig. 3.16), indicating a transition from calcite to more Fe-rich carbonates, possibly siderite. Conversely, Twyfelskupje displayed an inverse trend (Fig. 3.17), possibly reflecting different crystallisation or alteration histories. Lastly, VNIR-based iron oxide mapping at Dicker Willem showed a shift in goethite absorption features toward shorter wavelengths from core to periphery, compatible with decreasing crystallinity consistent with fluid-driven alteration and a decreasing crystallinity gradient [84]. Although REEs absorptions have been detected in other hyperspectral missions such as EnMAP [29], no clear REEs features were observed in this study, likely due to the masking effect of iron oxides and/or EMIT's lower spatial resolution relative to the scale of REE-bearing structures.

Nevertheless, regarding the CRMs, the mineralogical patterns identified in both study areas have important implications for exploration targeting. In the Haib porphyry system, although copper mineralisation itself cannot be directly detected through SWIR hyperspectral methods, the mapped hydrothermal alteration assemblages and muscovite compositional variations may act as indirect vectors toward potentially mineralised zones. Variations in white mica chemistry have commonly been associated with evolving hydrothermal fluid conditions in porphyry systems and therefore provide useful indicators for identifying areas of increased Cu exploration potential.

Similarly, in the Kudu carbonatite complexes, the observed carbonate and Fe-oxide zonation patterns may provide indirect information relevant to REE exploration. Carbonatites are among the most important geological hosts for REE mineralisation, and compositional variations within carbonate minerals commonly reflect magmatic differentiation and hydrothermal processes associated with REE enrichment. Although no direct REE-related absorption features were resolved using EMIT data in this study, the spatial mineralogical variations identified may still serve as exploration vectors for recognising potentially prospective domains within carbonatite systems.

Overall, despite the relatively coarse 60-meter spatial resolution of EMIT, hyperspectral data effectively addressed the geological questions for both study areas.

The main limitation encountered was the difficulty in analysing small, fine-grained features such as Twyfelskupje, where pixel mixing likely obscured subtle mineralogical signals. However, EMIT's high spectral fidelity allowed the detection of subtle (~10–20 nm) shifts in key mineral absorption features, demonstrating that meaningful mineralogical information can be extracted even at moderate spatial resolutions. This capability expands the application of spaceborne hyperspectral sensors for regional geological mapping, particularly in arid terrains with good surface exposure. The integration of wavelength mapping and simple band ratios proved to be an effective strategy to maximise the mineralogical interpretability of EMIT data in geological contexts.

In conclusion, EMIT represents a significant step forward for spaceborne hyperspectral applications in Earth sciences, proving that detailed mineralogical information can be retrieved even at moderate spatial resolutions.

Chapter 4

Laboratory-based analysis of DW carbonatite samples

4.1 Introduction

This chapter presents a preliminary ground-based investigation carried out to support and contextualise the hyperspectral observations derived from EMIT data over the Dicker Willem carbonatite complex. A suite of hand specimens collected from the study area was analysed using complementary laboratory and field-based analytical techniques in order to characterise their mineralogical and geochemical properties and to assess the detectability of REEs using spectroscopic methods.

A particular focus is placed on neodymium (Nd), as it is among the most spectrally active and readily detectable REEs in the VNIR–SWIR range, owing to its characteristic absorption features [86, 85]. The primary objective of this work is to identify which samples contain measurable Nd and to explore whether a minimum concentration threshold can be inferred for the appearance of diagnostic absorption features in reflectance spectra.

To this end, twenty rock samples from the Dicker Willem carbonatite complex were analysed using hyperspectral imaging, field spectroscopy, X-ray diffraction (XRD), and portable X-ray fluorescence (pXRF). Inductively Coupled Plasma Mass Spectrometry (ICP-MS) analyses were also performed; however, due to uncertainties

related to digestion and dilution procedures, these results are not discussed and are not used for quantitative interpretation.

4.2 REE: Overview and Economic Importance

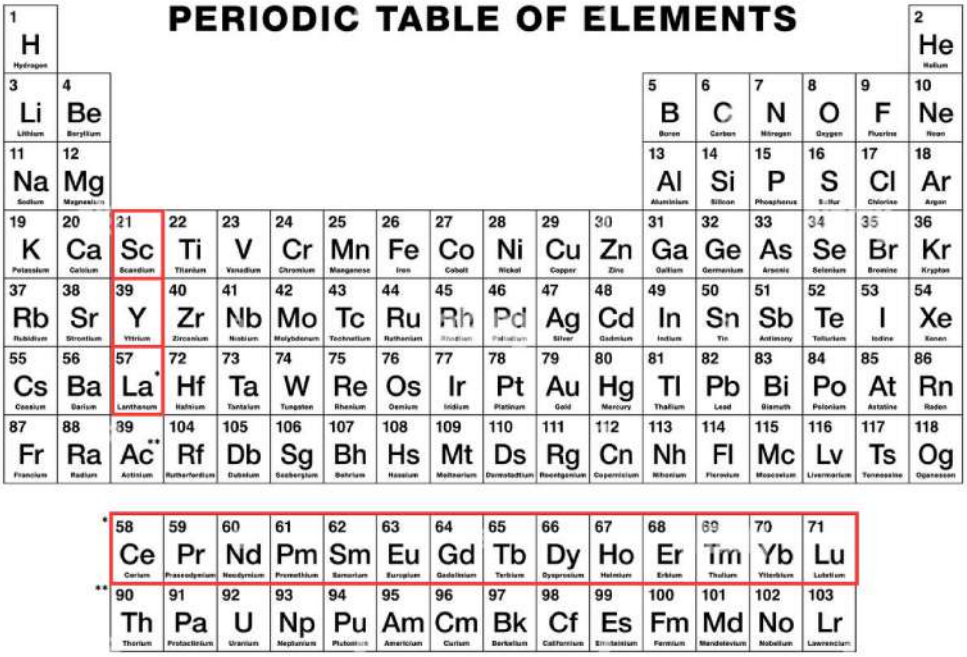

Fig. 4.1 Periodic table of the elements with the Rare Earth Elements (REE) highlighted in red. REE include the lanthanide series (La–Lu) as well as yttrium (Y) and scandium (Sc), which exhibit similar ionic radii and geochemical behaviour and are therefore commonly grouped with the lanthanides.

REEs form a coherent group of seventeen chemical elements defined by the International Union of Pure and Applied Chemistry (IUPAC) as comprising the fifteen lanthanides (from lanthanum to lutetium), together with yttrium and scandium [87]. The lanthanides occupy atomic numbers 57 to 71 in the periodic table and are subdivided by geochemists into Light REE (LREE) and Heavy REE (HREE), a distinction that reflects differences in ionic radii and electron configurations related to the progressive filling of the 4f orbitals [87].

Contrary to the implication of their name, most REEs are not particularly scarce in the continental crust; rather, they are oocasionally concentrated in economically exploitable deposits. For example, cerium (Ce), the most abundant REE, has an average concentration of approximately 60–70 ppm in the upper continental crust, comparable to that of copper, while neodymium (Nd), the primary focus of this thesis, has an average crustal abundance of about 38 ppm [87]. The therm "rare" originates from historical mineralogical terminology and reflects the tendency of REEs to occur in dispersed forms rather than as highly concentrated, isolated mineral phases.

REEs are typically found in nature as oxide-bearing minerals, a characteristic that historically motivated the use of the term "earths" in early mineralogical literature [88]. Common REE-hosting minerals include bastnäsite, monazite, and allanite, which are generally enriched in LREE. Deposits containing REEs in concentrations suitable for economic extraction are relatively uncommon, which underpins the strategic importance of REEs resources and concerns related to supply security.

In natural geological systems, REEs tend to behave coherently as a group and do not readily fractionate into individual elements, complicating both extraction and separation processes [89]. From a geological perspective, two principal categories of REEs deposits are recognised: (1) high-temperature systems, notably carbonatites and their associated hydrothermal derivatives; and (2) low-temperature systems, such as regolith-hosted deposits in weathered bauxites and laterites. Among these, carbonatites represent the most important class of primary REEs sources worldwide. A prominent example is the Bayan Obo Fe–REE–Nb deposit in China, the largest known REEs deposit globally, with high-grade reserves estimated at approximately 48 Mt at $\sim$6 wt. % REO [90].

REEs are indispensable to a wide range of modern technologies. Their applications include fluid cracking catalysts, specialised glass and alloy production, YAG lasers. Of particular strategic importance are permanent neodymium–iron–boron (Nd–Fe–B) magnets, which are essential components in wind turbines, electric vehicles, aerospace systems, and defence technologies, as well as in advanced ceramics and high-performance electronic devices [91, 88]. Recent market analyses indicate that the highest global demand among REEs is for neodymium, together with selected heavy REEs such as europium, terbium, and dysprosium, which are critical for high-performance magnetic and luminescent applications.

From a historical perspective, the evolution of REEs mining is commonly divided into three broad eras: (1) early monazite placer mining; (2) the development of the Mountain Pass deposit in the United States; and (3) the emergence and subsequent dominance of Chinese production in the global REEs market [87]. The onset of the "Chinese era" in the mid-1980s was characterised by the availability of REEs at prices significantly lower than those of competing producers, leading to the closure of many mining operations outside China. As of the mid-2020s, China continues to dominate the global REEs supply chain, controlling a substantial proportion of both known reserves and downstream processing capacity.

Geopolitical and economic considerations have intensified efforts to diversify REEs supply beyond China. While major deposits such as Bayan Obo (China), Mount Weld (Australia), and Lovozero (Russia) continue to play a central role in global REEs production, new mining and processing initiatives in regions including Australia and North America aim to mitigate supply risks. In parallel, recycling and urban mining strategies are increasingly recognised as essential components of a sustainable REEs supply framework, given the environmental footprint and energy intensity associated with primary REEs extraction and processing.

In summary, the economic and strategic importance of REEs has increased markedly in recent decades due to their critical role in clean energy technologies, advanced electronics, and defence systems. The interplay between geological occurrence, market dynamics, and growing demand highlights the need for diversified supply sources, enhanced recycling pathways, and environmentally responsible management of REEs resources.

4.3 The Dicker Willem Carbonatite

4.3.1 Geology

The Dicker Willem carbonatite complex is a multiphase intrusive body emplaced within high-grade gneisses of the Mesoproterozoic Namaqua Province [80]. The complex is dominated by carbonatite lithologies, whereas associated silicate rocks are volumetrically minor and occur mainly as enclosed xenoliths, as well as thin screens and marginal sheets surrounding the intrusion.

Carbonatites constitute the most important primary source of REEs worldwide. They are defined as igneous rocks containing more than 50 vol.% of primary magmatic carbonate minerals [92]. This distinctive composition reflects the highly alkaline and volatile-rich nature of their parental magmas and underpins their exceptional ability to concentrate incompatible elements, including REEs, Nb, and P. Within this framework, carbonatite complexes such as Dicker Willem represent key geological environments for investigating REEs mineralisation.

Geochronological data indicate an emplacement age of approximately 49 ± 1 Ma, placing the Dicker Willem complex within a broader phase of alkaline magmatism that affected southern Namibia during the Late Cretaceous to early Tertiary [78]. This interval, spanning roughly from 133 to 29 Ma, was characterised by widespread emplacement of alkaline and carbonatitic magmas across the region.

Two main stages of carbonatite emplacement can be recognised [80, 93]. The earliest phase consists of coarse-grained calcite-rich carbonatites (sövites), which were subsequently intruded, disrupted, and locally brecciated by a younger generation of medium- to fine-grained carbonatites forming multiple concentric ring dykes of alvikite composition. The early sövites are typically white and display variable but generally coarse grain sizes, with a mineralogical assemblage dominated by calcite.

Based on previous petrographic studies, the sövite facies contains euhedral magnetite, clinopyroxene crystals showing compositional zoning from aegirine–augite cores to aegirine rims, and accessory pyrochlore [93]. Additional mineral phases include tabular biotite and rounded prismatic apatite, whereas dolomite has not been reported within the sövite assemblage. The sövites are further characterised by abundant inclusions of silicate rocks, predominantly represented by various types of ijolite.

The younger alvikite phase is generally finer grained and exhibits buff to pale brown colours. Porphyritic alvikites contain phenocrysts of magnetite and pyrochlore set within a carbonate-rich groundmass dominated by rhombohedral ferroan–manganoan dolomite [93].

In addition to the two main carbonatite phases, the Dicker Willem complex is characterised by late-stage dykes and vein systems, which record the final stages of magmatic and hydrothermal activity associated with the evolution of the complex [93].

4.3.2 Sample set and sampling strategy

Fig. 4.2 Overview of the Dicker Willem carbonatite complex in southern Namibia. (b) Brecciated carbonatite exposed at outcrop scale, characterised by angular to sub-angular clasts within a finer-grained matrix. (c) Medium- to coarse-grained whitish-grey carbonatite cross-cut by orange–brown dykelets, offsetting the main carbonatite body and locally highlight internal structural and compositional heterogeneity.

The analysed dataset consists of twenty rock samples collected from the Dicker Willem carbonatite complex on 15 March 2025. Sample selection was coordinated in collaboration with Dr. Mbili Tshiningayamwe (University of Namibia) and was designed to represent the main lithological units and alteration domains identified in the field and from previous geological studies of the area. Although the physical sampling was not carried out directly by the author, the sampling strategy and subsequent analytical workflow were defined to ensure consistency with the objectives of this study.

The initial sampling plan aimed to investigate the mineralogical zonation highlighted by wavelength mapping through the collection of samples along two orthogonal transects oriented approximately east–west and north–south across the intrusion.

This approach was intended to capture systematic compositional variations from the core toward the margins of the carbonatite. However, the implementation of a fully transect-based sampling strategy proved impractical due to logistical constraints and field accessibility. The Dicker Willem carbonatite is a large and topographically challenging structure, extending over approximately 3 km in length and reaching elevations of up to 600 m above its base, characterised by steep slopes and the absence of established access tracks (Fig. 4.2). As a result, sampling was restricted to accessible areas on one side of the complex, yielding a total of twenty hand specimens as shown in Appendix A.1.

Despite these limitations, pronounced variations in texture, colour, and visible mineralogy were observed during sampling, indicating significant internal heterogeneity within the intrusion. The collected samples therefore encompass both fresh and variably altered carbonatite lithologies, with particular attention given to materials potentially enriched in REE-bearing phases.

Sample locations were recorded using handheld GPS and are shown in Fig. 4.3. A summary of sample identifiers and geographic coordinates is provided in Table 4.1. The sample set is considered suitable for preliminary ground-based validation of hyperspectral observations and for guiding future, more systematic sampling campaigns.

Table 4.1 Sample locations and synthesised field descriptions for the Dicker Willem carbonatite complex.

Sample ID	Latitude (S)	Longitude (E)	Field description
DW_01	26.46577	16.03037	Fine-grained orange–brown carbonatite dyke cross-cutting the main intrusion.
DW_02	26.46575	16.03032	Porphyritic orange carbonatite with plagioclase and calcite phenocrysts in a fine-grained matrix.
DW_03	26.46531	16.02998	Porphyritic orange carbonatite with disseminated plagioclase–calcite phenocrysts.
DW_04	26.46498	16.02954	Orange–brown carbonatite breccia with randomly oriented clasts in a fine-grained matrix.
DW_05	26.46474	16.02945	Medium-grained whitish-grey carbonatite with scattered dark minerals.
DW_06	26.46420	16.02872	Fine-grained grey to orange carbonatite with secondary Fe-oxide staining.
DW_07	26.46387	16.02859	Medium-grained whitish-grey carbonatite with minor dark mineral content.
DW_08	26.46387	16.02840	Medium-grained whitish-grey carbonatite with dispersed dark minerals.
DW_09	26.46443	16.02784	Medium-grained whitish-grey carbonatite.
DW_10	26.46484	16.02782	Coarse-grained calcite-rich carbonatite with locally aligned dark minerals.
DW_11	26.46528	16.02747	Massive, fine-grained dark carbonatite.
DW_12	26.46591	16.02701	Medium-grained whitish-grey carbonatite with minor dark minerals.
DW_13	26.46720	16.02675	Massive, fine-grained dark carbonatite.
DW_14	26.46733	16.02676	Massive, fine-grained dark carbonatite.
DW_15	26.46766	16.02713	Orange–brown carbonatite breccia with coarse clasts in a fine-grained matrix.
DW_16	26.46779	16.02713	Orange–brown carbonatite breccia similar to DW_15.
DW_17	26.46815	16.02715	Medium-grained whitish-grey carbonatite.
DW_18	26.46821	16.02723	Coarse-grained calcite-rich carbonatite with aligned dark minerals.
DW_19	26.46823	16.02733	Coarse-grained calcite-rich carbonatite, similar to DW_18.
DW_20	26.46823	16.02733	Massive, fine-grained dark carbonatite.

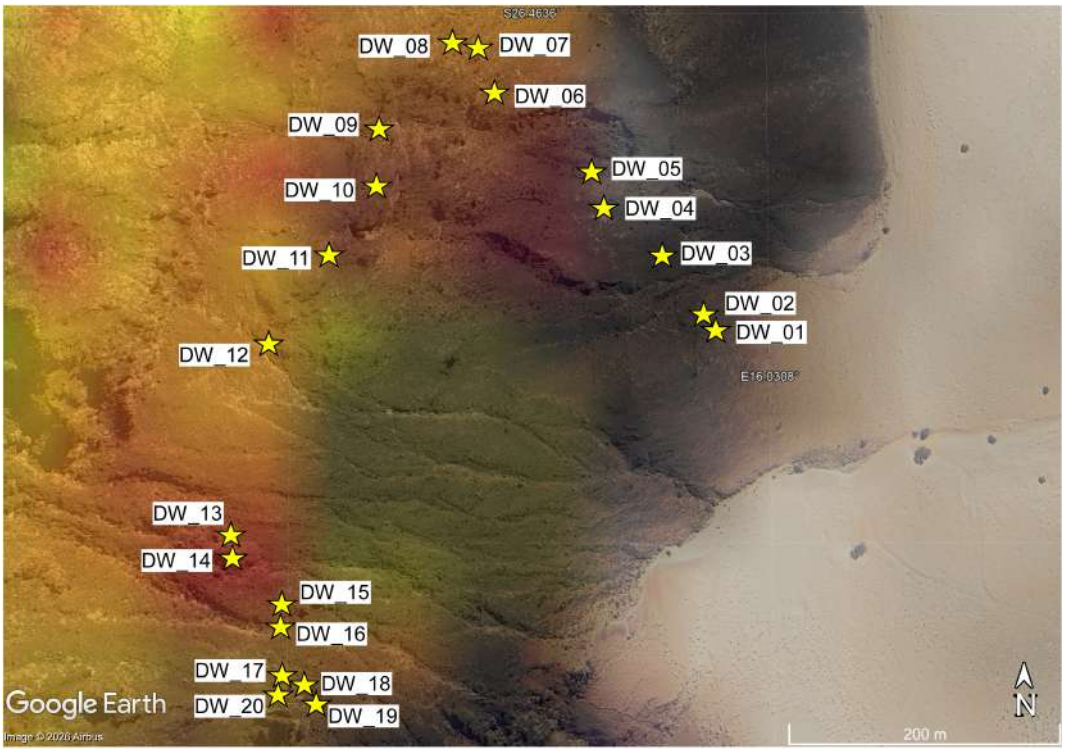

Fig. 4.3 Map showing the location of the twenty samples (DW_01–DW_20) collected at the Dicker Willem carbonatite complex and represented as yellow stars on a Google Earth basemap. The background colours represent the 2320–2350 nm wavelength map (WM 2), used to characterise carbonate-related spectral variability across the study area.

4.4 Hyperspectral imaging of hand specimens

Hyperspectral imaging of all samples was conducted using a SPECIM SisuCHEMA hyperspectral camera system at the Spectroscopy Laboratory of the Faculty of Geo-Information Science and Earth Observation (ITC), University of Twente (Fig. 4.4). The system comprises two imaging spectrometers operating in the VNIR and SWIR spectral regions. The VNIR sensor covers the 350–1000 nm wavelength range with 768 spectral bands and 1024 spatial pixels, while the SWIR sensor operates between 1000 and 2500 nm, acquiring data in 288 spectral bands with 384 spatial pixels. Together, the two sensors provide continuous hyperspectral coverage across the VNIR–SWIR domain, including the diagnostic wavelength regions relevant for mineralogical investigations and REEs detection. A summary of the main instrumental characteristics and acquisition parameters is provided in Table 4.2.

Table 4.2 Specifications and acquisition setup of the SPECIM SisuCHEMA hyperspectral imaging system used for laboratory measurements at the ITC Spectroscopy Laboratory.

Parameter	**Specification**
Instrument	SPECIM SisuCHEMA hyperspectral imaging system
Laboratory	ITC Spectroscopy Laboratory, University of Twente
Imaging mode	Pushbroom (line-scanning)
Spectral regions	Visible–Near Infrared (VNIR) and Shortwave Infrared (SWIR)
VNIR spectral range	350–1000 nm
VNIR spectral bands	768 bands
VNIR spatial resolution	1024 spatial pixels
SWIR spectral range	1000–2500 nm
SWIR spectral bands	288 bands
SWIR spatial resolution	384 spatial pixels
Illumination	Calibrated halogen light sources
Acquisition geometry	Nadir-looking, fixed sensor configuration
Sample positioning	Motorised translation stage
Radiometric calibration	White reference panel and dark current correction
Measured surfaces	Intact sample surfaces and freshly sawn faces

All hyperspectral acquisitions were performed under controlled laboratory conditions using a fixed imaging geometry. Samples were positioned on a motorised translation stage beneath the sensors, which were mounted in a nadir-looking configuration to ensure uniform spatial coverage. Illumination was provided by calibrated halogen light sources arranged to minimise shadows and specular reflections, ensuring stable and homogeneous illumination across the sample surface throughout image acquisition. Data were collected using a pushbroom scanning mode, with scan speed and integration time optimised for each sensor to maximise signal-to-noise ratios while avoiding saturation.

The raw hyperspectral images consist of uncalibrated digital numbers and therefore require a dedicated preprocessing workflow prior to any mineralogical analysis (Fig. 4.5). Radiometric calibration was first applied using a white reference, together with dark current correction, to convert the raw data into relative reflectance. This

step is essential to ensure spectral comparability between samples and to allow quantitative interpretation of absorption features.

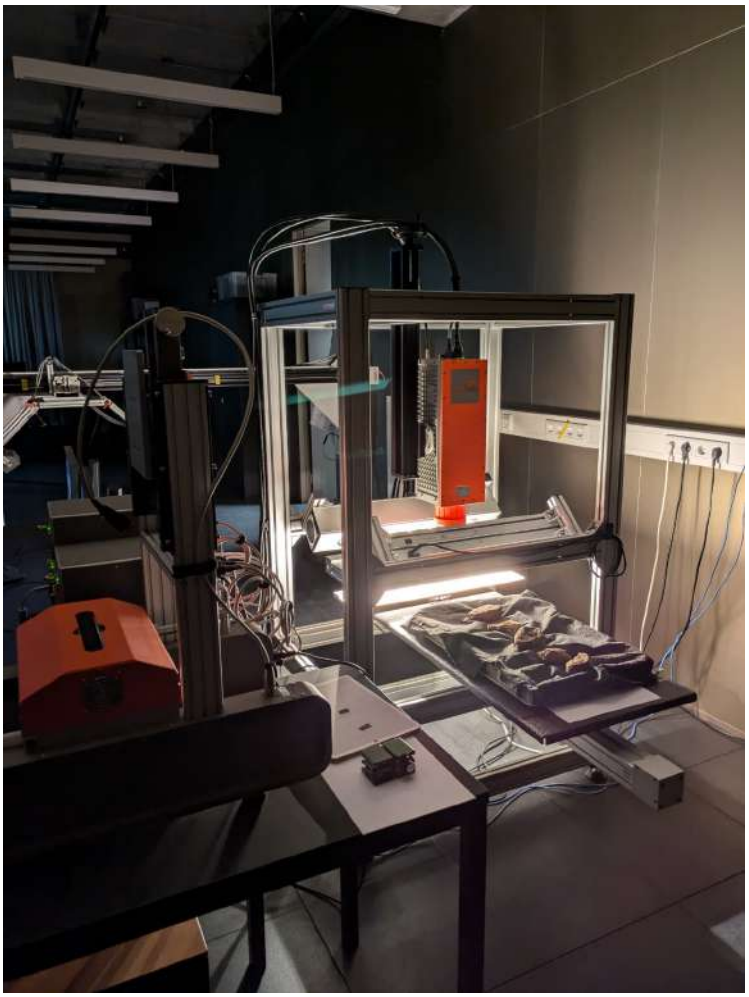

Fig. 4.4 Laboratory setup of the SPECIM SisuCHEMA hyperspectral imaging system at the ITC Faculty, University of Twente. The instrument was used for imaging spectroscopy in the VNIR and SWIR spectral ranges, enabling detailed spatial and spectral characterization of rock samples.

Following reflectance calibration, a spatial subset was applied to each hyperspectral image to remove non-relevant portions of the scene, such as background areas and image margins. This operation restricts subsequent analyses to the sample surface only, reducing noise and improving the robustness of statistical and spectral processing steps.

A spectral subset was then performed to remove bands affected by low signal-to-noise ratios or limited spectral information. Band selection was guided by statistical tools available within the processing software, allowing the identification and exclusion of noisy or uninformative spectral regions, particularly at the edges of the sensor range. This step enhances data quality and reduces the risk of artefacts in downstream analyses.

Finally, destriping and bad pixel removal were applied to correct sensor-related artefacts and defective detector elements, improving spatial consistency and spectral reliability across the images. These preprocessing steps were carried out using a combination of the Hyppy and ENVI software environments, which provide complementary tools for hyperspectral calibration and correction.

Hyperspectral images were acquired for both the intact outer surfaces and the freshly sawn faces of each sample. The fully preprocessed datasets form the basis for subsequent wavelength mapping and spectral feature extraction.

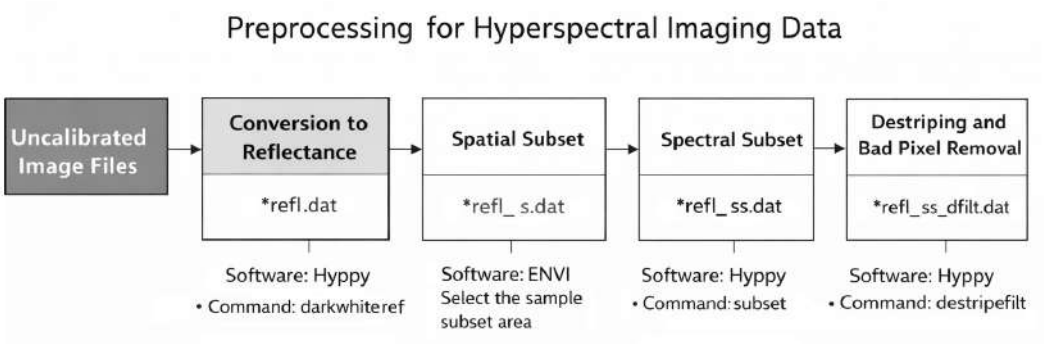

Fig. 4.5 Preprocessing workflow for laboratory hyperspectral data, including reflectance calibration using white and dark references, spatial and spectral subsetting, and destriping and bad pixel removal prior to spectral analysis.

4.4.1 SWIR hyperspectral analysis: carbonates

SWIR hyperspectral data were used to investigate the mineralogical variability of the Dicker Willem hand specimens, with a particular focus on the identification and classification of carbonate phases. The SWIR analysis is based on laboratory hyperspectral images acquired with the Specim SisuCHEMA imaging spectroscopy system and processed using a dedicated workflow developed at the University of Twente.

The SWIR datasets were not processed directly within the scope of this study, but were provided in a pre-processed form by Prof. Frank van Ruitenbeek, Prof. Wim Bakker, and Prof. Harald van der Werff (University of Twente). Their processing workflow relies on proprietary scripts designed to automatically extract diagnostic spectral parameters from continuum-removed SWIR spectra and to generate wavelength maps and mineral classification products. The scripts are optimised for carbonate mineral discrimination.

The analysis presented here focuses on the spectral range between 2100 and 2400 nm, which encompasses the main carbonate absorption features related to the asymmetric stretching vibrations of the CO_3^{2-} group. Variations in the position and shape of these absorption features are well known to reflect differences in carbonate composition, particularly the relative abundance of Ca, Mg, Fe, and Mn in calcite-, dolomite-, ankerite-, and magnesite-group minerals.

For each hand specimen (DW_01–DW_20), wavelength maps were derived by identifying, on a pixel-by-pixel basis, the position of the deepest absorption feature within the 2100–2400 nm interval. These wavelength maps provide a spatially explicit representation of spectral variability across the samples and allow first-order assessment of carbonate compositional heterogeneity at the centimetre to sub-millimetre scale (see Fig. A.4 in Appendix A).

In addition to the wavelength maps, a decision tree–based classification scheme was applied to the SWIR data to assign each pixel to a specific carbonate class or to non-carbonate categories (Fig. A.6 in Apendix A). The decision tree uses a series of threshold conditions based on the wavelength positions of multiple absorption bands (b1–b4) and on spectral depth parameters to progressively discriminate between different carbonate species. This hierarchical approach enables the separation of calcite, dolomite, ankerite, magnesite, Fe–Mg–rich carbonates, mixed illite–carbonate signatures, and spectrally ambiguous or non-carbonate pixels.

The resulting carbonate classification maps document systematic differences in carbonate assemblages between samples, as well as pronounced intra-sample heterogeneity linked to textural variability.

4.4.2 VNIR hyperspectral analysis: Nd-related spectral features

VNIR index computation

VNIR hyperspectral data were analysed to investigate the spatial distribution of Nd-related spectral features within the Dicker Willem hand specimens. The analysis is based on laboratory hyperspectral images acquired with the Specim SisuCHEMA imaging spectroscopy system and focuses on absorption features associated with Nd-bearing phases.

The VNIR analysis employs an average spectral index originally proposed by Bakker et al. (unpublished; [94]) for mapping monazite in carbonatite-hosted systems. The index was kindly shared by Bakker and collaborators and is applied here with appropriate acknowledgement. In the original study, the index was implemented using the *Hyppy* software package through spectral math and band math operations [60].

The motivation for using an averaging index lies in the relatively high noise level that can affect VNIR hyperspectral reflectance data. Rather than relying on single band ratios or individual absorption depths, the index combines multiple spectral intervals to enhance robustness and reduce sensitivity to noise.

The index targets two unique Nd-related absorption features centred at approximately 740 nm and 800 nm. In its original formulation, the hyperspectral reflectance image S_1 is partitioned into four spectral subsets: two absorption regions and two adjacent shoulder regions. Specifically, the shoulder regions are defined by $S_1[764{:}783]$ and $S_1[819{:}853]$, while the absorption regions correspond to $S_1[735{:}749]$ and $S_1[790{:}805]$. Mean reflectance values within these intervals are combined to derive a single index value representative of the combined strength of both Nd-related absorption features.

In this study, slightly modified wavelength intervals were adopted in order to better match the spectral characteristics of the Dicker Willem samples. The index was computed as:

$$\frac{\left(\overline{S_1[749{:}777]} + \overline{S_1[807{:}823]}\right)}{\left(\overline{S_1[738{:}746]} + \overline{S_1[792{:}803]}\right)} \tag{4.1}$$

where $\overline{S_1[a{:}b]}$ denotes the mean reflectance within the wavelength interval *a*–*b* nm.

To enhance contrast and facilitate visual interpretation, the index was further scaled according to:

$$\left(\frac{\left(\overline{S_1[749{:}777]} + \overline{S_1[807{:}823]} \right)}{\left(\overline{S_1[738{:}746]} + \overline{S_1[792{:}803]} \right)} - 1.0 \right) \times 100 \tag{4.2}$$

This amplification step preserves relative spatial variations while improving the visual separation of areas characterised by enhanced Nd-related spectral responses.

The resulting VNIR index maps provide a spatially resolved representation of Nd-related spectral variability across the hand specimens (Fig.A.3 in Appendix A). Interpretation of these patterns and their geological significance is presented in the following subsection section together with the SWIR-derived products.

ROI-based spectral inspection

4.4.3 ROI-based spectral inspection

Following the generation of the VNIR index map based on the average index method, individual spectral responses were inspected to evaluate the robustness of the index-derived signal. The index map provides a spatial indication of relative variations associated with the targeted Nd-related absorption features, but single-pixel spectra are inherently affected by instrumental noise and local surface heterogeneities.

To reduce the influence of pixel-scale variability and improve spectral interpretability, a Region of Interest (ROI)-based approach was adopted. ROIs correspond to groups of adjacent pixels selected within areas characterised by relatively high index values and homogeneous spectral behaviour.

An initial inspection was performed by extracting the spectrum of a single pixel selected from a high-index area in the VNIR index map (Fig.4.6). The resulting spectrum shows the overall reflectance trend across the VNIR range, but the diagnostic absorption features are difficult to identify clearly due to noise and pixel-scale variability.

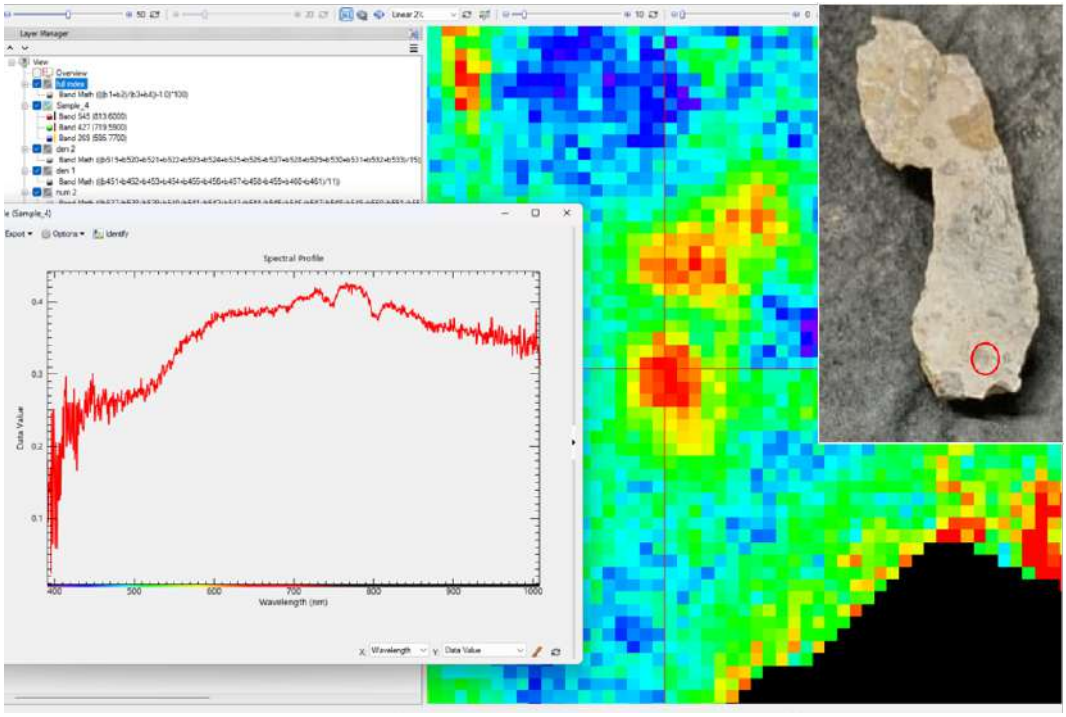

Fig. 4.6 VNIR hyperspectral index map of sample DW_04 with extraction of a single-pixel spectrum. The spectral profile shown corresponds to an individual pixel selected from the index map, illustrating a noisy VNIR reflectance spectrum. The inset photograph displays the DW_04 hand specimen, where the red circle indicates the approximate area corresponding to the selected pixel used for spectral extraction.

To improve the signal quality, a ROI was manually defined around the selected pixel, encompassing a small cluster of adjacent pixels with similar index values (Fig. 4.7). This approach assumes that neighbouring pixels represent the same material and allows random noise to be reduced through spectral averaging.

Spectral statistics were then calculated for the ROI using the statistical tools available in the ENVI software (Fig. 4.7). Compared to the single-pixel spectrum, the ROI-averaged spectrum displays a smoother reflectance curve and more clearly resolved absorption features in the VNIR range.

This workflow—moving from single-pixel inspection to ROI-based spectral averaging—provides a more reliable representation of the spectral characteristics of the material of interest and supports the use of the VNIR index as a qualitative screening tool prior to detailed mineralogical interpretation.

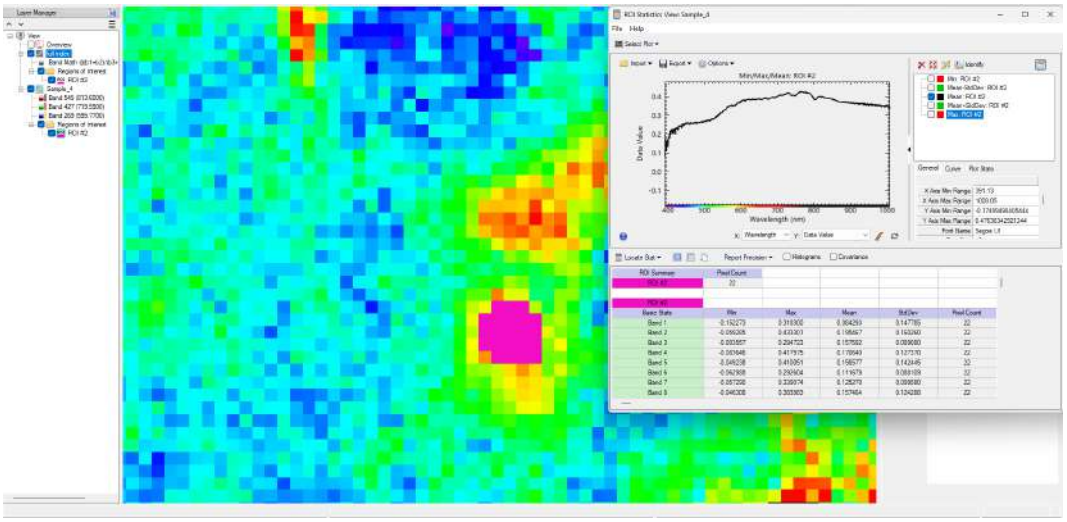

Fig. 4.7 VNIR hyperspectral index map of sample DW_04 with ROI–based spectral averaging. The displayed spectrum represents the mean reflectance extracted from a user-defined ROI encompassing multiple pixels, resulting in a smoother and more representative spectral signature in which Nd-related absorption features are more clearly resolved.

4.4.4 Results

SWIR results (2100–2400 nm)

The SWIR wavelength mapping in the 2100–2400 nm range (Fig. A.4 in Appendix A) reveals systematic variations in the position of carbonate-related absorption features across the analysed hand specimens. In the majority of the samples, particularly those imaged on unpolished surfaces, the wavelength maps are dominated by pixels displaying absorption features between approximately 2300 and 2400 nm, expressed by magenta hues. This distribution indicates a predominance of carbonate compositions characterised by longer-wavelength SWIR absorptions.

In contrast, samples DW_02, DW_03, DW_05, DW_06, and DW_07 exhibit a larger proportion of yellow to orange pixels, reflecting absorption features centred at shorter wavelengths within the investigated interval. These samples also locally display green-coloured domains, corresponding to absorption minima in the ∼2200–2250 nm range, suggesting intra-sample heterogeneity in carbonate composition.

Carbonate classification maps derived using the decision tree–based approach (Fig. A.5 in Appendix A) show a predominance of the calcite class across most

samples, represented by green pixels. Subordinate yellowish domains, classified as ankerite, occur within several specimens, indicating compositional variations within the carbonate assemblage. Dolomite-class pixels are particularly evident in samples DW_01, DW_02, DW_03, DW_05, and DW_06, and occur to a lesser extent in samples DW_04 and DW_20. Overall, the classification results highlight both inter-sample and intra-sample variability in carbonate mineralogy across the Dicker Willem suite.

VNIR results (Nd-related index)

VNIR hyperspectral analysis was applied to the sawn surfaces of the hand specimens using an average index approach targeting Nd-related absorption features. The resulting VNIR index maps (Fig. A.3 in Appendix A) display distinct spatial patterns, in which warm colours (red to orange) correspond to high index values, whereas cooler colours (green to blue) indicate low index values.

Pixels with high index values (red) mark zones where the Nd-related absorption features are more strongly expressed, while lower index values dominate the surrounding matrix. These high-index areas are spatially heterogeneous and occur as discrete patches within individual samples, suggesting a non-uniform distribution of Nd-bearing mineral phases at the centimetre to sub-millimetre scale.

Inspection of representative VNIR spectra extracted from high-index regions shows the presence of two characteristic absorption features centred at approximately 740 nm and 800 nm, which are consistent with Nd-related electronic transitions. The VNIR results therefore provide a first-order spatial proxy for the distribution of potential Nd-bearing phases within the carbonatite samples.

4.5 Field spectroscopy (Halo TerraSpec)

Fig. 4.8 (a) Portable Halo TerraSpec spectrometer used for point-based reflectance measurements. (b) Example of spectral acquisition on a hand specimen using the contact probe configuration.

In addition to laboratory hyperspectral imaging, point-based reflectance spectra were acquired using a portable Halo TerraSpec spectrometer (Malvern Panalytical; Fig. 4.8). The instrument operates over a broad spectral range spanning the visible, near-infrared, and shortwave infrared regions (350–2500 nm), fully covering the diagnostic wavelengths relevant for mineralogical and REEs investigations.

The spectrometer provides high spectral resolution, with approximately 3 nm in the VNIR region (at 700 nm) and between ∼8 and 10 nm in the SWIR region (at 1400–2100 nm), combined with dense spectral sampling (≈1.4 nm in the VNIR and ≈1.1 nm in the SWIR). The high signal-to-noise ratio of the instrument (up to ∼9000:1 in the VNIR and SWIR1, and ∼4000:1 at 2100 nm) ensures reliable detection of subtle absorption features associated with REE-bearing and alteration minerals.

For each hand specimen, five independent spot measurements were collected on representative areas to account for surface heterogeneity and to evaluate intra-sample spectral variability. Measurements were acquired using a contact probe configuration

under controlled illumination conditions. The short acquisition time (∼100 ms per scan) allowed rapid data collection while maintaining spectral stability.

Each individual spectrum was analysed independently. For every spectral feature identified within each spectrum, the corresponding peak position (nm) and peak depth were quantified, and a possible cause of the absorption feature (e.g. Fe-related, carbonate, H_2O/OH) as well as the associated mineral phase were interpreted. A comprehensive summary of all spectral measurements, including the detailed feature-by-feature analysis for each spectrum and each hand sample (approximately five spectra per sample), is reported in Appendix B.

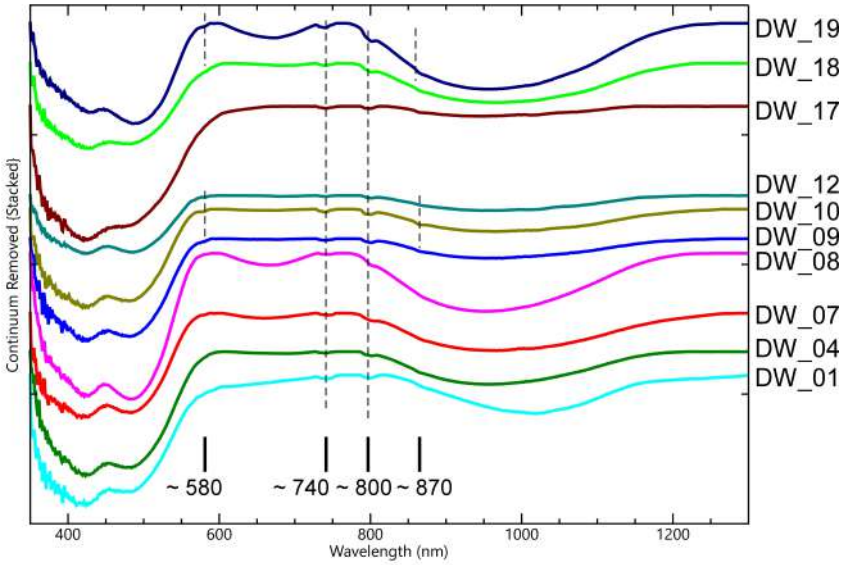

Fig. 4.9 Continuum-removed and vertically stacked VNIR reflectance spectra for samples exhibiting Nd-related absorption features. The dashed vertical lines indicate the main diagnostic absorption positions at approximately 580, 740, 800, and 870 nm. All displayed samples show the characteristic Nd^{3+} absorptions at ∼740 and ∼800 nm, while additional features at ∼580 and ∼870 nm are observed in a subset of samples (e.g., DW_10 and DW_19). Spectra are offset for clarity.

The resulting point spectra were used to (i) identify diagnostic absorption features associated with REE-bearing mineral phases, (ii) support mineralogical interpretation of laboratory hyperspectral images, and (iii) provide a direct comparison between point-based spectroscopy and image-derived spectra. This multi-scale spectral approach strengthens the linkage between laboratory measurements and spaceborne hyperspectral observations, such as those acquired by the EMIT sensor.

Following spectral acquisition, ten samples (DW_01, DW_04, DW_07, DW_08, DW_09, DW_10, DW_12, DW_17, DW_18, and DW_19) exhibit distinct absorption features in the VNIR region that are consistent with rare REE signatures. All these samples display two recurrent absorption features commonly attributed to neodymium (Nd), centred at approximately 740 nm and 800 nm. In addition, two samples, DW_10 and DW_19, also shows weaker absorptions around ∼580 nm and ∼870 nm, further supporting the presence of Nd-related electronic transitions (Fig. 4.9).

4.6 Geochemical screening: XRD

4.6.1 Sample preparation

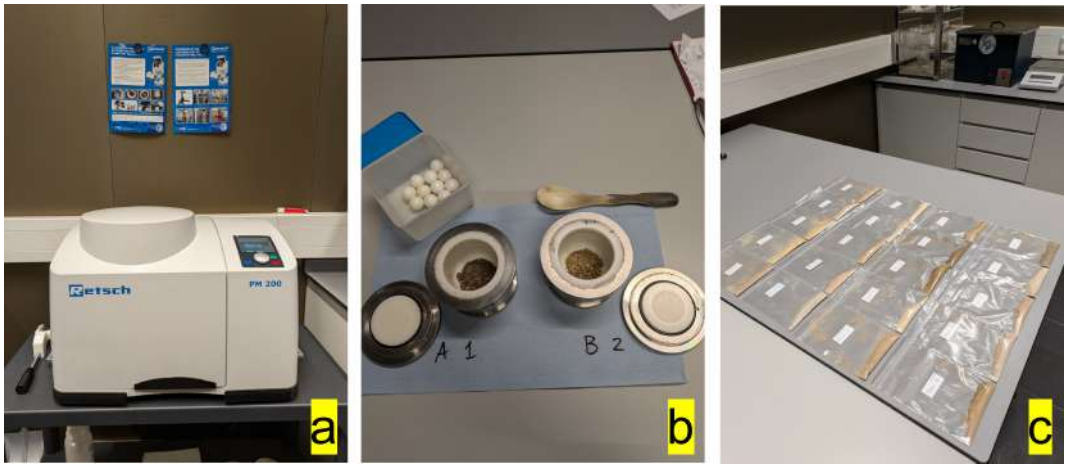

Fig. 4.10 Sample preparation for XRD analysis: (a) Retsch PM 200 planetary ball mill, (b) grinding jars with samples prior to milling, and (c) powdered samples stored in labelled plastic bags.

Rock samples selected for X-ray diffraction (XRD) analysis were previously cut in half in order to preserve a reference hand specimen. One half of each sample was retained as archive material, while the other half was used for laboratory preparation.

The selected material was first coarsely fragmented using a geological hammer, reducing the samples to centimetre-scale chips. These fragments were subsequently pulverized and finely ground using a Retsch PM 200 planetary ball mill at the laboratories of the ITC Faculty, University (Fig. 4.10a, b).

The planetary ball mill operates through high-energy impacts generated by grinding jars rotating around a central axis while simultaneously rotating around their own axes. This configuration allows efficient and reproducible grain-size reduction, ensuring the production of homogeneous fine powders suitable for XRD analysis and minimizing mineral segregation effects.

For each original rock sample, a single powdered subsample was produced. The resulting powders were stored in labelled plastic bags (Fig. 4.10c) and prepared for subsequent XRD measurements.

4.6.2 Analysis

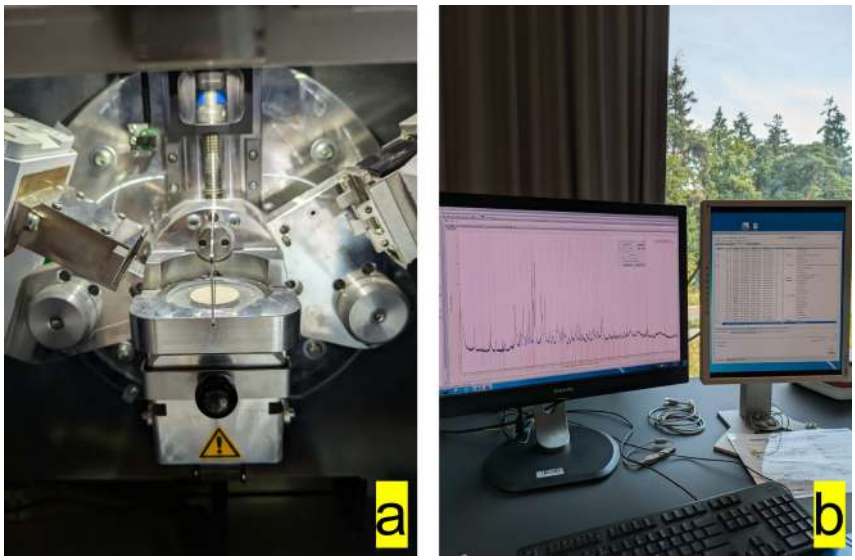

Fig. 4.11 (a) Internal configuration of the X-ray diffractometer used for powder sample analysis, showing the sample mounted on the sample holder during measurement. (b) Data acquisition and processing interface displaying a representative XRD pattern, processed and interpreted using DIFFRAC.EVA (Bruker) software for crystalline phase identification and analysis of diffraction peaks as a function of the 2θ angle.

XRD analysis were conducted on the powdered samples to investigate their bulk mineralogical composition. Following the grinding procedure, each sample was placed into a standard XRD sample holder and carefully levelled to obtain a flat and homogeneous surface. The powder was gently smoothed using a glass slide in order to reduce surface roughness and minimize preferred orientation effects, while avoiding full compaction of the material.

XRD measurements were performed at the ITC laboratories of the University of Twente using a Bruker D2 PHASER diffractometer (Fig. 4.11a). The instrument is designed for routine phase identification and quantitative mineralogical analysis and is equipped with a sealed X-ray source and a solid-state detector, providing stable acquisition conditions and adequate angular resolution for geological materials. For each sample, the acquisition time was approximately one hour, allowing the collection of diffraction patterns with sufficient signal quality and well-defined diffraction peaks.

Diffraction data were acquired over a 2θ angular range suitable for the identification of the main crystalline phases expected in the investigated samples. The resulting diffractograms were processed and interpreted using the Diffrac.EVA software package (Fig. 4.11b), through comparison with reference diffraction patterns from standard crystallographic databases in order to identify the mineral phases present.

4.6.3 Results

The stacked XRD patterns obtained for all analysed samples (Fig. 4.12) display a largely consistent diffraction signature across the dataset, indicating a broadly similar bulk mineralogical composition. Variations in peak intensities and the presence or absence of minor reflections indicate differences in the relative abundance of specific mineral phases among the samples.

A prominent diffraction peak observed in the majority of samples, from DW_07 to DW_20, as well as in DW_04, and with lower intensity in DW_02 and DW_03, is attributed to calcite and corresponds to one of its characteristic reflections. This suggests that calcite represents a dominant mineral phase within most of the analysed material.

Dolomite is identified in several samples based on the presence of its diagnostic reflection at approximately 31° in 2θ. This phase is clearly observed in DW_01 and is also present in DW_02 and DW_03, with weaker contributions detected in DW_05 and DW_06, indicating variable but locally significant dolomite contents.

Quartz (Qz) is recognised in a subset of samples, particularly from DW_01 to DW_06 and in DW_15, based on the presence of its characteristic reflection at

around 27° 2θ. The occurrence of quartz suggests minor silicate contamination or the presence of associated silicate lithologies within these samples.

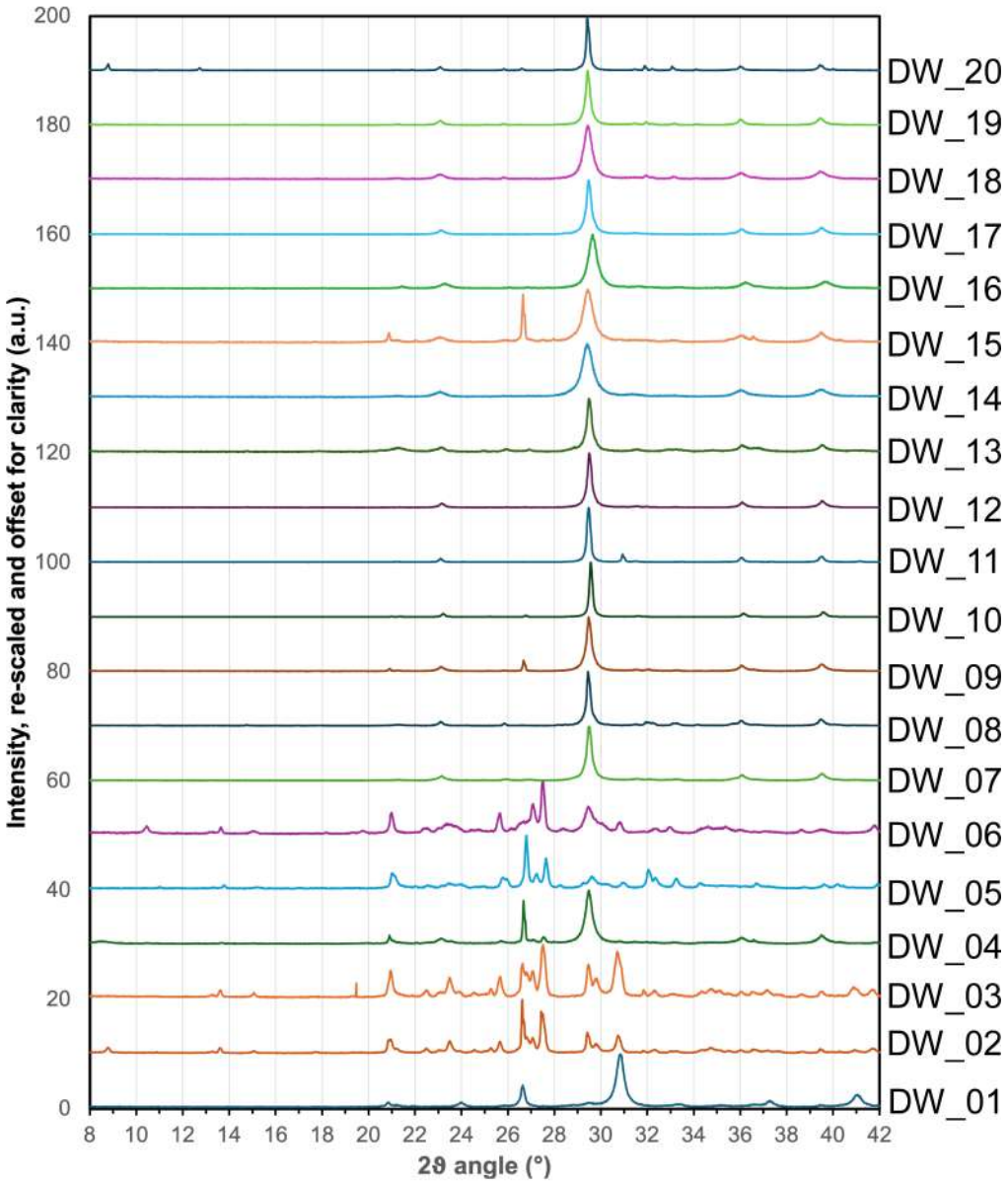

Fig. 4.12 Stacked XRD patterns of samples DW_01–DW_20 (from bottom to top), acquired on powdered material. Diffractograms are vertically offset for clarity and cover the 2θ range of 8–42°. Variations in peak positions and relative intensities reflect differences in mineralogical composition among the samples.

Additional mineral phases occur in minor to trace abundances across the dataset. These include goethite, biotite, feldspar, pyrochlore, and possible fluorapatite, inferred from weak and less systematic diffraction peaks. Due to their low intensities, these phases likely represent accessory components rather than major constituents of the samples.

For completeness, the full set of individual XRD diffraction patterns and their possible mineralogical interpretations are presented in the Appendix C, with one figure per sample.

4.7 Geochemical screening: pXRF

4.7.1 Analysis

Fig. 4.13 (a) Portable pXRF instrument used for geochemical screening, a SciAps X-555 handheld X-ray fluorescence spectrometer operating up to 55 kV. (b) Powdered samples prepared for pXRF analysis, placed in plastic sample cups and sealed with thin film.

Portable X-ray fluorescence (pXRF) analyses were carried out to obtain a first-order geochemical screening of the Dicker Willem samples, with particular emphasis on the detectable REEs. Measurements were performed using a SciAps X-555 handheld XRF analyser equipped with a high-voltage X-ray tube operating up to 55 kV.

The availability of a 55 kV excitation voltage significantly enhances the analytical capability of the instrument for REE-bearing materials. Compared to lower-voltage handheld systems, the higher tube voltage provides substantially increased X-ray energy, allowing more efficient excitation of the K-lines of light rare LREEs and the first HREEs, notably gadolinium (Gd) and europium (Eu). Although handheld XRF instruments cannot reach sufficiently high voltages to reliably quantify all HREEs, the SciAps X-555 allows highly sensitive detection of yttrium (Y), which is commonly used as a pathfinder element for HREE enrichment.

All measurements were conducted using the *soil mode*, which is optimized for fine-grained and heterogeneous materials. The powders of the twenty samples were placed into dedicated sample cups sealed with X-ray transparent film. This preparation ensured a flat, homogeneous analytical surface and minimized grain-size and surface effects during measurement. A photograph of the prepared sample cups and the instrument setup is shown in Fig. 4.13.

To assess analytical performance and data quality, measurements were also performed on two certified reference materials, OREAS 461 and OREAS 462. These reference materials originate from the Mount Weld rare earth deposit (Western Australia) and represent waste, low-grade, and medium-grade REE ores. The inclusion of these standards provided an internal check on instrument response and consistency for REE concentrations.

For each powdered sample, the detectable rare earth elements were measured, and the resulting concentrations are reported in detail in Appendix D. The pXRF dataset provides a rapid and non-destructive geochemical overview of the samples and serves as a screening tool to guide subsequent high-precision analyses.

4.7.2 Results

Portable XRF analysis indicate that neodymium (Nd), which represents the main focus of this study, occurs in the investigated samples over a wide concentration range. The highest Nd contents were measured in sample DW_13, reaching values of approximately 5000 ppm. The majority of the analysed samples display intermediate Nd concentrations, typically ranging between about 1100 and 3000 ppm. In contrast, the lowest Nd value was recorded in sample DW_06, with concentrations of the order of 30 ppm.

To assess the analytical performance of the pXRF measurements, two certified reference materials (OREAS 461 and OREAS 462) were analysed alongside the samples. Comparison between measured and certified Nd concentrations indicates a systematic underestimation of approximately 10–20%. For instance, Nd measured in OREAS 461 yielded a value of 1379 ppm, compared to a certified concentration of 1629 ppm, corresponding to a relative error of –15.3%. Such deviations are considered acceptable for pXRF-based geochemical screening of geological materials and do not compromise the interpretation of relative Nd variations between samples.

Given that neodymium is the primary element of interest in this research, the discussion in this section is restricted to Nd, while the full pXRF dataset for all detectable REEs is reported in Appendix D.

4.8 Discussion

This section integrates mineralogical, geochemical, and hyperspectral datasets acquired at the hand-specimen scale to evaluate the potential and limitations of imaging spectroscopy for the detection of Nd-bearing phases in carbonatite samples from the Dicker Willem complex. Nd was selected as the primary target element, as it exhibits some of the most prominent and diagnostically useful electronic absorption features among the rare earth elements in the VNIR–SWIR spectral range [86], making it a suitable proxy for assessing REEs detectability using spectroscopic techniques.

Integration of XRD, pXRF, and SWIR hyperspectral results.

The decision tree–based carbonate classification derived from SWIR hyperspectral data indicates that samples DW_07 to DW_19, together with DW_04, are predominantly dominated by calcite, whereas samples DW_01, DW_02, DW_03, and to a lesser extent DW_05 and DW_06, are characterised by a stronger dolomite component. This distribution is consistent with the XRD results, which show a prominent calcite peak at approximately 29–30° 2θ in samples DW_07–DW_20 and DW_04, while the characteristic dolomite peak at around 31° 2θ is observed in samples DW_01, DW_02, DW_03, and, more weakly, in DW_05 and DW_06.

Based on XRD mineralogical assemblages and macroscopic characteristics, samples DW_01, DW_02, DW_03, and DW_06 can be classified as alvikite, whereas samples DW_04, DW_05, DW_15, and DW_16 correspond to brecciated litholo-

gies. The remaining samples are dominated by coarse-grained calcite and can be classified as sövite, in agreement with classifications reported in the literature (e.g. [93]). In addition, XRD patterns for samples DW_17 and DW_18 show peaks at approximately 28.3° and 14.7° 2θ, which may indicate the presence of pyrochlore, a mineral commonly associated with REEs enrichment in carbonatite systems.

The SWIR wavelength maps in the 2100–2400 nm range further support the carbonate mineralogical framework inferred from XRD and decision tree classification. Most samples display dominant absorption features between 2330 and 2400 nm, reflected by reddish-magenta-coloured pixels in the wavelength maps, consistent with calcite-rich compositions. Samples DW_01, DW_02,DW_03, DW_05 and DW_06, exhibit a shift towards shorter wavelengths, expressed by yellowish to orange colours, suggesting a stronger contribution from Mg-bearing carbonate phases. Minor green-coloured domains, corresponding to absorption features between approximately 2200 and 2250 nm, are locally observed in samples DW_02, DW_03, DW_05, and DW_06, indicating intra-sample compositional heterogeneity.

Nd distribution from pXRF and spectroscopic detectability.

Portable XRF analyses highlight a wide range of Nd concentrations across the sample set, with values spanning from approximately 30 ppm to around 5000 ppm. The highest Nd concentrations were measured in sample DW_13, while most samples fall within the range of 1100–3000 ppm. Measurements performed on OREAS reference materials indicate that the pXRF-derived Nd concentrations are generally underestimated by approximately 10–20% relative to certified values, an error margin that is considered acceptable for rapid geochemical screening of geological materials.

Despite the presence of elevated Nd concentrations in several samples, the correspondence between Nd abundance and spectroscopic detectability is not straightforward. VNIR hyperspectral analysis of the sawn sample surfaces, based on an average index approach targeting the characteristic Nd absorption features at approximately 740 nm and 800 nm, reveals spatially heterogeneous distributions of high index values. These high-index zones occur as discrete patches at the centimetre to sub-millimetre scale, suggesting that Nd-bearing phases are unevenly distributed within the samples.

Spectral inspection confirms that, where the VNIR index yields elevated values, averaged ROI spectra display subtle but recognisable absorption features centred at $\sim$740 nm and $\sim$800 nm, consistent with Nd electronic transitions reported in

the literature. However, these features are generally weak and close to the noise level of VNIR hyperspectral data, highlighting the intrinsic difficulty of detecting REE-related absorptions using imaging spectroscopy alone.

Limitations of VNIR indices and comparison with Halo spectroscopy.

A key outcome of this study is that high Nd concentrations measured by pXRF do not necessarily translate into clear VNIR spectroscopic signatures. Sample DW_13 provides a notable example: despite exhibiting the highest Nd concentration in the dataset, neither the VNIR index maps nor the averaged ROI spectra show well-defined Nd absorption features (Fig. 4.14). This observation indicates that Nd concentration alone is not sufficient to ensure spectroscopic detectability in the VNIR range.

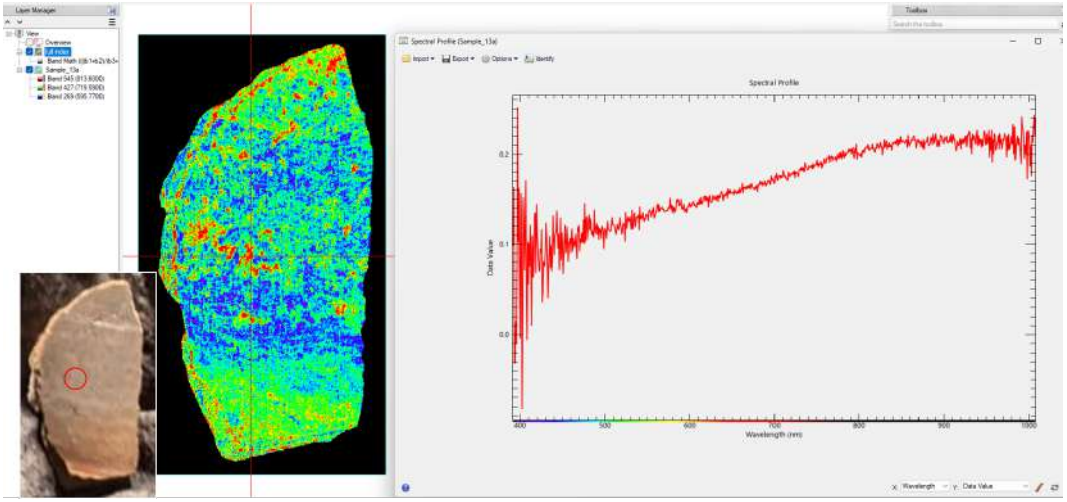

Fig. 4.14 VNIR index map and corresponding point spectrum for sample DW_13. The left panel presents the VNIR index map highlighting a pixel with high index values, interpreted as a potential Nd-enriched zone. The inset photograph shows the analysed hand specimen (DW_13), with the red circle indicating the approximate location of the selected pixel area. The spectrum extracted from this pixel is shown in the right panel. Despite the elevated index value, the spectrum does not exhibit the characteristic Nd-related absorption features at approximately 740 and 800 nm, illustrating a case where high index responses are not associated with clearly identifiable Nd spectral signatures.

Several factors may contribute to this mismatch. First, Nd-related absorption features are inherently narrow and of low intensity, making them particularly sensitive to signal-to-noise limitations in VNIR hyperspectral data. Second, Nd-bearing phases may occur at grain sizes smaller than the spatial resolution of the imaging system

or be finely disseminated within a spectrally dominant carbonate matrix, resulting in spectral dilution at the pixel scale. Third, XRD analyses indicate the presence of accessory phases such as goethite in several samples; although not quantified in this study, such phases may introduce broad VNIR absorptions that interfere with or mask the relatively weak Nd-related features, particularly around 800 nm.

Point spectroscopy acquired with the Halo spectrometer provides an important benchmark for evaluating the VNIR hyperspectral results. Halo measurements reveal recognisable Nd-related absorption features in 10 out of the 20 samples (DW_01, DW_04, DW_07, DW_08, DW_09, DW_10, DW_12, DW_17, DW_18, and DW_19), demonstrating that Nd features can be spectroscopically detected under favourable conditions. However, Halo measurements are inherently point-based and therefore may not always be fully representative of the bulk mineralogical composition of a hand specimen. As a result, the absence of Nd-related absorption features in some Halo spectra does not necessarily imply their absence at the sample scale, but may reflect local heterogeneity and the limited spatial representativeness of individual spot measurements.

The partial mismatch between Halo point spectroscopy and VNIR hyperspectral index maps thus highlights the complementary nature of the two approaches. While point spectroscopy offers higher spectral sensitivity for detecting subtle electronic absorptions, hyperspectral imaging provides spatial context and reveals centimetre-scale heterogeneity, albeit with reduced sensitivity to weak features.

Implications for hyperspectral REE exploration.

The combined results demonstrate that, while hyperspectral imaging provides valuable spatial context and mineralogical information, the detection of REE-related spectral features—especially for Nd—remains challenging at the hand-specimen scale. The VNIR index approach, although useful as a qualitative screening tool, does not yield a robust concentration threshold above which Nd absorption features become consistently detectable. This limitation is evident from the lack of a systematic relationship between pXRF-derived Nd concentrations and VNIR spectral responses.

Consequently, the results highlight the importance of integrating hyperspectral data with independent mineralogical and geochemical analyses. Further validation, including high-quality ICP-MS data and refinement of VNIR indices, is required

before reliable quantitative thresholds for REEs detectability can be established. Nonetheless, this study provides initial insights into the conditions under which REE-related spectral features may emerge and underscores both the potential and the current limitations of hyperspectral techniques for REEs exploration in carbonatite systems.

Chapter 5

Conclusions

This thesis investigated the potential of satellite-based hyperspectral remote sensing as a tool to support sustainable mineral exploration in the context of CRMs, with particular emphasis on the recently launched EMIT mission. Framed within the evolving European policy landscape on raw materials security, the research aimed to bridge strategic objectives with practical, scalable exploration methodologies applicable at regional scale.

Building on the policy framework introduced in Chapter 1, this work highlighted how remote sensing can contribute to improving geological knowledge in strategically relevant regions while minimising environmental impact. Hyperspectral satellite data were shown to be particularly suited to early-stage exploration and regional screening activities, enabling the identification of mineralogical and spatial variations across large and often remote areas where traditional field-based approaches are logistically challenging.

Chapter 2 established the theoretical and methodological foundations of the study, outlining the physical principles of mineral spectroscopy and the advantages of hyperspectral imaging over conventional multispectral approaches. Within this framework, the EMIT mission was presented as a still underexplored data source for geological applications, characterised by high spectral fidelity and contiguous VNIR–SWIR coverage, making it especially suitable for detecting subtle compositional variations in surface mineralogy.

The methodological approach adopted in this research focused on transparent and reproducible spectral analysis techniques, notably wavelength mapping and

band ratios. These methods were selected for their ability to capture variations in absorption feature position and depth while remaining interpretable and well adapted to spaceborne hyperspectral data. Their application does not rely on complex training datasets and allows direct geological interpretation of spectral outputs, which is particularly relevant for exploration-oriented workflows.

The application of these methods to two contrasting geological case studies in Namibia, presented in Chapter 3, demonstrated that EMIT data can effectively discriminate mineralogical and spatial variations associated with economically relevant mineral systems. In the Haib porphyry copper system, EMIT hyperspectral imagery enabled the mapping of hydrothermal alteration patterns through shifts in the Al–OH absorption feature of white micas, consistent with established models of porphyry-style mineralisation. These results confirm EMIT's capability to act as a reliable proxy for alteration-related mineralogical variability at regional scale.

In the carbonatite systems along the Kudu Lineament, EMIT data revealed systematic spatial variations in carbonate mineralogy, allowing calcite- and dolomite-dominated domains to be distinguished based on shifts in the main carbonate absorption features. This carbonate zonation provides first-order insights into magmatic and hydrothermal processes relevant to REEs mineralisation. However, EMIT data alone did not allow the direct detection of diagnostic spectral features related to REEs, likely due to the combined effects of spatial resolution, signal-to-noise limitations, and spectral masking by other dominant mineral phases.

Chapter 4 complemented the satellite-scale analysis with laboratory-based hyperspectral imaging, XRD, and pXRF investigations of carbonatite hand specimens from the Dicker Willem complex. This multi-scale integration demonstrated that neodymium-related VNIR absorption features can be observed under controlled laboratory conditions, but also showed that high elemental concentrations do not necessarily translate into strong or unambiguous spectral signatures. These results highlight the importance of integrating spaceborne observations with laboratory-scale mineralogical and geochemical validation to avoid over-interpretation of hyperspectral data.

Overall, the results of this thesis indicate that EMIT hyperspectral imagery represents a valuable new resource for regional-scale CRMs exploration. While not intended to replace detailed field investigations, airborne surveys, or laboratory analyses, EMIT provides an effective tool for screening large areas, guiding targeted

follow-up activities, and supporting exploration strategies aligned with sustainability and resource efficiency principles. In this sense, satellite-based hyperspectral remote sensing can contribute not only to exploration but also to selected stages of resource evaluation and production monitoring, as reflected by the growing interest of industry actors adopting similar approaches.

Recent developments in the private sector, including companies such as VRIFY (Canada), TheiaX (Germany), and TERRAEYE (Poland), illustrate how hyperspectral data and advanced analytics are increasingly being integrated into exploration and mining workflows. In parallel, the rapid evolution of artificial intelligence and machine learning techniques offers new opportunities for handling large hyperspectral datasets and extracting complex patterns. While this thesis deliberately focused on physically interpretable and transparent methods, future research should explore the integration of EMIT data with AI-driven approaches, ensuring that data-driven models remain grounded in geological understanding.

In conclusion, this work demonstrates that the effective application of spaceborne hyperspectral remote sensing to CRMs exploration requires a careful balance between technological capability, physical interpretation, and multi-scale validation. When embedded within a robust methodological framework, EMIT data have the potential to become an increasingly important component of responsible and informed mineral exploration strategies aimed at securing CRMs.

References

[1] Hund K., La Porta D., Fabregas T. P., Laing T., and Drexhage J. Minerals for Climate Action: The Mineral Intensity of the Clean Energy Transition. Technical report, World Bank, Washington, DC, 2020.

[2] European Commission. Directorate General for Internal Market, Industry, Entrepreneurship and SMEs. *Study on the critical raw materials for the EU 2023: final report.* Publications Office, LU, 2023.

[3] European Union. Regulation (EU) 2023/1605 establishing a framework for ensuring a secure and sustainable supply of critical raw materials (Critical Raw Materials Act), 2023. CELEX: 32023R1605.

[4] Baranzelli C., Blengini G. A., Josa S. O., and Lavalle C. EU–Africa Strategic Corridors and critical raw materials: two-way approach to regional development and security of supply. *International Journal of Mining, Reclamation and Environment*, 36(9):607–623, October 2022.

[5] Bastida A. E. From extractive to transformative industries: paths for linkages and diversification for resource-driven development. *Mineral Economics*, 27(2-3):73–87, December 2014.

[6] European Commission. Joint Research Centre. and European Commission. Directorate General for International Partnerships. *Identification, characterisation and ranking of strategic corridors in Africa: CUSA project : phase 1.* Publications Office, LU, 2022.

[7] European Commission. Memorandum of Understanding between the European Union and Namibia on a strategic partnership on sustainable raw materials and renewable hydrogen. Memorandum of Understanding, European Commission, Brussels, 2022.

[8] Sabins F. F. Remote sensing for mineral exploration. *Ore Geology Reviews*, 14(3-4):157–183, September 1999.

[9] Agar B. and Coulter D. Remote Sensing for Mineral Exploration – A Decade Perspective 1997-2007. 7(Proceedings of Exploration):109–136, 2007.

[10] Van Der Meer F. D., Van Der Werff H., Van Ruitenbeek F. J. A., Hecker C., Bakker W., M. F. Noomen, Van Der Meijde M., Carranza E. J. M., J. J. B. D., Smeth, and Woldai T. Multi- and hyperspectral geologic remote sensing: A review. *International Journal of Applied Earth Observation and Geoinformation*, 14(1):112–128, February 2012.

[11] Gupta R. P. *Remote Sensing Geology*. Springer Berlin Heidelberg, Berlin, Heidelberg, 2018.

[12] Bishop C., Rivard B., De Souza Filho C., and Van Der Meer F. Geological remote sensing. *International Journal of Applied Earth Observation and Geoinformation*, 64:267–274, February 2018.

[13] Hunt G. R. Spectral signatures of particulate minerals in the visible and near infrared. *GEOPHYSICS*, 42(3):501–513, April 1977.

[14] Salisbury J. W., Walter L. S., and Vergo N. Availability of a library of infrared (2.1-25.0 μm) mineral spectra. *American Mineralogist*, 74:938–939, August 1989.

[15] Goetz A. F. and Rowan C. Geologic Remote Sensing. *Science*, 211(4484):781–791, February 1981.

[16] Lawrence R. D. and Herzog J.H. Geology and forestry classification from ERTS-1 digital data. 41(10):1241–1251, 1975.

[17] Abrams M. The Advanced Spaceborne Thermal Emission and Reflection Radiometer (ASTER): Data products for the high spatial resolution imager on NASA's Terra platform. *International Journal of Remote Sensing*, 21(5):847–859, January 2000.

[18] Abrams M. and Hook S. J. Simulated Aster data for geologic studies. *IEEE Transactions on Geoscience and Remote Sensing*, 33(3):692–699, May 1995.

[19] Yamaguchi Y., Kahle A. B., Tsu H., Kawakami T., and Pniel M. Overview of Advanced Spaceborne Thermal Emission and Reflection Radiometer (ASTER). *IEEE Transactions on Geoscience and Remote Sensing*, 36(4):1062–1071, July 1998.

[20] Mars J. C. and Rowan C. Spectral assessment of new ASTER SWIR surface reflectance data products for spectroscopic mapping of rocks and minerals. *Remote Sensing of Environment*, 114(9):2011–2025, September 2010.

[21] Booysen R., Gloaguen R., Lorenz S., Zimmermann R., and Nex P. A. M. Geological Remote Sensing. In *Encyclopedia of Geology*, pages 301–314. Elsevier, 2021.

[22] Hewson R. D., Van Ruitenbeek F. J. A., C. Hecker, Soszynska A., Van Der Werff H., Bakker W., Portela B., and Van Der Meer F. D. Geological Remote Sensing From Continental to Exploration scales. In *Reference Module in Earth Systems and Environmental Sciences*. Elsevier, 2024.

[23] Pearlman J. S., Barry P. S., Segal C. C., Shepanski J., Beiso D., and Carman S. L. Hyperion, a space-based imaging spectrometer. *IEEE Transactions on Geoscience and Remote Sensing*, 41(6):1160–1173, June 2003.

[24] Caruso A. S., Clarke K. D., Tiddy C. J., and Lewis M. M. Airborne hyperspectral characterisation of hydrothermal alteration in a regolith-dominated terrain, southern Gawler Ranges, South Australia. *Australian Journal of Earth Sciences*, 68(4):590–608, May 2021. Publisher: Informa UK Limited.

[25] Naleto J. L. C., Perrotta M. M., Costa F. G. D., and Souza Filho C. R. D. Point and imaging spectroscopy investigations on the Pedra Branca orogenic gold deposit, Troia Massif, Northeast Brazil: Implications for mineral exploration in amphibolite metamorphic-grade terrains. *Ore Geology Reviews*, 107:283–309, April 2019.

[26] Portela B., Sepp M. D., Van Ruitenbeek F. J. A., Hecker C., and Dilles J. H. Using hyperspectral imagery for identification of pyrophyllite-muscovite intergrowths and alunite in the shallow epithermal environment of the Yerington porphyry copper district. *Ore Geology Reviews*, 131:104012, April 2021.

[27] Portela B., Van Der Werff H., Hecker C., and Der Meijde Van M. Characterising mineral chemistry variation as a proxy for fluid composition using EMIT spaceborne hyperspectral data. *Ore Geology Reviews*, 182:106673, July 2025. Publisher: Elsevier BV.

[28] Rockwell B. W., Cunningham C. G., Breit G. N., and Rye R. O. Spectroscopic Mapping of the White Horse Alunite Deposit, Marysvale Volcanic Field, Utah: Evidence of a Magmatic Component. *Economic Geology*, 101(7):1377–1395, November 2006.

[29] Asadzadeh S., Zhou X., and Chabrillat S. Assessment of the spaceborne EnMAP hyperspectral data for alteration mineral mapping: A case study of the Reko Diq porphyry Cu Au deposit, Pakistan. *Remote Sensing of Environment*, 314:114389, December 2024. Publisher: Elsevier BV.

[30] Sorrentino A., Chirico R., Corrado F., Laukamp C., Di Martire D., and Mondillo N. The application of PRISMA hyperspectral satellite imagery in the delineation of distinct hydrothermal alteration zones in the Chilean Andes: The Marimaca IOCG and the Río Blanco-Los Bronces Cu-Mo porphyry districts. *Ore Geology Reviews*, 167:105998, April 2024.

[31] Chirico R., Mondillo N., Laukamp C., Mormone A., Di Martire D., Novellino A., and Balassone G. Mapping hydrothermal and supergene alteration zones associated with carbonate-hosted Zn-Pb deposits by using PRISMA satellite imagery supported by field-based hyperspectral data, mineralogical and geochemical analysis. *Ore Geology Reviews*, 152:105244, January 2023. Publisher: Elsevier BV.

[32] Kurz T. H. and Buckley S. J. A review of Hyperspectral imaging in close range applications. *The International Archives of the Photogrammetry, Remote Sensing and Spatial Information Sciences*, XLI-B5:865–870, June 2016.

[33] Hodgetts D. Laser scanning and digital outcrop geology in the petroleum industry: A review. *Marine and Petroleum Geology*, 46:335–354, September 2013.

[34] Tappert M., Rivard B., Giles D., Tappert R., and Mauger A. Automated drill core logging using visible and near-infrared reflectance spectroscopy: a case study from the Olympic Dam IOCG Deposit, South Australia. *Economic Geology*, 106(2):289–296, March 2011.

[35] Tappert M., Rivard B., Fulop A., Rogge D., Feng J., Tappert R., and Stalder R. Characterizing Kimberlite Dilution by Crustal Rocks at the Snap Lake Diamond Mine (Northwest Territories, Canada) using SWIR (1.90–2.36 m) and LWIR (8.1–11.1 m) Hyperspectral Imagery Collected from Drill Core. *Economic Geology*, 110(6):1375–1387, September 2015.

[36] Turner D., Groat L. A., Rivard B., and Belley P. M. Reflectance Spectroscopy and Hyperspectral Imaging of Sapphire-Bearing Marble From the Beluga Occurrence, Baffin Island, Nunavut. *The Canadian Mineralogist*, 55(4):787–797, July 2017.

[37] Speta M., Rivard B., Feng J., Lipsett M., and Gingras M. Hyperspectral imaging for the determination of bitumen content in Athabasca oil sands core samples. *AAPG Bulletin*, 99(07):1245–1259, July 2015.

[38] Speta M., Gingras M. K., and Rivard B. Shortwave Infrared Hyperspectral Imaging: A Novel Method For Enhancing the Visibility of Sedimentary And Biogenic Features In Oil-Saturated Core. *Journal of Sedimentary Research*, 86(7):830–842, July 2016.

[39] Shchepetkina A., Speta M., Gingras M. K., Rivard B., Pemberton S. G., and Keighley D. Hyperspectral imaging as an aid for facies analysis in massive-appearing sediments: a case study from the middle McMurray Formation. *Bulletin of Canadian Petroleum Geology*, 65(2):262–278, June 2017.

[40] Cudahy T., Caccetta M., Thomas M., Hewson R., Abrams M., Kato M., Kashimura O., Ninomiya Y., Yamaguchi Y., Collings S., Laukamp C., Ong C., Lau I., Rodger A., Chia J., Warren P., Woodcock R., Fraser R., Rankine T., Vote J., De Caritat P., English P., Meyer D., Doescher C., Fu B., Shi P., and Mitchell R. Satellite-derived mineral mapping and monitoring of weathering, deposition and erosion. *Scientific Reports*, 6(1):23702, March 2016.

[41] Rockwell B. W., Bonham L. C., and Giles S. A. USGS National Map of Surficial Mineralogy: US Geological Survey Online Map Resource, 2015.

[42] Guanter L., Richter R., and Kaufmann H. On the application of the MODTRAN4 atmospheric radiative transfer code to optical remote sensing. *International Journal of Remote Sensing*, 30(6):1407–1424, March 2009.

[43] Richter R. Atmospheric correction of DAIS hyperspectral image data. *Computers & Geosciences*, 22(7):785–793, August 1996.

[44] Richter R. Correction of satellite imagery over mountainous terrain. *Applied Optics*, 37(18):4004, June 1998.

[45] Richter R. and Schläpfer D. Geo-atmospheric processing of airborne imaging spectrometry data. Part 2: Atmospheric/topographic correction. *International Journal of Remote Sensing*, 23(13):2631–2649, January 2002.

[46] Ben-Dor E. and Levin N. Determination of surface reflectance from raw hyperspectral data without simultaneous ground data measurements: A case study of the GER 63-channel sensor data acquired over Naan, Israel. *International Journal of Remote Sensing*, 21(10):2053–2074, January 2000.

[47] Ferrier G. and Trahair N. S. Evaluation of apparent surface reflectance estimation methodologies. *International Journal of Remote Sensing*, 16(12):2291–2297, August 1995.

[48] Green R. O., Mahowald N., Ung C., Thompson D. R., Bator L., Bennet M., Bernas M., Blackway N., Bradley C., Cha J., Clark P., Clark R., Cloud D., Diaz E., Ben Dor E., Duren R., Eastwood M., Ehlmann B. L., Fuentes L., Ginoux P., Gross J., He Y., Kalashnikova O., Kert W., Keymeulen D., Klimesh M., Ku D., Kwong-Fu H., Liggett E., Li L., Lundeen S., Makowski M. D., Mazer A., Miller R., Mouroulis P., Oaida B., Okin G. S., Ortega A., Oyake A., Nguyen H., Pace T., Painter T. H., Pempejian J., Garcia-Pando C. P., Pham T., Phillips B., Pollock R., Purcell R., Realmuto V., Schoolcraft J., Sen A., Shin S., Shaw L., Soriano M., Swayze G., Thingvold E., Vaid A., and Zan J. The Earth Surface Mineral Dust Source Investigation: An Earth Science Imaging Spectroscopy Mission. In *2020 IEEE Aerospace Conference*, pages 1–15, Big Sky, MT, USA, March 2020. IEEE.

[49] Thompson D. R., Green R. O., Bradley C., Brodrick P. G., Mahowald N., Dor E. B., Bennett M., Bernas M., Carmon N., Chadwick D. K., Clark R. N., Coleman R. W., Cox E., Diaz E., Eastwood M. L., Eckert R., Ehlmann B. L., Ginoux P., Ageitos M. G., Grant K., Guanter L., Pearlshtien D. H., Helmlinger M., Herzog H., Hoefen T., Huang Y., Keebler A., Kalashnikova O., Keymeulen D., Kokaly R., Klose M., Li L., Lundeen S. R., Meyer J., Middleton E., Miller R. L., Mouroulis P., Oaida B., Obiso V., Ochoa F., Olson-Duvall W., Okin G. S., Painter T. H., Pérez García-Pando C., Pollock R., Realmuto V., Shaw L., Sullivan P., Swayze G., Thingvold E., Thorpe A. K., Vannan S., Villarreal C., Ung C., Wilson D. W., and Zandbergen S. On-orbit calibration and performance of the EMIT imaging spectrometer. *Remote Sensing of Environment*, 303:113986, March 2024. Publisher: Elsevier BV.

[50] Coleman R. W., Thompson D. R., Brodrick P. G., Dor E. B., Cox E., Pérez García-Pando C., Hoefen T., Kokaly R. F., Meyer J. M., Ochoa F., Okin G. S., Pearlshtien D. H., Swayze G., and Green R. O. An accuracy assessment of the surface reflectance product from the EMIT imaging spectrometer. *Remote Sensing of Environment*, 315:114450, December 2024. Publisher: Elsevier BV.

[51] Cardoso-Fernandes J., Teodoro A. C., Lima A., Perrotta M., and Roda-Robles E. Detecting Lithium (Li) Mineralizations from Space: Current Research and Future Perspectives. *Applied Sciences*, 10(5):1785, March 2020.

[52] Clark R. N., Swayze G. A., Livo K. E., Brodrick P. G., Noe Dobrea E., Vijayarangan S., Green R. O., Wettergreen D., Candela A., Hendrix A., Pérez García-Pando C., Pearson N. C., Lane M. D., González-Romero A., Querol X., and the EMIT and TREX teams. Imaging Spectroscopy: Earth and Planetary Remote Sensing with the PSI Tetracorder and Expert Systems from Rovers to EMIT and Beyond. *The Planetary Science Journal*, 5(12):276, December 2024. Publisher: American Astronomical Society.

[53] Clark R. N., King T. V., Klejwa M., Swayze G. A., and Vergo N. High spectral resolution reflectance spectroscopy of minerals. *Journal of Geophysical Research: Solid Earth*, 95(B8):12653–12680, August 1990.

[54] Pontual S., Merry N., and Gamson P. *G-MEX: Spectral Analysis Guide for Mineral Exploration. Vol.1: Spectral Interpretation Field Manual.* AusSpec International Pty. Ltd., Victoria, Australia, 1997.

[55] Laukamp C., Rodger A., LeGras M., Lampinen H., Lau I. C., Pejcic B., Stromberg J., Francis N., and Ramanaidou E. Mineral Physicochemistry Underlying Feature-Based Extraction of Mineral Abundance and Composition from Shortwave, Mid and Thermal Infrared Reflectance Spectra. *Minerals*, 11(4):347, March 2021.

[56] Hecker C., Van Ruitenbeek F. J. A., Van Der Werff H., Bakker W., Hewson R. D., and Van Der Meer F. D. Spectral Absorption Feature Analysis for Finding Ore: A Tutorial on Using the Method in Geological Remote Sensing. *IEEE Geoscience and Remote Sensing Magazine*, 7(2):51–71, June 2019.

[57] Bakker W., Van Ruitenbeek F. J. A., and Van Der Werff H. Hyperspectral image mapping by automatic color coding of absorption features : abstract. In *Abstract from 7th EARSEL Workshop on Imaging Spectroscopy 2011*, pages 56–57, Edinburgh, United Kingdom, 2011.

[58] Van Ruitenbeek F. J. A., Bakker W., Van Der Werff H., Zegers T. E., Oosthoek J. H. P., Omer Z. A., Marsh S. H., and Van Der Meer F. D. Mapping the wavelength position of deepest absorption features to explore mineral diversity in hyperspectral images. *Planetary and Space Science*, 101:108–117, October 2014.

[59] Hecker C., Van Ruitenbeek F. J. A., Bakker W., Fagbohun B. J., Riley D., Van Der Werff H., and Van Der Meer F. D. Mapping the wavelength position of mineral features in hyperspectral thermal infrared data. *International Journal of Applied Earth Observation and Geoinformation*, 79:133–140, July 2019.

[60] Bakker W., Van Ruitenbeek F., Van Der Werff H., Hecker C., Dijkstra A., and Van Der Meer F. Hyperspectral Python: HypPy. *Algorithms*, 17(8):337, August 2024.

[61] Cudahy T., Jones M., Thomas M., Laukamp C., Caccetta M., Hewson R., Rodger A., and Verrall M. Next Generation Mineral Mapping: Queensland airborne HyMap and satellite ASTER surveys 2006-2008, 2008.

[62] Cudahy T., Caccetta M., Lau I., Rodger A., Laukamp C., Ong C., Chia J., Collings S., Rankine T., Fraser R., Woodcock R., Vote J., Warren P., Thomas M., Tyler I., Mauger A., Close D., Jones M., and Abrams M. Satellite ASTER Geoscience Map of Australia, 2012.

[63] Van Der Werff H. and Van Der Meer F. Sentinel-2 for Mapping Iron Absorption Feature Parameters. *Remote Sensing*, 7(10):12635–12653, September 2015. Publisher: MDPI AG.

[64] Carano G., Portela B., Van Der Werff H., and Blengini G. A. Compositional zonation in carbonatite complexes along the Kudu Lineament, Namibia, from EMIT spaceborne hyperspectral imagery. *Journal of African Earth Sciences*, 240:106174, August 2026.

[65] Begg G. C., Griffin W. L., Natapov L. M., O'Reilly S. Y., Grand S. P., O'Neill C. J., Hronsky J. M. A., Djomani Y. P., Swain C. J., Deen T., and Bowden P. The lithospheric architecture of Africa: Seismic tomography, mantle petrology, and tectonic evolution. *Geosphere*, 5(1):23–50, February 2009.

[66] Colliston W. P. and Schoch A. E. Mid-Proterozoic tectonic evolution along the Orange River on the border between South Africa and Namibia. *Communications - Geological Survey of Namibia*, 12:57–66, 2000.

[67] Blignault H. J. Geological Map of Haib area., 1972.

[68] Barr J. M. and Reid D. L. Hydrothermal alteration at the Haib porphyry copper deposit, Namibia: Stable isotope and fluid inclusion patterns. *Communications - Geological Survey of Namibia*, 8:23–35, 1992.

[69] Chinkaka E. Integrating Worldview-3, Aster and aeromagnetic data for lineament structural intepretation and tectonic evolution of the Haib Area, Nambia. MS thesis., February 2019.

[70] Thompson D. R., Natraj V., Green R. O., Helmlinger M. C., Gao B., and Eastwood M. L. Optimal estimation for imaging spectrometer atmospheric correction. *Remote Sensing of Environment*, 216:355–373, October 2018.

[71] Van Ruitenbeek F. J. A., Cudahy T., Hale M., and Van Der Meer F. D. J. Tracing fluid pathways in fossil hydrothermal systems with near-infrared spectroscopy. *Geology*, 33(7):597, 2005.

[72] Van Ruitenbeek F. J. A., Debba P., Van Der Meer F. D., Cudahy T., Van Der Meijde M., and Hale M. Mapping white micas and their absorption wavelengths using hyperspectral band ratios. *Remote Sensing of Environment*, 102(3-4):211–222, June 2006.

[73] Laukamp C., Lau I. C., and Wang R. Tracing exchange vectors in hydrothermal systems using SWIR and TIR infrared active functional groups. pages 135–136, Sydney, Australia, September 2015.

[74] Meyer J. M., Kokaly R. F., and Holley E. Hyperspectral remote sensing of white mica: A review of imaging and point-based spectrometer studies for mineral resources, with spectrometer design considerations. *Remote Sensing of Environment*, 275:113000, June 2022.

[75] Yang K., Huntington J. F., Gemmell J. B., and Scott K. M. Variations in composition and abundance of white mica in the hydrothermal alteration system at Hellyer, Tasmania, as revealed by infrared reflectance spectroscopy. *Journal of Geochemical Exploration*, 108(2):143–156, February 2011.

[76] Walter B., Giebel R. J., Marlow A., Siegfried P., Marks M., Markl G., Palmer M., and Kolb J. The Kieshöhe carbonatites of southwestern Namibia -the post-magmatic role of silicate xenoliths on REE mobilisation. *Communications - Geological Survey of Namibia*, 25, July 2022.

[77] Marlow A. G. and Palmer M., R. A preliminary study of the rare earth element-enriched Twyfelskupje carbonatite complex, southern Namibia. *Geological Magazine*, 160(2):305–321, February 2023.

[78] Reid D. L., Cooper A. F., Rex D. C., and Harmer R. R. E. Timing of post–Karoo alkaline volcanism in southern Namibia. *Geological Magazine*, 127(5):427–433, September 1990.

[79] Verwoerd W. J. Update on carbonatites of South Africa and Namibia. *South African Journal of Geology*, 96(3):75–95, 1993.

[80] Cooper A. F. Geology of Dicker Willem, a subvolcanic carbonatite complex in south-west Africa. *ommunications of the Geological Survey South West Africa/Namibia*, 4:3–12, 1988.

[81] Kemmler L., Giebel R. J., Walter B. F., Marks M. A. W., Reid D. L., Raza M., Kluge T., and Gregor M. Transformation of calcite-bearing ijolites to biotite calcite carbonatites – A case study from Dicker Willem, southern Namibia. *Lithos*, 530-531:108485, June 2026.

[82] Streckeisen A. Classification and nomenclature of volcanic rocks, lamprophyres, carbonatites, and melilitic rocks: Recommendations and suggestions of the IUGS Subcommission on the Systematics of Igneous Rocks. *Geology*, 7(7):331, 1979.

[83] Cooper A. F. and Reid D. L. Textural evidence for calcite carbonatite magmas, Dicker Willem, southwest Namibia. *Geology*, 19(12):1193, 1991.

[84] Jiang Z., Liu Q., Colombo C., Barrón V., Torrent J., and Hu P. Quantification of Al-goethite from diffuse reflectance spectroscopy and magnetic methods. *Geophysical Journal International*, 196(1):131–144, January 2014.

[85] Dijkstra A., Bakker W., Deon F., Marcatelli C., Plokker M. P., and Hintzen H. T. Identification of rare earth elements in synthetic and natural monazite and xenotime by visible-to-shortwave infrared reflectance spectroscopy. *Physics and Chemistry of Minerals*, 51(2):16, June 2024.

[86] Turner D. J., Rivard B., and Groat L.A. Visible and short-wave infrared reflectance spectroscopy of REE fluorocarbonates. *American Mineralogist*, 99(7):1335–1346, July 2014. Publisher: Mineralogical Society of America.

[87] Haque N., Hughes A., Lim S., and Vernon C. Rare Earth Elements: Overview of Mining, Mineralogy, Uses, Sustainability and Environmental Impact. *Resources*, 3(4):614–635, October 2014.

[88] Marien C. The Hydrothermal Rare Earth Element Mineralisation at the peralkaline carbonatite Fen Complex in Norway , 2019.

[89] Chakhmouradian A. R. and Wall F. Rare Earth Elements: Minerals, Mines, Magnets (and More). *Elements*, 8(5):333–340, October 2012.

[90] Drew L. J., Qingrun M., and Weijun S. The Bayan Obo iron-rare-earth-niobium deposits, Inner Mongolia, China. *Lithos*, 26(1-2):43–65, December 1990.

[91] Charalampides G., Vatalis K. I., Apostoplos B., and Ploutarch-Nikolas B. Rare Earth Elements: Industrial Applications and Economic Dependency of Europe. *Procedia Economics and Finance*, 24:126–135, 2015.

[92] Le Maitre R. W. and International Union of Geological Sciences, editors. *Igneous rocks: a classification and glossary of terms: recommendation of the International Union of Geological Sciences, Subcommission on the Systematics of Igneous Rocks*. Cambridge Univ. Press, Cambridge, 2. ed edition, 2005.

[93] Reid D. L. and Cooper A. F. Oxygen and carbon isotope patterns in the Dicker Willem carbonatite complex, southern Namibia. *Chemical Geology: Isotope Geoscience section*, 94(4):293–305, May 1992.

[94] Bakker W., Dijkstra A., Van Der Werff H., and Van Der Meer F. Mapping rare-earth elements in VNIR hyperspectral images of rock samples.

Appendix A

Dicker Willem Samples

Fig. A.1 Photographic documentation of the twenty hand specimens collected from the Dicker Willem carbonatite complex. Panels (a–t) show samples DW_01 to DW_20, respectively, illustrating the macroscopic variability in colour, texture, and fabric across the sampled lithologies.

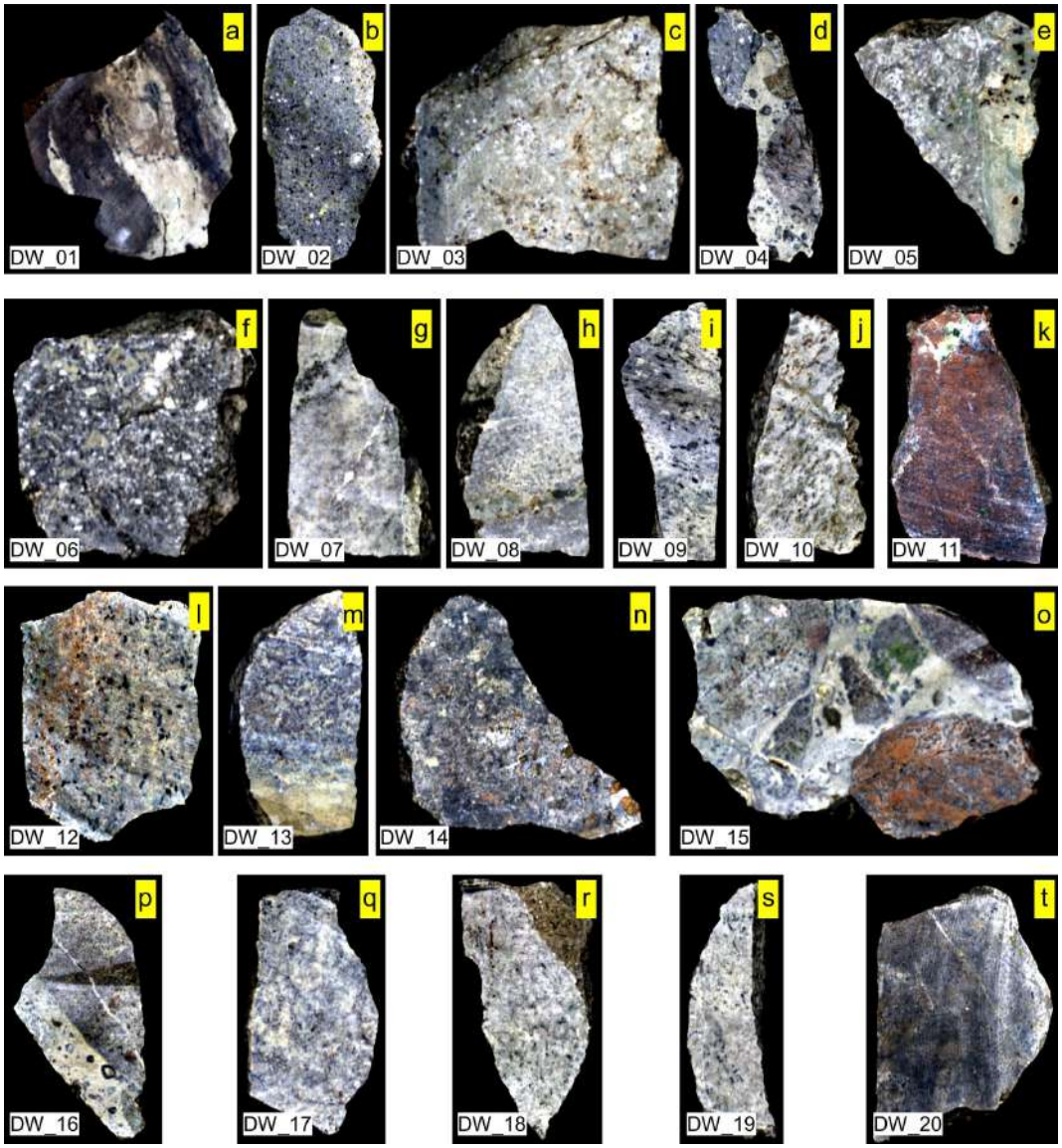

Fig. A.2 Photographic documentation of the twenty hand specimens collected from the Dicker Willem carbonatite complex. Panels (a–t) show samples DW_01 to DW_20, respectively, imaged on sawn slab surfaces using the VNIR camera of the Specim SisuCHEMA hyperspectral imaging system.

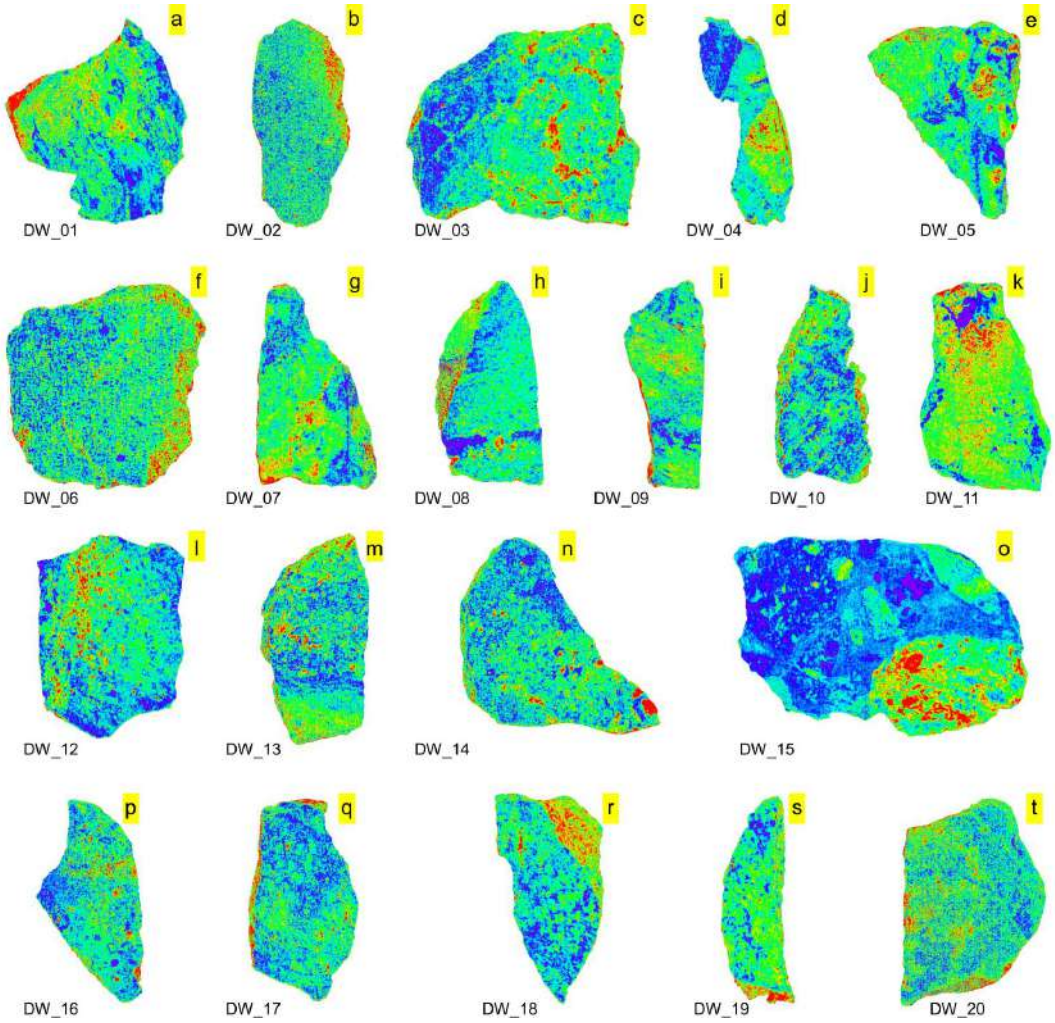

Fig. A.3 VNIR spectral index maps for the twenty hand specimens from the Dicker Willem carbonatite complex. Panels (a–t) show samples DW_01 to DW_20, respectively. The images were derived from VNIR hyperspectral data acquired with the Specim SisuCHEMA system using an average index method designed to enhance spectral features in the 740–800 nm range. Colour variations represent relative index values across the sample surfaces.

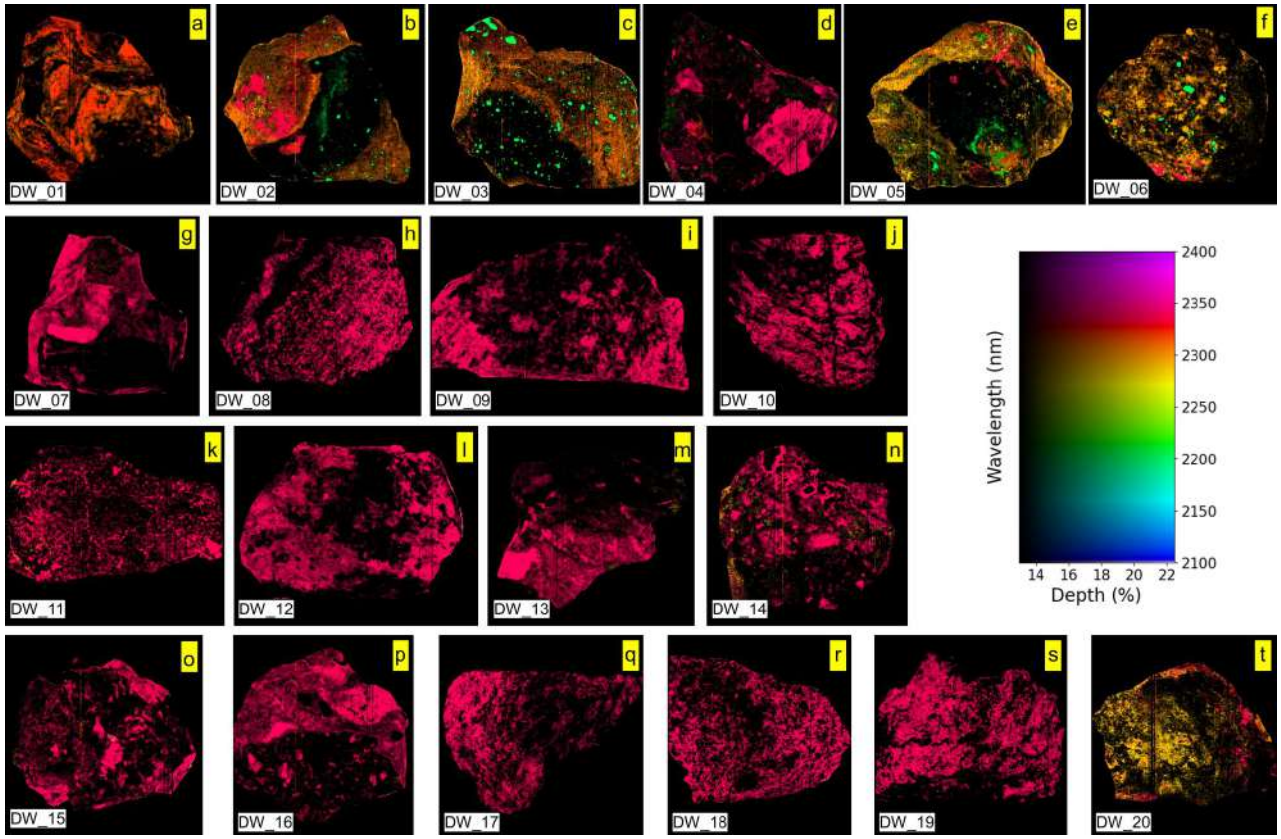

Fig. A.4 Wavelength maps in the 2100—2400 nm spectral range derived from hyperspectral images of the Dicker Willem hand specimens (DW_01–DW_20) acquired using the Specim SisuCHEMA imaging spectroscopy system. Panels (a–t) correspond to individual samples. For each specimen, the wavelength map represents the position of the deepest absorption feature within the SWIR range. The colour scale indicates the wavelength position (in nm) of the dominant spectral absorption feature, highlighting variations in mineralogical composition across and within samples.

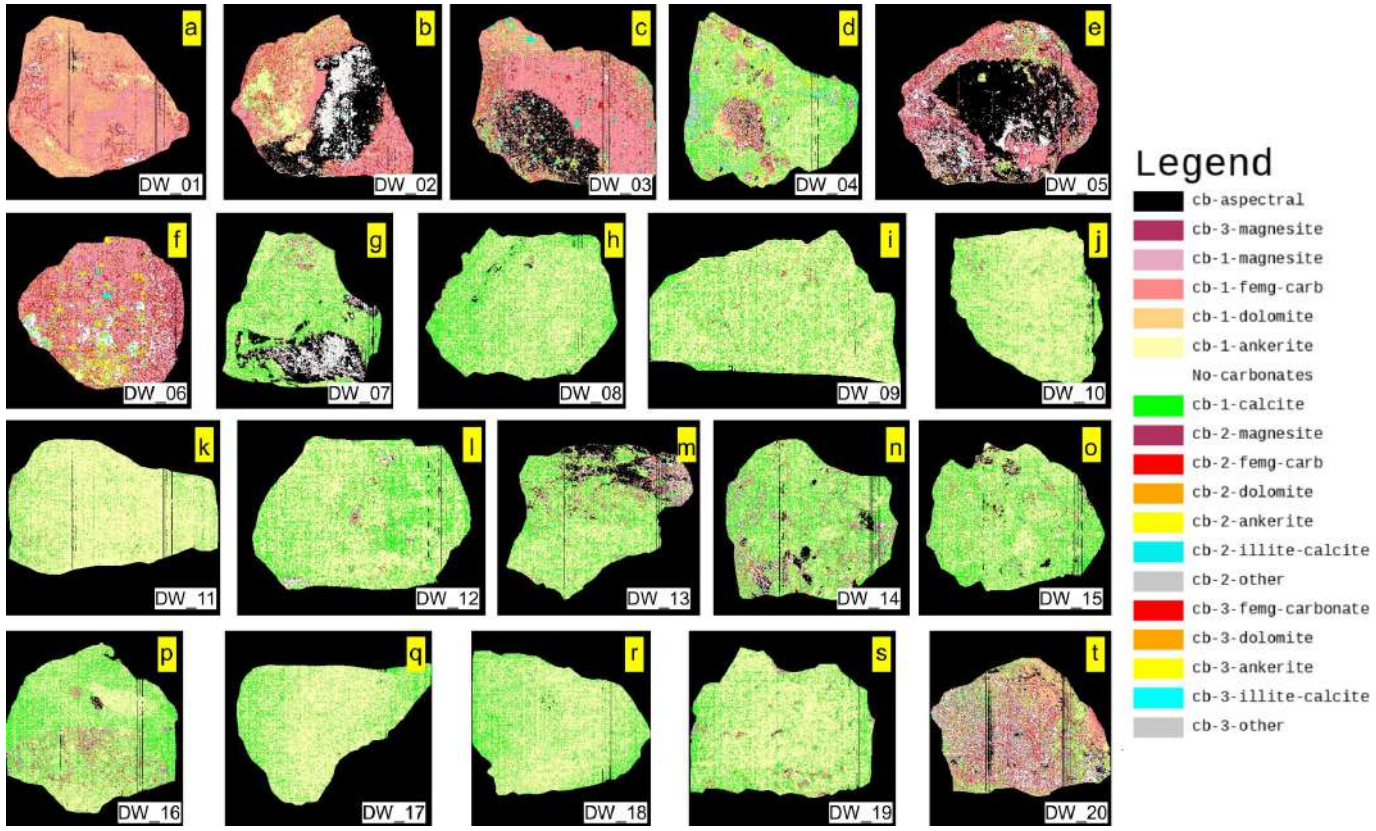

Fig. A.5 Carbonate mineral classification maps derived from hyperspectral images of the Dicker Willem hand specimens (DW_01–DW_20) acquired using the Specim SisuCHEMA imaging spectroscopy system. Panels (a–t) correspond to individual samples. Carbonate phases were classified using a decision-tree–based approach applied to diagnostic absorption features in the SWIR spectral range. The colour-coded maps illustrate the spatial distribution of different carbonate mineral groups (e.g., calcite, dolomite, magnesite, ankerite and Fe–Mg carbonates) as well as non-carbonate materials within each specimen, highlighting both inter- and intra-sample mineralogical variability.

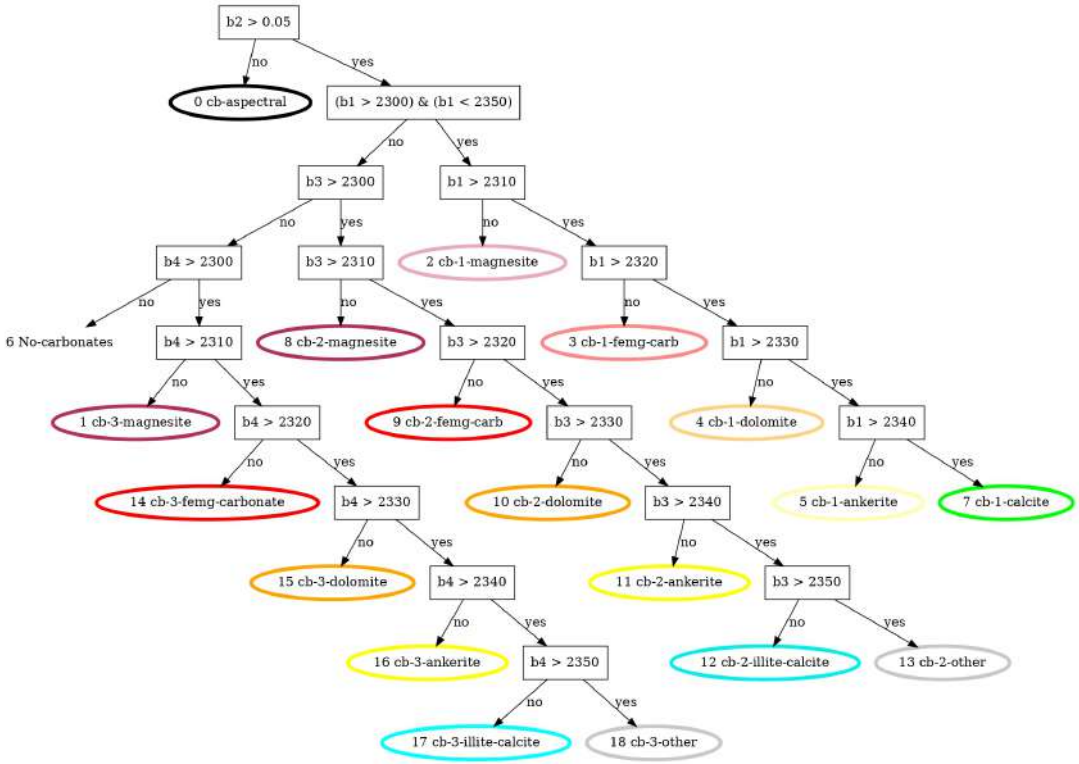

Fig. A.6 Decision tree used for carbonate mineral classification based on hyperspectral SWIR data. The diagram illustrates the rule-based decision tree applied to diagnostic absorption parameters derived from the 2100–2400 nm spectral range. Thresholds on absorption band positions (b1–b4) and spectral quality metrics are used to discriminate between carbonate mineral classes, including calcite, dolomite, magnesite, ankerite, Fe–Mg carbonates, mixed illite–carbonate phases, and non-carbonate materials. The resulting class labels (cb-1, cb-2, cb-3) correspond to distinct carbonate spectral groups used in the classification maps shown in Fig. A.5.

Appendix B

Halo TerraSpec spectral features

Table B.1 Summary of diagnostic absorption features identified in point-based reflectance spectra. For each spectrum acquired on individual hand specimens, the table reports the wavelength position (nm) and depth of each absorption feature. Possible spectral causes (e.g., Fe, $CaCO_3$, H_2O, OH) are indicated together with the mineral phase for which the feature is considered diagnostic.

Sample_Id	Spectrum_Id	Position	Depth	Cause	Mineral
DW_01	DW_01_001	489	0.7	Fe	Goethite
DW_01	DW_01_001	640	0.96	Fe	Goethite
DW_01	DW_01_001	980	0.83	Fe	Goethite
DW_01	DW_01_001	1298	0.99	–	–
DW_01	DW_01_001	1926	0.9	H_2O	–
DW_01	DW_01_001	2143	0.99	–	–
DW_01	DW_01_001	2324	0.92	$CaCO_3$	Dolomite
DW_01	DW_01_001	2560	0.98	–	–
DW_01	DW_01_002	427	0.72	Fe	Goethite
DW_01	DW_01_002	484	0.71	Fe	Goethite
DW_01	DW_01_002	966	0.92	Fe	Goethite
DW_01	DW_01_002	1302	0.99	–	–
DW_01	DW_01_002	1332	0.99	–	–
DW_01	DW_01_002	1421	0.99	H_2O	–
DW_01	DW_01_002	1943	0.95	H_2O	–
DW_01	DW_01_002	2323	0.92	$CaCO_3$	Dolomite
DW_01	DW_01_002	2462	0.98	–	–

Continuation of Table B.1					
Sample_Id	Spectrum_Id	Position	Depth	Cause	Mineral
DW_01	DW_01_003	423	0.75	Fe	Goethite
DW_01	DW_01_003	475	0.77	Fe	Goethite
DW_01	DW_01_003	1012	0.93	Fe	Goethite
DW_01	DW_01_003	1414	0.97	–	–
DW_01	DW_01_003	1941	0.95	H_2O	–
DW_01	DW_01_003	2329	0.92	$CaCO_3$	Dolomite
DW_01	DW_01_003	2471	0.99	–	–
DW_01	DW_01_004	419	0.70	Fe	Goethite
DW_01	DW_01_004	484	0.73	Fe	Goethite
DW_01	DW_01_004	–	–	–	–
DW_01	DW_01_004	744	0.99	REE	Nd
DW_01	DW_01_004	800	0.99	REE	Nd
DW_01	DW_01_004	1028	0.87	–	–
DW_01	DW_01_004	1296	0.90	–	–
DW_01	DW_01_004	1415	0.92	H_2O/OH	–
DW_01	DW_01_004	1931	0.86	H_2O	–
DW_01	DW_01_004	2136	0.99	–	–
DW_01	DW_01_004	2323	0.83	$CaCO_3$	Dolomite
DW_01	DW_01_005	435	0.68	Fe	Goethite
DW_01	DW_01_005	488	0.67	Fe	Goethite
DW_01	DW_01_005	999	0.87	Fe	Goethite
DW_01	DW_01_005	1421	0.97	H_2O/OH	–
DW_01	DW_01_005	1937	0.91	H_2O	–
DW_01	DW_01_005	2148	0.99	–	–
DW_01	DW_01_005	2324	0.85	$CaCO_3$	Dolomite
DW_01	DW_01_005	2461	0.97	–	–
DW_01	DW_01_006	430	0.63	Fe	Goethite
DW_01	DW_01_006	484	0.62	Fe	Goethite
DW_01	DW_01_006	974	0.83	Fe	Goethite
DW_01	DW_01_006	1428	0.98	H_2O/OH	–
DW_01	DW_01_006	1938	0.90	H_2O	–
DW_01	DW_01_006	2323	0.87	$CaCO_3$	Dolomite
DW_01	DW_01_006	2461	0.97	–	–

Continuation of Table B.1					
Sample_Id	Spectrum_Id	Position	Depth	Cause	Mineral
DW_02	DW_02_001	484	0.61	Fe	Goethite
DW_02	DW_02_001	672	0.97	Fe	Goethite
DW_02	DW_02_001	966	0.79	Fe	Goethite
DW_02	DW_02_001	1419	0.98	H_2O/OH	–
DW_02	DW_02_001	1926	0.93	H_2O	–
DW_02	DW_02_001	2213	0.99	AlOH	–
DW_02	DW_02_001	2408	0.97	–	–
DW_02	DW_02_002	488	0.73	Fe	Goethite
DW_02	DW_02_002	690	0.94	Fe	Goethite
DW_02	DW_02_002	999	0.76	Fe	Goethite
DW_02	DW_02_002	1413	0.93	H_2O/OH	–
DW_02	DW_02_002	1915	0.87	H_2O	–
DW_02	DW_02_002	2206	0.99	AlOH	–
DW_02	DW_02_002	2313	0.94	$CaCO_3$	Dolomite
DW_02	DW_02_002	2390	0.99	–	–
DW_02	DW_02_003	427	0.66	Fe	Goethite?
DW_02	DW_02_003	484	0.64	Fe	Goethite
DW_02	DW_02_003	681	0.94	Fe	Goethite
DW_02	DW_02_003	992	0.77	Fe	Goethite
DW_02	DW_02_003	1412	0.96	H_2O/OH	–
DW_02	DW_02_003	1919	0.93	H_2O	–
DW_02	DW_02_003	2201	0.99	AlOH	–
DW_02	DW_02_003	2340	0.98	$CaCO_3$	Calcite
DW_02	DW_02_004	428	0.77	Fe	Goethite?
DW_02	DW_02_004	492	0.71	Fe	Goethite
DW_02	DW_02_004	689	0.91	Fe	Goethite
DW_02	DW_02_004	992	0.71	Fe	Goethite
DW_02	DW_02_004	1412	0.94	H_2O/OH	–
DW_02	DW_02_004	1921	0.91	H_2O	–
DW_02	DW_02_004	2201	0.99	AlOH	–
DW_02	DW_02_004	2335	0.95	$CaCO_3$	Calcite
DW_02	DW_02_005	431	0.77	Fe	Goethite
DW_02	DW_02_005	492	0.70	Fe	Goethite

Continuation of Table B.1					
Sample_Id	Spectrum_Id	Position	Depth	Cause	Mineral
DW_02	DW_02_005	686	0.89	Fe	Goethite
DW_02	DW_02_005	980	0.68	Fe	Goethite
DW_02	DW_02_005	1411	0.92	H_2O/OH	–
DW_02	DW_02_005	1921	0.91	H_2O	–
DW_02	DW_02_005	2202	0.98	AlOH	–
DW_02	DW_02_005	2331	0.95	$CaCO_3$	Calcite
DW_03	DW_03_001	428	0.64	Fe	–
DW_03	DW_03_001	487	0.61	Fe	–
DW_03	DW_03_001	673	0.94	Fe	–
DW_03	DW_03_001	966	0.72	Fe	–
DW_03	DW_03_001	1428	0.97	H_2O/OH	–
DW_03	DW_03_001	1933	0.86	H_2O	–
DW_03	DW_03_001	2327	0.93	$CaCO_3$	Dol/Cal
DW_03	DW_03_001	2463	0.98	–	–
DW_03	DW_03_002	426	0.74	Fe	–
DW_03	DW_03_002	493	0.69	Fe	–
DW_03	DW_03_002	670	0.92	Fe	–
DW_03	DW_03_002	968	0.75	Fe	–
DW_03	DW_03_002	1391	0.97	H_2O/OH	–
DW_03	DW_03_002	1419	0.95	H_2O/OH	–
DW_03	DW_03_002	1914	0.80	H_2O	–
DW_03	DW_03_002	2215	0.99	AlOH	–
DW_03	DW_03_002	2313	0.92	$CaCO_3$	–
DW_03	DW_03_003	422	0.74	Fe	–
DW_03	DW_03_003	488	0.74	Fe	–
DW_03	DW_03_003	670	0.97	Fe	–
DW_03	DW_03_003	966	0.85	–	–
DW_03	DW_03_003	1413	0.93	H_2O/OH	–
DW_03	DW_03_003	1917	0.87	H_2O	–
DW_03	DW_03_003	2024	0.97	AlOH	–
DW_03	DW_03_003	2334	0.95	$CaCO_3$	–
DW_03	DW_03_004	426	0.67	Fe	–
DW_03	DW_03_004	488	0.62	Fe	–

Continuation of Table B.1					
Sample_Id	Spectrum_Id	Position	Depth	Cause	Mineral
DW_03	DW_03_004	671	0.94	Fe	–
DW_03	DW_03_004	966	0.72	Fe	–
DW_03	DW_03_004	1419	0.97	H_2O/OH	–
DW_03	DW_03_004	1925	0.88	H_2O	–
DW_03	DW_03_004	2204	0.99	AlOH	–
DW_03	DW_03_004	2327	0.95	$CaCO_3$	–
DW_03	DW_03_005	426	0.68	Fe	–
DW_03	DW_03_005	484	0.70	Fe	–
DW_03	DW_03_005	937	0.95	Fe	–
DW_03	DW_03_005	1017	0.96	–	–
DW_03	DW_03_005	1415	0.96	H_2O/OH	–
DW_03	DW_03_005	1918	0.88	H_2O	–
DW_03	DW_03_005	2207	0.97	AlOH	–
DW_04	DW_04_001	419	0.56	Fe	Goethite
DW_04	DW_04_001	482	0.59	Fe	Goethite
DW_04	DW_04_001	951	0.87	Fe	Goethite
DW_04	DW_04_001	1419	0.98	H_2O/OH	–
DW_04	DW_04_001	1922	0.93	H_2O	–
DW_04	DW_04_001	2341	0.98	$CaCO_3$	Calcite?
DW_04	DW_04_002	423	0.72	Fe	Goethite
DW_04	DW_04_002	484	0.73	Fe	Goethite
DW_04	DW_04_002	740	0.99	–	Nd
DW_04	DW_04_002	800	0.99	–	Nd
DW_04	DW_04_002	962	0.92	Fe	Goethite
DW_04	DW_04_002	1414	0.98	H_2O/OH	–
DW_04	DW_04_002	1928	0.93	H_2O	–
DW_04	DW_04_002	2154	0.98	AlOH?	Calcite?
DW_04	DW_04_002	2339	0.77	–	Calcite
DW_04	DW_04_003	426	0.62	Fe	Goethite
DW_04	DW_04_003	479	0.63	Fe	Goethite
DW_04	DW_04_003	673	0.97	Fe	Goethite
DW_04	DW_04_003	951	0.86	Fe	Goethite
DW_04	DW_04_003	1424	0.98	H_2O/OH	–

Continuation of Table B.1					
Sample_Id	Spectrum_Id	Position	Depth	Cause	Mineral
DW_04	DW_04_003	1917	0.90	H_2O	–
DW_04	DW_04_003	2301	0.95	$CaCO_3$	–
DW_04	DW_04_003	2337	0.96	$CaCO_3$	Calcite
DW_04	DW_04_003	2484	0.99	–	Calcite?
DW_04	DW_04_004	427	0.77	Fe	Goethite
DW_04	DW_04_004	488	0.76	Fe	Goethite
DW_04	DW_04_004	683	0.99	Fe	Goethite
DW_04	DW_04_004	921	0.92	Fe	–
DW_04	DW_04_004	1419	0.87	H_2O/OH	–
DW_04	DW_04_004	1919	0.64	H_2O	–
DW_04	DW_04_004	2220	0.94	AlOH	–
DW_04	DW_04_004	2255	0.97	FeOH	–
DW_04	DW_04_004	2338	0.88	$CaCO_3$	Calcite
DW_04	DW_04_004	2483	0.98	–	Calcite?
DW_04	DW_04_005	426	0.73	Fe	Goethite
DW_04	DW_04_005	484	0.74	Fe	Goethite
DW_04	DW_04_005	934	0.94	Fe	Goethite
DW_04	DW_04_005	1418	0.83	H_2O/OH	–
DW_04	DW_04_005	1921	0.57	H_2O	–
DW_04	DW_04_005	2158	0.99	–	Calcite?
DW_04	DW_04_005	2220	0.92	AlOH	–
DW_04	DW_04_005	2256	0.96	FeOH	–
DW_04	DW_04_005	2338	0.86	$CaCO_3$	Calcite
DW_04	DW_04_005	2486	0.98	–	Calcite?
DW_04	DW_04_006	423	0.72	Fe	Goethite
DW_04	DW_04_006	482	0.85	Fe	Goethite
DW_04	DW_04_006	922	0.97	Fe	Goethite
DW_04	DW_04_006	1418	0.89	H_2O/OH	–
DW_04	DW_04_006	1920	0.68	H_2O	–
DW_04	DW_04_006	2220	0.94	AlOH	–
DW_04	DW_04_006	2257	0.97	FeOH	–
DW_04	DW_04_006	2347	0.97	$CaCO_3$	–
DW_04	DW_04_006	2416	0.97	$CaCO_3$	–

Continuation of Table B.1					
Sample_Id	Spectrum_Id	Position	Depth	Cause	Mineral
DW_05	DW_05_001	427	0.78	Fe	Goethite
DW_05	DW_05_001	488	0.76	Fe	Goethite
DW_05	DW_05_001	673	0.96	Fe	Goethite
DW_05	DW_05_001	974	0.78	Fe	Goethite
DW_05	DW_05_001	1432	0.98	H_2O/OH	–
DW_05	DW_05_001	1927	0.88	H_2O	–
DW_05	DW_05_001	2202	0.99	AlOH	–
DW_05	DW_05_001	2333	0.98	$CaCO_3$	–
DW_05	DW_05_002	417	0.83	Fe	Goethite
DW_05	DW_05_002	481	0.86	Fe	Goethite
DW_05	DW_05_002	973	0.93	Fe	Goethite
DW_05	DW_05_002	1418	0.98	H_2O/OH	–
DW_05	DW_05_002	1917	0.91	H_2O	–
DW_05	DW_05_002	2200	0.99	AlOH	–
DW_05	DW_05_002	2313	0.98	$CaCO_3$	Dolomite?
DW_05	DW_05_003	423	0.73	Fe	Goethite
DW_05	DW_05_003	484	0.75	Fe	Goethite
DW_05	DW_05_003	977	0.89	Fe	Goethite
DW_05	DW_05_003	1421	0.96	H_2O/OH	–
DW_05	DW_05_003	1928	0.84	H_2O	–
DW_05	DW_05_003	2207	0.99	AlOH	–
DW_05	DW_05_004	422	0.73	Fe	Goethite
DW_05	DW_05_004	484	0.72	Fe	Goethite
DW_05	DW_05_004	670	0.97	Fe	Goethite
DW_05	DW_05_004	966	0.82	Fe	Goethite
DW_05	DW_05_004	1432	0.98	H_2O/OH	–
DW_05	DW_05_004	1923	0.92	H_2O	–
DW_05	DW_05_005	422	0.83	Fe	Goethite
DW_05	DW_05_005	487	0.82	Fe	Goethite
DW_05	DW_05_005	966	0.86	Fe	Goethite
DW_05	DW_05_005	1428	0.98	H_2O/OH	–
DW_05	DW_05_005	1933	0.92	H_2O	–
DW_06	DW_06_001	417	0.81	Fe	Goethite

Continuation of Table B.1					
Sample_Id	Spectrum_Id	Position	Depth	Cause	Mineral
DW_06	DW_06_001	490	0.84	Fe	Goethite
DW_06	DW_06_001	666	0.97	Fe	Goethite
DW_06	DW_06_001	919	0.91	Fe	Goethite
DW_06	DW_06_001	1426	0.98	H_2O/OH	–
DW_06	DW_06_001	1912	0.87	H_2O	–
DW_06	DW_06_001	2308	0.94	$CaCO_3$	–
DW_06	DW_06_001	2386	0.98	$CaCO_3$	–
DW_06	DW_06_002	493	0.93	Fe	Goethite
DW_06	DW_06_002	666	0.96	Fe	Goethite
DW_06	DW_06_002	899	0.89	Fe	Goethite
DW_06	DW_06_002	1417	0.90	H_2O/OH	–
DW_06	DW_06_002	1910	0.70	H_2O	–
DW_06	DW_06_002	2199	0.98	AlOH	–
DW_06	DW_06_002	2245	0.97	FeOH	–
DW_06	DW_06_002	2298	0.94	FeOH/$CaCO_3$	Dolomite?
DW_06	DW_06_002	2384	0.97	–	–
DW_06	DW_06_003	422	0.72	Fe	Goethite
DW_06	DW_06_003	482	0.75	Fe	Goethite
DW_06	DW_06_003	660	0.98	Fe	Goethite
DW_06	DW_06_003	918	0.92	Fe	Goethite
DW_06	DW_06_003	1419	0.97	H_2O/OH	–
DW_06	DW_06_003	1911	0.85	H_2O	–
DW_06	DW_06_003	2296	0.95	FeOH/$CaCO_3$	Dolomite?
DW_06	DW_06_003	2386	0.98	–	–
DW_06	DW_06_004	488	0.84	Fe	Goethite
DW_06	DW_06_004	670	0.96	Fe	Goethite
DW_06	DW_06_004	980	0.85	Fe	Goethite
DW_06	DW_06_004	1420	0.96	H_2O/OH	–
DW_06	DW_06_004	1914	0.84	H_2O	–
DW_06	DW_06_004	2298	0.96	FeOH/$CaCO_3$	Dolomite?
DW_06	DW_06_004	2391	0.98	–	–
DW_06	DW_06_005	501	0.94	Fe	–
DW_06	DW_06_005	670	0.92	Fe	–

Continuation of Table B.1					
Sample_Id	Spectrum_Id	Position	Depth	Cause	Mineral
DW_06	DW_06_005	892	0.89	Fe	–
DW_06	DW_06_005	1425	0.97	H_2O/OH	–
DW_06	DW_06_005	1912	0.84	H_2O	–
DW_06	DW_06_005	2302	0.92	$CaCO_3$	Dolomite?
DW_06	DW_06_005	2387	0.97	–	–
DW_07	DW_07_001	418	0.76	Fe	Goethite
DW_07	DW_07_001	484	0.77	Fe	Goethite
DW_07	DW_07_001	659	0.98	Fe	Goethite
DW_07	DW_07_001	746	0.99	–	Nd
DW_07	DW_07_001	805	0.98	–	Nd
DW_07	DW_07_001	959	0.91	Fe	Goethite
DW_07	DW_07_001	1458	0.94	H_2O/OH	–
DW_07	DW_07_001	1759	0.99	OH	–
DW_07	DW_07_001	1931	0.81	H_2O	–
DW_07	DW_07_001	2156	0.97	AlOH	–
DW_07	DW_07_001	2339	0.70	$CaCO_3$	Calcite
DW_07	DW_07_001	2483	0.95	–	Calcite
DW_07	DW_07_002	427	0.75	Fe	Goethite
DW_07	DW_07_002	484	0.73	Fe	Goethite
DW_07	DW_07_002	659	0.97	Fe	Goethite
DW_07	DW_07_002	949	0.85	Fe	Goethite
DW_07	DW_07_002	1436	0.98	H_2O/OH	–
DW_07	DW_07_002	1931	0.92	H_2O	–
DW_07	DW_07_002	2339	0.90	$CaCO_3$	Calcite
DW_07	DW_07_002	2482	0.98	–	Calcite
DW_07	DW_07_003	423	0.75	Fe	Goethite
DW_07	DW_07_003	484	0.73	Fe	Goethite
DW_07	DW_07_003	674	0.97	Fe	Goethite
DW_07	DW_07_003	745	0.99	–	Nd
DW_07	DW_07_003	802	0.97	–	Nd
DW_07	DW_07_003	948	0.87	Fe	Goethite
DW_07	DW_07_003	1457	0.95	H_2O/OH	–
DW_07	DW_07_003	1932	0.81	H_2O	–

Continuation of Table B.1					
Sample_Id	Spectrum_Id	Position	Depth	Cause	Mineral
DW_07	DW_07_003	2158	0.98	–	Calcite
DW_07	DW_07_003	2338	0.71	$CaCO_3$	Calcite
DW_07	DW_07_003	2482	0.94	–	Calcite
DW_07	DW_07_004	426	0.71	Fe	Goethite
DW_07	DW_07_004	486	0.68	Fe	Goethite
DW_07	DW_07_004	666	0.96	Fe	Goethite
DW_07	DW_07_004	745	0.99	–	Nd
DW_07	DW_07_004	803	0.96	–	Nd
DW_07	DW_07_004	944	0.83	Fe	Goethite
DW_07	DW_07_004	1444	0.96	H_2O/OH	–
DW_07	DW_07_004	1758	0.99	OH	Calcite
DW_07	DW_07_004	1933	0.85	H_2O	–
DW_07	DW_07_004	2154	0.99	–	Calcite
DW_07	DW_07_004	2339	0.75	$CaCO_3$	Calcite
DW_07	DW_07_004	2484	0.95	–	Calcite
DW_07	DW_07_005	422	0.75	Fe	Goethite
DW_07	DW_07_005	482	0.78	Fe	Goethite
DW_07	DW_07_005	959	0.93	Fe	Goethite
DW_07	DW_07_005	1417	0.97	H_2O/OH	–
DW_07	DW_07_005	1924	0.87	H_2O	–
DW_07	DW_07_005	2208	0.98	AlOH	–
DW_08	DW_08_001	423	0.68	Fe	Goethite
DW_08	DW_08_001	487	0.68	Fe	Goethite
DW_08	DW_08_001	664	0.98	Fe	Goethite
DW_08	DW_08_001	745	0.99	–	Nd
DW_08	DW_08_001	803	0.97	–	Nd
DW_08	DW_08_001	947	0.88	Fe	Goethite
DW_08	DW_08_001	1445	0.97	H_2O/OH	–
DW_08	DW_08_001	1934	0.90	H_2O	–
DW_08	DW_08_001	2155	0.99	–	Calcite
DW_08	DW_08_001	2340	0.80	$CaCO_3$	Calcite
DW_08	DW_08_001	2484	0.96	–	Calcite
DW_08	DW_08_002	422	0.67	Fe	Goethite

Continuation of Table B.1					
Sample_Id	Spectrum_Id	Position	Depth	Cause	Mineral
DW_08	DW_08_002	484	0.67	Fe	Goethite
DW_08	DW_08_002	671	0.97	Fe	Goethite
DW_08	DW_08_002	745	0.99	–	Nd
DW_08	DW_08_002	802	0.97	–	Nd
DW_08	DW_08_002	951	0.86	Fe	Goethite
DW_08	DW_08_002	1456	0.96	H_2O/OH	–
DW_08	DW_08_002	1759	0.99	OH	Calcite
DW_08	DW_08_002	1934	0.83	H_2O	–
DW_08	DW_08_002	2154	0.98	–	Calcite
DW_08	DW_08_002	2339	0.76	$CaCO_3$	Calcite
DW_08	DW_08_002	2483	0.95	–	Calcite
DW_08	DW_08_003	419	0.74	Fe	Goethite
DW_08	DW_08_003	485	0.76	Fe	Goethite
DW_08	DW_08_003	747	0.99	–	Nd
DW_08	DW_08_003	800	0.99	–	Nd
DW_08	DW_08_003	956	0.95	Fe	Goethite
DW_08	DW_08_003	1437	0.97	H_2O/OH	–
DW_08	DW_08_003	1930	0.86	H_2O	–
DW_08	DW_08_003	2211	0.99	AlOH	–
DW_08	DW_08_003	2340	0.94	$CaCO_3$	Calcite
DW_08	DW_08_003	2482	0.98	–	Calcite
DW_08	DW_08_004	427	0.66	Fe	Goethite
DW_08	DW_08_004	484	0.64	Fe	Goethite
DW_08	DW_08_004	600	0.96	?	–
DW_08	DW_08_004	664	0.94	Fe	Goethite
DW_08	DW_08_004	975	0.72	Fe	Goethite
DW_08	DW_08_004	1342	0.99	–	–
DW_08	DW_08_004	1440	0.96	H_2O/OH	–
DW_08	DW_08_004	1935	0.86	H_2O	–
DW_08	DW_08_004	2152	0.99	–	Calcite
DW_08	DW_08_004	2339	0.83	$CaCO_3$	Calcite
DW_08	DW_08_004	2483	0.97	–	Calcite
DW_08	DW_08_005	426	0.68	Fe	Goethite

Continuation of Table B.1					
Sample_Id	Spectrum_Id	Position	Depth	Cause	Mineral
DW_08	DW_08_005	478	0.69	Fe	Goethite
DW_08	DW_08_005	959	0.95	Fe	Goethite
DW_08	DW_08_005	1417	0.98	H_2O/OH	–
DW_08	DW_08_005	1927	0.92	H_2O	–
DW_08	DW_08_005	2208	0.99	AlOH	–
DW_08	DW_08_005	2340	0.90	$CaCO_3$	Calcite
DW_08	DW_08_005	2484	0.98	–	Calcite
DW_09	DW_09_001	422	0.76	Fe	Goethite
DW_09	DW_09_001	482	0.77	Fe	Goethite
DW_09	DW_09_001	742	0.99	–	Nd
DW_09	DW_09_001	801	0.99	–	Nd
DW_09	DW_09_001	966	0.95	Fe	Goethite
DW_09	DW_09_001	1458	0.95	–	–
DW_09	DW_09_001	1759	0.99	–	–
DW_09	DW_09_001	1935	0.83	H_2O	–
DW_09	DW_09_001	2155	0.98	AlOH?	–
DW_09	DW_09_001	2339	0.73	$CaCO_3$	Calcite
DW_09	DW_09_001	2482	0.95	–	–
DW_09	DW_09_002	418	0.73	Fe	Goethite
DW_09	DW_09_002	471	0.76	Fe	Goethite
DW_09	DW_09_002	742	0.99	–	Nd
DW_09	DW_09_002	801	0.99	–	Nd
DW_09	DW_09_002	942	0.96	Fe	Goethite
DW_09	DW_09_002	1457	0.98	H_2O/OH	–
DW_09	DW_09_002	1760	0.99	OH	–
DW_09	DW_09_002	1933	0.89	H_2O	–
DW_09	DW_09_002	2154	0.99	AlOH?	–
DW_09	DW_09_002	2338	0.83	–	Calcite
DW_09	DW_09_002	2480	0.97	–	–
DW_09	DW_09_003	418	0.80	Fe	Goethite
DW_09	DW_09_003	484	0.81	Fe	Goethite
DW_09	DW_09_003	742	0.99	–	Nd
DW_09	DW_09_003	802	0.98	–	Nd

Continuation of Table B.1					
Sample_Id	Spectrum_Id	Position	Depth	Cause	Mineral
DW_09	DW_09_003	999	0.91	Fe	Goethite
DW_09	DW_09_003	1451	0.92	H_2O/OH	–
DW_09	DW_09_003	1754	0.99	OH	–
DW_09	DW_09_003	1933	0.80	H_2O	–
DW_09	DW_09_003	2152	0.98	–	–
DW_09	DW_09_003	2338	0.71	$CaCO_3$	Calcite
DW_09	DW_09_003	2482	0.94	–	–
DW_09	DW_09_004	428	0.67	Fe	Goethite
DW_09	DW_09_004	480	0.68	Fe	Goethite
DW_09	DW_09_004	671	0.98	Fe	Goethite
DW_09	DW_09_004	966	0.82	Fe	Goethite
DW_09	DW_09_004	1453	0.94	H_2O/OH	–
DW_09	DW_09_004	1760	0.99	OH	–
DW_09	DW_09_004	1933	0.81	H_2O	–
DW_09	DW_09_004	2154	0.98	–	–
DW_09	DW_09_004	2338	0.79	$CaCO_3$	Calcite
DW_09	DW_09_004	2483	0.96	–	–
DW_09	DW_09_005	423	0.81	Fe	Goethite
DW_09	DW_09_005	484	0.83	Fe	Goethite
DW_09	DW_09_005	966	0.94	Fe	Goethite
DW_09	DW_09_005	1463	0.98	–	–
DW_09	DW_09_005	1763	0.99	OH	–
DW_09	DW_09_005	1933	0.87	H_2O	–
DW_09	DW_09_005	2155	0.99	–	–
DW_09	DW_09_005	2338	0.85	$CaCO_3$	Calcite
DW_09	DW_09_005	2483	0.97	–	–
DW_10	DW_10_001	423	0.77	Fe	Goethite
DW_10	DW_10_001	479	0.79	Fe	Goethite
DW_10	DW_10_001	741	0.99	–	Nd
DW_10	DW_10_001	800	0.98	–	Nd
DW_10	DW_10_001	867	0.96	–	Nd
DW_10	DW_10_001	966	0.94	Fe	Goethite
DW_10	DW_10_001	1457	0.96	–	–

Continuation of Table B.1					
Sample_Id	Spectrum_Id	Position	Depth	Cause	Mineral
DW_10	DW_10_001	1759	0.99	OH	–
DW_10	DW_10_001	1931	0.88	H_2O	–
DW_10	DW_10_001	2155	0.98	–	–
DW_10	DW_10_001	2339	0.72	$CaCO_3$	Calcite
DW_10	DW_10_001	2480	0.95	–	–
DW_10	DW_10_002	426	0.77	Fe	Goethite
DW_10	DW_10_002	484	0.77	Fe	Goethite
DW_10	DW_10_002	740	0.99	–	Nd
DW_10	DW_10_002	800	0.98	–	Nd
DW_10	DW_10_002	867	0.95	–	Nd
DW_10	DW_10_002	966	0.94	Fe	Goethite
DW_10	DW_10_002	1454	0.96	–	–
DW_10	DW_10_002	1760	0.99	OH	–
DW_10	DW_10_002	1936	0.86	H_2O	–
DW_10	DW_10_002	2156	0.98	–	–
DW_10	DW_10_002	2340	0.70	$CaCO_3$	Calcite
DW_10	DW_10_002	2483	0.94	–	–
DW_10	DW_10_003	428	0.76	Fe	Goethite
DW_10	DW_10_003	484	0.77	Fe	Goethite
DW_10	DW_10_003	740	0.99	Fe	Nd
DW_10	DW_10_003	800	0.98	–	Nd
DW_10	DW_10_003	867	0.94	–	Nd
DW_10	DW_10_003	974	0.92	Fe	Goethite
DW_10	DW_10_003	1459	0.97	–	–
DW_10	DW_10_003	1759	0.99	OH	–
DW_10	DW_10_003	1938	0.91	H_2O	–
DW_10	DW_10_003	2157	0.99	–	–
DW_10	DW_10_003	2339	0.80	$CaCO_3$	Calcite
DW_10	DW_10_003	2482	0.96	–	–
DW_10	DW_10_004	423	0.79	Fe	Goethite
DW_10	DW_10_004	480	0.81	Fe	Goethite
DW_10	DW_10_004	740	0.99	–	Nd
DW_10	DW_10_004	800	0.99	–	Nd

Continuation of Table B.1

Sample_Id	Spectrum_Id	Position	Depth	Cause	Mineral
DW_10	DW_10_004	867	0.97	–	Nd
DW_10	DW_10_004	974	0.95	Fe	Goethite
DW_10	DW_10_004	1459	0.96	–	–
DW_10	DW_10_004	1758	0.99	OH	–
DW_10	DW_10_004	1930	0.87	H_2O	–
DW_10	DW_10_004	2156	0.98	–	–
DW_10	DW_10_004	2339	0.74	$CaCO_3$	Calcite
DW_10	DW_10_004	2482	0.95	–	–
DW_10	DW_10_005	423	0.73	Fe	Goethite
DW_10	DW_10_005	488	0.72	Fe	Goethite
DW_10	DW_10_005	579	0.99	–	Nd?
DW_10	DW_10_005	675	0.97	Fe	Goethite
DW_10	DW_10_005	739	0.98	–	Nd
DW_10	DW_10_005	802	0.96	–	Nd
DW_10	DW_10_005	870	0.89	–	Nd
DW_10	DW_10_005	966	0.85	Fe	Goethite
DW_10	DW_10_005	1452	0.97	–	–
DW_10	DW_10_005	1754	0.99	OH	–
DW_10	DW_10_005	1940	0.89	H_2O	–
DW_10	DW_10_005	2154	0.98	–	–
DW_10	DW_10_005	2338	0.75	$CaCO_3$	Calcite
DW_10	DW_10_005	2482	0.95	–	–
DW_11	DW_11_001	423	0.61	Fe	Goethite?
DW_11	DW_11_001	974	0.97	Fe	Goethite?
DW_11	DW_11_001	1416	0.96	H_2O/OH	–
DW_11	DW_11_001	1918	0.87	H_2O	–
DW_11	DW_11_001	2009	0.97	AlOH	–
DW_11	DW_11_001	2253	0.99	FeOH	–
DW_11	DW_11_001	2299	0.99	–	–
DW_11	DW_11_001	2343	0.98	$CaCO_3$	–
DW_11	DW_11_002	480	0.68	Fe	–
DW_11	DW_11_002	1027	0.98	Fe	Goethite?
DW_11	DW_11_002	1425	0.99	H_2O/OH	–

Continuation of Table B.1					
Sample_Id	Spectrum_Id	Position	Depth	Cause	Mineral
DW_11	DW_11_002	1913	0.93	H_2O	–
DW_11	DW_11_002	1963	0.94	H_2O	–
DW_11	DW_11_002	1995	0.95	H_2O	–
DW_11	DW_11_002	2158	0.99	–	–
DW_11	DW_11_002	2338	0.86	$CaCO_3$	Calcite
DW_11	DW_11_002	2485	0.97	–	–
DW_11	DW_11_003	427	0.67	Fe	Goethite
DW_11	DW_11_003	481	0.68	Fe	Goethite
DW_11	DW_11_003	709	0.99	–	–
DW_11	DW_11_003	963	0.94	Fe	Goethite
DW_11	DW_11_003	1424	0.99	H_2O/OH	–
DW_11	DW_11_003	1915	0.95	H_2O	–
DW_11	DW_11_003	1997	0.96	H_2O	–
DW_11	DW_11_003	2159	0.99	–	–
DW_11	DW_11_003	2338	0.90	$CaCO_3$	Calcite
DW_11	DW_11_003	2483	0.98	–	–
DW_11	DW_11_004	427	0.67	Fe	Goethite?
DW_11	DW_11_004	724	0.99	–	–
DW_11	DW_11_004	1051	0.97	Fe	Goethite?
DW_11	DW_11_004	1419	0.96	H_2O/OH	–
DW_11	DW_11_004	1918	0.95	H_2O	–
DW_11	DW_11_004	2154	0.99	H_2O	–
DW_11	DW_11_004	2332	0.90	$CaCO_3$	Calcite
DW_11	DW_11_004	2468	0.98	–	–
DW_11	DW_11_005	427	0.63	Fe	Goethite
DW_11	DW_11_005	485	0.63	Fe	Goethite
DW_11	DW_11_005	992	0.86	Fe	Goethite
DW_11	DW_11_005	1434	0.97	H_2O/OH	–
DW_11	DW_11_005	1930	0.91	H_2O	–
DW_11	DW_11_005	2333	0.92	$CaCO_3$	Calcite
DW_12	DW_12_001	426	0.71	Fe	Goethite
DW_12	DW_12_001	480	0.73	Fe	Goethite
DW_12	DW_12_001	741	0.99	–	Nd

Continuation of Table B.1

Sample_Id	Spectrum_Id	Position	Depth	Cause	Mineral
DW_12	DW_12_001	800	0.99	–	Nd
DW_12	DW_12_001	870	0.98	–	Nd
DW_12	DW_12_001	942	0.97	Fe	Goethite
DW_12	DW_12_001	1023	0.97	–	–
DW_12	DW_12_001	1455	0.97	–	–
DW_12	DW_12_001	1930	0.86	H_2O	–
DW_12	DW_12_001	2156	0.98	–	–
DW_12	DW_12_001	2339	0.76	$CaCO_3$	Calcite
DW_12	DW_12_001	2483	0.95	–	–
DW_12	DW_12_002	419	0.69	Fe	Goethite
DW_12	DW_12_002	480	0.74	Fe	Goethite
DW_12	DW_12_002	937	0.97	Fe	Goethite
DW_12	DW_12_002	1417	0.97	–	–
DW_12	DW_12_002	1925	0.89	H_2O	–
DW_12	DW_12_002	2159	0.99	–	–
DW_12	DW_12_002	2211	0.99	AlOH	–
DW_12	DW_12_002	2339	0.83	$CaCO_3$	Calcite
DW_12	DW_12_002	2483	0.97	–	–
DW_12	DW_12_003	426	0.86	Fe	Goethite
DW_12	DW_12_003	487	0.87	Fe	Goethite
DW_12	DW_12_003	582	0.99	–	Nd
DW_12	DW_12_003	740	0.99	–	Nd
DW_12	DW_12_003	800	0.99	–	Nd
DW_12	DW_12_003	947	0.96	Fe	Goethite
DW_12	DW_12_003	1454	0.98	–	–
DW_12	DW_12_003	1879	0.97	–	–
DW_12	DW_12_003	1930	0.93	H_2O	–
DW_12	DW_12_003	1996	0.94	H_2O	–
DW_12	DW_12_003	2155	0.99	–	–
DW_12	DW_12_003	2339	0.80	$CaCO_3$	Calcite
DW_12	DW_12_003	2482	0.96	–	–
DW_12	DW_12_004	422	0.73	Fe	Goethite
DW_12	DW_12_004	482	0.74	Fe	Goethite

Continuation of Table B.1					
Sample_Id	Spectrum_Id	Position	Depth	Cause	Mineral
DW_12	DW_12_004	934	0.93	Fe	Goethite
DW_12	DW_12_004	1419	0.87	H_2O/OH	–
DW_12	DW_12_004	1921	0.62	H_2O	–
DW_12	DW_12_004	2157	0.99	–	–
DW_12	DW_12_004	2220	0.94	AlOH	–
DW_12	DW_12_004	2256	0.96	FeOH	–
DW_12	DW_12_004	2340	0.81	$CaCO_3$	Calcite
DW_12	DW_12_004	2485	0.87	–	–
DW_12	DW_12_005	427	0.79	Fe	Goethite
DW_12	DW_12_005	488	0.78	Fe	Goethite
DW_12	DW_12_005	627	0.96	–	–
DW_12	DW_12_005	740	0.99	–	Nd
DW_12	DW_12_005	800	0.99	–	Nd
DW_12	DW_12_005	950	0.94	–	–
DW_12	DW_12_005	1458	0.97	–	–
DW_12	DW_12_005	1759	0.99	OH	–
DW_12	DW_12_005	1933	0.86	H_2O	–
DW_12	DW_12_005	2156	0.98	–	–
DW_12	DW_12_005	2339	0.70	$CaCO_3$	Calcite
DW_12	DW_12_005	2482	0.94	–	–
DW_13	DW_13_001	426	0.71	Fe	Goethite
DW_13	DW_13_001	484	0.71	Fe	Goethite
DW_13	DW_13_001	666	0.98	Fe	Goethite
DW_13	DW_13_001	966	0.89	Fe	Goethite
DW_13	DW_13_001	1444	0.99	H_2O/OH	–
DW_13	DW_13_001	1880	0.98	H_2O	–
DW_13	DW_13_001	1949	0.95	H_2O	–
DW_13	DW_13_001	1997	0.95	H_2O	–
DW_13	DW_13_001	2155	0.99	–	–
DW_13	DW_13_001	2339	0.84	$CaCO_3$	Calcite
DW_13	DW_13_001	2482	0.97	–	–
DW_13	DW_13_002	427	0.72	Fe	Goethite
DW_13	DW_13_002	484	0.71	Fe	Goethite

Continuation of Table B.1

Sample_Id	Spectrum_Id	Position	Depth	Cause	Mineral
DW_13	DW_13_002	592	0.95	–	–
DW_13	DW_13_002	636	0.96	–	–
DW_13	DW_13_002	959	0.89	Fe	Goethite
DW_13	DW_13_002	1293	0.99	–	–
DW_13	DW_13_002	1441	0.99	H_2O/OH	–
DW_13	DW_13_002	1878	0.96	–	–
DW_13	DW_13_002	1961	0.93	H_2O	–
DW_13	DW_13_002	1995	0.93	H_2O	–
DW_13	DW_13_002	2159	0.98	–	–
DW_13	DW_13_002	2340	0.74	$CaCO_3$	Calcite
DW_13	DW_13_002	2482	0.95	–	–
DW_13	DW_13_003	431	0.64	Fe	Goethite
DW_13	DW_13_003	486	0.61	Fe	Goethite
DW_13	DW_13_003	974	0.84	Fe	Goethite
DW_13	DW_13_003	1442	0.99	H_2O/OH	–
DW_13	DW_13_003	1879	0.97	–	–
DW_13	DW_13_003	1954	0.93	H_2O	–
DW_13	DW_13_003	1996	0.94	H_2O	–
DW_13	DW_13_003	2154	0.99	–	–
DW_13	DW_13_003	2338	0.80	$CaCO_3$	Calcite
DW_13	DW_13_003	2484	0.96	–	–
DW_13	DW_13_004	426	0.64	Fe	Goethite
DW_13	DW_13_004	486	0.62	Fe	Goethite
DW_13	DW_13_004	670	0.91	–	–
DW_13	DW_13_004	974	0.76	Fe	Goethite
DW_13	DW_13_004	1455	0.98	–	–
DW_13	DW_13_004	1938	0.90	H_2O	–
DW_13	DW_13_004	2338	0.94	$CaCO_3$	Calcite
DW_13	DW_13_004	2485	0.98	–	–
DW_13	DW_13_005	433	0.71	Fe	Goethite
DW_13	DW_13_005	488	0.68	Fe	Goethite
DW_13	DW_13_005	666	0.94	Fe	–
DW_13	DW_13_005	966	0.81	Fe	Goethite

Continuation of Table B.1					
Sample_Id	Spectrum_Id	Position	Depth	Cause	Mineral
DW_13	DW_13_005	1446	0.98	H_2O/OH	–
DW_13	DW_13_005	1878	0.96	–	–
DW_13	DW_13_005	1957	0.92	H_2O	–
DW_13	DW_13_005	1997	0.93	H_2O	–
DW_13	DW_13_005	2155	0.99	–	–
DW_13	DW_13_005	2340	0.77	$CaCO_3$	Calcite
DW_13	DW_13_005	2483	0.96	–	–
DW_14	DW_14_001	423	0.72	Fe	Goethite
DW_14	DW_14_001	482	0.73	Fe	Goethite
DW_14	DW_14_001	593	0.99	–	–
DW_14	DW_14_001	670	0.98	Fe	Goethite
DW_14	DW_14_001	1954	0.95	H_2O	–
DW_14	DW_14_001	2340	0.89	$CaCO_3$	Calcite
DW_14	DW_14_001	2483	0.98	–	–
DW_14	DW_14_002	423	0.66	Fe	Goethite
DW_14	DW_14_002	476	0.67	Fe	Goethite
DW_14	DW_14_002	974	0.93	Fe	Goethite
DW_14	DW_14_002	1454	0.98	–	–
DW_14	DW_14_002	1955	0.95	H_2O	–
DW_14	DW_14_002	2159	0.99	–	–
DW_14	DW_14_002	2340	0.86	$CaCO_3$	Calcite
DW_14	DW_14_002	2482	0.97	–	–
DW_14	DW_14_003	427	0.68	Fe	Goethite
DW_14	DW_14_003	480	0.70	Fe	Goethite
DW_14	DW_14_003	942	0.97	Fe	Goethite
DW_14	DW_14_003	1941	0.96	H_2O	–
DW_14	DW_14_003	2161	0.99	AlOH	–
DW_14	DW_14_003	2340	0.89	$CaCO_3$	Calcite
DW_14	DW_14_003	2485	0.98	–	–
DW_14	DW_14_004	423	0.65	Fe	Goethite
DW_14	DW_14_004	484	0.67	Fe	Goethite
DW_14	DW_14_004	973	0.95	Fe	Goethite
DW_14	DW_14_004	1941	0.95	H_2O	–

Continuation of Table B.1

Sample_Id	Spectrum_Id	Position	Depth	Cause	Mineral
DW_14	DW_14_004	2160	0.99	AlOH	–
DW_14	DW_14_004	2340	0.85	$CaCO_3$	Calcite
DW_14	DW_14_004	2485	0.97	–	–
DW_14	DW_14_005	426	0.68	Fe	Goethite
DW_14	DW_14_005	475	0.69	Fe	Goethite
DW_14	DW_14_005	966	0.96	Fe	Goethite
DW_14	DW_14_005	1934	0.96	H_2O	–
DW_14	DW_14_005	2155	0.99	–	–
DW_14	DW_14_005	2340	0.85	$CaCO_3$	Calcite
DW_14	DW_14_005	2482	0.97	–	–
DW_15	DW_15_001	426	0.77	Fe	Goethite
DW_15	DW_15_001	484	0.76	Fe	Goethite
DW_15	DW_15_001	942	0.92	Fe	Goethite
DW_15	DW_15_001	1418	0.94	H_2O/OH	–
DW_15	DW_15_001	1920	0.79	H_2O	–
DW_15	DW_15_001	2156	0.99	–	–
DW_15	DW_15_001	2220	0.98	AlOH	–
DW_15	DW_15_001	2339	0.86	$CaCO_3$	Calcite
DW_15	DW_15_001	2485	0.97	–	–
DW_15	DW_15_002	428	0.69	Fe	Goethite
DW_15	DW_15_002	479	0.70	Fe	Goethite
DW_15	DW_15_002	966	0.92	Fe	Goethite
DW_15	DW_15_002	1417	0.97	H_2O/OH	–
DW_15	DW_15_002	1921	0.88	H_2O	–
DW_15	DW_15_002	2208	0.99	AlOH	–
DW_15	DW_15_002	2340	0.94	$CaCO_3$	Calcite
DW_15	DW_15_002	2483	0.98	–	–
DW_15	DW_15_003	427	0.70	Fe	Goethite
DW_15	DW_15_003	484	0.70	Fe	Goethite
DW_15	DW_15_003	966	0.94	Fe	Goethite
DW_15	DW_15_003	1931	0.96	H_2O	–
DW_15	DW_15_003	2154	0.99	–	–
DW_15	DW_15_003	2339	0.89	$CaCO_3$	Calcite

Continuation of Table B.1					
Sample_Id	Spectrum_Id	Position	Depth	Cause	Mineral
DW_15	DW_15_003	2484	0.98	–	–
DW_15	DW_15_004	423	0.71	Fe	Goethite
DW_15	DW_15_004	484	0.74	Fe	Goethite
DW_15	DW_15_004	927	0.95	Fe	Goethite
DW_15	DW_15_004	1418	0.90	H_2O/OH	–
DW_15	DW_15_004	1919	0.67	H_2O	–
DW_15	DW_15_004	2154	0.99	–	–
DW_15	DW_15_004	2220	0.96	AlOH	–
DW_15	DW_15_004	2257	0.98	FeOH	–
DW_15	DW_15_004	2339	0.83	$CaCO_3$	Calcite
DW_15	DW_15_004	2485	0.97	–	–
DW_15	DW_15_005	422	0.74	Fe	Goethite
DW_15	DW_15_005	482	0.86	Fe	Goethite
DW_15	DW_15_005	951	0.95	Fe	Goethite
DW_15	DW_15_005	1418	0.97	H_2O/OH	–
DW_15	DW_15_005	1921	0.87	H_2O	–
DW_15	DW_15_005	2211	0.99	AlOH	–
DW_15	DW_15_005	2340	0.92	$CaCO_3$	Calcite
DW_15	DW_15_005	2484	0.98	–	–
DW_16	DW_16_001	426	0.74	Fe	Goethite
DW_16	DW_16_001	486	0.72	Fe	Goethite
DW_16	DW_16_001	942	0.86	Fe	Goethite
DW_16	DW_16_001	1445	0.99	H_2O/OH	–
DW_16	DW_16_001	1941	0.94	H_2O	–
DW_16	DW_16_001	2338	0.92	$CaCO_3$	Calcite
DW_16	DW_16_001	2482	0.98	–	–
DW_16	DW_16_002	426	0.69	Fe	Goethite
DW_16	DW_16_002	486	0.69	Fe	Goethite
DW_16	DW_16_002	666	0.98	Fe	Goethite
DW_16	DW_16_002	923	0.90	Fe	Goethite
DW_16	DW_16_002	1419	0.84	H_2O/OH	–
DW_16	DW_16_002	1919	0.59	H_2O	–
DW_16	DW_16_002	2154	0.99	–	–

Continuation of Table B.1					
Sample_Id	Spectrum_Id	Position	Depth	Cause	Mineral
DW_16	DW_16_002	2220	0.94	AlOH	Illite/smectite?
DW_16	DW_16_002	2256	0.97	FeOH	–
DW_16	DW_16_002	2340	0.84	$CaCO_3$	Calcite
DW_16	DW_16_002	2482	0.97	–	–
DW_16	DW_16_003	426	0.68	Fe	Goethite
DW_16	DW_16_003	484	0.66	Fe	Goethite
DW_16	DW_16_003	652	0.94	Fe	Goethite
DW_16	DW_16_003	966	0.81	Fe	Goethite
DW_16	DW_16_003	1431	0.99	H_2O/OH	–
DW_16	DW_16_003	1931	0.93	H_2O	–
DW_16	DW_16_003	2153	0.99	–	–
DW_16	DW_16_003	2339	0.82	$CaCO_3$	Calcite
DW_16	DW_16_003	2482	0.97	–	–
DW_16	DW_16_004	427	0.51	Fe	Goethite
DW_16	DW_16_004	475	0.53	Fe	Goethite
DW_16	DW_16_004	951	0.92	Fe	Goethite
DW_16	DW_16_004	1416	0.98	H_2O/OH	–
DW_16	DW_16_004	1919	0.92	H_2O	–
DW_16	DW_16_004	2207	0.99	AlOH	–
DW_16	DW_16_004	2339	0.95	$CaCO_3$	Calcite
DW_16	DW_16_004	2485	0.99	–	–
DW_16	DW_16_005	427	0.67	Fe	Goethite
DW_16	DW_16_005	484	0.66	Fe	Goethite
DW_16	DW_16_005	678	0.98	Fe	Goethite
DW_16	DW_16_005	947	0.90	Fe	Goethite
DW_16	DW_16_005	1931	0.95	H_2O	–
DW_16	DW_16_005	2152	0.99	–	–
DW_16	DW_16_005	2339	0.84	$CaCO_3$	Calcite
DW_16	DW_16_005	2482	0.97	–	–
DW_17	DW_17_001	422	0.69	Fe	Goethite
DW_17	DW_17_001	480	0.73	Fe	Goethite
DW_17	DW_17_001	742	0.99	–	Nd
DW_17	DW_17_001	800	0.99	–	Nd

Continuation of Table B.1					
Sample_Id	Spectrum_Id	Position	Depth	Cause	Mineral
DW_17	DW_17_001	867	0.98	–	Nd
DW_17	DW_17_001	951	0.97	Fe	Goethite
DW_17	DW_17_001	1416	0.98	H_2O/OH	–
DW_17	DW_17_001	1928	0.91	H_2O	–
DW_17	DW_17_001	2158	0.99	–	–
DW_17	DW_17_001	2339	0.82	$CaCO_3$	Calcite
DW_17	DW_17_001	2482	0.97	–	–
DW_17	DW_17_002	426	0.79	Fe	Goethite
DW_17	DW_17_002	484	0.80	Fe	Goethite
DW_17	DW_17_002	742	0.99	–	Nd
DW_17	DW_17_002	800	0.99	–	Nd
DW_17	DW_17_002	867	0.98	–	Nd
DW_17	DW_17_002	947	0.97	Fe	Goethite
DW_17	DW_17_002	1455	0.97	H_2O/OH	–
DW_17	DW_17_002	1933	0.88	H_2O	–
DW_17	DW_17_002	2154	0.98	–	–
DW_17	DW_17_002	2339	0.70	$CaCO_3$	Calcite
DW_17	DW_17_002	2480	0.95	–	–
DW_17	DW_17_003	426	0.69	Fe	Goethite
DW_17	DW_17_003	484	0.71	Fe	Goethite
DW_17	DW_17_003	743	0.99	–	Nd
DW_17	DW_17_003	801	0.99	–	Nd
DW_17	DW_17_003	951	0.96	–	–
DW_17	DW_17_003	1416	0.98	H_2O/OH	–
DW_17	DW_17_003	1931	0.88	H_2O	–
DW_17	DW_17_003	2154	0.98	–	–
DW_17	DW_17_003	2339	0.76	$CaCO_3$	Calcite
DW_17	DW_17_003	2482	0.95	–	–
DW_17	DW_17_004	431	0.68	Fe	Goethite
DW_17	DW_17_004	742	0.99	–	Nd
DW_17	DW_17_004	800	0.99	–	Nd
DW_17	DW_17_004	948	0.98	Fe	Goethite
DW_17	DW_17_004	1417	0.97	H_2O/OH	–

Continuation of Table B.1					
Sample_Id	Spectrum_Id	Position	Depth	Cause	Mineral
DW_17	DW_17_004	1922	0.90	H_2O	–
DW_17	DW_17_004	2158	0.99	–	–
DW_17	DW_17_004	2209	0.99	AlOH	–
DW_17	DW_17_004	2339	0.86	$CaCO_3$	Calcite
DW_17	DW_17_004	2481	0.97	–	–
DW_17	DW_17_005	426	0.70	Fe	Goethite
DW_17	DW_17_005	482	0.72	Fe	Goethite
DW_17	DW_17_005	743	0.99	–	Nd
DW_17	DW_17_005	801	0.99	–	Nd
DW_17	DW_17_005	947	0.95	Fe	Goethite
DW_17	DW_17_005	1427	0.98	H_2O/OH	–
DW_17	DW_17_005	1930	0.92	H_2O	–
DW_17	DW_17_005	2156	0.98	–	–
DW_17	DW_17_005	2339	0.75	$CaCO_3$	Calcite
DW_17	DW_17_005	2480	0.95	–	–
DW_18	DW_18_001	427	0.80	Fe	Goethite
DW_18	DW_18_001	482	0.81	Fe	Goethite
DW_18	DW_18_001	687	0.99	–	–
DW_18	DW_18_001	740	0.99	–	Nd
DW_18	DW_18_001	802	0.99	–	Nd
DW_18	DW_18_001	975	0.91	Fe	Goethite
DW_18	DW_18_001	1453	0.95	–	–
DW_18	DW_18_001	1756	0.99	OH	–
DW_18	DW_18_001	1932	0.82	H_2O	–
DW_18	DW_18_001	2154	0.97	–	–
DW_18	DW_18_001	2339	0.72	$CaCO_3$	Calcite
DW_18	DW_18_001	2484	0.95	–	–
DW_18	DW_18_002	418	0.75	Fe	Goethite
DW_18	DW_18_002	482	0.76	Fe	Goethite
DW_18	DW_18_002	674	0.98	Fe	Goethite
DW_18	DW_18_002	742	0.99	–	Nd
DW_18	DW_18_002	803	0.95	–	Nd
DW_18	DW_18_002	974	0.83	Fe	Goethite

Continuation of Table B.1					
Sample_Id	Spectrum_Id	Position	Depth	Cause	Mineral
DW_18	DW_18_002	1454	0.94	–	–
DW_18	DW_18_002	1759	0.99	OH	–
DW_18	DW_18_002	1930	0.79	H_2O	–
DW_18	DW_18_002	2154	0.97	–	–
DW_18	DW_18_002	2338	0.70	$CaCO_3$	Calcite
DW_18	DW_18_002	2480	0.94	–	–
DW_18	DW_18_003	419	0.77	Fe	Goethite
DW_18	DW_18_003	484	0.78	Fe	Goethite
DW_18	DW_18_003	673	0.99	Fe	Goethite
DW_18	DW_18_003	742	0.99	–	Nd
DW_18	DW_18_003	802	0.97	–	Nd
DW_18	DW_18_003	974	0.89	Fe	Goethite
DW_18	DW_18_003	1449	0.94	H_2O/OH	–
DW_18	DW_18_003	1756	0.99	OH	–
DW_18	DW_18_003	1929	0.79	H_2O	–
DW_18	DW_18_003	2156	0.97	–	–
DW_18	DW_18_003	2339	0.69	$CaCO_3$	Calcite
DW_18	DW_18_003	2482	0.94	–	–
DW_18	DW_18_004	426	0.70	Fe	Goethite
DW_18	DW_18_004	484	0.69	Fe	Goethite
DW_18	DW_18_004	666	0.94	Fe	Goethite
DW_18	DW_18_004	975	0.78	Fe	Goethite
DW_18	DW_18_004	1445	0.97	H_2O/OH	–
DW_18	DW_18_004	1759	0.99	–	–
DW_18	DW_18_004	1935	0.86	H_2O	–
DW_18	DW_18_004	2156	0.99	–	–
DW_18	DW_18_004	2339	0.82	$CaCO_3$	Calcite
DW_18	DW_18_004	2484	0.97	–	–
DW_18	DW_18_005	419	0.84	Fe	Goethite
DW_18	DW_18_005	484	0.85	Fe	Goethite
DW_18	DW_18_005	598	0.99	–	–
DW_18	DW_18_005	659	0.99	Fe	Goethite
DW_18	DW_18_005	742	0.99	–	Nd

Continuation of Table B.1					
Sample_Id	Spectrum_Id	Position	Depth	Cause	Mineral
DW_18	DW_18_005	803	0.97	–	Nd
DW_18	DW_18_005	974	0.89	Fe	Goethite
DW_18	DW_18_005	1455	0.95	–	–
DW_18	DW_18_005	1757	0.99	OH	–
DW_18	DW_18_005	1932	0.85	–	–
DW_18	DW_18_005	2156	0.98	–	–
DW_18	DW_18_005	2339	0.73	$CaCO_3$	Calcite
DW_18	DW_18_005	2482	0.95	–	–
DW_19	DW_19_001	427	0.79	Fe	Goethite
DW_19	DW_19_001	486	0.77	Fe	Goethite
DW_19	DW_19_001	673	0.96	Fe	Goethite
DW_19	DW_19_001	741	0.98	–	Nd
DW_19	DW_19_001	802	0.95	–	Nd
DW_19	DW_19_001	960	0.85	Fe	Goethite
DW_19	DW_19_001	1452	0.91	–	–
DW_19	DW_19_001	1759	0.99	OH	–
DW_19	DW_19_001	1930	0.74	H_2O	–
DW_19	DW_19_001	2154	0.96	–	–
DW_19	DW_19_001	2339	0.66	$CaCO_3$	Calcite
DW_19	DW_19_001	2483	0.94	–	–
DW_19	DW_19_002	426	0.74	Fe	Goethite
DW_19	DW_19_002	484	0.75	Fe	Goethite
DW_19	DW_19_002	666	0.98	Fe	Goethite
DW_19	DW_19_002	742	0.99	–	Nd
DW_19	DW_19_002	802	0.96	–	Nd
DW_19	DW_19_002	974	0.86	Fe	Goethite
DW_19	DW_19_002	1446	0.94	H_2O/OH	–
DW_19	DW_19_002	1755	0.99	OH	–
DW_19	DW_19_002	1938	0.79	H_2O	–
DW_19	DW_19_002	2156	0.98	–	–
DW_19	DW_19_002	2339	0.76	$CaCO_3$	Calcite
DW_19	DW_19_002	2483	0.96	–	–
DW_19	DW_19_003	426	0.70	Fe	Goethite

Continuation of Table B.1					
Sample_Id	Spectrum_Id	Position	Depth	Cause	Mineral
DW_19	DW_19_003	484	0.72	Fe	Goethite
DW_19	DW_19_003	677	0.98	Fe	Goethite
DW_19	DW_19_003	742	0.99	–	Nd
DW_19	DW_19_003	803	0.97	–	Nd
DW_19	DW_19_003	976	0.87	Fe	Goethite
DW_19	DW_19_003	1449	0.95	H_2O/OH	–
DW_19	DW_19_003	1760	0.99	OH	–
DW_19	DW_19_003	1929	0.83	H_2O	–
DW_19	DW_19_003	2157	0.98	–	–
DW_19	DW_19_003	2338	0.80	$CaCO_3$	Calcite
DW_19	DW_19_003	2482	0.96	–	–
DW_19	DW_19_004	427	0.77	Fe	Goethite
DW_19	DW_19_004	484	0.77	Fe	Goethite
DW_19	DW_19_004	579	0.98	–	Nd
DW_19	DW_19_004	666	0.96	Fe	–
DW_19	DW_19_004	740	0.98	–	Nd
DW_19	DW_19_004	802	0.96	–	Nd
DW_19	DW_19_004	959	0.85	Fe	Goethite
DW_19	DW_19_004	1454	0.92	–	–
DW_19	DW_19_004	1757	0.99	OH	–
DW_19	DW_19_004	1930	0.77	H_2O	–
DW_19	DW_19_004	2154	0.97	–	–
DW_19	DW_19_004	2339	0.67	$CaCO_3$	Calcite
DW_19	DW_19_004	2482	0.94	–	–
DW_19	DW_19_005	419	0.68	Fe	Goethite
DW_19	DW_19_005	484	0.69	Fe	Goethite
DW_19	DW_19_005	672	0.98	Fe	–
DW_19	DW_19_005	742	0.99	–	Nd
DW_19	DW_19_005	803	0.97	–	Nd
DW_19	DW_19_005	966	0.87	Fe	Goethite
DW_19	DW_19_005	1444	0.96	H_2O/OH	–
DW_19	DW_19_005	1758	0.99	–	–
DW_19	DW_19_005	1931	0.83	H_2O	–

Continuation of Table B.1

Sample_Id	Spectrum_Id	Position	Depth	Cause	Mineral
DW_19	DW_19_005	2156	0.98	–	–
DW_19	DW_19_005	2338	0.79	$CaCO_3$	Calcite
DW_19	DW_19_005	2482	0.96	–	–
DW_20	DW_20_001	430	0.83	Fe	Goethite
DW_20	DW_20_001	1226	0.97	–	–
DW_20	DW_20_001	1971	0.98	H_2O	–
DW_20	DW_20_001	2337	0.94	$CaCO_3$	Calcite
DW_20	DW_20_002	471	0.82	Fe	Goethite
DW_20	DW_20_002	1053	0.97	Fe	Goethite
DW_20	DW_20_002	1414	0.98	H_2O/OH	–
DW_20	DW_20_002	1950	0.94	H_2O	–
DW_20	DW_20_002	2338	0.92	$CaCO_3$	Calcite
DW_20	DW_20_002	2482	0.98	–	–
DW_20	DW_20_003	419	0.89	Fe	Goethite
DW_20	DW_20_003	484	0.91	Fe	Goethite
DW_20	DW_20_003	974	0.89	Fe	Goethite
DW_20	DW_20_003	1388	0.98	H_2O/OH	–
DW_20	DW_20_003	1424	0.96	H_2O/OH	–
DW_20	DW_20_003	1927	0.89	H_2O	–
DW_20	DW_20_003	2335	0.91	$CaCO_3$	Calcite
DW_20	DW_20_003	2388	0.97	$CaCO_3$	–
DW_20	DW_20_003	2483	0.98	–	–
DW_20	DW_20_004	425	0.75	Fe	Goethite
DW_20	DW_20_004	474	0.77	Fe	Goethite
DW_20	DW_20_004	928	0.95	Fe	Goethite
DW_20	DW_20_004	1927	0.96	H_2O	–
DW_20	DW_20_004	2337	0.94	$CaCO_3$	Calcite
DW_20	DW_20_005	486	0.83	Fe	Goethite
DW_20	DW_20_005	1069	0.96	Fe	Goethite
DW_20	DW_20_005	1419	0.98	H_2O/OH	–
DW_20	DW_20_005	1925	0.95	H_2O	–
DW_20	DW_20_005	2338	0.97	$CaCO_3$	Calcite

Appendix C

XRD patterns

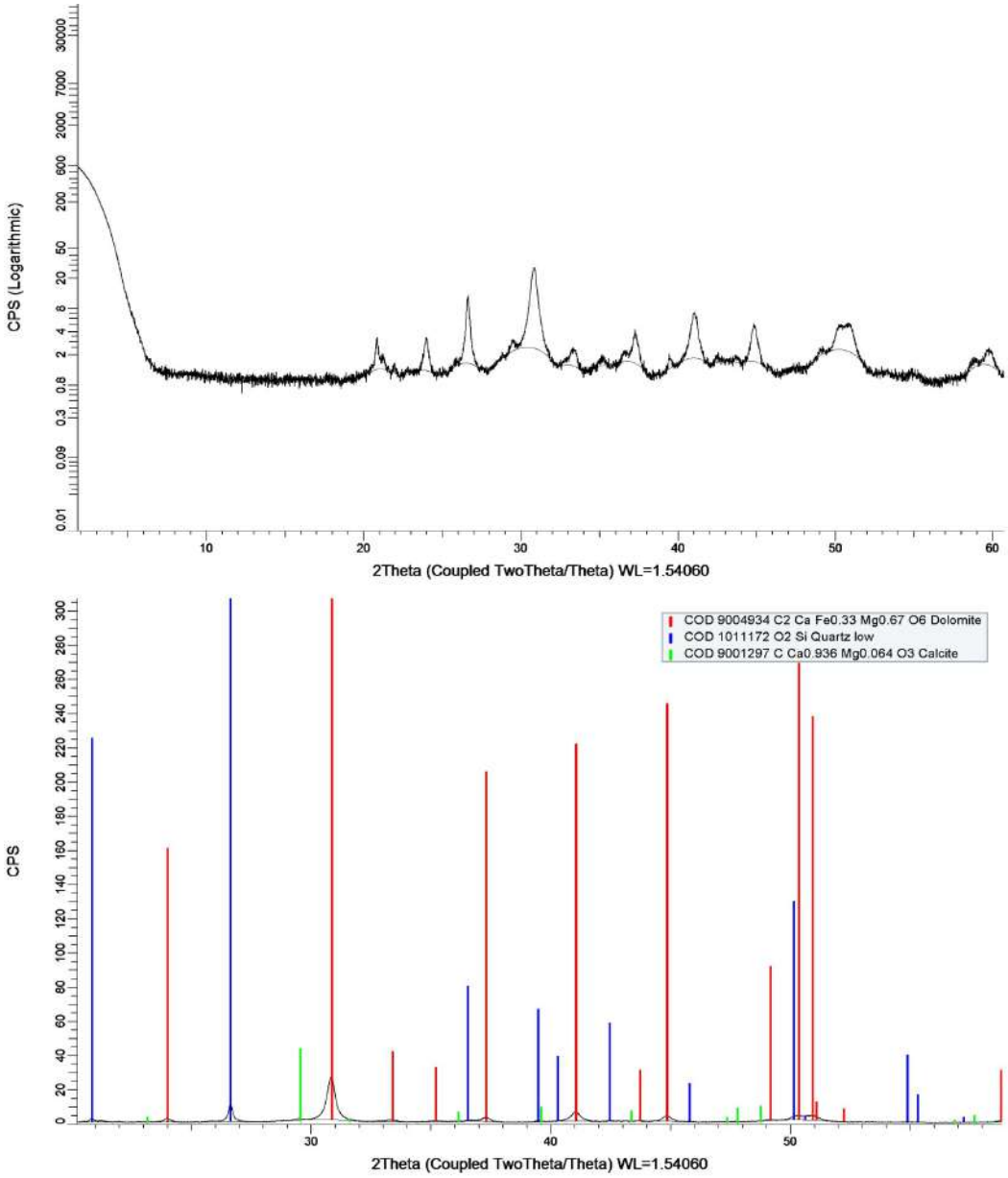

Fig. C.1 Top panel, XRD pattern of sample DW_01; bottom panel, phase identification performed using DIFFRAC.EVA.

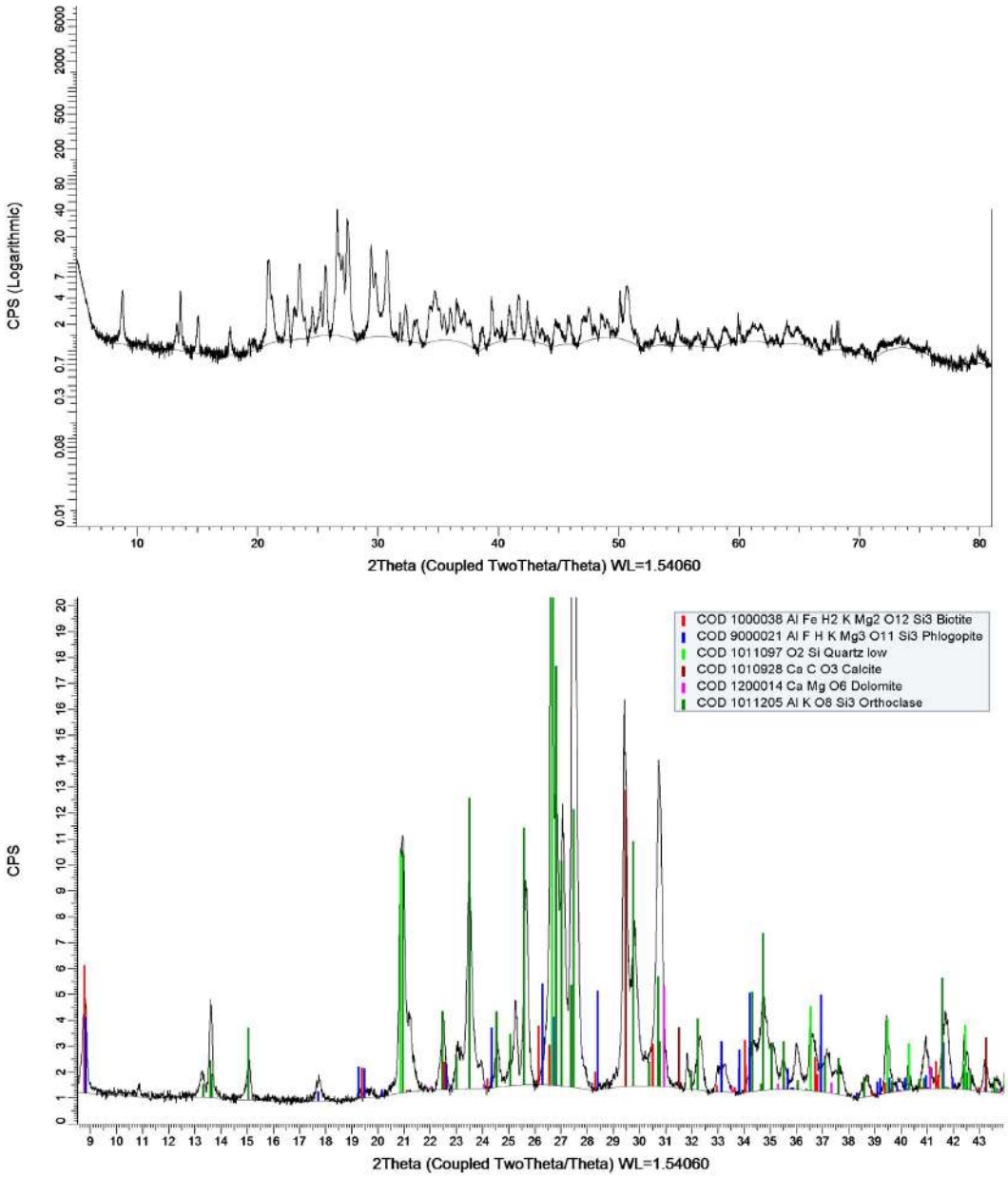

Fig. C.2 Top panel, XRD pattern of sample DW_02; bottom panel, phase identification performed using DIFFRAC.EVA.

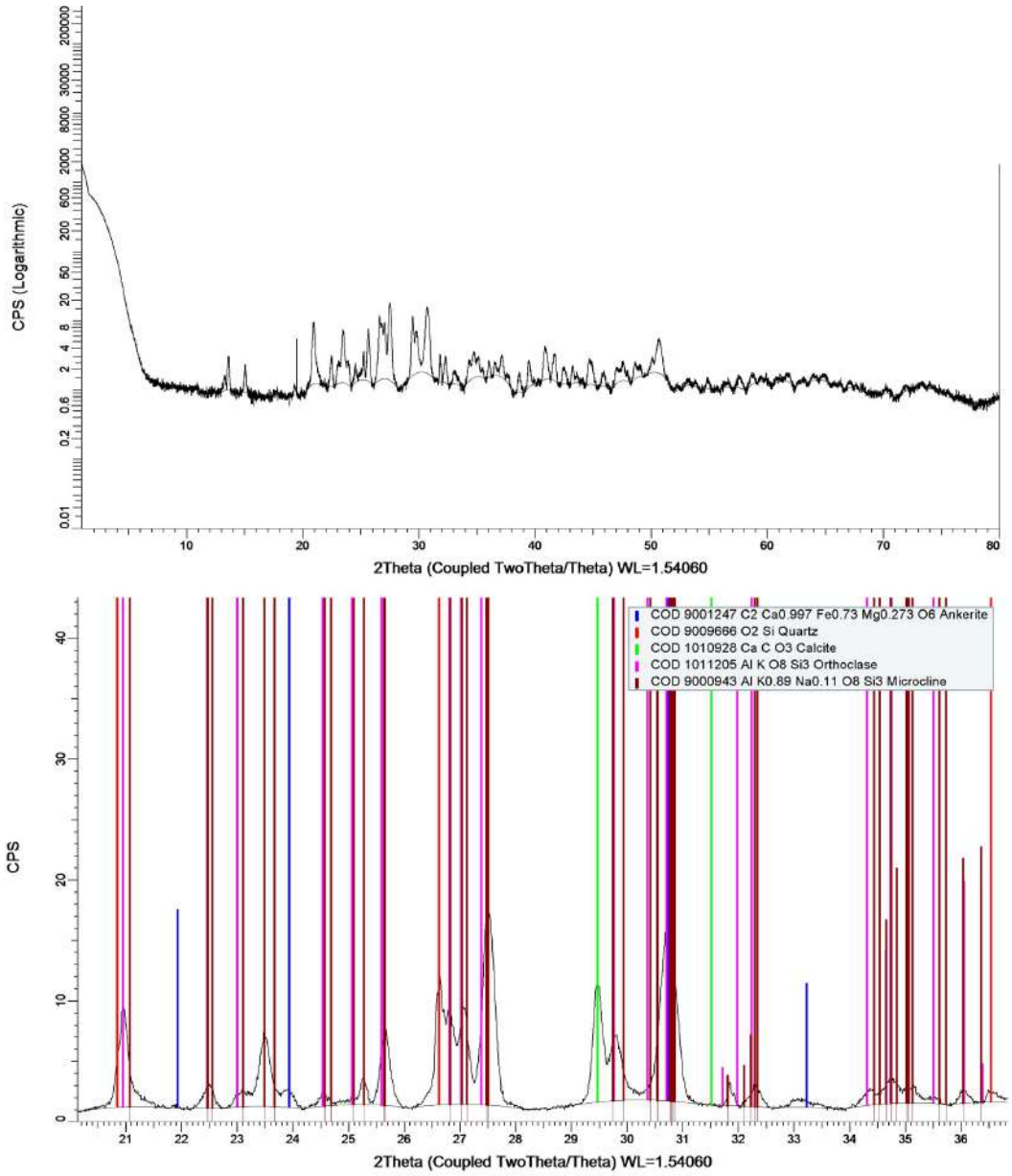

Fig. C.3 Top panel, XRD pattern of sample DW_03; bottom panel, phase identification performed using DIFFRAC.EVA.

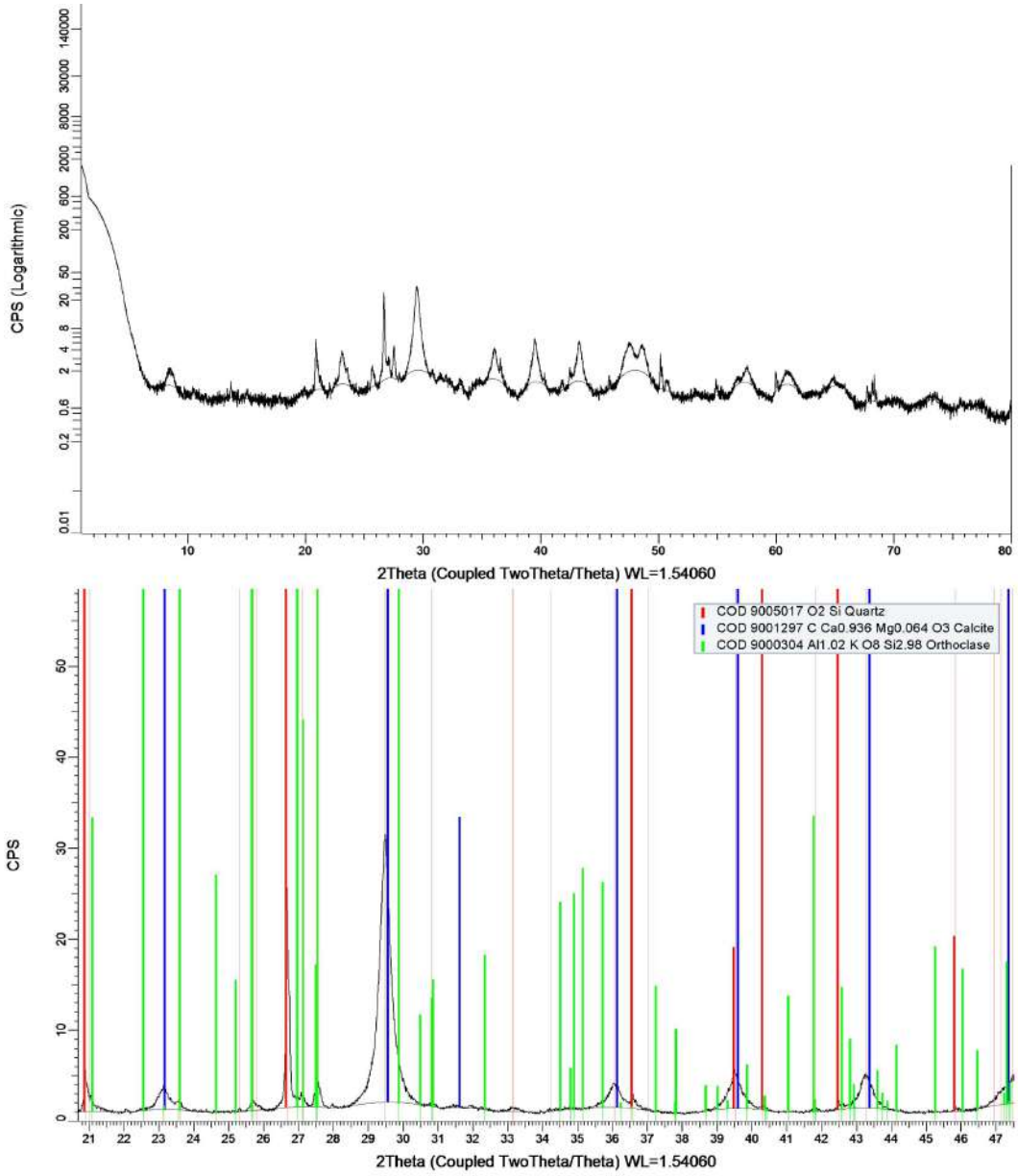

Fig. C.4 Top panel, XRD pattern of sample DW_04; bottom panel, phase identification performed using DIFFRAC.EVA.

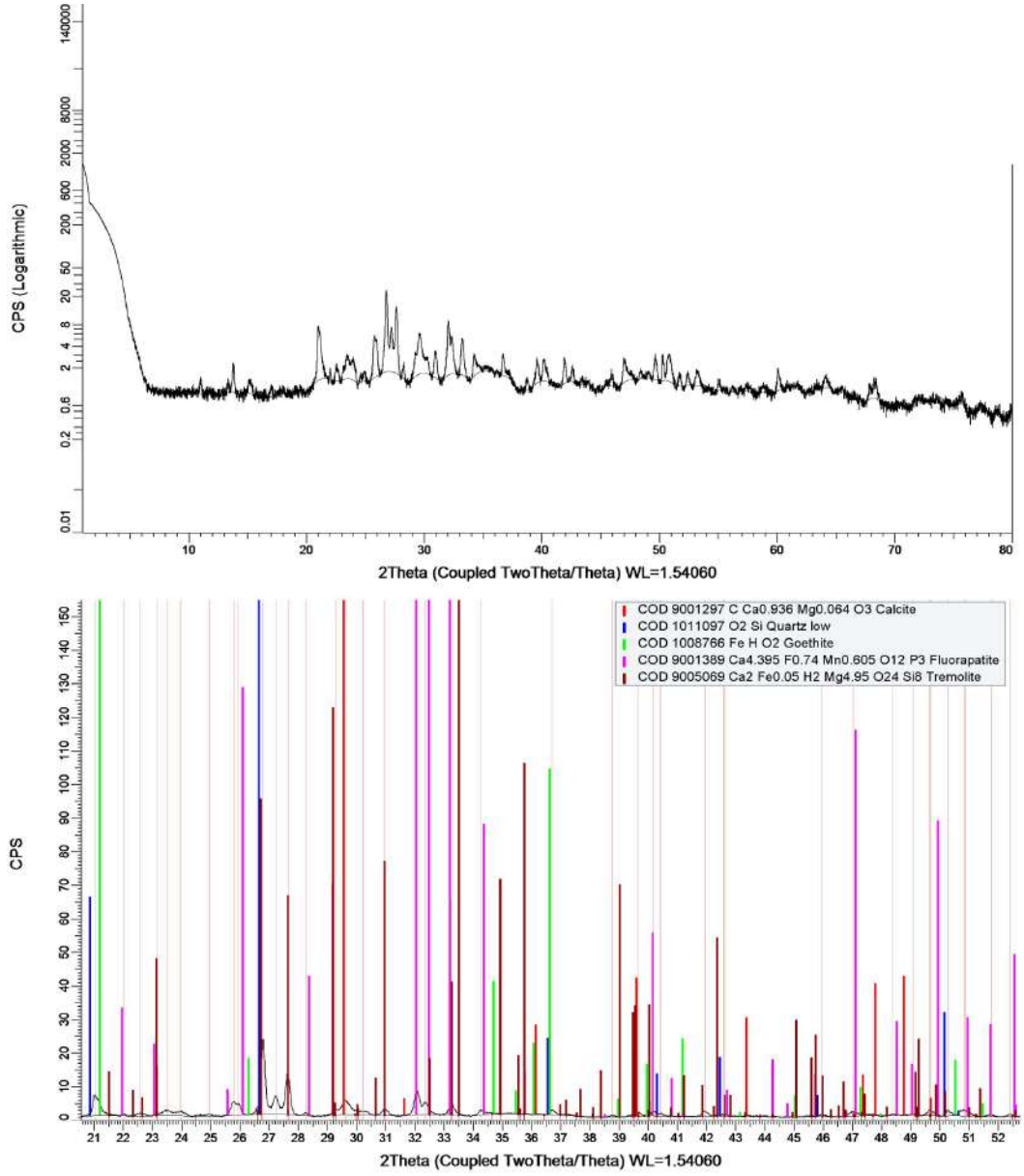

Fig. C.5 Top panel, XRD pattern of sample DW_05; bottom panel, phase identification performed using DIFFRAC.EVA.

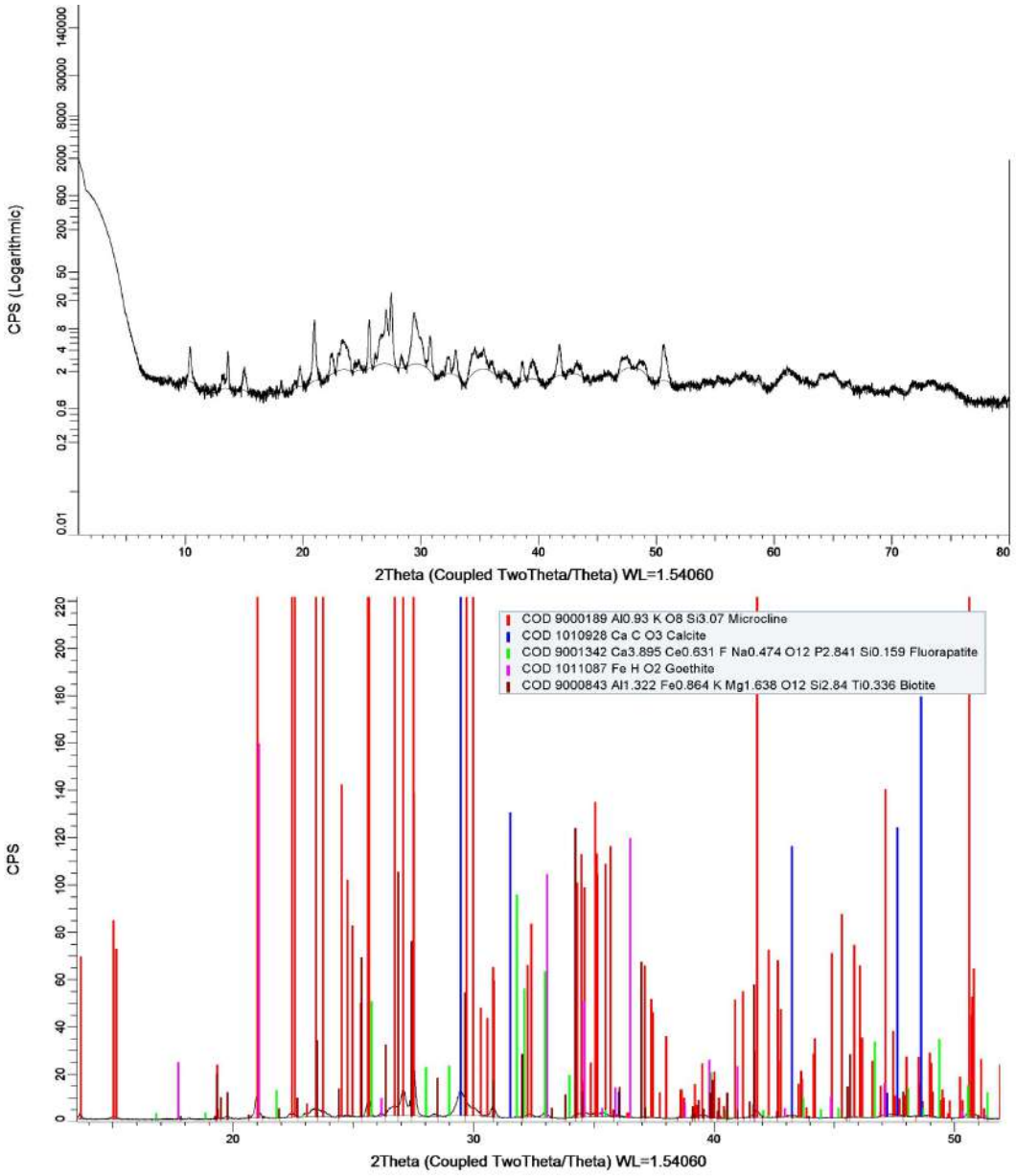

Fig. C.6 Top panel, XRD pattern of sample DW_06; bottom panel, phase identification performed using DIFFRAC.EVA.

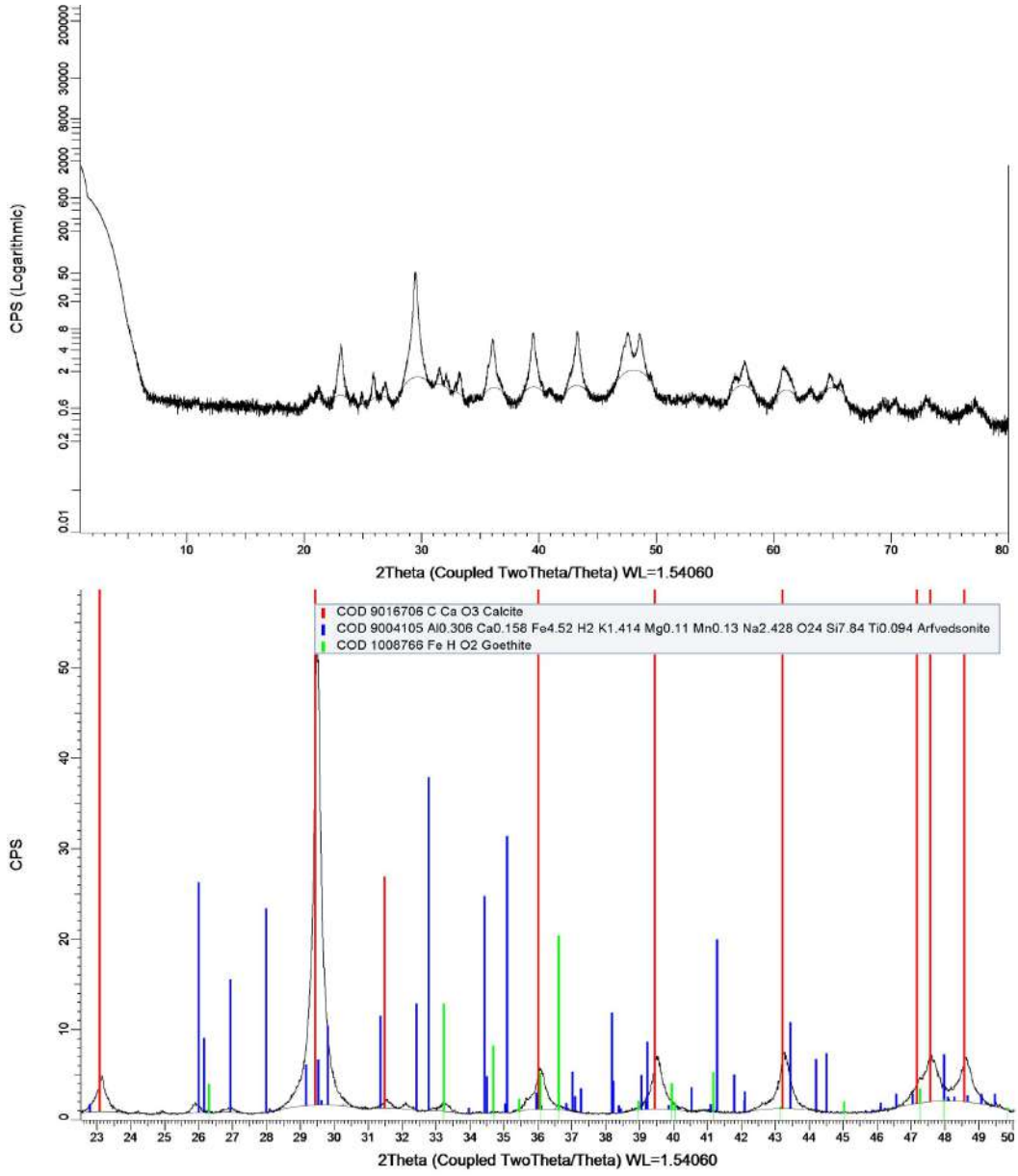

Fig. C.7 Top panel, XRD pattern of sample DW_07; bottom panel, phase identification performed using DIFFRAC.EVA.

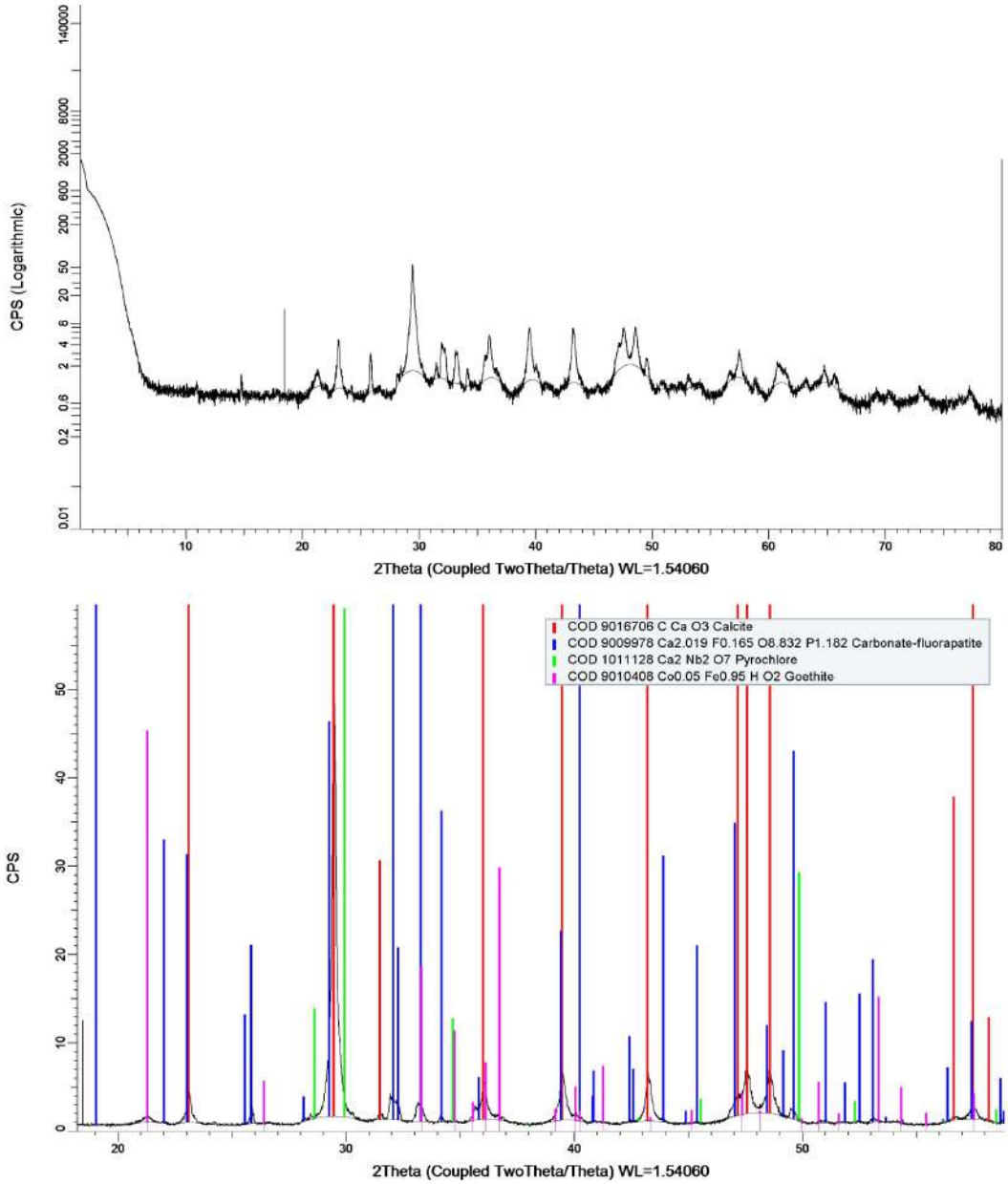

Fig. C.8 Top panel, XRD pattern of sample DW_08; bottom panel, phase identification performed using DIFFRAC.EVA.

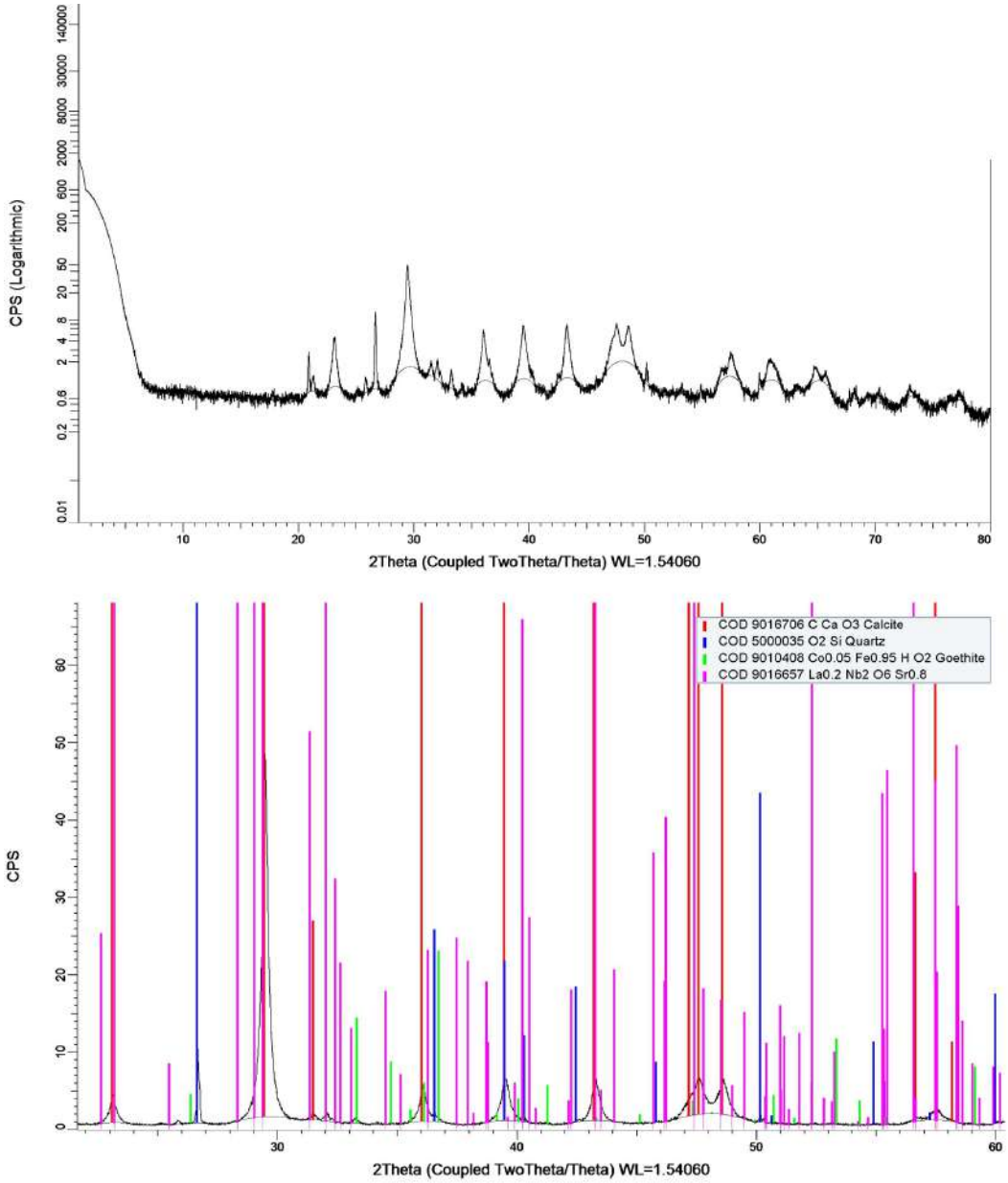

Fig. C.9 Top panel, XRD pattern of sample DW_09; bottom panel, phase identification performed using DIFFRAC.EVA.

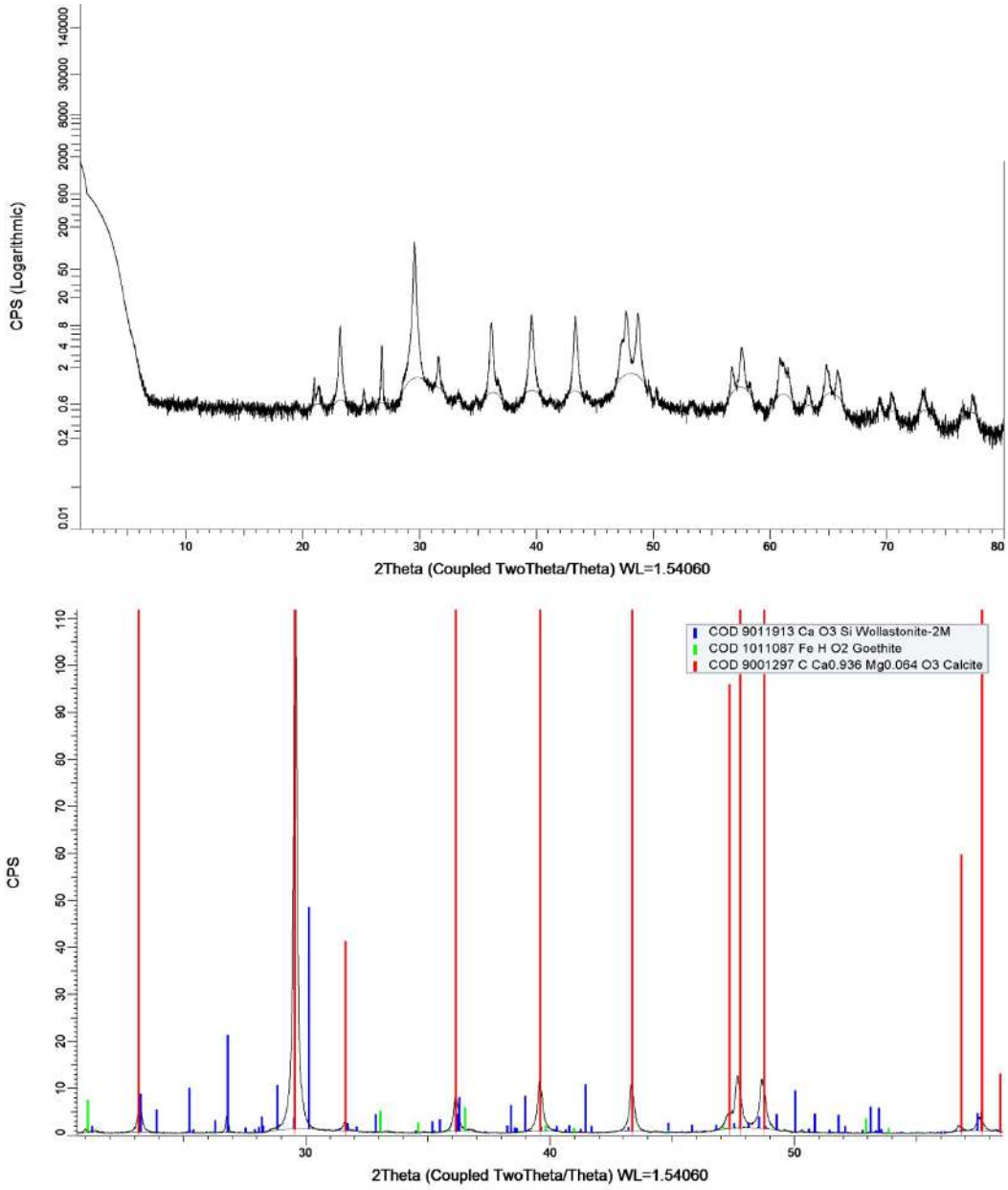

Fig. C.10 Top panel, XRD pattern of sample DW_10; bottom panel, phase identification performed using DIFFRAC.EVA.

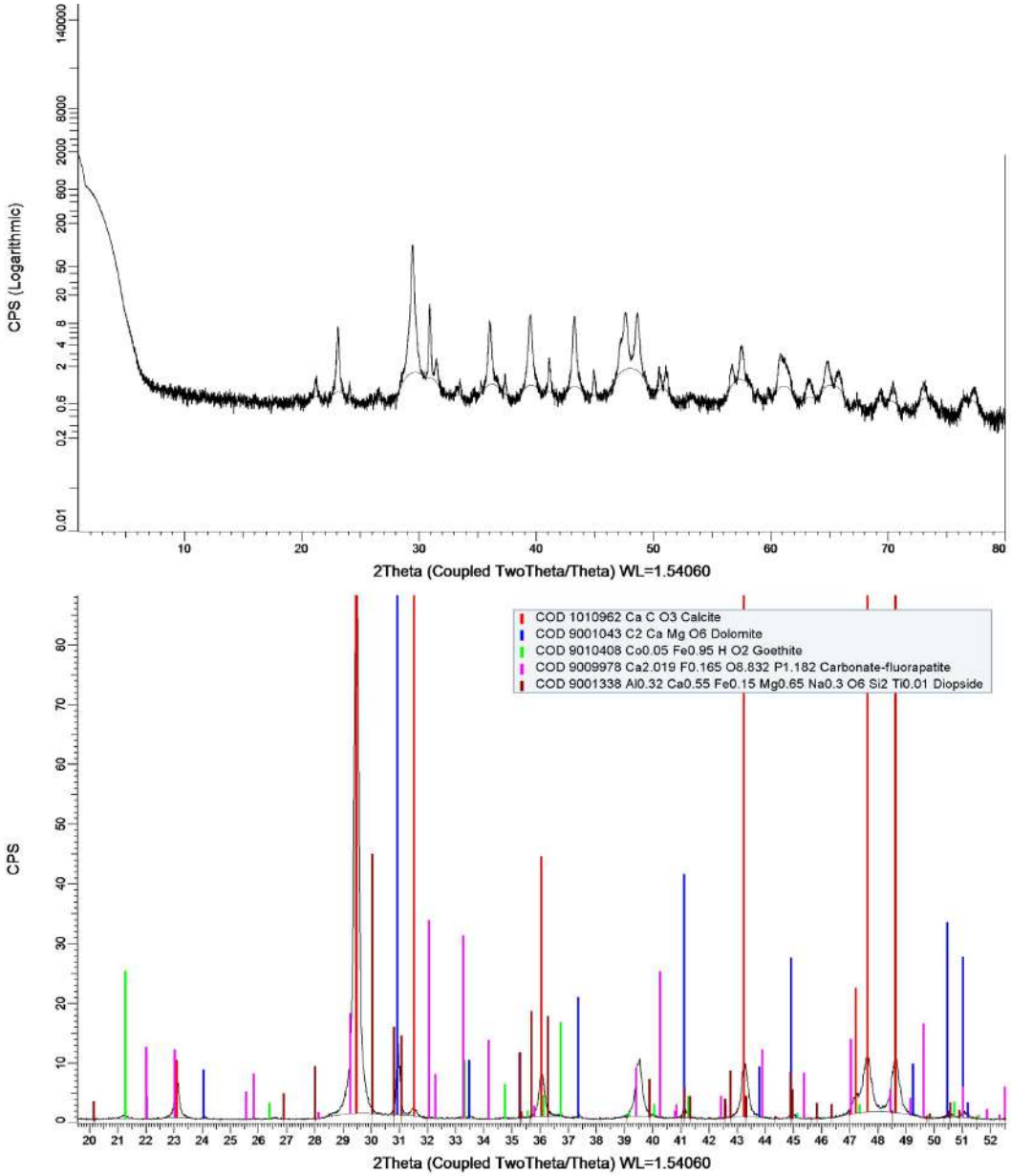

Fig. C.11 Top panel, XRD pattern of sample DW_11; bottom panel, phase identification performed using DIFFRAC.EVA.

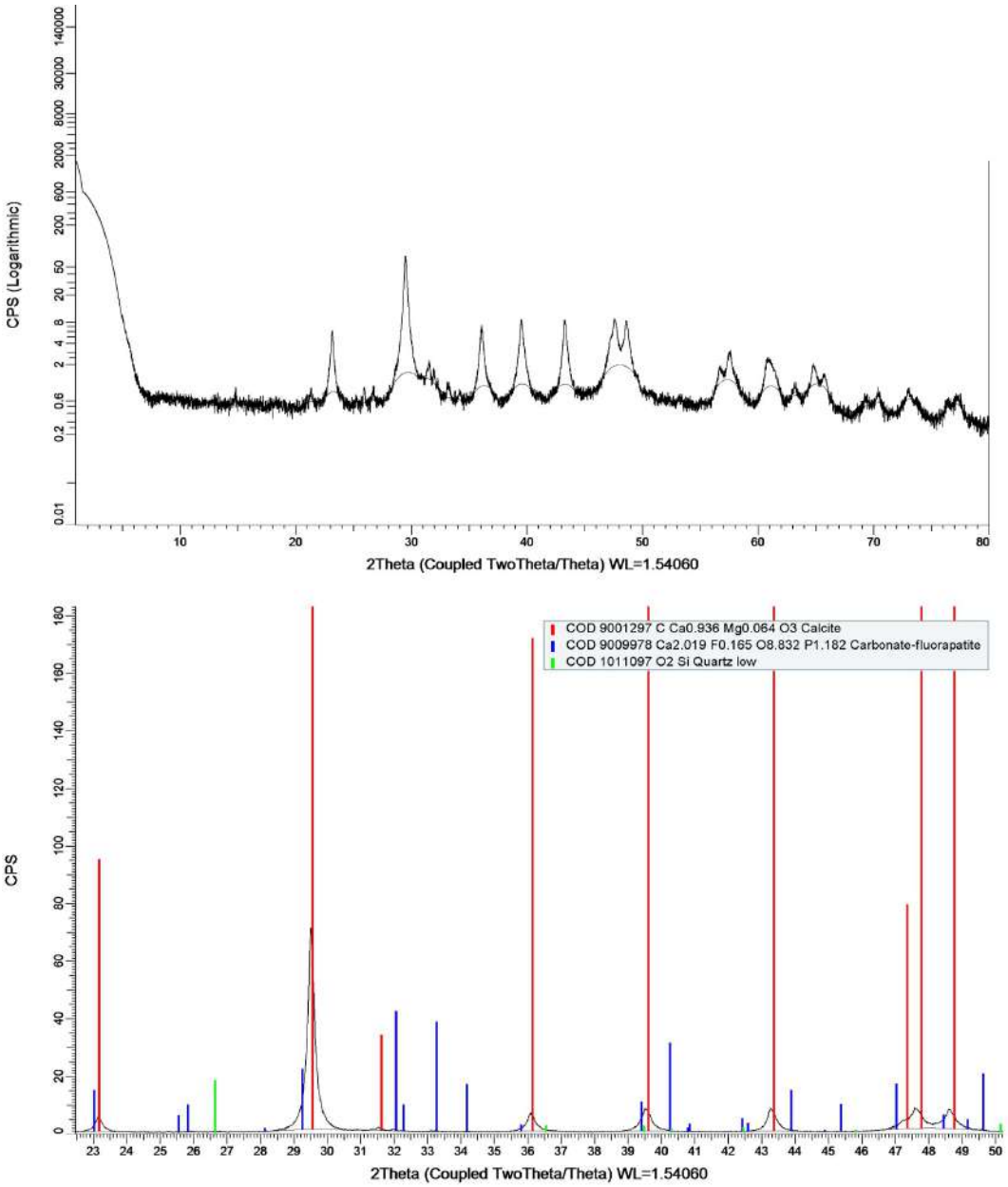

Fig. C.12 Top panel, XRD pattern of sample DW_12; bottom panel, phase identification performed using DIFFRAC.EVA.

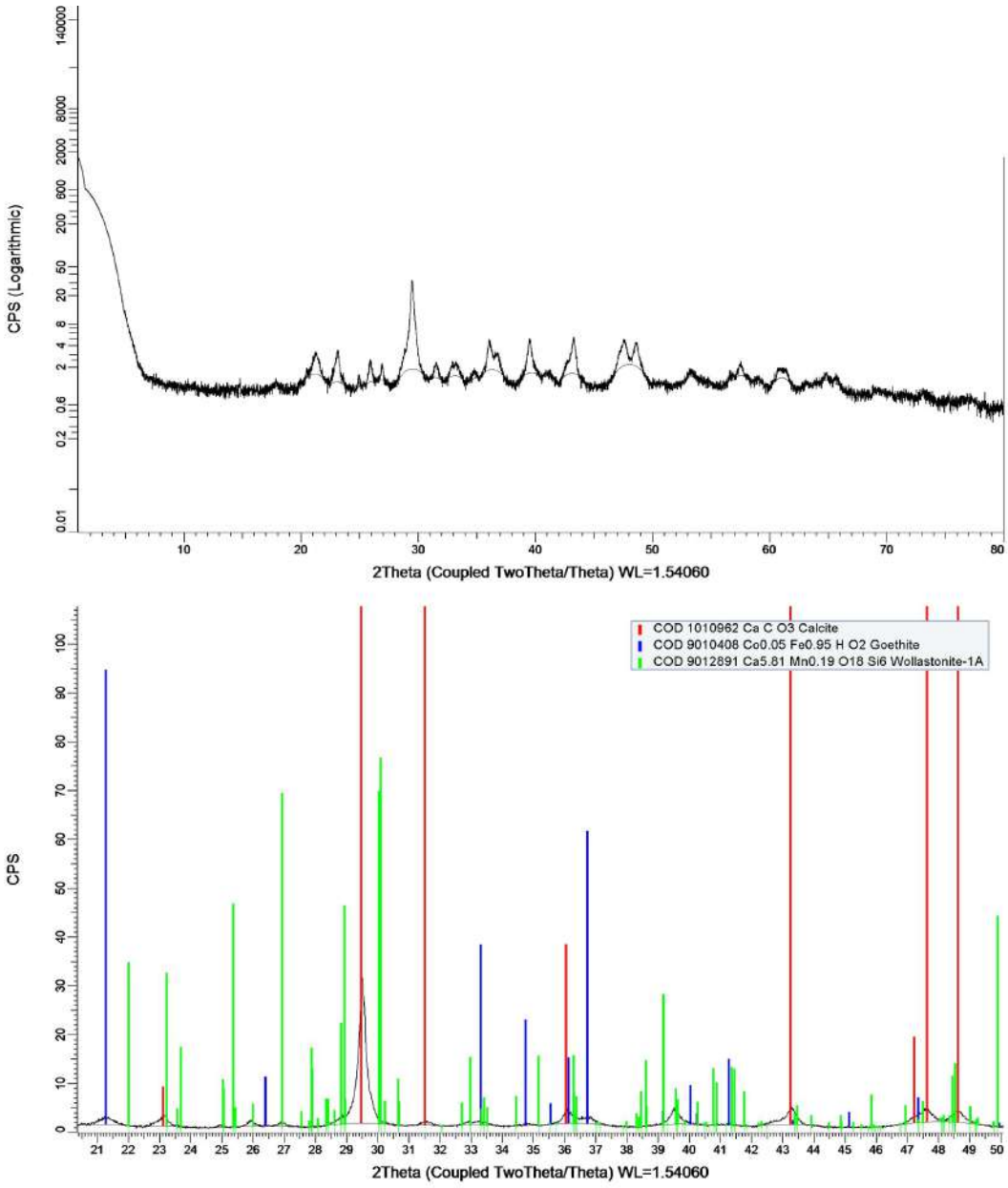

Fig. C.13 Top panel, XRD pattern of sample DW_13; bottom panel, phase identification performed using DIFFRAC.EVA.

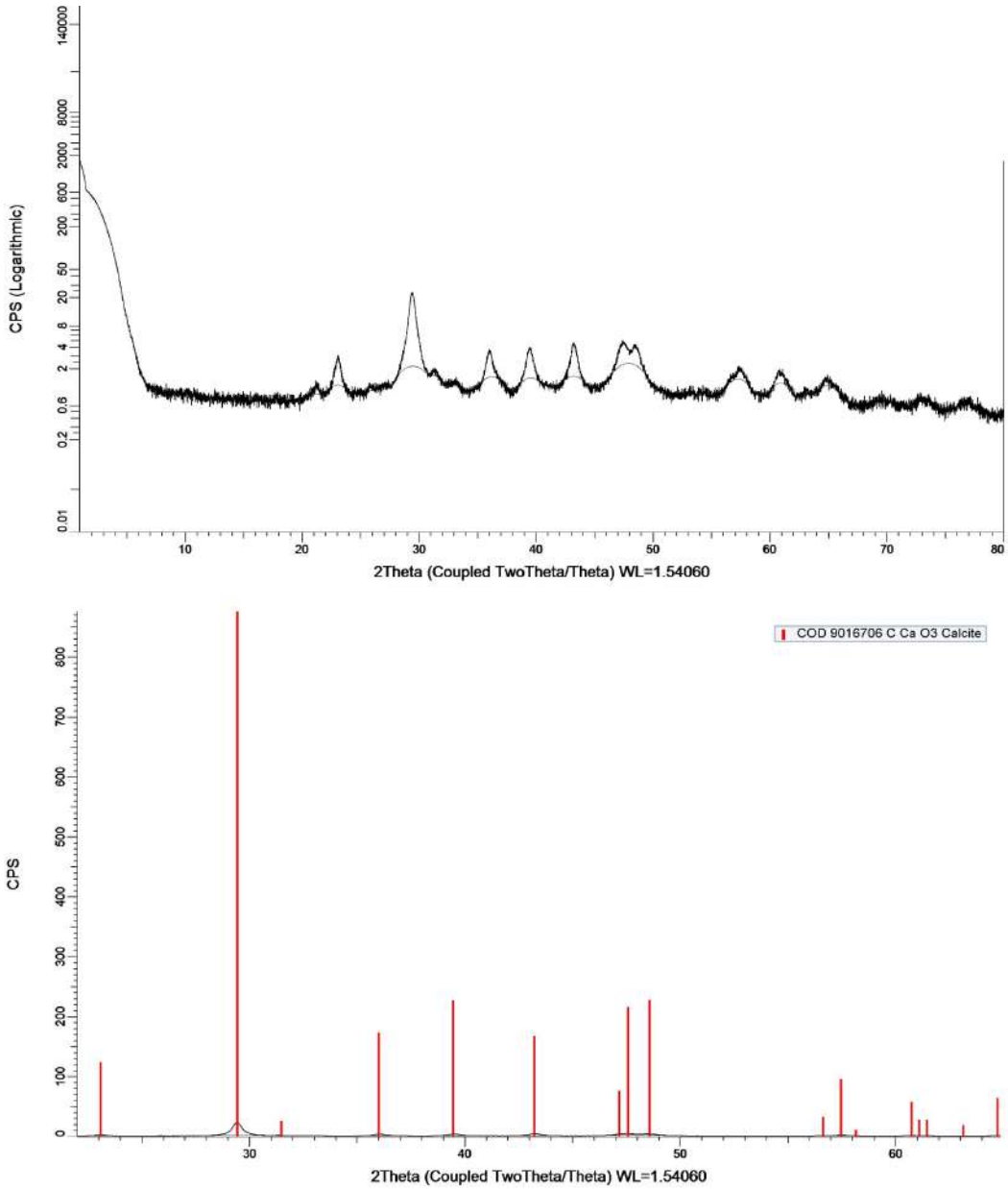

Fig. C.14 Top panel, XRD pattern of sample DW_14; bottom panel, phase identification performed using DIFFRAC.EVA.

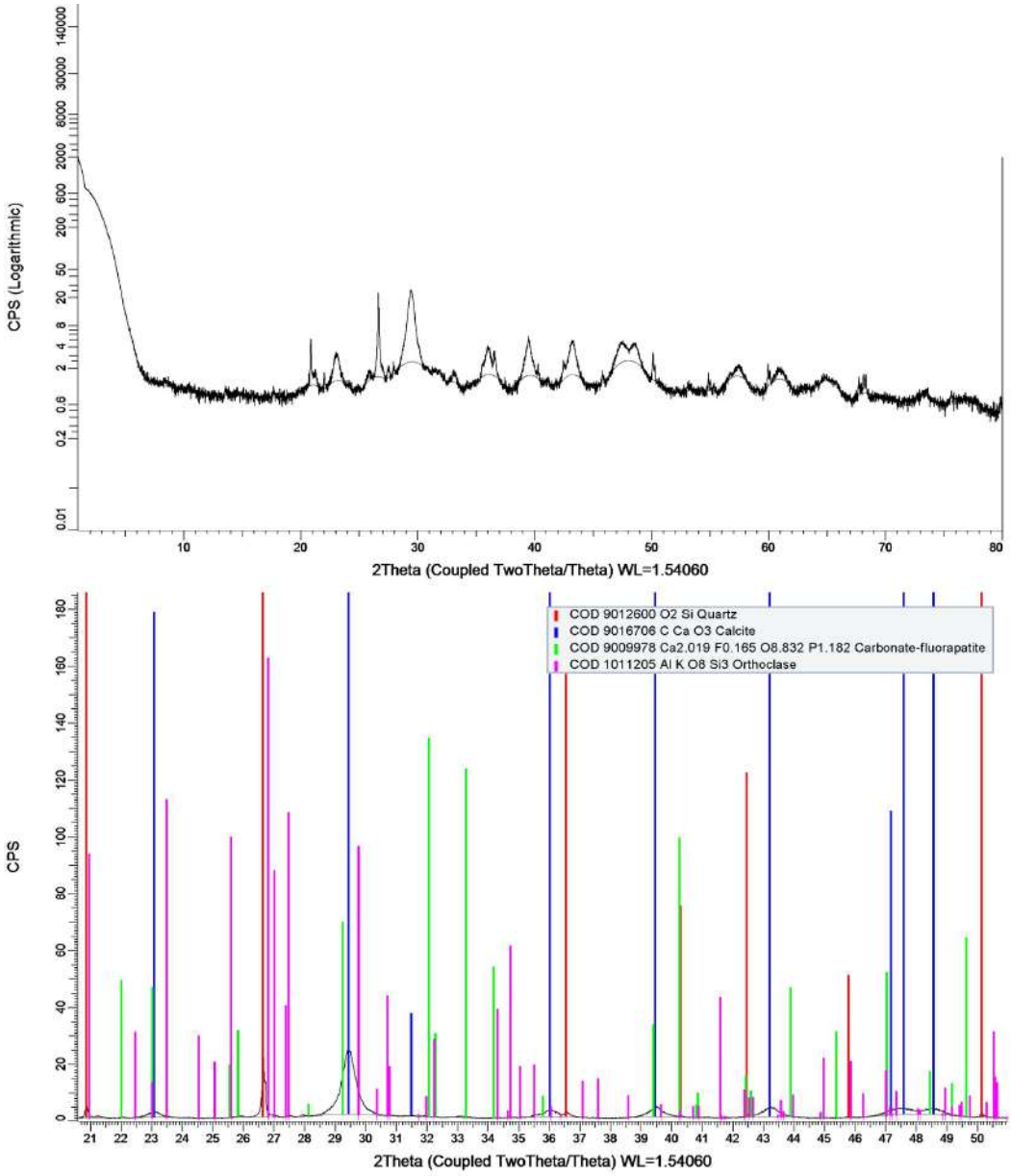

Fig. C.15 Top panel, XRD pattern of sample DW_15; bottom panel, phase identification performed using DIFFRAC.EVA.

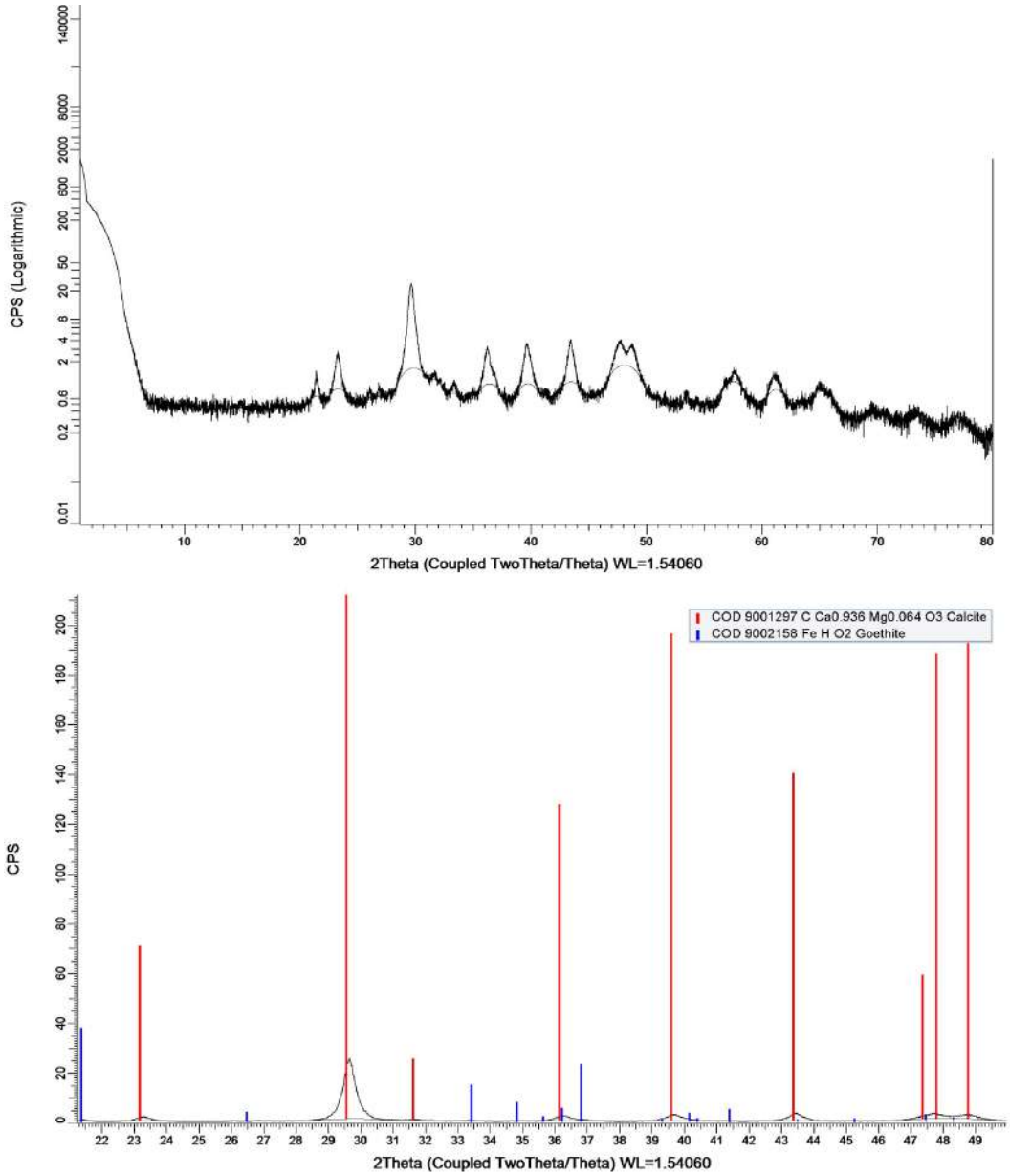

Fig. C.16 Top panel, XRD pattern of sample DW_16; bottom panel, phase identification performed using DIFFRAC.EVA.

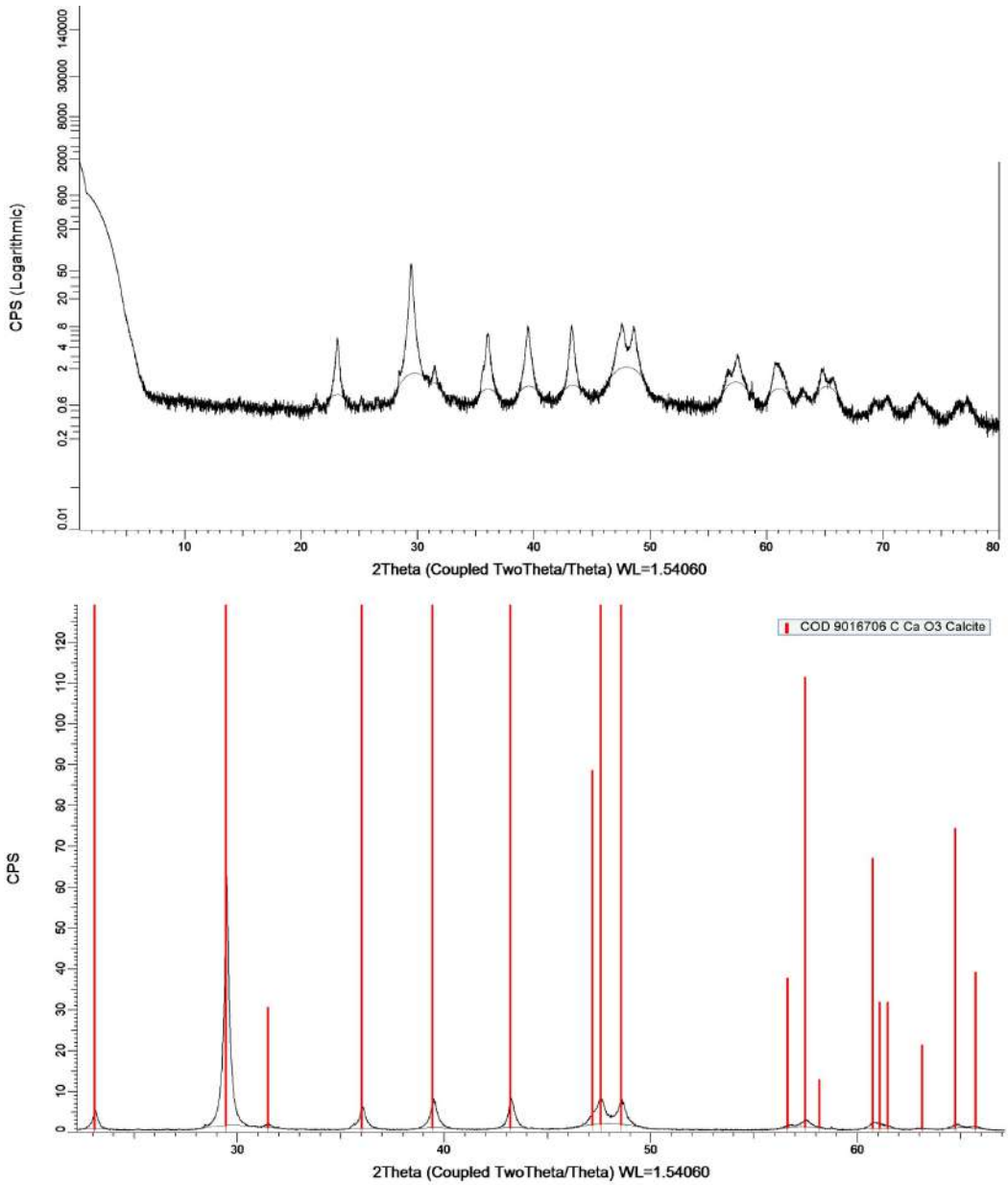

Fig. C.17 Top panel, XRD pattern of sample DW_17; bottom panel, phase identification performed using DIFFRAC.EVA.

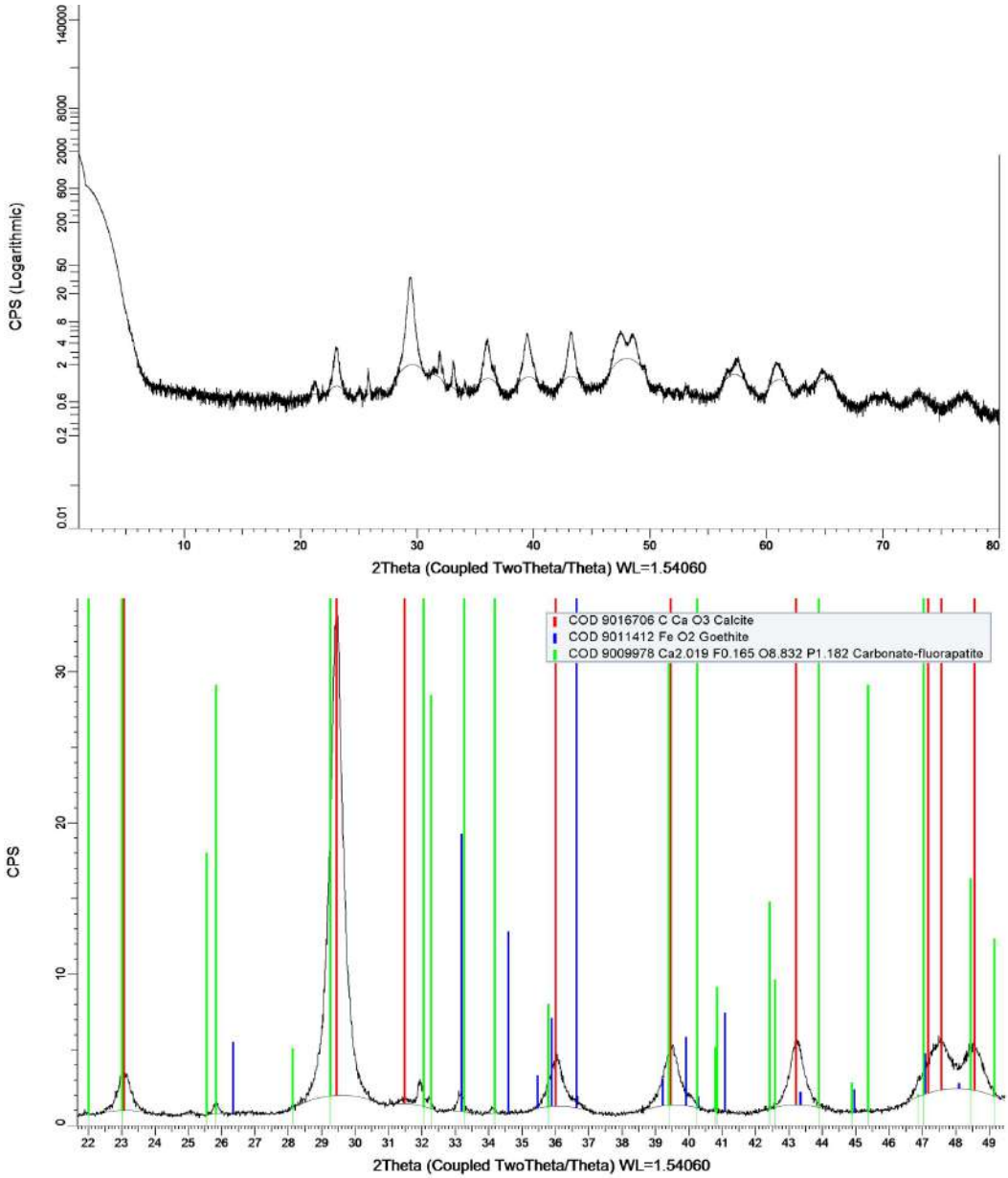

Fig. C.18 Top panel, XRD pattern of sample DW_18; bottom panel, phase identification performed using DIFFRAC.EVA.

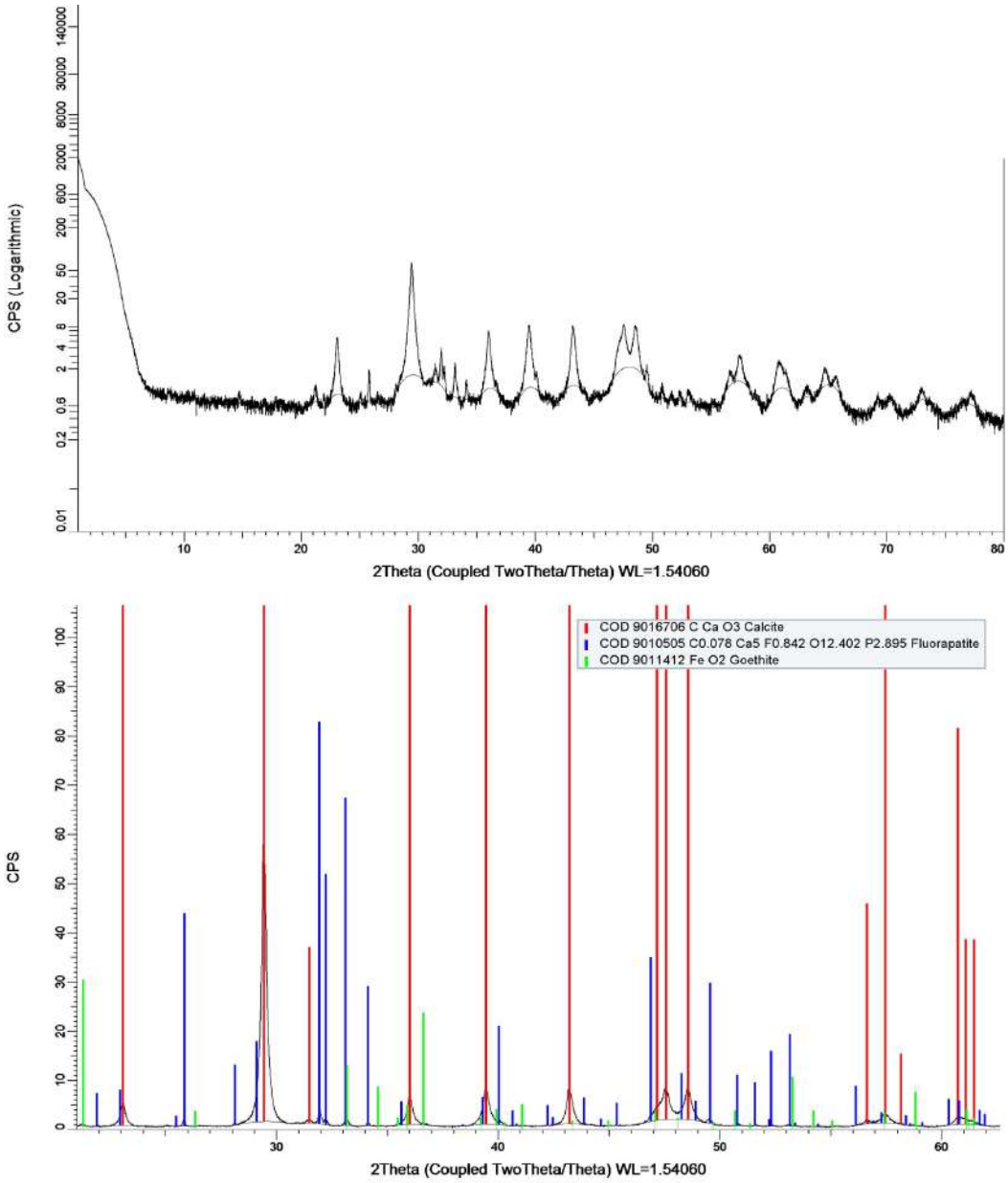

Fig. C.19 Top panel, XRD pattern of sample DW_19; bottom panel, phase identification performed using DIFFRAC.EVA.

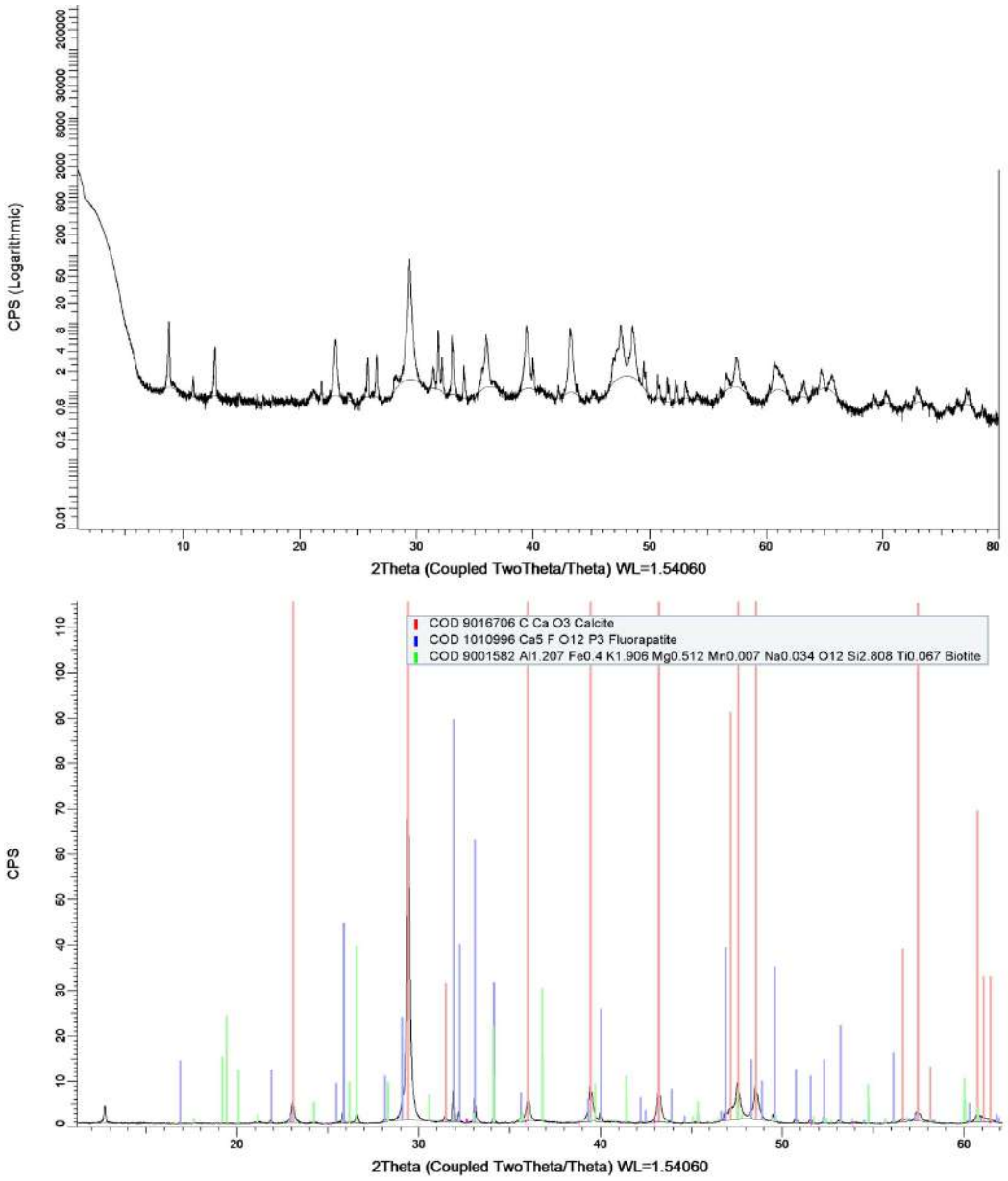

Fig. C.20 Top panel, XRD pattern of sample DW_20; bottom panel, phase identification performed using DIFFRAC.EVA.

Appendix D

pXRF patterns

Table D.1 REEs concentrations (ppm) and associated analytical uncertainties for the analysed samples. Reported values follow the original laboratory output notation (ND = not detected; < = below detection limit).

Sample ID	Y	Y ±	Nd	Nd ±	La	La ±	Ce	Ce ±	Pr	Pr ±	Sm	Sm ±	Eu	Eu ±	Gd	Gd ±
DW_01			3014	86	2049	28	3510	42	ND	<116	232	32	ND	<455	ND	<795
DW_02	82	10	54	9	119	11	194	14	ND	<44	ND	<34	ND	<331	ND	<581
DW_03			797	48	188	11	373	14	ND	<48	ND	<34	ND	<335	ND	<584
DW_04			1457	54	539	13	1125	18	ND	<59	89	23	ND	<338	ND	<587
DW_05			1150	54	1056	15	1987	22	ND	<45	174	24	ND	<354	ND	<621
DW_06	31	6.6	32	8.8	105	11	162	14	ND	<42	ND	<34	ND	<326	ND	<574
DW_07			2322	62	543	14	1116	19	ND	<94	98	25	ND	<381	ND	<670
DW_08			1113	49	407	11	976	16	ND	<47	73	23	ND	<335	ND	<588
DW_09			1317	55	694	14	1527	21	ND	<50	116	24	ND	<371	ND	<660
DW_10			1292	56	676	14	1479	21	ND	<48	91	25	ND	<401	ND	<717
DW_11	15	4.1	62	8.7	75	10	69	13	ND	<45	ND	<33	ND	<321	ND	<559
DW_12			1047	51	507	12	1105	17	ND	<45	103	23	ND	<342	ND	<600
DW_13			5176	111	1268	25	2935	42	ND	<208	238	34	ND	<459	ND	<979
DW_14			3606	89	2085	28	4180	48	ND	<120	272	31	ND	<458	ND	<795
DW_15			2293	60	607	14	1174	19	ND	<89	113	24	ND	<356	ND	<626
DW_16			2094	57	917	14	2000	22	ND	<58	163	24	ND	<342	ND	<596
DW_17			1441	51	776	13	1790	20	ND	<42	130	23	ND	<318	ND	<551
DW_18			1489	54	905	14	1701	21	ND	<55	127	23	ND	<346	ND	<602
DW_19			1228	51	741	13	1524	19	ND	<44	111	23	ND	<335	ND	<587
DW_20	159	14	84	9.5	237	11	365	15	ND	<52	52	24	ND	<371	ND	<662
OREAS-461-begin	56	2.3	1362	70	2475	29	3241	38	354	35	235	29	ND	<475	ND	<842
OREAS-462-begin	80	16	2141	68	3454	32	4534	42	649	31	316	26	ND	<407	ND	<722
OREAS-461-end			1379	60	2419	25	3182	32	327	30	196	25	ND	<412	ND	<734
OREAS-462-end			2236	66	3381	31	4463	41	650	31	300	26	ND	<397	ND	<706